



School of Civil Engineering of Barcelona
UPC BARCELONATECH

**Experimental and Numerical Analysis of the Unsaturated Soil
Shrinkage and Swelling Behaviour under Different
Compaction Conditions**

PhD Thesis

Submitted by:

Abdallah Najdi

Supervised by:

Alberto Ledesma

Pere Prat

Doctoral Program in GEOTECHNICAL ENGINEERING
Department of Civil and Environmental Engineering
Division of Geotechnical Engineering and Geosciences

Barcelona - May, 2023

To Mom and Dad

To Nour

Abstract

This thesis presents part of an ongoing investigation on the Thermo-Hydro-Mechanical behaviour and cracking of deformable unsaturated soils undergoing cycles of drying and wetting. An experimental approach was first adopted to understand the principal mechanisms of the THM behaviour of the unsaturated soils. One of the main principal variables characterising unsaturated soils is the negative porewater pressure (i.e., matric suction). Measuring and quantifying suction is of utmost importance, as it relates to the different constitutive relations and parameters. It is only possible, to this date, to carry out direct measurements at high suction range using High Capacity Tensiometers (HCTs). As such, the novel Northumbria HCTs (N-HCTs), with an extended suction measuring range (3.5 MPa), were sought after, as a first step in the experimental approach. The N-HCTs were then employed, in conjunction with other established and proposed direct and indirect suction measurement techniques, to provide the full suction measurement range for porewater content ranging from full saturation to dry conditions. Additionally, a unifying volumetric measurement technique is proposed, based on defining a mathematical model that describes the unique relationship between the void ratio and water content, referred to as the Soil Shrinkage and Swelling Curves (SSCs). Having a well-defined SSC, along with the full suction range measurements allows obtaining full experimental Soil Water Retention Curves (SWRCs), for the drying and wetting paths. SWRCs are one of the main characterising components of constitutive models for describing the unsaturated soil-moisture retaining capacity and flow in deformable porous material. Obtaining both the SWRCs and the SSCs provides the relationship between the evolution of the three main variables characterising the unsaturated soil behaviour: porewater, suction, and void ratio. Additionally, the desaturation and saturation rates were computed. Eventually a novel approach is proposed to divide the soil drying into five distinct stages, and the wetting to another four stages. Different yielding points are suggested to mark the transition between the proposed stages, where each transitional point holds a coupled hydromechanical significance. While some of the transitional points are considered conventional in the unsaturated soil mechanics domain, the role of the inflexion point of the SWRC is yet to be established. A strong correlation between the latter and the shrinkage limit is determined and verified for various soils from the literature encompassing different soil types, fabrics, and textures. Finally, the implication on the mechanical constitutive relations is studied, and a modification to the suction modulus, describing the effect of suction on the change in void ratio, is proposed.

The principal aim of this thesis was to finally achieve a fully capable numerical model that can replicate, to a high accuracy, the THM behaviour of soils exposed to external atmospheric

conditions. Having such a fully capable model would significantly reduce the uncertainties during the design process of any infrastructure and earthworks project using soils as engineered material (e.g., embankments, liners, slopes, landfills, etc.). To obtain such a powerful model, the constitutive equations and their corresponding parameters must be well-defined. Therefore, the implemented experimental campaign provided the mechanical component, the SWRCs, and the hydraulic, relative, and thermal conductivities for the soils to be simulated.

In addition to obtaining the constitutive parameters from the experimental soil characteristics, the applied atmospheric conditions on the soil surface were to be translated adequately into imposed numerical boundary conditions. This entailed translating all the relevant atmospheric factors: wind, temperature, relative humidity, rainfall, and solar radiation. Each of these factors were accounted for in the formulation of the imposed numerical boundary condition. The relevant formulation to translate these factors into a numerical boundary condition was obtained by comparing against established energy balance equations, and from meteorological science. The factors were translated into liquid infiltration rate from rainfall, imposed vapour concentration from atmospheric relative humidity, imposed heat flow rate from net solar radiation and atmospheric temperature, and transfer coefficients from wind speed and soil surface resistance. The developed model successfully captures with high responsiveness the THM behaviour and estimate the cracking intensity of the soil exposed to different atmospheric conditions. The simulations were carried out on seven different laboratory specimens in an environmental chamber with controlled imposed atmospheric conditions and one larger-scale field experiment exposed to free external atmospheric conditions. Having a developed model capable of simulating soils prepared at a wide variety of different initial conditions and exposed to varying imposed atmospheric conditions can prove to be a valuable feature to predict cracking and shrinkage behaviour for advanced designs of infrastructures using soils as engineering materials.

Resumen

Esta tesis presenta parte de una investigación en curso sobre el comportamiento termo-hidro-mecánico y el agrietamiento de suelos no saturados deformables sometidos a ciclos de secado y humectación. Primero se adoptó un enfoque experimental para comprender los principales mecanismos del comportamiento THM de los suelos no saturados. Una de las variables principales que caracterizan los suelos no saturados es la presión de poros negativa (es decir, la succión matricial). La medición y cuantificación de la succión es de suma importancia, ya que se relaciona con las diferentes leyes y parámetros constitutivos. Las mediciones directas de la presión de poros negativa para rangos de succión altos solo son posibles actualmente utilizando tensiómetros de alta capacidad (HCT). Para ello se han desarrollado los nuevos tensiómetros Northumbria HCT (N-HCT), con un rango de medición de succión extendido (3.5 MPa), como primer paso en el enfoque experimental. Los N-HCT se han empleado, junto con otras técnicas de medición de succión directa e indirecta ya establecidas o propuestas, para proporcionar el rango completo de medición de la succión que va desde la saturación total hasta las condiciones secas. Además, se ha propuesto una técnica de medición volumétrica unificadora, basada en la definición de un modelo matemático que describe la relación única entre el índice de poros y el contenido de agua, conocida como curvas de retracción e hinchamiento del suelo (SSC). Tener una SSC bien definida, junto con las mediciones de rango completo de succión permite obtener las curvas de retención (SWRC) experimentales completas, para las trayectorias de secado y mojado. Las SWRC son una de las principales componentes características de los modelos constitutivos para describir la capacidad de retención de humedad en suelos no saturados y el flujo en material poroso deformable. La obtención tanto de las SWRC como de las SSC proporciona la relación entre la evolución de las tres variables principales que caracterizan el comportamiento del suelo no saturado: agua intersticial, succión e índice de poros. Por otra parte, se han calculado también las velocidades de desaturación y saturación. Finalmente, se propone un enfoque novedoso para dividir el secado del suelo en cinco etapas características, y el mojado en otras cuatro etapas. Se sugieren diferentes puntos de transición para marcar el umbral entre las etapas propuestas, donde cada punto de transición tiene un significado hidromecánico acoplado. Si bien algunos de los puntos de transición son bien conocidos en el campo de la mecánica de suelos no saturados, el papel del punto de inflexión de la SWRC aún no se ha establecido. Se ha determinado y verificado una buena correlación entre este último y el límite de retracción para varios suelos a partir de la literatura que abarca diferentes tipos de suelo, estructuras y texturas. Finalmente, se ha estudiado la implicación sobre las relaciones constitutivas mecánicas y se ha propuesto una modificación del módulo de succión, describiendo el efecto de la succión sobre los cambios del índice de poros.

El objetivo principal de esta tesis ha sido la obtención de un modelo numérico totalmente capaz que pueda replicar, con una alta precisión, el comportamiento THM de los suelos expuestos a condiciones atmosféricas externas. Tener un modelo tan capaz reduciría significativamente las incertidumbres durante el proceso de diseño de cualquier proyecto de infraestructura y movimiento de tierras utilizando suelos como material de ingeniería (por ejemplo, terraplenes, revestimientos, taludes, vertederos, etc.). Para obtener un modelo de calidad, las ecuaciones constitutivas y sus parámetros correspondientes deben estar bien definidos. La campaña experimental implementada proporcionó el componente mecánico, las SWRC y las conductividades hidráulicas y térmicas para los suelos a simular.

Además de representar numéricamente las características del suelo en términos de los parámetros constitutivos, las condiciones atmosféricas aplicadas en la superficie del suelo deben traducirse adecuadamente en condiciones de contorno impuestas. Para ello es necesario implementar todos los factores atmosféricos relevantes: viento, temperatura, humedad relativa, precipitaciones y radiación solar. Todos estos factores se han tenido en cuenta en la formulación de las condiciones de contorno impuestas. La formulación relevante para implementar estos factores en una condición de contorno numérica se obtuvo comparando con las ecuaciones de balance de energía clásicas y con las de la meteorología. Estos factores se tradujeron en la velocidad de infiltración del agua de lluvia, la concentración de vapor impuesta a partir de la humedad relativa atmosférica, la velocidad del flujo de calor impuesto a partir de la radiación solar neta y de la temperatura atmosférica, y los coeficientes de transferencia a partir de la velocidad del viento y la resistencia de la superficie del suelo. El modelo desarrollado reproduce con precisión el comportamiento THM y permite estimar la intensidad de agrietamiento del suelo expuesto a diferentes condiciones atmosféricas. Las simulaciones con siete probetas de laboratorio diferentes se llevaron a cabo en una cámara ambiental con condiciones atmosféricas impuestas controladas y un ensayo de campo a mayor escala expuesto a condiciones atmosféricas externas libres. Un modelo capaz de simular suelos preparados con una amplia variedad de condiciones iniciales diferentes, y expuestos a diferentes condiciones atmosféricas es una herramienta valiosa para predecir el comportamiento del agrietamiento y retracción en el proceso de diseños avanzados de infraestructuras que utilizan suelos como materiales de ingeniería.

Resum

Aquesta tesi presenta part d'una recerca en curs sobre el comportament termo-hidro-mecànic i l'esquerdament de sòls no saturats deformables sotmesos a cicles d'assecamment i mullat. Primer es va adoptar un enfocament experimental per comprendre els principals mecanismes del comportament THM dels sòls no saturats. Una de les variables principals que caracteritzen els sòls no saturats és la pressió de porus negativa (és a dir, la succió matricial). El mesurament i quantificació de la succió té molta importància, ja que es relaciona amb les diferents lleis i paràmetres constitutius. Els mesuraments directes de la pressió de porus negativa per a rangs de succió alts només són possibles actualment utilitzant tensiòmetres d'alta capacitat (HCT). Per a això s'han desenvolupat els nous tensiòmetres Northumbria HCT (N-HCT), amb un rang de mesurament de succió estès (3.5 MPa), com a primer pas en l'enfocament experimental. Els N-HCT s'han emprat, juntament amb altres tècniques de mesurament de succió directa i indirecta ja establertes o proposades, per proporcionar el rang complet de mesurament de la succió que va des de la saturació total fins a les condicions seques. A més, s'ha proposat una tècnica de mesurament volumètric unificador, basada en la definició d'un model matemàtic que descriu la relació única entre l'índex de porus i el contingut d'aigua, coneguda com a corbes de retracció i inflament del sòl (SSC). Tenir una SSC ben definida, juntament amb els mesuraments de rang complet de succió permet obtenir les corbes de retenció (SWRC) experimentals completes, per a les trajectòries d'assecamment i mullat. Les SWRC són una de les principals components característiques dels models constitutius per a descriure la capacitat de retenció d'humitat en sòls no saturats i el flux en material porós deformable. L'obtenció tant de les SWRC com de les SSC proporciona la relació entre l'evolució de les tres variables principals que caracteritzen el comportament del sòl no saturat: aigua intersticial, succió i índex de porus. D'altra banda, s'han calculat també les velocitats de desaturació i saturació. Finalment, es proposa un enfocament novedós per dividir l'assecamment del sòl en cinc etapes característiques, i el mullat en quatre etapes. Se suggereixen diferents punts de transició per marcar el llindar entre les etapes proposades, on cada punt de transició té un significat hidromecànic acoblat. Si bé alguns dels punts de transició són ben coneguts en el camp de la mecànica de sòls no saturats, el paper del punt d'inflexió de la SWRC encara no s'ha establert. S'ha determinat i verificat una bona correlació entre aquest últim i el límit de retracció per a diversos sòls a partir de la literatura que abasta diferents tipus de sòl, estructures i textures. Finalment, s'ha estudiat la implicació sobre les relacions constitutives mecàniques i s'ha proposat una modificació del mòdul de succió, descrivint l'efecte de la succió sobre els canvis de l'índex de porus.

L'objectiu principal d'aquesta tesi ha estat l'obtenció d'un model numèric totalment capaç que pugui replicar, amb una alta precisió, el comportament THM dels sòls exposats a condicions

atmosfèriques externes. Tenir un model tan capaç reduiria significativament les incerteses durant el procés de disseny de qualsevol projecte d'infraestructures i moviment de terres utilitzant sòls com material d'enginyeria (per exemple, terraplens, revestiments, talussos, abocadors, etc.). Per obtenir un model de qualitat, les equacions constitutives i els seus paràmetres corresponents han d'estar ben definits. La campanya experimental implementada va proporcionar el component mecànic, les SWRC i les conductivitats hidràuliques i tèrmiques per als sòls a simular.

A més de representar numèricament les característiques del sòl en termes dels paràmetres constitutius, les condicions atmosfèriques aplicades a la superfície del sòl s'han de traduir adequadament en condicions de contorn imposades. Per a això és necessari implementar tots els factors atmosfèrics rellevants: vent, temperatura, humitat relativa, precipitacions i radiació solar. Tots aquests factors s'han tingut en compte en la formulació de les condicions de contorn imposades. La formulació rellevant per implementar aquests factors en una condició de contorn numèrica s'ha obtingut comparant amb les equacions de balanç d'energia clàssiques i amb les de la meteorologia. Aquests factors s'han traduït en la velocitat d'infiltració de l'aigua de pluja, la concentració de vapor imposada a partir de la humitat relativa atmosfèrica, la velocitat del flux de calor imposat a partir de la radiació solar neta i de la temperatura atmosfèrica, i els coeficients de transferència a partir de la velocitat del vent i la resistència de la superfície del sòl. El model desenvolupat reproduïx amb precisió el comportament THM i permet estimar la intensitat d'esquerdament del sòl exposat a diferents condicions atmosfèriques. Les simulacions amb set provetes de laboratori diferents es van dur a terme en una cambra ambiental amb condicions atmosfèriques imposades controlades i un assaig de camp a major escala exposat a condicions atmosfèriques externes lliures. Un model capaç de simular sòls preparats amb una àmplia varietat de condicions inicials diferents, i exposats a diferents condicions atmosfèriques és una eina valuosa per predir el comportament de l'esquerdament i retracció en el procés de dissenys avançats d'infraestructures que utilitzen sòls com materials de enginyeria.

Résumé

Cette thèse fait part d'une investigation en cours concernant le comportement Thermo-Hydro-Mécanique et la fissuration de sols déformables et non saturés subissant des cycles de séchage et mouillage. Une approche expérimentale a été initialement adoptée afin de comprendre les principaux mécanismes du comportement THM des sols non saturés. Une des variables principales caractérisant les sols non saturés est la pression capillaire négative (c'est à dire, la succion matricielle). La mesure et la quantification de la succion est d'une importance primordiale, étant donné qu'elle est liée aux différentes lois et paramètres constitutifs. Les mesures directes de la pression capillaire négative à haute succion sont uniquement possibles actuellement utilisant des tensiomètres à haute capacité (THC). En tant que tels, les nouveaux Northumbria HCT (N-HCT), avec un intervalle de mesure de succion étendu (3.5 MPa), comme premier pas de l'approche expérimentale. Les N-HCT ont alors été utilisés, en conjonction avec d'autres techniques de mesure de succion directe et indirecte, déjà établies ou proposées, afin de fournir l'étendue complète de mesure de la succion depuis la saturation totale jusqu'aux conditions sèches. De plus, une mesure volumétrique unificatrice est proposée, basée sur la définition d'un modèle mathématique qui décrit la relation unique entre la porosité et la teneur en eau, connue sous le nom de courbes de retrait et gonflement du sol (SSC). Avoir une SSC bien définie, ainsi que les mesures de succion de complète étendue, permet d'obtenir les courbes de rétention (SWRC) expérimentales complètes, pour les trajectoires de séchage et mouillage. Les SWRC sont une des composantes caractéristiques principales des modèles constitutifs pour décrire la capacité de rétention d'humidité dans les sols non saturés et le flux dans le matériel poreux déformable. L'obtention des SWR et des SSC fournit la relation entre l'évolution des trois principales variables caractérisant le comportement du sol non saturé : eau interstitielle, succion et indice de porosité. D'autre part, les vitesses de désaturation et saturation ont été calculées. Enfin, une approche novatrice pour diviser le séchage du sol en cinq étapes, et le mouillage en quatre étapes, est proposée. Différents points de transition sont suggérés afin de marquer le passage de seuil entre les étapes proposées, où chaque point de transition porte une signification hydromécanique couplée. Alors que certains points de transition sont considérés conventionnels dans le domaine des mécaniques de sols non saturés, le rôle du point d'inflexion des SWRC reste à établir. Une forte corrélation entre celui-ci et la limite de retrait est déterminée et vérifiée pour divers sols de la littérature englobant différents types de sols, structures et textures. Enfin, l'implication sur les liens mécaniques constitutifs est étudiée et une modification au module de succion, décrivant l'effet de succion sur le changement de l'indice de porosité, est proposée.

L'objectif principal de cette thèse est finalement d'établir un modèle numérique complètement capable qui puisse répliquer, à un niveau de précision élevée, le comportement THM des sols exposés aux conditions atmosphériques externes. Avoir un tel modèle réduirait de manière significative les incertitudes présentes dans le processus d'élaboration de tout projet d'infrastructure ou de mouvement de la terre utilisant les sols en tant que matériaux d'ingénierie (par exemple, digue, revêtements, pentes, décharges, etc.). Afin d'obtenir un tel modèle puissant, les équations constitutives et leur paramètres correspondants doivent être bien définis. La campagne expérimentale implémentée fournit la composante mécanique, les SWRC ainsi que les conductivités hydrauliques et thermiques des sols à simuler.

En plus de représenter de manière numérique les caractéristiques du sol en termes de paramètres constitutifs, les conditions atmosphériques appliquées sur la surface du sol doivent être traduites de manière adéquate en conditions de contour imposées. A cette fin, il est nécessaire d'implémenter tous les facteurs atmosphériques : vent, température, humidité relative, précipitation et radiation solaire. Tous ces facteurs ont été pris en considération dans la formulation des conditions de contour imposées. La formulation pertinente pour traduire ces facteurs en condition de contour numériques a été obtenue en comparant aux équations établies de balance d'énergie, et des sciences météorologiques. Les facteurs ont été traduits en vitesse d'infiltration de l'eau de pluie, la concentration de vapeur imposée à partir de l'humidité relative atmosphérique et les coefficients de transfert de la vitesse du vent et la résistance de la superficie du sol. Le modèle développé capture avec précision le comportement THM et estime l'intensité de fissuration du sol expose aux différentes conditions atmosphériques. Les simulations ont été faites sur sept spécimens de laboratoires différents dans une chambre environnementale avec des conditions atmosphériques contrôlées ainsi que dans le cadre d'une expérimentation terrain à plus large échelle soumise aux conditions atmosphériques externes libres. Un modèle capable de simuler des sols préparés sous une grande variété de conditions initiales et soumis à des conditions atmosphériques variées est un outil de valeur dans la prédiction du comportement de fissuration et retrait pour les élaborations avancées d'infrastructures utilisant des sols en tant que matériaux de construction.

Acknowledgements

En primer lugar, quiero agradecer a mis directores, Alberto Ledesma y Pere Prat, sin ellos no hubiera podido realizar esta tesis. Gracias por darme la oportunidad, por su paciencia y por estar un sistema de soporte magnificante a todos niveles. Everything always went so smoothly knowing that you are always there no matter what to answer my concerns. I honestly could never wish for better supervisors!

El trio fantástico del confinamiento y las parrilladas famosas: Stefano, David, y Alessandro. ¡Gracias caballeros por todo, gracias por hacer los últimos años tan agradables y por el apoyo técnico y emocional mientras todo! Agustín (el bomber), gracias por ayudarme a iniciar mi investigación y gracias por ser un gran amigo! I would also like to thank my UPC and Newcastle comrade Lluís Monforte for the support. Raul Oorthuis (el pavo real), moltes gràcies per les aventures! I would like also to thank Ivan Puig, Hao Zeng (lets publish at least 10 papers together this year... at least...), Davide y Paul (best baristas), and the whole UPC laboratory team especially Josbel, Rodrigo, Ferran, Aris Leidy, Clara, and Laura for their help.

Joao and Chryssa: thank you guys for all the support, guidance and valuable advice in life and research and career path. Joao, thank you for having me in Northumbria University and taking the time to teach me about the amazing sensors! I would like to thank my Newcastle roomie, gym partner and programming buddy Babis for the best fresh frozen pizzas. Bless you!

I would like to thank Mo Rouainia for offering me the opportunity to work with him once again which is always a pleasure. I will always have a lot to learn from you.

I want to thank my friends in Lebanon (P, H, B, S, W, C, M). Thank you guys for all the support, and of course for always the best laughs I can get. I hope you get an idea now on what I have been doing in Barcelona the past few years... I know wold at least does..

I would like to take the opportunity to thank my parents in law Wajdi and Ghada for their support.

Finally, I would like to thank my family. First, and above all, I want to thank my mother and father. Mom, Dad, without you none of this would have been possible. Thank you for encouraging me and believing in me. I hope I can one day repay you for all what you have done to me and given me, but we all know that even with 10 more lifetimes it is still going to be impossible. I want to thank my amazing brother and sister, and the new little nephew addition, and my amazing cousins. You guys are my support system. I am proud to be your older brother,

and I hope I can make you one day as proud of me as I am of you. Finally, I want to of course thank my love and my beautiful Nour. Thank you for all the support, patience, trust, and encouragement during the past years. It was a difficult path made much easier and enjoyable having you by my side. I cannot imagine doing this without you. Thank you for loving me so much and being my number 1 supporter and fan. I love you.

Table of Contents

Abstract	i
Resumen	iii
Resum	v
Résumé	vii
Acknowledgements	ix
Table of Contents	viii
List of Figures	xv
List of Tables	xxi
List of notations	xxiii
List of Relevant Publications	xxviii
1. Introduction	1
1.1. Background.....	4
1.2. Motivation and objectives.....	5
1.3. Scope of the study.....	6
1.4. Thesis organization.....	7
2. The Use of Novel High Capacity Tensiometers	10
2.1. Introduction.....	11
2.2. Tensiometric measurement principles.....	14

2.2.1. AEV	15
2.3. N-HCT AND C-HCT designs	16
2.4. Building the datalogger	18
2.5. Pressure vessel and connections.....	20
2.6. First Saturation, calibration and first cavitation	21
2.7. Cavitation tests	22
2.8. Post-cavitation re-saturation.....	24
2.9. Soil suction measurements	25
2.9.1. Discrete measurements.....	25
2.9.2. Continuous drying	27
2.10. Conclusions	30
3. Laboratory Experimental Campaign: Evaluating Different Suction and Volumetric Measurement Techniques.....	32
3.1. Introduction	33
3.2. Materials and methods	35
3.2.1. Soil characteristics.....	35
3.2.2. Soil batches	36
3.2.3. Suction measurement techniques	38
3.2.4. Volumetric measurement techniques	46
3.3. Evaluating the novel N-HCT performance	51
3.3.1. Discrete versus continuous drying methods.....	51
3.3.2. Comparing against matric suction measurement techniques.....	55

3.3.3. Continuous uninterrupted suction measurement in large-scale soil specimens	58
3.3.4. Osmotic suction.....	63
3.3.5. VE Technique: evaluation of equilibration times.....	64
3.4. Volumetric measurements.....	65
3.4.1. Evaluating direct and indirect volumetric measurement techniques for determining SSC.....	65
3.4.2. SSC modelling.....	69
3.5. Obtaining the SWRCs	70
3.6. Conclusions	75
4. The Role of Inflexion-Point of the SWRC in the Shrinkage and Swelling Mechanism of Partially Saturated Soils.....	79
4.1. Introduction.....	80
4.2. Experimental campaign.....	82
4.2.1. Properties of the soils	82
4.2.2. “Porewater – Voids – Suction” datasets and dependence	83
4.3. Mathematical data fitting	86
4.4. Desaturation stages and the corresponding transition-points	88
4.4.1. Stage-1 (initial to saturation-suction).....	90
4.4.2. Stage-2 (saturation-suction to AEV)	91
4.4.3. Stage-3 (AEV to ‘dry-IP’/’SL’)	92
4.4.4. Stage-4 (dry-IP to residual-suction)	93
4.4.5. Stage-5 (residual-suction to dry conditions)	94

4.5. Saturating (wetting) stages and the corresponding transition points.....	94
4.5.1. Stage-1 (dry conditions to WEV).....	96
4.5.2. Stage-2 (WEV to wetting-IP).....	97
4.5.3. Stage-3 (wetting-IP to air expulsion value).....	97
4.5.4. Stage-4 (AXV to constant saturation).....	98
4.5. Inflexion-points of the SWRC.....	98
4.5.1. Locating the ‘inflexion-point’ analytically.....	99
4.5.2. Validation.....	100
4.5.3. Fitting divergence.....	103
4.6. Constitutive relations.....	105
4.7. Phenomenon of hysteresis.....	108
4.7.1. Saturation-suction and AXV.....	109
4.7.2. The inflexion points.....	110
4.7.3. The AEV and the wetting path inflexion point.....	110
4.7.4. The residual suction and the WEV.....	111
4.7.5. The AEV and the AXV.....	111
4.8. Implications on geotechnical design.....	111
4.8.1. Applicability to different initial conditions.....	111
4.8.2. Estimate of the shrinkage potential.....	112
4.8.3. Estimate of ψ_{IP} through ψ_{SL}	112
4.9. Conclusion.....	112
5. Numerical Simulation of Soil Desiccation Behaviour.....	114

5.1. Introduction	115
5.2. Numerical model	117
5.2.1. CODE_BRIGHT	117
5.2.2. Balance equations.....	119
5.2.3. Constitutive equations and equilibrium constraints	123
5.2.4. Boundary conditions	131
5.2.5. Model geometry	140
5.3. Experimental test.....	142
5.3.1. Soil characteristics.....	142
5.3.2. Environmental chamber	142
5.3.3. The drying specimen	142
5.3.4. Experimental results.....	142
5.3.5. Imposed conditions in the environmental chamber.....	143
5.3.6. Internal wind circulation	143
5.4. Numerical simulations.....	144
5.4.1. Material constitutive parameters	145
5.4.2. Boundary conditions	145
5.4.3. Discussion	149
5.5. Constitutive parametrical study.....	151
5.5.1. Effect of porosity change on intrinsic permeability	152
5.5.2. Effect of porosity change on SWRCs.....	153
5.5.3. Liquid phase relative permeability	154
5.5. Conclusions	156

6. Numerical Simulation of Laboratory Desiccation Tests and a Large-Scale Field Experiment.....	157
6.1. Introduction	158
6.2. Experiments.....	159
6.2.1. Environmental chamber tests	159
6.2.3. Large-scale field experiment.....	163
6.2.4. Constitutive parameters.....	165
6.3. Numerical approach	167
6.4. Boundary conditions	169
6.4.1. Flux boundary conditions.....	169
6.4.3. Heat transfer	173
6.4.4. Rainfall.....	176
6.4.5. Lateral boundary: evaporation from cracks.....	177
6.5. Constitutive equations	179
6.5.1. Mechanical component	179
6.5.2. Thermo-hydraulic component.....	180
6.6. Results.....	182
6.6.1. Suction results	182
6.6.2. Gravimetric water content results.....	184
6.6.3. CIF results	184
6.6.4. Temperature results	187
6.6.5. Field experiment results	188
6.7. Discussion	191

6.8. Conclusion.....	193
7. Thesis Conclusions	195
7.1. Brief summary.....	195
7.1.2. Chapter 2: Novel High Capacity Tensiometer	195
7.1.3. Chapter 3: Laboratory Experimental Campaign: Evaluating Different Suction and Volumetric Measurement Techniques.....	196
7.1.4. Chapter 4: The Role of Inflexion-Point of the SWRC in the Shrinkage and Swelling Mechanism of Partially Saturated Soils	197
7.1.5. Chapter 5: Numerical Simulation of the Soil Desiccation Behaviour.....	198
7.1.6. Chapter 6: Numerical Simulation of Laboratory Desiccation Tests at Different Initial conditions, and one Large-Scale Field Experiment Exposed to Free Atmospheric Conditions	198
7.2. General conclusion.....	199
7.3. Future works.....	200
7.3.1. Experimental	201
7.3.2. Environmental chamber	201
7.3.3. Field experiments	202
7.3.4. Numerical	202
References	203

List of Figures

Figure 1-1. Images of desiccation cracks portrayed on: (a) (NASA, 2005); (b) (Reuters, 2021) and (Copernicus, 2022); (c) (The World Bank, 2021); and (d) (EDF, 2019).	2
Figure 1-2. Mastcam (sol 1555) and Mars Hand Lens Imager (MAHLI) images of Old Soaker (OS) rock slab, Mars (Stein et al., 2018).....	3
Figure 1-3. Comparison between large features on the floor of Mawrth Vallis (left, HiRISE image PSP_006755_2030) and the large desiccation features in Lucerne Dry Lake in California, US (El-Maarry et al., 2014).....	3
Figure 2-1 (a) Contact angle; and (b) Capillary rise of water (Marinho et al., 2008).	15
Figure 2-2. Imperial College HCT (Ridley & Burland, 1993).	17
Figure 2-3. Schematics for the (a) N-HCT and (b) the C-HCT designs (sizes in mm); and (c) image of the sensor.....	17
Figure 2-4. (a) PX600 pressure transducer, and the (b) design scheme.....	18
Figure 2-5. Datalogger parts: (a) signal conditioner, (b) power supply, and (c) NI USB 6000. 19	
Figure 2-6. Assembled setup in the laboratories of Northumbria University: (a) the two N-HCTs in the saturation vessel; (b) the datalogger; and (c) the data acquisition computer.	19
Figure 2-7. Design scheme of the pressure vessel.....	20
Figure 2-8. The N-HCT saturation setup.....	21
Figure 2-9. Evaporation test with N-HCT and C-HCT after initial saturation (Mendes et al., 2022).	23
Figure 2-10. Pore size distributions of the N-HCT and C-HCT ceramic filters used, obtained using Mercury Intrusion Porosimetry (Mendes et al., 2022).	24
Figure 2-11. Discrete measurements setup.....	26
Figure 2-12. Best overall evaporation test results with the N-HCTs at UPC-Barcelona Tech (Mendes et al., 2022).....	27

Figure 2-13. Schematic of the setup used the for continuous drying test.....	28
Figure 2-14. Continuous drying test with N-HCTs on the Barcelona silty clay specimen prepared from slurry with an initial water content of 34% and on four specimens from the Agròpolis clay, dynamically compacted using the Proctor hammer with an initial water content of 19% (Mendes et al., 2022).	29
Figure 3-1. Compaction curves and initial conditions of the different specimens to be tested for SWRCs and SSCs.	38
Figure 3-2. UMS T5 sensor components (UMS AG, 2018).....	39
Figure 3-3. MPS-6 sensor components.	40
Figure 3-4. WP4-T and one of the specimens in the stainless-steel mould.....	41
Figure 3-5. 5TE Decagon moisture, temperature, and electrical conductivity sensor.....	43
Figure 3-6. Soil specimens in Dew-point Hygrometer recipients hanging over NaCl solutions with different concentrations.....	44
Figure 3-7. (a) Desiccators with the NaCl solution and (b) core samples prepared from different initial conditions in the closed desiccators, hanging above saline solution.	45
Figure 3-8. DIA procedure applied to a separate specimen.	47
Figure 3-9. Schematic representation of a soil shrinkage characteristic curve of a non-structured soil (solid line, 1) and a well-structured soil (dashed line, 2). The subscripts S, N, R, and Z, indicate the limits of structural, normal, residual and zero-shrinkage stages (Cornelis et al., 2006)..	49
Figure 3-10. Discrete specimen preparation.....	52
Figure 3-11. (a) Continuous drying setup sketch, with (b) Vertical, and (c) horizontal shrinkage surface images.....	53
Figure 3-12. Continuous versus Discrete drying methods. ...	54
Figure 3-13. Scheme of the second continuous drying setup.....	55
Figure 3-14. Image of the second continuous drying laboratory setup.	56

Figure 3-15. Images of (a) horizontal shrinkage; and (b) vertical shrinkage.....	56
Figure 3-16. Different suction readings from the different sensors over the experiment time. .	57
Figure 3-17. Schematic cross-section of the environmental chamber sample.	58
Figure 3-18. Environmental chamber sample (a) image top view (drying initiation); and (b) image top view (end of first drying stage). ...	60
Figure 3-19. (a) Complete continuous suction evolution during drying and wetting cycles; and (b) Early-stage suction measured using different sensors at different locations during first and second drying (see Figure 3.16 for sensor position). *z: distance from top soil surface.	62
Figure 3-20. Changes in the “global” electrical conductivity and water content in the environmental chamber setup.....	63
Figure 3-21. Total suction equilibration times for the VE method, measured using Hygrometer.	64
Figure 3-22. Experimental SSCs for soil batches (a) A-S3; (b) A-S4; and (c) A-MP3. (see Table 3.4 for information on the soil batches). ...	67
Figure 3-23. Full range SWRCs for soil batches (a) A-S3; (b) A-S4; and (c) A-MP3.	73
Figure 3-24. Additional SWRCs for specimens (a) A-S1; (b) A-S2; (c) A-MP1; (d) A-MP2; (e) A-SH1; (f) A-SH2; (g) A-LL; and (h) A-SL.	74
Figure 4-1. 3D schematic example of $(\theta Sr - e - \psi)$ dataset for Agròpolis soil in the drying path, with projections on the SWRC, SSC and SVC 2D domains.....	84
Figure 4-2. 3D schematic of the (a) $(\theta V - e - \psi)$ dataset showing the wetting path and (b) a different angle of the 3D scheme showing the hysteresis in the 3D domain.	85
Figure 4-3. Experimental SWRC for Agropolis soil, compacted near standard Proctor optimum (A1). Model-vG and -FX SWRC fittings are shown along with the desaturation rate (1 st derivative), desaturation rate slope (2 nd derivative), and the four transition points from Figure 4.1.....	89

Figure 4-4. Generalised conceptual model of desaturation shrinkage stages, indicating the mechanical shrinkage regime (preceded by the order number), and the corresponding transition point (in <i>italic</i>). The dotted-line shapes depict the original location of particles.	90
Figure 4-5. Wetting SWRC with corresponding saturation-rate, saturation-rate slope, the five wetting phases and the four transition-points from Figure 4.2.....	96
Figure 4-6. SVCs and SWRCs to the saturation degree scale for the Agròpolis soil [CL], for (a) A1 and A2; and (b) A3 and A4 initial conditions.	100
Figure 4-7. (a) The USCS classification of the different soils used for the model validation. (b) Validation of the inflexion point of the wetting path based on the θ_{s_r} -SWRC fitting parameters using model-vG; and of the drying paths using (c) model-FX and (d) model-vG.....	103
Figure 4-8. Fit-divergence for the different moisture-content scales for (a) model-FX; and (b) model-vG.....	104
Figure 4-9. The drying SVC with the projection of the inflexion point.....	84
Figure 5-1. Thermo-Hydraulic processes in an unsaturated porous medium.....	119
Figure 5-2. Constructed model geometry showing (a) the mesh, boundary conditions, and global gravimetric water content calculation on an element; and (b) the post-processor geometrical reflection analysis method for sensors location.....	141
Figure 5-3. Anemometer mounted inside the environmental chamber for wind measurements under test conditions similar to the original.	144
Figure 5-4. Node-release technique replicating the sequential crack-opening.....	148
Figure 5-5. Final simulation results showing numerical versus experimental results for the (a) global gravimetric water content loss; (b) early stage suction; and (c) soil relative humidity..	150
Figure 5-6. Intrinsic permeability change with decrease in porosity, following equation 5.58.	153
Figure 5-7. Liquid phase relative permeability dependence on liquid saturation degree, using Corey's power law.	155

Figure 6-1. Proctor compaction curves for the Agròpolis soil, showing the specimens initial conditions.....	160
Figure 6-2. Atmospheric conditions (<i>RHa</i> and <i>Ta</i>) imposed in the laboratory environmental chamber for (a) <i>NC-LL</i> , <i>A-SL</i> and <i>A-MP3</i> ; (b) <i>A-S1</i> and <i>A-S4</i> ; (c) <i>A-S2</i> and <i>A-S3</i>	161
Figure 6-3. Laboratory specimen mould with projected locations of the embedded sensors around the axis of symmetry onto the modelled part.	162
Figure 6-4. Field experiment: (a) setup at the Agròpolis site, (b) empty tray with different embedded sensors locations, and (c) filled tray showing thin water film forming at the surface (Cordero et al., 2021).	164
Figure 6-5. $e - \ln\Psi + 0.10.1$ diagram as estimated from the environmental chamber, for the (a) compacted specimens, and (b) slurry specimens.....	166
Figure 6-6. Hydraulic conductivity for the Agròpolis soil at different initial conditions, obtained using different methods (Najdi et al., <i>c</i>).	167
Figure 6-7. Measurements at the two altitudes ($z=0.1\text{m}$, and $z=2.0\text{m}$) of the: (a) air temperature Ta [$^{\circ}\text{C}$], and (b) relative humidity <i>RHa</i> [%].	170
Figure 6-8. Computed r_s values for the Field Experiment <i>A-FE</i>	171
Figure 6-9. Average wind speeds as recorded at two altitudes: $z=0.1\text{ m}$, and $z=2.0\text{ m}$	173
Figure 6-10. Computed βg values from readings at different altitudes (Najdi et al., <i>c</i>).	173
Figure 6-11. Global and net solar radiation [$\text{W}\cdot\text{m}^{-2}$].	175
Figure 6-12. Prescribed liquid flow rate, as calculated directly from rainfall data.	176
Figure 6-13. Vertical periphery segmentation replicating the perimeter crack progressive opening (Najdi et al., <i>c</i>).	177
Figure 6-14. Numerical and experimental suction development at different embedded sensors locations, for specimens: (a) <i>A-MP3</i> ; and (b) <i>A-S3</i> (Najdi et al., <i>c</i>).	183
Figure 6-15. Final state shrinkage profile for two simulations on the same specimen (<i>A-S3</i>), considering rough versus smooth bottom mechanical boundary conditions.....	185

Figure 6-16. Experimental versus numerical gravimetric water content evolution for (a) *A-MP3*; (b) *A-S1* and *A-S4*; (c) *A-S2* and *A-S3*; and (d) *NC-LL* and *A-SL*; and CIF for (e) *A-MP3*; (f) *A-S1* and *A-S4*; (g) *A-S2* and *A-S3*; and (h) *NC-LL* and *A-SL*. 186

Figure 6-17. Experimental and numerical results of soil temperature evolution for specimens: (a) *A-S1* and *A-S2*, and (b) *A-S3* and *A-S4*..... 187

Figure 6-18. Numerical and physical results of the field experiment, showing evolution of: (a) gravimetric water content; (b) CIF; soil temperature at (c) 15 cm, and (d) 40 cm depth; (e) suction; and (f) volumetric water content..... 190

List of Tables

Table 3.1. Suction measurement techniques, adapted from Bulut and Leong (2008).	33
Table 3.2. Soil characteristics.....	36
Table 3.3. Optimum compaction conditions.....	36
Table 3.4. Initial conditions of remaining specimens.....	37
Table 3.5. Initial conditions of remaining specimens.....	37
Table 3.6. Water Potential of NaCl in Megapascals MPa at different concentrations	44
Table 3.7. Experimental methods used for each set.	51
Table 3.8. Residual void ratio for the residual specimens.....	66
Table 4.1. Basic properties of the B2-Bentonite and C2-Kaolin used in the preliminary experimental investigation.	82
Table 5.1. Equilibrium, constraint and constitutive equations with associated state variables.	120
Table 5.2. Wind measurements in the central axis of the environmental chamber showing the vertical measurement height above the soil surface (z); the number of measurements taken (N); the average wind speed (U) and the mean burst speed (U') recorded.	143
Table 5.3. Constitutive equation parameters for Blocks A, B and C.....	145
Table 5.4. Conversion of measured atmospheric variables in the chamber into prescribed vapour mass fraction and gas density for the imposed boundary condition.....	146
Table 5.5. Boundary conditions for Block A.....	146
Table 5.6. Boundary conditions for Block B.....	147
Table 5.7. Sequential crack segments activation time for B1 and B2.	148
Table 5.8. Boundary conditions for Block C.....	148

Table 5.9. Sequential crack segments activation time for C3.....	149
Table 6.1. Initial conditions of the different experimental specimens.....	160
Table 6.2. Transfer coefficients per crack segments assigned for the different models.....	178
Table 6.3. Constitutive parameters summary for each model.	179

List of notations

Abbreviations

HCT	High Capacity Tensiometer
N-HCT	Northumbria High Capacity Tensiometer
SWRC	Soil Water Retention Curve
SSC	Soil Shrinkage Curve
AEV	Air Entry Value
AXV	Air Expulsion Value
WEV	Water Entry Value
Dry-IP	Inflexion Point of the drying path SWRC
Wet-IP	Inflexion Point of the wetting path SWRC
PSD	Particle Size Distribution
PL	Plastic Limit
LL	Liquid Limit
PI	Plasticity Index
SL	Shrinkage Limit
SW	Swelling Limit
RH	Relative Humidity
FDR	Frequency Domain Reflectometry
<i>OS</i>	Osmotic Suction
<i>EC</i>	Electrical Conductivity
VE	Vapour Equilibrium
DIA	Digital Image Analysis
PC	Paraffin-Coating
ModGG	modified Groenevelt and Grant SSC model
ModCC	Chertkov SSC model
Dry-IP	Inflexion Point of the drying path SWRC
Wet-IP	Inflexion Point of the wetting path SWRC
USCS	Unified Soil Classification System
model- <i>vG</i>	van Genuchten SWRC model
model- <i>FX</i>	Fredlund and Xing SWRC model
THM	Thermo-Hydro-Mechanical
CIF	Crack Intensity Factor

Symbols

σ_w	air-water surface tension
u_{wm}	water pressure at the meniscus back
u_a	air pressure
d_{pores}	pore diameter
R	the universal gas constant
T	absolute temperature
M_w	molecular mass of water
M_a	molecular mass of dry air
ρ_w	pure water density

θ_w	gravimetric water content
θ_V	volumetric water content
θ_{Sr}	liquid degree of saturation
θ_e	water ratio
θ_{AEV}	moisture ratio at air entry
θ_{rl}	residual moisture ratio
θ_{ls}	saturated water content
θ_{LL}	moisture content at Liquid Limit
e	void ratio
e_i	initial void ratio
e_r	residual void ratio
Φ	soil porosity
ϕ_i	initial porosity
ϕ_0	residual porosity
ε_v	volumetric strains
w_h	hygroscopic water content
ρ_s	solid particles density
C_u	coefficient of uniformity
C_c	coefficient of curvature
h	specimen height
\varnothing	specimen diameter
γ_D	dry density
γ_s	soil particles unit weight
γ_w	water unit weight
G_s	specific gravity
ω_{opt}	optimum water content
Ψ	suction
Ψ_0	suction at saturation-suction
Ψ_{AEV}	suction at AEV
Ψ_{infD}	suction at SWRC inflexion point (drying path)
Ψ_{infW}	suction at SWRC inflexion point (wetting path)
ψ_{SL}	suction at Shrinkage Limit
ψ_{SW}	suction at Swelling Limit
$\gamma_{GG} / \xi_{GG} / \zeta_{GG}$	ModGG fitting parameters
σ_{CC}	SSC intercept in the proportional shrinkage zone (for ModCC)
μ_{CC}	ModCC model coefficient
β_{NS}	normal shrinkage slope
A_{ST}	area of exposed soil specimen surface
V_T	total specimen volume
α_i	SWRC fitting parameter related to the AEV
n_i / m_i	SWRC shape fitting parameters related to the pore-size distribution
P_0	SWRC parameter related to the AEV
a_p	coefficient of porosity change effect on P_0
a_n	coefficient of porosity change effect on the shape parameter n

P_{atm}	atmospheric pressure
P_g	gas pressure
P_l	liquid pressure
$\boldsymbol{\sigma}$	total stress tensor
p_{net}	net pressure
p'	average skeleton stress (effective pressure)
χ	Bishop's coefficient
v	specific volume
p_{ref}	reference pressure
κ	elastic swelling index
λ	plastic index
ω_α^i	mass fraction of a species i as a component of phase α
\mathbf{j}_α^i	advective flux of a species i in the phase α
E_α^i	specific internal energies of the species in the phases
\mathbf{j}_{Estg}	advective term of heat caused by mass motions
\mathbf{u}	displacements (momentum balance)
ρ_g^w	vapour concentration in gas phase
\mathbf{q}_l	liquid advective flux (Darcy's velocity vector)
\mathbf{q}_g	gas advective flux
\mathbf{i}_g^w	non-advective vapour flux
\mathbf{i}_c	conductive heat flux
∇	divergence operator
Θ	generic property
f^w	external water source term
f^Q	energy supply
S_g	gas degree of saturation
a_1	coefficient accompanying the changes in mean effective stress
a_2	coefficient accompanying the changes in suction
a_3	coupling coefficient between the effective stress and suction
ν_p	Poisson's ratio
σ_c	soil tensile strength
K	stiffness modulus
ε	deformation strains
\mathbf{K}_r	permeability tensor
\mathbf{k}_i	intrinsic permeability tensor
\mathbf{g}	gravity vector
μ_α	temperature dependent dynamic viscosity of the species α
K_{HC}	hydraulic conductivity of the soil
k_{rl}	liquid phase relative permeability
k_{rg}	gas phase relative permeability
A_{rl}	Corey's function constant adjusting parameter (relative permeability)
r_{rl}	Corey's function power adjusting parameter (relative permeability)
\mathbf{D}_g^w	vapour dispersion tensor

D_m^w	dispersion coefficient corresponding to molecular diffusion of vapour in air
\mathbf{D}'_α	mechanical dispersion tensor
d_l	longitudinal dispersivity
d_t	transversal dispersivity
τ_r	tortuosity
A_τ	tortuosity constant coefficient
m_τ	tortuosity power coefficient
c_α	specific heat of the phase α
λ_h	thermal conductivity
β_{CL}	liquid compressibility
α_{VTE}	volumetric thermal expansion coefficient for water
γ_{sv}	solute variation
A_α	preexponential phase viscosity coefficient
B_α	exponential phase viscosity coefficient
H_{nc}	Henry's constant
γ_m	mechanical multiplier
P_v	vapour pressure
ρ_v	vapour density
β_g	vapour transfer coefficient
j_e^0	prescribed heat flow flux
R_n	net solar radiation
H	sensible heat
LE	latent heat of evaporation
G	heat flow
C_p	specific heat capacity
r_s	soil surface resistance to evaporation
r_h / r_a	aerodynamic resistance factors
γ_e	heat transfer coefficient
k	von Karmen's constant
\bar{U}	average profile of wind speed
ψ_{HM}	atmospheric stability factors for heat flux (H) and for momentum flux (M)
ζ	dimensionless atmospheric stability parameter (Monin-Obukhov length)
D_a	vapour diffusivity in air at a given temperature
α_{albedo}	soil surface albedo
σ_{SB}	Stefan-Boltzmann constant
m_{cld} / n_{cld}	cloud factors
m_{e1} / n_{e1}	emissivity factors
T_d	dewpoint temperature
R_{si}	global radiation measurements
R_{so}	clear sky solar radiation
EL_{mst}	elevation above sea level
R_{sa}	extra-terrestrial solar radiation

G_{sc}	solar constant
φ_{lat}	specific latitude
δ_{dc}	solar declination angle
d_r	relative distance between the earth and the sun
ζ_1 / ζ_2	solar time angles
LST	time of the day in hours
t_n^{act}	crack activation time
Cr_n	crack width at this crack segment level

List of Relevant Publications

The following articles were published as part of or during the work done for completing this thesis:

- 1- (Cordero et al., 2020) - E-UNSAT 2020
- 2- (Cuadrado et al., 2022) - Computers and Geotechnics Journal
- 3- (Mendes et al., 2022) - Canadian Geotechnical Journal
- 4- (Mendes et al., 2023) - UNSAT 2023
- 5- (Encalada et al., 2023) - UNSAT 2023

Submitted, pending review:

- 6- (Najdi et al., 2023a) - Engineering Geology Journal
- 7- (Najdi et al., *b*) - Géotechnique
- 8- (Najdi et al., *c*) - Computers and Geotechnics Journal

Chapter 1

Introduction

Vital signs of the planet show how the increasing temperatures and global warming are causing a continuous transformation in the normal weather patterns and disturbing the usual balance of nature (IPCC, 2022). More severe weather conditions, storms, and increased droughts are foreseen over the coming years, with changes in precipitation and wind patterns and water levels are expected to become scarcer. The need arises to mitigate the risks of the climate change, and to study its effects especially on the soil surfaces.

One of the main indications of prolonged drought is the appearance of desiccation cracks on the soil surfaces. Signs of formation of desiccation cracks have long been associated with severe droughts, dryer environments, deteriorated agricultural lands, and more generally to the global warming and climate change. Figure 1 shows few of the many existing images of desiccation cracks mentioned in various European and international reports and publications regarding the climate change.

While most of the climate change reports portray the desiccation cracks while discussing the problem, very few examine the mechanism, causes and direct and indirect effects of the crack formation. The formation of desiccation cracks and their propagation to greater depths create preferential hydraulic pathways through the surface. The preferential pathways trigger an accelerated water seepage through the surface cracks, create new interfaces for soil-atmosphere interactions (Stirling et al., 2017; Levatti et al., 2019b), and cause the further disintegration of the soil structure (Yesiller et al., 2000; Costa et al., 2013), rendering it unworkable for agricultural or constructional use (Drumm et al., 1977; Alonso et al., 2006).

Much of the research regarding desiccation cracking has been dedicated to investigating the morphology of formed cracks (Morris et al., 1992; Konrad & Ayad, 1997; Kodikara et al., 2000). Some authors attributed crack initiation to heterogeneity and developing tensile stresses at the drying soil surface (Abu-Hejleh & Znidarčić, 1995; Konrad & Ayad, 1997; Trabelsi et al., 2012).

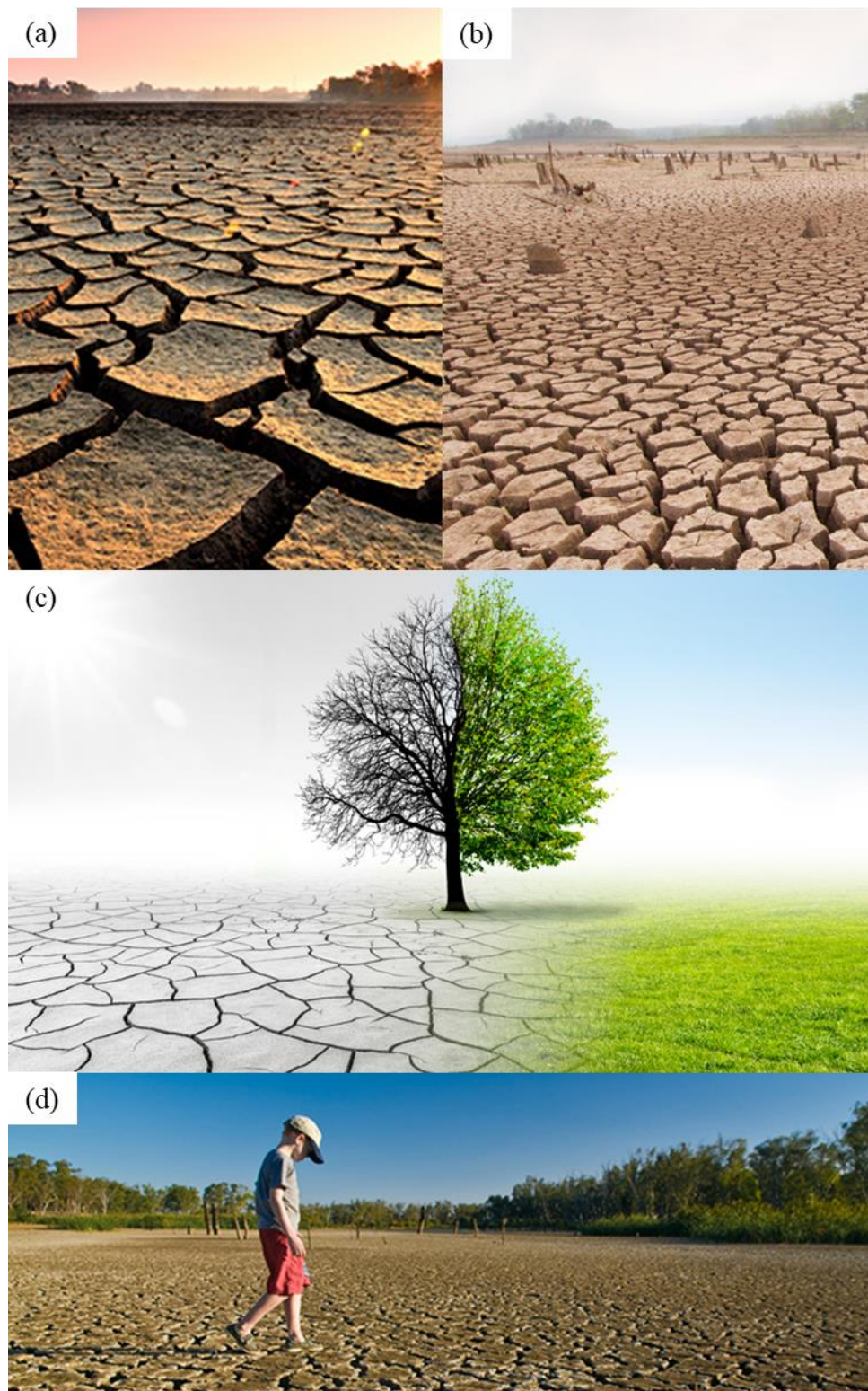


Figure 1-1. Images of desiccation cracks portrayed on: **(a)** (NASA, 2005); **(b)** (Reuters, 2021) and (Copernicus, 2022); **(c)** (The World Bank, 2021); and **(d)** (EDF, 2019).

In general, the formation of desiccation cracks indicates the prior existence of porewater that has dissipated from the soil medium over time. Potential desiccation cracks can be identified on the surface of Mars either from surface images taken from orbit (El-Maarry et al., 2014), or through the NASA's Mars Science Laboratory (MSL) Curiosity rover (Grotzinger et al., 2005).

The MSL images were used to describe the morphology of the desiccation cracks observed in ancient lacustrine strata at Gale crater, Mars, indicating the pre-existence of perennial lakes and habitable environments. Figure 1.2 shows images of Old Soaker rock slab demonstrating a pattern of mud desiccation cracks (Stein et al., 2018).

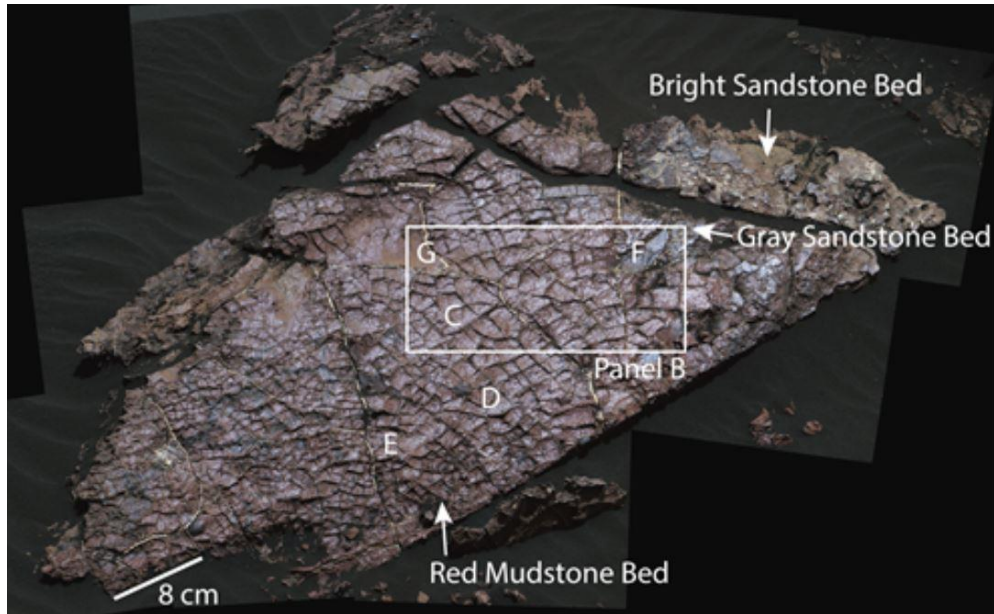


Figure 1-2. Mastcam (sol 1555) and Mars Hand Lens Imager (MAHLI) images of Old Soaker (OS) rock slab, Mars (Stein et al., 2018).

In some cases, the observed crack morphology shares a great resemblance to similar existing cracks on Earth in various locations. Figure 1.3 shows aerial images to the same scale taken of Mars (lefthand side) and Earth (righthand side) surfaces. Exceptional similarities are noticed between the morphological patterns and cracks size and propagation.

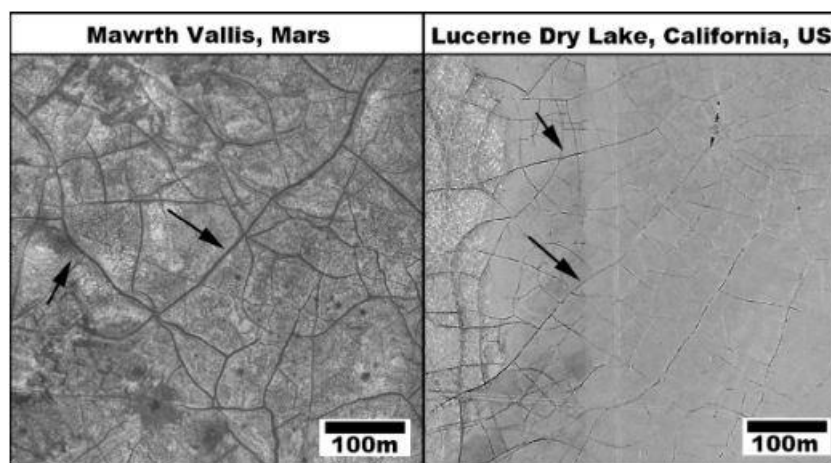


Figure 1-3. Comparison between large features on the floor of Mawrth Vallis (left, HiRISE image PSP_006755_2030) and the large desiccation features in Lucerne Dry Lake in California, US (El-Maarry et al., 2014).

The similarities found for the cracks in Mawrth Vallis on Mars with Lucerne Dry Lake in California indicate the pre-existence of a water body in that area on Mars that has long dried, leaving the soil with desiccation cracks visible on the surface.

That being stated, it is important to study the soil desiccation cracks, in order to understand the mechanism and factors that drive it, to establish a prediction tool, and to mitigate its risks.

Experimental analysis has long been employed to tackle the problem (Corte & Higashi, 1964; Nahlawi & Kodikara, 2006; Tollenaar et al., 2017a). Researchers have studied the cracking from fracture mechanics point of view (Ávila, 2004; Amarasiri et al., 2011; Amarasiri & Kodikara, 2013; Lakshmikantha et al., 2018), and investigated the effect of initial moisture content and compaction conditions on the crack formation among other factors (Kleppe & Olson, 1985). Many sophisticated numerical tools have been developed in this context (Rodríguez et al., 2007; Asahina et al., 2014; Sánchez et al., 2014; Cuadrado et al., 2022). Yet there is no definite standard testing developed.

To understand the crack initiation and propagation, a good comprehension of the principles of unsaturated soil mechanics and two-phase flow in deformable porous medium is needed. Achieving this full comprehension of the unsaturated medium requires defining the constitutive relations between the principal variables for soils undergoing changes: (a) the porewater content, (b) the porewater pressure, and (c) the volume of the pore space medium.

Additionally, the atmospheric conditions overlying the soil surfaces need to be rigorously studied and framed mathematically in order to adequately capture the ensuing soil-atmospheric interaction.

Eventually, having defined the soil constitutive relations and parameters and the soil-atmosphere interaction at the boundary conditions can create a fully functioning numerical simulator that can provide to high accuracy a prediction of the thermo-hydro-mechanical reaction of the soil exposed to the atmosphere. Such a numerical simulator is recognised as a powerful tool and can provide reliable predictions for the unsaturated soil behaviour undergoing drying or wetting paths.

1.1. Background

The research work in this thesis was aiming at a full numerical characterisation and simulation of a large-scale and long-duration field experiment, considering all the factors involved. To obtain such a full numerical model, a proper understanding of the constitutive formulations was

needed, and therefore a correct characterisation of the parameters involved. Therefore, a suitable set of constitutive and boundary condition parameters is to be obtained experimentally.

The work is divided into five chapters in a sequential order of how the work was carried out, to eventually get the full numerical simulation of the large-scale field experiment. For instance, the experimental campaign was first focused on acquiring some novel High Capacity Tensiometers from Northumbria University, UK (N-HCT). The N-HCT, along with multiple other direct and indirect suction and volumetric measurement techniques were used to obtain the Soil Shrinkage and Swelling Curves (SSCs) and the Soil Water Retention Curves (SWRCs) for different soils at various compaction conditions. Having acquired a numerous amount of SWRCs and SSCs, distinct stages were noticed in the main drying and main wetting paths. The stages were limited with transitional points which serve as yielding points for describing the mechanical behaviour. The acquired constitutive relations (e.g., SWRCs and suction modulus from the experimental campaign) are used to identify the numerical constitutive relations and corresponding parameters. Eventually, through comparison with formulations of meteorological sciences, the overlying atmospheric conditions were transformed into formulations of imposed numerical boundary conditions to achieve a full replication of physical conditions in the constructed numerical modelling tool.

Therefore, the thesis can be thought to comprise separate parts of research work, encompassing experimental, conceptual, and numerical work. As such, a relative background to each of the aforementioned parts is provided in the introduction of each of the chapters.

1.2. Motivation and Objectives

The main objective of the thesis is to characterize the soil parameters, the multiple factors involved, the meteorological data, the energy fluxes, and the constitutive formulations governing the soil-atmosphere interaction problem. This was essential to investigate the resulting thermo-hydro-mechanical changes and the desiccation shrinkage and cracking. The novelty of this research is that it includes all the following study approaches: instrumentation development, laboratory work, large-scale field experimentation, theoretical application and study, and numerical Finite-Element modelling. The study approaches in the thesis are organized as follows:

- Contributing to the development and testing process of a new High Capacity Tensiometer in collaboration with Northumbria University in the UK.
- Evaluating the tensiometer's functionality and performance with respect to different established direct and indirect suction measurement methods.

- Obtaining Soil Water Retention Curves (SWRCs) and Soil Shrinkage Curves (SSCs) in the laboratory for soils at different initial compaction conditions, using a combination of different measurement methods.
- Carrying out a theoretical analysis on the SWRCs and SSCs, and suggesting accordingly five consecutive drying phases, giving the hydromechanical characteristics and changes in the soil macro and microstructure for each phase.
- Building a numerical finite element model in CODE_BRIGHT that can simulate the soil drying process in an environmental chamber.
- Applying the numerical model to model the drying shrinkage of different specimens prepared at different initial compaction conditions and instrumented with a variety of embedded sensors to compare the numerical results to the physical results.
- Simulating a large-scale field experiment exposed to free atmospheric conditions over the span of a full year.

1.3. Scope of the Study

This thesis is carried out in the general framework of theoretical, experimental, instrumentational, constitutive, and numerical analysis of soil desiccation shrinkage.

The research work carried out in this thesis ranges from (a) instrumentation development; (b) laboratory experiments on key unsaturated soil characteristic parameters; (c) multiple highly instrumented environmental chamber tests; (d) numerical analysis of large-scale and long-term field experiments; (e) numerical simulation of all the drying tests whether in the laboratory or in the field; and (f) studying the effect of compaction level and initial conditions on the drying and wetting process.

The laboratory research work carried out involved new tensiometers capable of measuring high range of matric suction, evaluation of different direct and indirect suction measurement techniques, evaluation of different direct and indirect volumetric measurement techniques, the improvement of an existing environmental chamber by equipping it with additional sensors embedded in the soil specimens subjected to cycles of drying and wetting, and carrying out different drying and wetting tests on specimens with different initial conditions. The theoretical work involved the analysis of the Soil Water Retention Curves (SWRCs), Soil Shrinkage Curves (SSCs), Suction-Voids Curves (SVCs), and the desaturation-rate and desaturation-rate slope of the SWRCs (i.e., first and second order derivatives, respectively). The analysis of the mentioned curves was carried out in parallel, in order to identify five main phases of

unsaturation shrinkage of drying soils, and to pinpoint the importance of the SWRC inflexion point as an indicator of the established shrinkage limit. The numerical research work involved the extension of an existing finite element code with a unique constitutive formulation set and calibrated parameters, and a highly responsive and realistic hydraulic boundary condition. The model was capable of simulating the complex soil-atmosphere interaction problem and replicating the physical thermo-hydro-mechanical changes measured both in laboratory and field experiments.

1.4. Thesis Organization

The research work in this thesis is divided into six chapters. Each of the chapters presents a separate piece of work that has been published or is in the progress of being published in a scientific journal. The chapters are sequenced in the way the work in this research has been handled, by first obtaining experimental characteristics of soils, carrying out a theoretical analysis, and finally simulating numerically the whole unsaturated drying shrinkage process.

Chapter 1 is the introduction that discusses the background to the problem, providing a glimpse on the recent research related to the general thesis topic. The necessity of the work for the ongoing investigation on the soil-atmosphere interaction problem is explained. The scope and objectives of the present work, and the organization of the thesis are provided.

Chapter 2 presents some of the work carried out in collaboration with Northumbria University in the UK, towards the development of the Northumbria High Capacity Tensiometer (N-HCT). As part of the collaboration, two N-HCTs were built at Northumbria University and transferred to the Technical University of Catalonia (UPC-BarcelonaTech) to carry out some validation testing. Parts of this work, concerning the first saturation, re-saturation and testing in soils were published in the Canadian Geotechnical Journal under the title “Towards the Development on New High Capacity Tensiometers Capable of Measuring Soil Matric Suction Beyond 3 MPa.” (Mendes et al., 2022). The paper demonstrates how decreasing the largest pore size within the ceramic results in an increase of the measuring range. The ceramic filter in HCTs was replaced from the typically used 1.5 MPa Air Entry Value (AEV) ceramic filter with a new alumina ceramic filter with an estimated AEV of 5.8 MPa. Early results show that the maximum measuring matric suction range is beyond 3 MPa.

Additionally, the chapter starts by briefly explaining the building process of the tensiometers and the process underwent to prepare the full testing setup in the laboratories of UPC (e.g., building the datalogger, saturation vessel, and the connections to the pressure controller).

Chapter 3 presents the work carried out to evaluate different suction and volumetric measurement methods, by assessing the measuring ranges and functionalities of each of the different methods used. At the same time, different volumetric measurement techniques were assessed in order to establish an understanding of Soil Shrinkage Curves (SSCs) that describe the moisture-voids relationship during drying and has the potential to be used for indirect determination of volumetric dimensions of soil specimens. An established SSC model is proposed in this work and is fitted to experimental data in order to indirectly estimate volumetric measurements from the water content of small-scale specimens. The proposed novel approach standardises volumetric measurements determination, leading to obtaining uniform and complete-range SWRCs. Parts of this work were published in Engineering Geology Journal under the title “Evaluating innovative direct and indirect soil suction and volumetric measurement techniques for the determination of soil water retention curves following drying and wetting paths” (Najdi et al., 2023a). Additionally, a full characterization is given of the “Agròpolis” and “North Campus” silty clays that are the main soils under study in this thesis. The SWRCs of different compaction levels of the Agròpolis soil are presented. Additionally, the chapter presents results of the vapour equilibrium technique not mentioned originally in the published version.

Chapter 4 presents the work submitted for publication (pending review) under the title “The role of inflexion-point in the shrinkage mechanism of partially saturated soils” (Najdi et al., *b*). The work in this chapter is mainly theoretical in the context of unsaturated soil mechanics. The desaturation of a deformable partially saturated soil is categorised into five consecutive stages. The transition-points between the different stages (i.e., yielding points), were identified via coupling between the Soil Water Retention Curve (SWRC), Soil Shrinkage Curve (SSC), the Suction-Voids Curve (SVC), the SWRC desaturation-rate and the slope of the SWRC desaturation-rate. The desaturation-rate and desaturation-rate slope were computed from the first and second-order derivatives of the SWRC fitting function, respectively. The inflexion point is identified as the root of the second-order derivative (i.e., the desaturation-rate slope), of the SWRC fitting equation. A high correlation between the analytically-obtained inflexion point and the shrinkage limit is demonstrated graphically and conceptually. The newly proposed correlation is validated for a set of 31 different soils encompassing different soil types, fabrics, and textures. A similar analysis was carried for the wetting path by dividing into four stages

with three transitional points: water entry value, wetting inflexion point, and air expulsion value. Similarly, the inflexion point of the wetting path SWRC is correlated with the swelling limit on the SSC. The potential implications of the findings on constitutive modelling and geotechnical design are addressed.

Chapter 5 presents some of the work published in *Computers and Geotechnics* under the title “THM analysis of a soil drying test in an environmental chamber: the role of boundary conditions”. The chapter starts by discussing the theory behind the finite element model used, i.e., CODE_BRIGHT, and the involved formulations, mass balance equations, the corresponding constitutive equations, and obtaining the relevant constitutive parameters. Later, the results from the published material (Cuadrado et al., 2021) are explained briefly, highlighting the main findings and conclusions.

Chapter 6 presents the work published in the 4th European Conference on Unsaturated Soils (E-UNSAT 2020), with the title: “Experimental and numerical analysis of soil desiccating cracks in compacted and non-compacted specimens” (Cordero et al., 2020); and the work being prepared to be submitted to *Computers and Geotechnics* under the title “Numerical analysis of soil desiccating cracks in different compaction levels and imposed atmospheric conditions” (Najdi et al., *c*). Further development is given on the topic of numerical analysis of soil desiccating cracks in different compaction levels and imposed atmospheric conditions in external field conditions. After the works of the previous chapter (Chapter 5), the numerical models were extended to simulate the mechanical aspect of the problem (i.e., capturing the drying shrinkage process), and to simulate the thermal component (i.e., capturing the soil temperature evolution). The experiments in this chapter are better instrumented with sensors measuring the full suction range in the drying soil specimens, giving a better calibration of the constitutive parameters used. The parameters used are all obtained experimentally in the laboratory for the specific initial conditions used. The obtained model is then applied on a larger-scale field experiment exposed to free atmospheric conditions for a long-term (i.e., 1 year). A proper interpretation of the meteorological data is given, a responsive boundary condition is created, and a replicative model is provided that simulates the full processes involved.

Finally, **Chapter 7** presents the conclusion of the thesis and some final remarks and future work suggestions.

Chapter 2

The Use of Novel High Capacity Tensiometers

Parts of this chapter have been published in:

1- The “Canadian Geotechnical” Journal, with the title:

“Towards The Development on New High Capacity Tensiometers Capable of Measuring Soil Matric Suction Beyond 3 MPa”.

on February 2022, with the co-authors:

Joao Mendes, Abdallah Najdi, David Encalada, Pere C. Prat, Alberto Ledesma.

2- The proceedings of the “UNSAT 2023” (International Conference on Unsaturated Soils), with the title:

“High-Capacity Tensiometers: Design Performance and Behaviours”.

on March 2023, with the co-authors:

Joao Mendes, Armin Jamali, Abdallah Najdi, David Toll, Domenico Gallipoli, Alberto Ledesma, Pere Prat, David Encalada, Agostino Walter Bruno.

2.1. Introduction

Suction, or negative (tensile) porewater pressure, is one of the main constituents in the unsaturated soil mechanics domain. Its values are directly associated with thermo-hydro-mechanical changes in the soil matrix, like the hydraulic conductivity (Romero et al., 1999; Cai et al., 2014; Romero et al., 2011; Zhang et al., 2020); thermal conductivity and temperature (Dong et al., 2015; Lu et al., 2015; Cao et al., 2021), volumetric strains (Alonso et al., 1990; Vanapalli et al., 1999; Romero & Vaunat, 2000; Vaunat et al., 2000), internal stresses and tensile strength (Abou Najm et al., 2009; Lakshmikantha et al., 2013; Stirling et al., 2015, 2017), soil cohesion (Ravindran & Gratchev, 2022) and shear properties (Fredlund & Morgenstern, 1977; Vanapalli et al., 1996; Nishimura & Fredlund, 2000). For this reason, direct quantification of suction values in soils has always been of high interest for studies in the unsaturated soil mechanics domain. While some researchers try to estimate the value of suction indirectly through temperature and relative humidity, others try to measure it directly through measuring the negative pore-water pressures. The latter is done using what can be referred to as “tensiometric” measurements, that is measurements using a tensiometer.

Tensiometers are sensors that can measure both positive (compressive) and negative pore-water pressures in the soil matrix directly. They are sometimes referred to as “suction sensors” or “suction probes” because tensiometers measure the pore suction in soils which, under atmospheric conditions, coincides with the negative pore-water pressure. Conventional tensiometers have a measuring range of 0 to 80 kPa (Stannard, 1992), while High Capacity Tensiometers (HCTs) can measure soil suctions beyond this value (up to 1.5-2 MPa). The measuring principle is the same as with direct tensiometers, however a higher measuring range is made possible due to the use of a porous stone preventing the influx of air in the water reservoir as the measuring interface with the soil (Ridley & Burland, 1993). HCTs are considered very versatile sensors, and have been used both in the field to monitor pore-water pressures inside unstable slopes or agricultural soils (Cui et al., 2008; Mendes et al., 2008; Toll et al., 2011), and in geotechnical laboratories to measure the evolution of soil suction during direct shear tests (Caruso & Tarantino, 2004), triaxial tests (Cunningham et al., 2003; Mendes & Toll, 2016), environmental chamber tests (Cordero et al., 2020; Najdi et al., 2023a), or obtaining Soil Water Retention Curves (SWRCs) (Toker et al., 2004; Marinho & Teixeira, 2009; Lourenço et al., 2011; Najdi et al., 2023a).

The first HCT was developed in the 1990s at Imperial College, London (IC-HCT), by Ridley and Burland (1993). Since the development of the IC-HCT, various similar HCT designs have emerged (Guan & Fredlund, 1997; Meilani et al., 2002; Take & Bolton, 2003; Mendes & Buzzi,

2013; Bagheri et al., 2018; Mendes et al., 2020). Commercially available pressure transducers and the same ceramic filter with an AEV of 1.5 MPa as in the IC-HCT was used in these subsequent HCT designs.

The ceramic filter and its Air Entry Value (AEV) are the main components in identifying the measurement range of the HCTs. The AEV of ceramic filter allows soil suction measurements beyond -100 kPa (absolute 0 kPa gauge pressure). The AEV is the maximum difference in pressure that can exist between the air and water pressures of the ceramic filter, beyond which, the air breaks through the ceramic filter. When measuring suction in a soil specimen, the AEV is equal to the difference in pressure between the pore pressure in the soil and the pressure in the water reservoir. When the pressure difference is larger than the AEV of the ceramic filter, cavitation (or water tension breakdown) in the HCT occurs. The cavitation is recognisable in the pressure transducer readings which show a sudden pressure drop to a value of -100 kPa. The cavitation can be also visually observed at the same moment that the air bubbles emerge in the water reservoir (Mendes & Buzzi, 2013).

Most existing HCTs are theoretically limited to a measuring range of 1.5 MPa, by using the same ceramic filter with an AEV of 1.5 MPa. However, as it has been reported by Tarantino and Mongiovi (2001), HCTs with this type of ceramic filter are able to measure soil suction well beyond their expected measuring range. Tarantino and Mongiovi (2001) reported measuring suction values in soil specimens in the range of 2.6 MPa. This is in line with observations by Mendes et al. (2020) where HCTs assembled with similar ceramics were able to sustain pressures beyond 2 MPa. This discrepancy in relation to the measuring range in HCTs is not yet fully understood, but it seems that the actual AEV in this type of ceramics varies greatly and inconsistently for each individual ceramic filter and between the nominal value of 1.5 MPa and 2 MPa.

Another factor playing an important role in increasing the HCT measuring range is the proper saturation of both the ceramic filter and the water reservoir (Take et al., 2003). The proper saturation ensures the hydraulic conductivity of the water inside the ceramic filter and the water reservoir of the HCT and the soil specimen to be tested. The water reservoir in the HCT serves only one purpose which is to provide space for the deflection of the pressure transducer. Contrary to previous belief, the water reservoir size does not influence the measuring range of HCTs. As it has been shown previously (Mendes et al., 2013), large size reservoirs with a volume of 1000 mm³ assembled with the ceramic filter with an AEV of 1.5 MPa were able to reach the nominal value of 1.5 MPa before cavitation. However, it can be noted that the phase of initial saturation of the HCT is crucial in determining both proper performance and measuring range of HCTs.

The measuring range of the pressure transducers used should take into consideration the AEV range of the ceramic filter used and its symmetrical response. The symmetrical response, that is the capability of measuring both positive and negative pressures, determines the capacity of suction measurement range (Tarantino & Mongiovi, 2001). This will enable the HCTs calibration to be performed in the positive range and then extrapolated linearly to the negative range. Ideally, the transducer range should extend beyond the ceramic filter AEV, enabling higher positive pressures to be applied to accelerate the tensiometers saturation phase without causing damage to the pressure transducer.

The novel HCTs, herein referred to as the Northumbria-HCTs (N-HCTs) were developed at Northumbria University by Mendes (Mendes et al., 2022). The main difference of the N-HCTs to other HCTs found in the literature is in the use of alumina porous ceramic filters that are designed with a smaller largest pore, hence a higher theoretically estimated AEV of 5.8 MPa, resulting in a suction measuring range up to 3.5 MPa, and assembled with pressure transducers with a 6.8 MPa pressure range. For assessment and comparison of the new ceramic filter, similar designed HCTs (herein C-HCTs), assembled with the typical ceramic filters with an AEV of 1.5 MPa, were also built. Early suction measurement results show that the N-HCTs can measure soil suction in the range of up to 3.5 MPa, twice the range of that of the C-HCTs. Moreover, it was also found that the response rate when measuring suction in soil specimens with the N-HCT was significantly faster.

N-HCTs are required to undergo calibration, saturation and re-saturation in case cavitation occurs as with other HCTs found in the literature. N-HCT calibration happens in the positive range by applying water pressures using a digital pressure-volume controller and a saturation vessel that directs the pressure onto the ceramic filter face. The calibration is then extrapolated to the negative range, as proposed by Tarantino and Mongiovi (2001). This pre-pressurization pressure has been found to be highly associated with measured sustainable suction limit (Guan & Fredlund, 1997) and in the case of the N-HCT a minimum pressure of 3 MPa should be applied. Equilibration time under positive pressure is typically in the range of 6-48 hours, as suggested by Lourenço et al. (2007). The advantage of using a saturation vessel with positive water pressure is the ease of reuse after cavitation. Re-saturation with the N-HCT can be done under 12 hours after each cavitation by reapplying positive pressure.

The principles of tensiometric measurements are explained in this chapter. Then, the design and build of the N-HCTs are explained, and the preparation of the setup for the first saturation and post-cavitation re-saturations, and the building of the datalogger.

The development of HCTs with larger measuring ranges enables the extended study of soil suction using direct methods necessary for the determination of soil water retention curves which, in turn, are crucial in the development of constitutive models for describing the behaviour of unsaturated soils. Moreover, these new HCTs will be important in the development of real-time soil suction monitoring systems, since the extended measuring range can potentially increase the longevity of continuous soil suction measurement helping in the prevention of early cavitation in HCTs. The acquired N-HCT suction measurements plays a crucial part in the rest of the laboratory work presented in the upcoming chapters of this thesis.

2.2. Tensiometric measurement principles

The tensiometric suction measurement technique, as that of the axis-translation technique, works on the principle of measuring the pressure differential across a high AEV porous ceramic filter. If the pressure is reduced to a value below the atmospheric pressure, it can be considered as negative if the fluid is water, or a vacuum if the fluid is air. However, when referring to pressure in absolute terms, the 0 kPa pressure is considered as absolute vacuum, positive water pressure signifies water in compression, while negative pressure signifies water in tension.

As mentioned earlier, a high AEV ceramic filter allows the HCT to measure high suctions before cavitating. The cavitation is normally controlled by the contact angle and the air-water surface tension. The air-water surface tension σ_w (72.8 mN·m⁻¹ at 293 K) is the force per unit length acting in the place of the surface of water in contact with its own vapour resulting from the unsymmetrical force field at water surface. Figure 2.1 shows the contact angle and capillary rise of water. For water on a solid surface and in equilibrium with its vapour, the angle between the solid surface and the gas-water interface at the three-phase line of contact is defined as the water contact angle θ_w (Figure 2.1a). It is the result of a balance between the cohesive forces in the water and the adhesive forces between the solid and the water. Capillarity occurs in fluid-surface systems with $\theta_w < 90^\circ$, causing the liquid to rise in small diameter pores of diameter d_{pores} (Figure 2b). The water pressure at the meniscus back, u_{wm} (Figure 2b) can be calculated using Young-Laplace equation (equation 2.1), by considering the vertical force equilibrium at the air-water interface and the air pressure u_a :

$$u_{wm} = u_a - \frac{4\sigma_w \cos \theta_w}{d_{pores}} \quad (2.1)$$

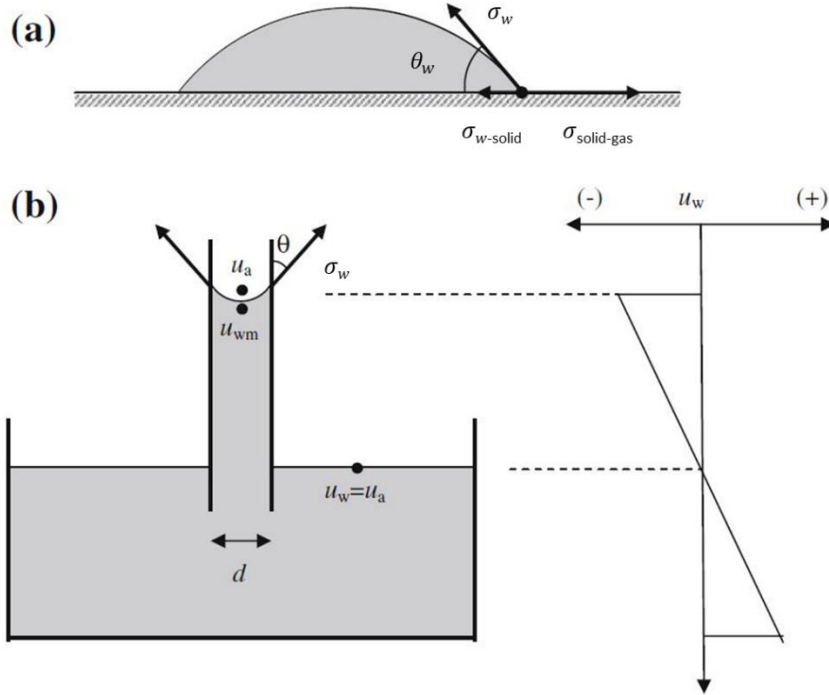


Figure 2-1 (a) Contact angle; and (b) Capillary rise of water (Marinho et al., 2008).

2.2.1. AEV

The air entry value (AEV) of a saturated porous ceramic filter can be explained as $u_w - u_a$ pressure differential which must be applied to the initially liquid-saturated material to initiate advective gas transport through the material, resulting from the menisci that form at the saturated-material boundary (Marinho et al., 2008). As mentioned earlier, $\theta_w < 90^\circ$ leads to a value of $\cos \theta_w > 0$ and eventually to $u_{wm} < u_a$. Therefore, until hydrostatic conditions are established, the meniscus will keep rising. The Young-Laplace equation (2.1) indicates that the water pressure will become more negative as the pore diameter d_{pores} decreases. The AEV is inversely related to the largest pore size in the ceramic filter, where a smaller largest pore size relates to a higher AEV and therefore, to a greater maximum suction range attainable. The AEV can be then theoretically calculated by considering the force equilibrium at the air-water interface in a single narrow pore at the material outer surface.

$$AEV = \frac{4\sigma_w \cos \theta_w}{d_{max}} \quad (2.2)$$

Where θ_w , the liquid-solid contact angle, can be assumed to be zero for simplicity (Philip & De Vries, 1957). In the alumina ceramic filter used by the N-HCT, the largest pore size diameter

was of $d_{max}=50$ nm, according to the manufacturer. This is about 3-4 times smaller than the largest pore size diameter of 165–220 nm in the 1.5 MPa AEV ceramic filter (Mendes et al., 2020), commonly used in most HCT designs.

In the N-HCT design, the ceramic filter used in the assembly was a 10 mm in diameter by 5 mm in height alumina ceramic filter. A rough estimation of about 5.8 MPa for the AEV of the new ceramic filter was obtained using equation 2.2. The filter material was considered to be perfectly wettable: $\theta_w=0^\circ$.

2.3. N-HCT AND C-HCT designs

Two unique and separate N-HCTs were mainly used in the work of this thesis. The two tensiometers were fabricated at Northumbria University under the supervision of Dr. Joao Mendes, during a trip to the facilities of Northumbria University at Newcastle Upon Tyne, in December 2019. The two tensiometers were then transferred to the geotechnical laboratories of UPC-BarcelonaTech for further validation tests to be used with existing equipment dedicated to the study of unsaturated shrinkage behaviour of soils. Two additional N-HCTs were fabricated and two C-HCTs were also assembled with the more commonly used 1.5 MPa ceramic filter at Northumbria University and were tested directly there in an earlier investigation. Comparatively with the N-HCTs, in the C-HCT design the only difference was the size of the ceramic filter measuring 15.4 mm in diameter while maintaining the 5 mm in height. The overall dimension, pressure transducer and water reservoir size were the same as in the N-HCT design.

The overall manufacturing process of each N-HCT required 3 consecutive days approximately, where each day one of the parts (i.e., pressure transducer, stainless steel sheath, and the alumina ceramic filter) is assembled to another using a clear epoxy with good performance for bonding metals and ceramics, allowing enough time for the epoxy to settle and take full strength before adding the next part.

The design of the N-HCT follows a similar design to that of the Imperial College HCT (IC-HCT) (Ridley & Burland, 1993). The latter consisted of a ceramic filter with an AEV of 15 bar (1.5 MPa) and an electronic pressure transducer separated by a small water reservoir (10 mm³) enabling the direct measurement of soil suction in the excess of 1.5 MPa. Figure 2.2 shows a scheme of the original IC-HCT design (Ridley & Burland, 1993).

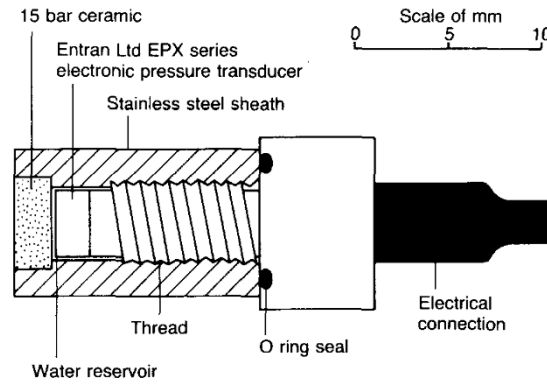


Figure 2-2. Imperial College HCT (Ridley & Burland, 1993).

The design of the N-HCT comprised of an alumina ceramic filter, water reservoir and pressure transducer encapsulated in a stainless-steel sheath. Figure 2.3 shows the dimensions of the N-HCT: 20 mm in diameter and about 20 mm in height (accounting for the back extension of the pressure transducer).

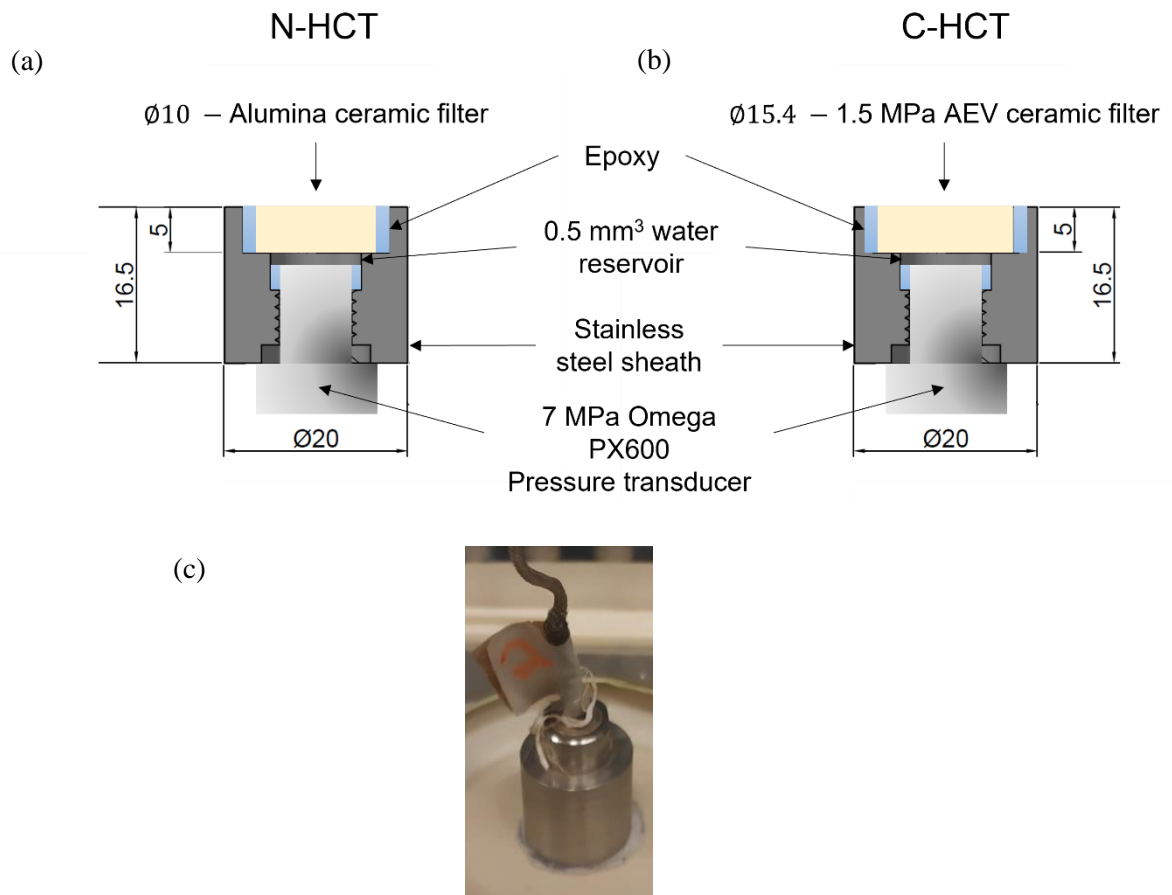


Figure 2-3. Schematics for the (a) N-HCT and (b) the C-HCT designs (sizes in mm); and (c) image of the sensor.

As mentioned before, the pressure transducer range of an HCT should be at least equal to the AEV of the ceramic filter to allow saturation of the ceramic filter at a pressure level matching the AEV. Thus, for an estimated AEV of 5.8 MPa of the ceramic filter, the pressure transducer

used in the assembly of the N-HCTs was the PX600 flush diaphragm subminiature pressure transducer with a pressure range of 6.8 MPa by Omega Engineering. Figure 2.4 shows the PX600 pressure transducer and its schematic design. The PX600 pressure transducer is designed with a thread just below the sensing face (Figure 2.4), facilitating the assembly and ensuring a precise placing within the stainless-steel sheath.

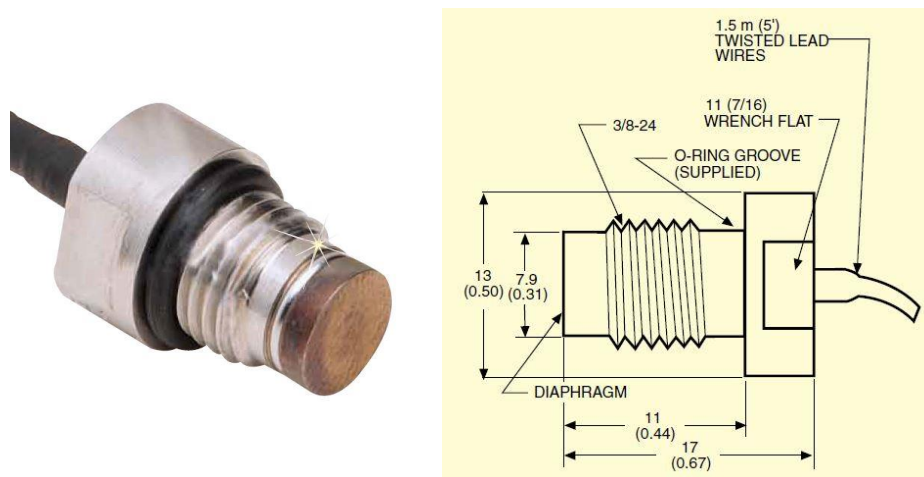


Figure 2-4. (a) PX600 pressure transducer, and the (b) design scheme.

The water reservoir, built within the protective stainless-steel sheath, was designed to be 50 mm³. This was large enough to allow deflection of the pressure transducer when under tension. PX600 is made of stainless steel, the same material as in the protective stainless sheath, reducing the temperature influence.

2.4. Datalogger

A datalogger was assembled at the laboratories of UPC to interpret the readings from the N-HCT, taking into consideration the specifications of the pressure transducer used (i.e., the PX600): an excitation of 5 VDC (Voltage Direct Current) at 15 mA; an output of 10 mV typical at 5 VDC; with a 2mV/V nominal sensitivity. The datalogger was built to accommodate readings from two sensors simultaneously. The following materials were needed: (a) 2 units of signal conditioners: Cel-10A (E: -/+ 2mV/V, Vexc: 5VDC, s: -10 / + 10VDC, at: 24VDC; see Figure 2.5a); (b) a 24 VDC power supply (DIN Rail mounting power supply, Mean Well, HDR, 1 output 24 VDC 630 mA 15.2 W; see Figure 2.5b); and (c) a 1 National Instruments USB 6000 (see Figure 2.5c).

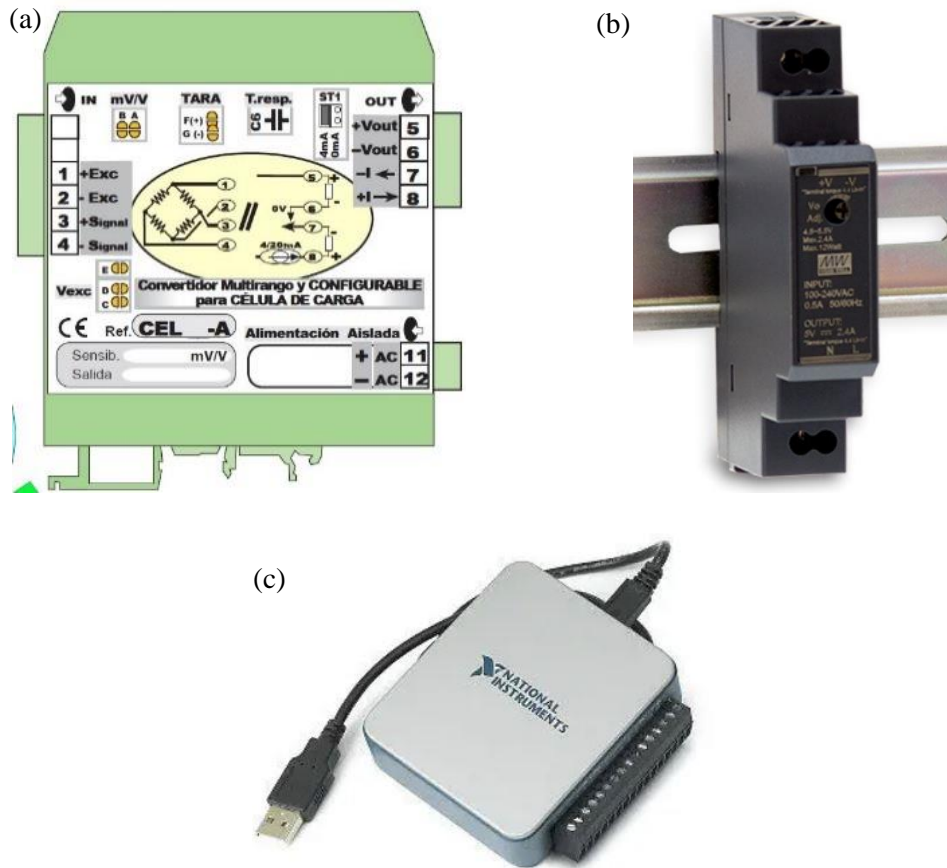


Figure 2-5. Datalogger parts: (a) signal conditioner, (b) power supply, and (c) NI USB 6000.

The different main parts are assembled inside a datalogger box (see part b, Figure 2.6). The datalogger connects the two N-HCTs (part a, Figure 2.6) to the data acquisition computer (part c, Figure 2.6) where the mVs readings are calibrated to pressure kPa readings.

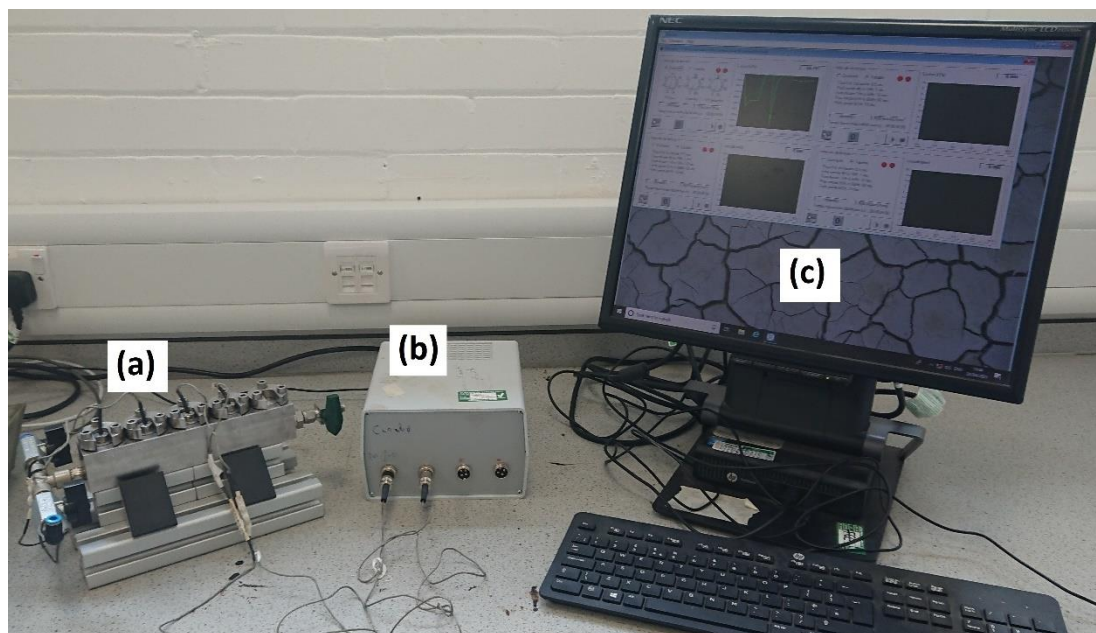


Figure 2-6. Assembled setup in the laboratories of Northumbria University: (a) the two N-HCTs in the saturation vessel; (b) the datalogger; and (c) the data acquisition computer.

2.5. Pressure vessel and connections

Each singular pressure vessel is made of stainless-steel to accommodate one of the N-HCTs at a time for the first saturation, calibration, and re-saturation purposes. Figure 2.7 shows the design scheme of the singular pressure vessel. The shaded area in green represents the stainless-steel material. The N-HCT position indicated on the figure is made of a slightly bigger diameter and of the same length as the N-HCT itself. It represents the position where the N-HCT is placed over an O-ring to tightly seal it and is locked in place. The water pressure is applied from beneath through one of the inlets (using a GDS Instruments pressure volume controller), and the vacuum through a different outlet (using a Pfeiffer DUO 11 two stage rotary vane vacuum pump, delivering an absolute pressure of $3 \cdot 10^{-4}$ kPa), while a third outlet is connected to a de-aired distilled water-filled beaker.

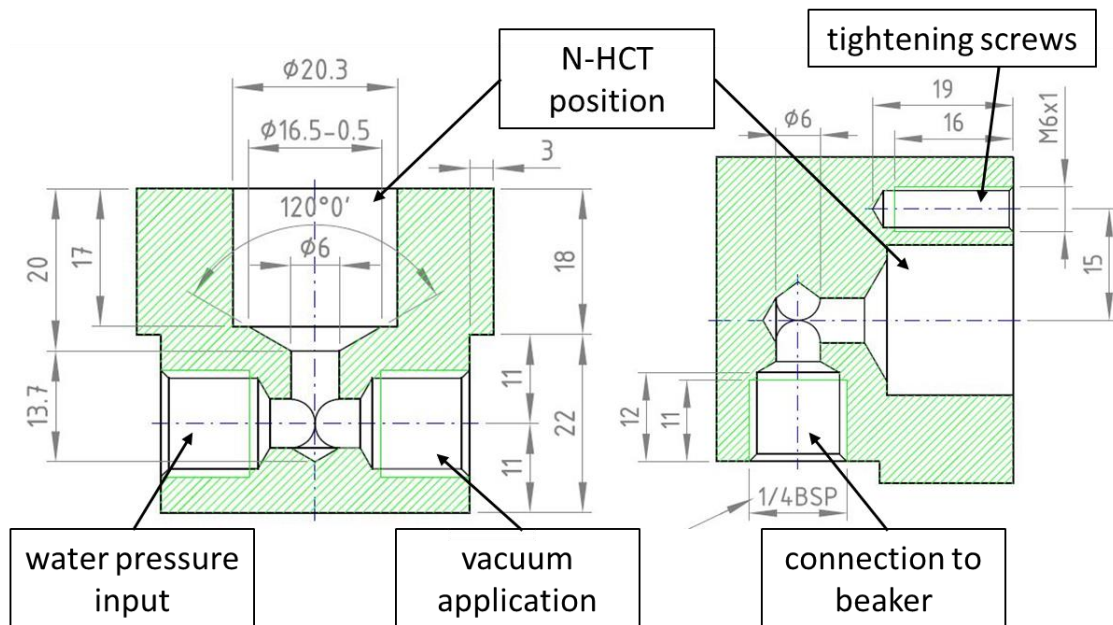


Figure 2-7. Design scheme of the pressure vessel.

To control the stream of water or vacuum at the inlets and outlets, a set of stainless-steel quarter turn plug valves was used, accommodating the applied water pressure and the 6 mm tube fitting size used. The plug valves operate in an independent manner, whether the N-HCT was subjected to first saturation or re-saturation (as explained in the following section). Figure 2.8 shows the pressure vessel and the connections to the pressure controller.

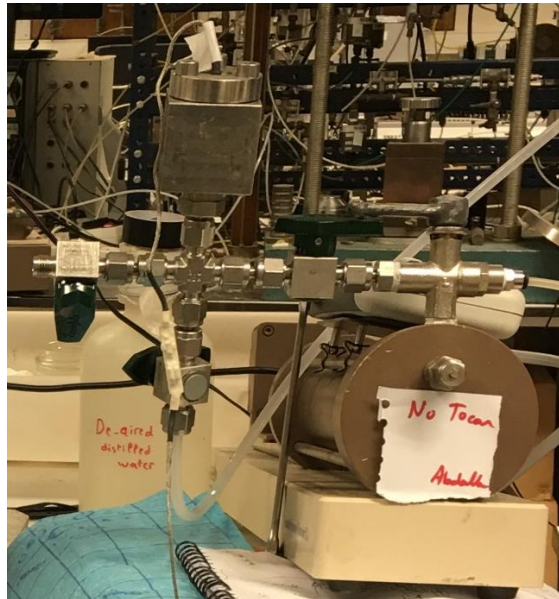


Figure 2-8. The N-HCT saturation setup.

Note that the water used to saturate the N-HCTs is deionised and de-aired distilled water. The de-airing is carried out at the laboratory directly by applying vacuum to a tightly sealed vessel with a beaker of deionised distilled water for a minimum duration of 30 minutes, or until no more air bubbles come out of the water.

2.6. First saturation, calibration and first cavitation

The first saturation of the N-HCT is an important procedure that needs to be implemented accurately as it highly influences the HCTs performance.

After assembly, the completely dry HCTs were placed and tightly sealed inside the saturation vessels connected to the vacuum pump, water beaker and pressure controller. Ideally, a pressure volume controller capable of delivering a higher pressure should have been used to apply a water pressure to the HCTs equivalent or above the AEV of the ceramic filter of 5.8 MPa, however, this equipment was not available at the time.

In the first stage of the first saturation procedure, the HCTs were subjected to vacuum for about 1 hour, allowing the evacuation of most of the air entrapped within the ceramic filter and water reservoir. In the second stage, the valve to the vacuum pump was closed, while briefly opening the beaker valve to flood the vacuumed space inside the saturation vessel and the HCT with the deaired water. This rapid flooding from the deaired water in the beaker compensates the short-comes from supplying the water directly from the pressure controller instead. This is due to the inability of the pressure controller to neither cope with negative pressures, nor with the flowrate necessary to fill the saturation vessel and HCTs. This second brief stage would typically last for few seconds before opening the valve to the pressure controller, already pressurised at the 4

MPa prescribed pressure. Shortly after, the beaker valve is closed, ensuring a tightly sealed medium within the pressure vessel and the HCTs. The HCTs were then left inside the saturation vessel overnight under the constant applied water pressure of 4 MPa.

After performing the first saturation, the HCTs were calibrated in the positive pressure range and the calibration is then extrapolated to the negative range (Tarantino and Mongioví, 2001). Voltage readings were recorded from the HCTs at different applied specific water pressures by the pressure/volume controller (3500 – 3000 – 2500 – 2000 – 1500 – 1000 – 500 – 250 – 100 – 50 – 25 – 50 – 100 – 250 – 500 – 1000 – 1500 – 2000 – 3000 – 3500 kPa).

The calibration curves did not show any significant hysteresis in the obtained HCTs readings within this pressure range. Moreover, the calibration curves of the N-HCT and C-HCT suggest that the ceramic filter has a minimal effect on the performance of the pressure transducer. Comparatively, the obtained slope values of the linear regression lines were very similar (0.5904 kPa· μ V⁻¹ for the N-HCT and 0.6089 kPa· μ V⁻¹ for the C-HCT; Mendes et al., 2022).

2.7. Cavitation tests

After the calibration process was carried out, the pressure was reduced and the HCTs were removed from the saturation vessel to be placed in the deaired water beaker. The HCTs were kept in the beaker to allow for equalisation with the the atmospheric absolute pressure. After the equalisation in readings, the measurements are set to 0 kPa, and the HCTs were subjected to evaporation tests until cavitation, to determine the maximum attainable measuring range.

Evaporation or cavitation tests are normally performed by exposing the HCT face (i.e. the ceramic filter) to the free atmosphere. As the ceramic filter water evaporates, HCT readings decrease gradually in value, as to match the relative humidity (RH) in the laboratory, and the maximum value recorded directly before cavitation identifies the maximum suction range. The minimum RH value that can be recorded can be estimated from the psychrometric law (Fredlund & Rahardjo, 1993).

$$Suction [kPa] = \frac{RT\rho_w}{M_w} \ln(RH) \quad (2.3)$$

Where R is the universal gas constant (8.314 J·mol⁻¹·K⁻¹), T is absolute temperature [K], M_w is the molecular mass of water (18.016 kg·kmol⁻¹) and ρ_w is pure water density (1000 kg·m⁻³).

RH at the laboratory is estimated to be in the 50-60 % range, signifying a suction in the 69-94 MPa range according to equation 2.3. These values extend well beyond the expected HCT measuring ranges, therefore, the cavitation is guaranteed in laboratory atmospheric conditions.

Figure 2.9 presents the results obtained in the first evaporation test of two N-HCTs and two C-HCTs carried out at open laboratory atmosphere conditions at Northumbria University (Mendes et al., 2022). The cavitation value (i.e. measuring suction range) was in the range of 2-2.25 MPa for the C-HCTs and 3.36-3.39 MPa for the N-HCTs.

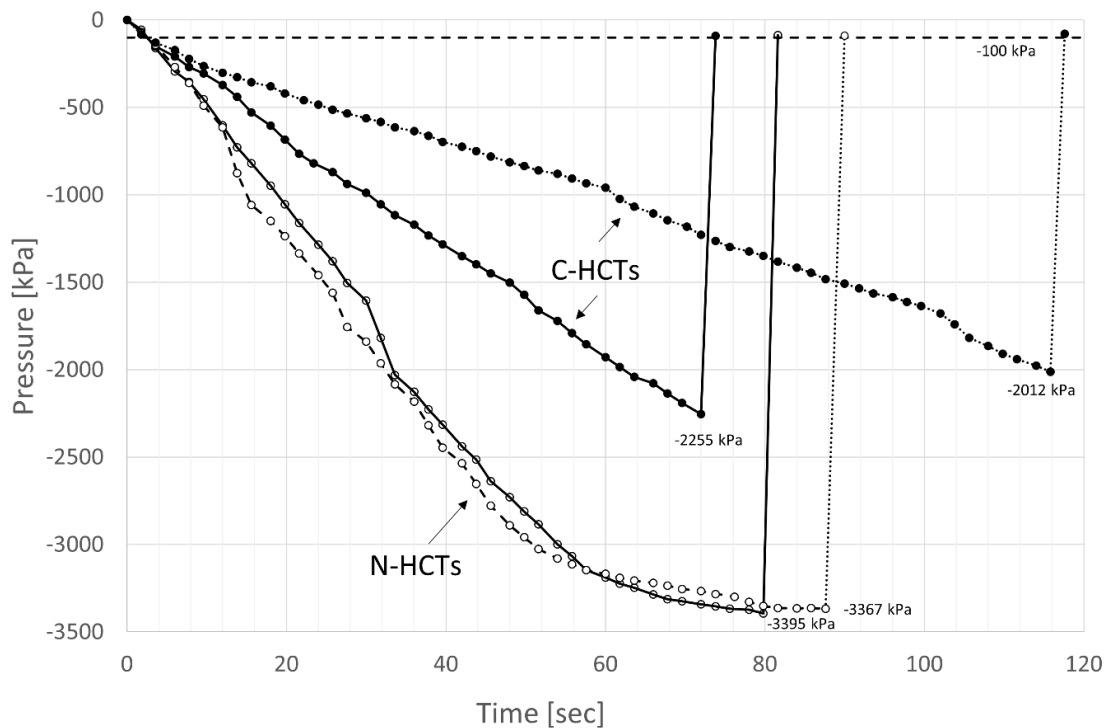


Figure 2-9. Evaporation test with N-HCT and C-HCT after initial saturation (Mendes et al., 2022).

The N-HCTs were able to attain a higher suction range than the C-HCTs, reaching values beyond -3.3 MPa. Nonetheless, these values were still well below the estimated 5.8 MPa ceramic filter AEV. This can be due to the misestimation of the AEV by underestimating the largest pore size diameter of 50 nm as given by the manufacturer, or due to the underpressuring to only 3.5 MPa, as limited by the pressure controller. In spite of these shortcomings, the N-HCTs were still able to surpass the measuring range of the C-HCTs by more than 1 MPa. Finally, the response rates of the N-HCTs were similar for both sensors and significantly faster when compared with the C-HCTs, even though the largest pore size within the ceramic filter of the N-HCTs is smaller to the largest pore size of the ceramic filter of the C-HCTs.

The observed behaviours could be explained by the effective pore size distribution, the difference in hydraulic conductivity, in both ceramic types. Figure 2.10 shows the pore size distributions of the N-HCT and C-HCT ceramic filters used, obtained using Mercury Intrusion

Porosimetry (Mendes et al., 2022). The pore size distribution for the C-HCT ceramic filter typically ranges between 2 nm and 220 nm (Mendes et al., 2020). This wide range of pore sizes can be responsible for the observed slower flow and pressure transmission within the C-HCTs ceramic, and for the distinct response rates due to different pore volume distribution in each ceramic. The pore size distribution of the alumina ceramic filter used in the N-HCT is nonmodal within 40 and 92 nm (as can be observed in Figure 2.10). This leads to an increased flow and pressure transmission, and faster and similar response rates of both N-HCTs.

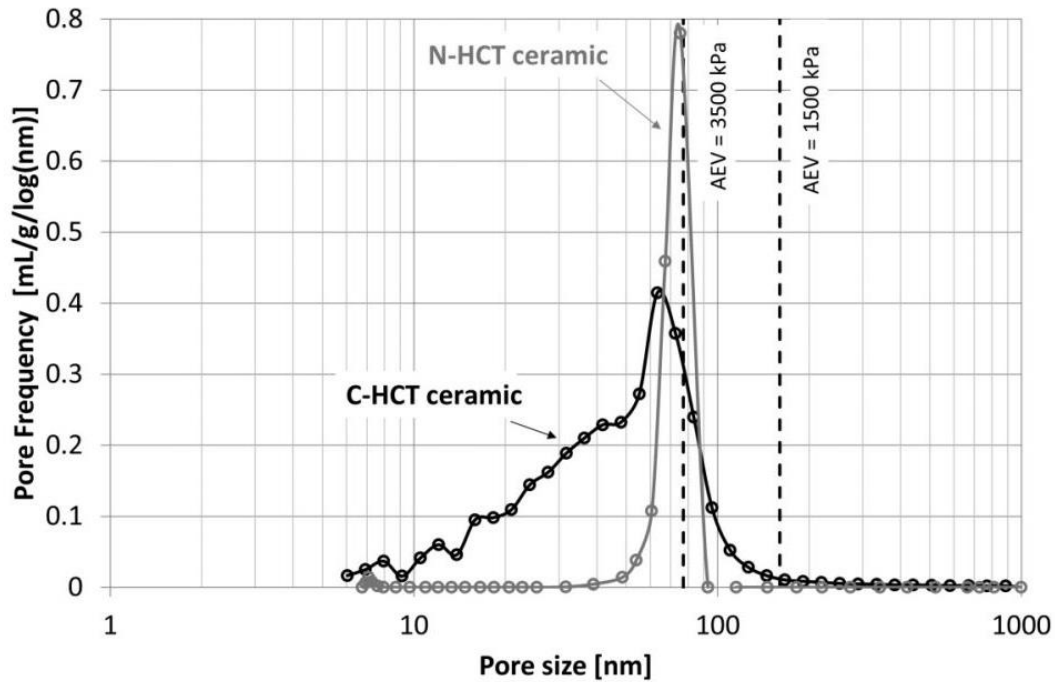


Figure 2-10. Pore size distributions of the N-HCT and C-HCT ceramic filters used, obtained using Mercury Intrusion Porosimetry (Mendes et al., 2022).

2.8. Post-cavitation re-saturation

When cavitation occurs, an immediate jump to values of -80 to -90 kPa is observed in the readings (close to absolute zero pressure). This jump corresponds to the time the air bubbles emerge in the water reservoir, resulting in the loss of hydraulic connection between the soil and pressure transducer (Mendes et al., 2013). The presence of these air bubbles in the water reservoir prevents any further measure of soil suction to take place and re-saturation of the HCTs is therefore required.

For the re-saturation process, the HCTs were placed in the saturation vessel and were re-pressurised at 4 MPa with deaired deionised water delivered by the GDS Instruments pressure volume controller. In contrast to the initial saturation, vacuum is not required and, in fact,

should be avoided as the change in phase of the water (from liquid to solid) due to the low pressure applied by the vacuum pump could damage the ceramic filter. The HCTs are recommended to be placed with the water reservoir facing downwards while the ceramic filter facing upwards during the re-saturation process. This would aid in the process of extracting or eliminating any air bubbles formed within the ceramic or reservoir of the HCTs.

The time required for re-saturation at high water pressures of HCTs after cavitation is normally stipulated to be in the range of 12 hours (overnight) up to several days. To study the time HCTs spent pressurised during re-saturation and the effect it has on their performance, a series of tests were conducted subjecting the HCTs to short pressurisation times. The results established that freshly cavitating HCTs can be reactivated in about 10 minutes of re-saturation at high water pressure, a significant reduction in the re-saturation time. These results can be of particular interest to researchers performing point suction measurements in multiple soil specimens in the laboratory.

2.9. Soil suction measurements

Point suction measurements and continuous drying tests with N-HCTs were conducted at UPC-BarcelonaTech. Point or discrete suction measurements are based on having multiple data points for soil specimens at different water contents by capturing single suction readings for a sample at known moisture conditions. The continuous method though, requires uninterrupted readings as the specimen continues to be exposed to the atmosphere and undergoes progressive drying until cavitation in the N-HCTs occurs.

2.9.1. Discrete measurements

To take a point measurement at a specific stage, a soil specimen of relatively low moisture content was prepared from the Agròpolis soil. The soil specifications are detailed in Chapter 3 (see section 3.2.1). The soil specimen is then drilled using a special round-cutting head of dimensions equal to the sensor's diameter (20 mm) at a low insertion depth of 2 mm, enough to ensure the N-HCT ceramic filter is in direct and intimate touch with the soil matrix. Plastic soil paste of the same material having a gravimetric water content in the range: $w_{Plastic\ Limit} \leq w_{paste} \leq w_{Liquid\ Limit}$, was applied on the periphery surrounding the N-HCT; and directly on the porous ceramic filter face. This paste will cut off any external atmosphere interference to the ceramic filter face and ensure the direct contact between the soil matrix and the N-HCT ceramic, respectively. The prepared setup is wrapped using an impermeable membrane, sealed with tape, set on a balance (to detect unwanted evaporation, if any), until suction readings equilibrated. A 1 kg weight is placed on top of the N-HCT pressuring the sensor towards the

soil to ensure continuous contact. Figure 2.11 shows the specimen-sensor setup after applying the paste and just before sealing (left), and the final setup being placed on the balance with the 1 kg load on top (right).

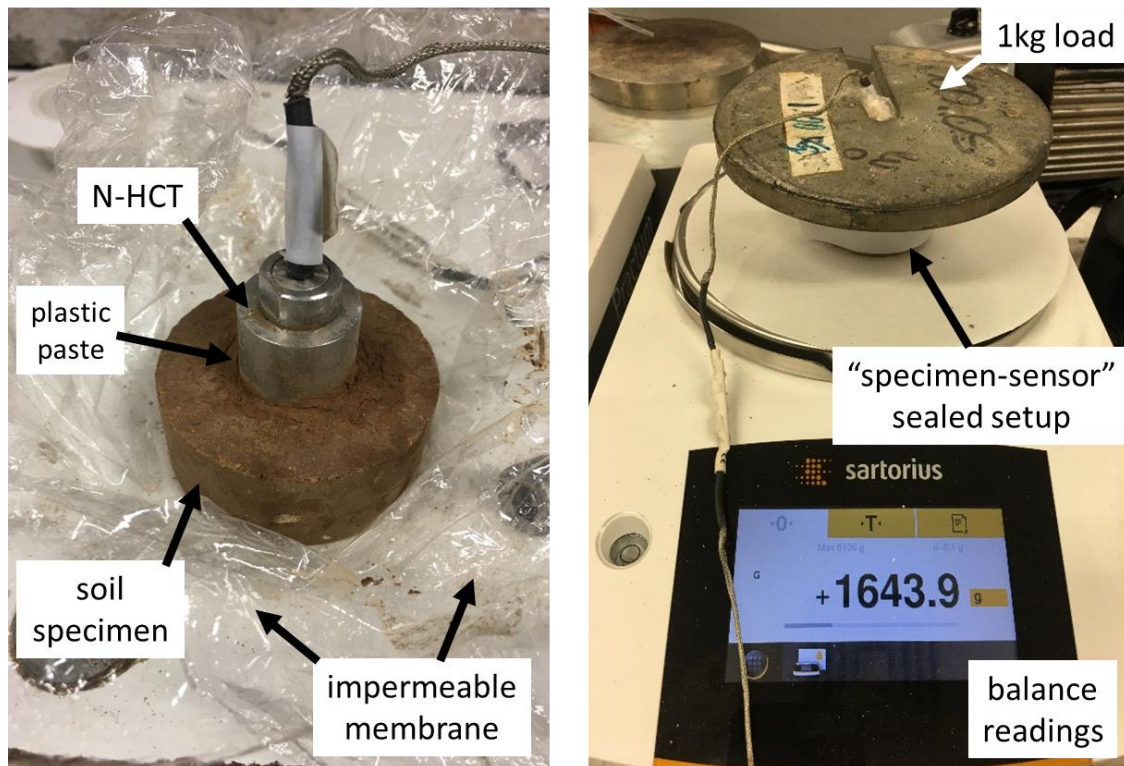


Figure 2-11. Discrete measurements setup

A series of evaporation tests were then performed to assess the N-HCTs maximum suction measuring range. The best overall results from the series of evaporation tests with the N-HCTs are presented in Figure 2.12. The two N-HCTs were able to reach pressures in the range of the applied positive saturation pressure (around 3 MPa).

A strong correlation can be noticed between the maximum N-HCTs suction measuring range and the applied positive pressure during saturation using the pressure controller. The N-HCTs were able to read negative pressure values equivalent to the applied positive pressures.

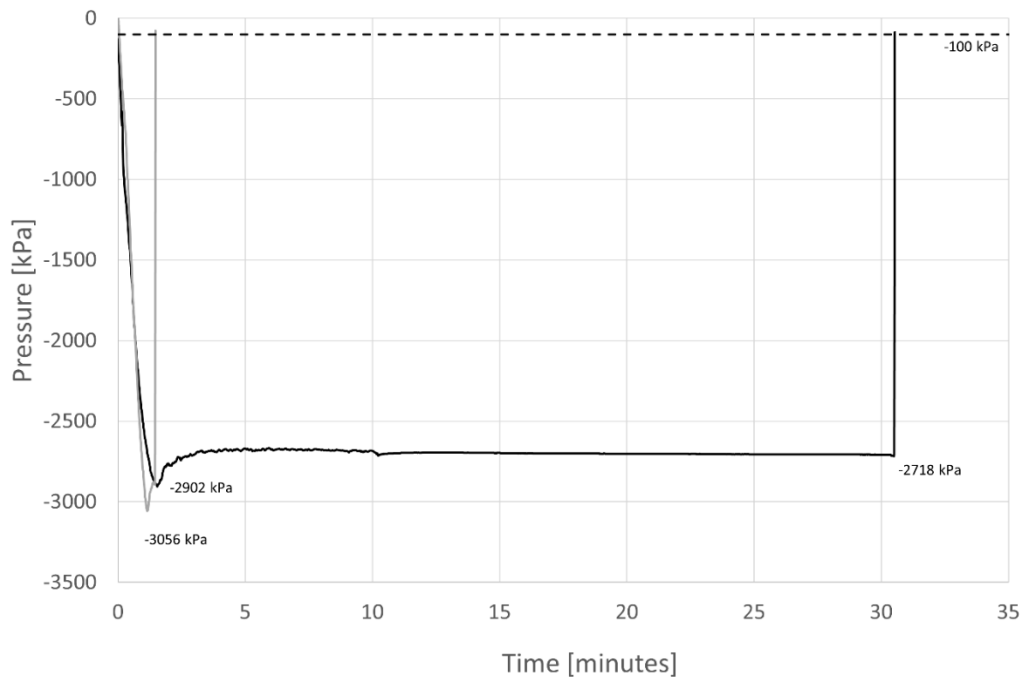


Figure 2-12. Best overall evaporation test results with the N-HCTs at UPC-Barcelona Tech (Mendes et al., 2022).

2.9.2. Continuous drying

Multiple continuous drying tests were then performed on the two aforementioned soils locally sourced in Barcelona, Spain: Agròpolis and North Campus Barcelona silty clay (see Chapter 3, section 3.2.1). Figure 2.13 shows the schematic design of the continuous drying setup. The tested specimens were 50 mm in diameter and 20 mm height (similar to the discrete specimens tested earlier). The specimens were placed on a specially designed mould that allows the N-HCT to be inserted from the bottom. The specimen placement procedure onto the top of the N-HCT was carried out in two different manners, depending on the specimen initial condition specifications: (a) dynamic compaction for the “compacted specimens” onto the specially fabricated stainless-steel surrounding mould accommodating a dummy sensor of identical dimensions to avoid damage to the ceramic filter; and (b) direct pouring for the one “slurry specimen” straight into the stainless-steel mould. Note that the stainless-steel mould can be detached when needed to accelerate the evaporation process by additionally exposing the lateral specimen surfaces. However, this can be only carried out when the specimen is structurally stable and would not collapse upon its removal. O-rings inside the holding frame ensure the N-HCT is locked in place and prevents any evaporation or leak from the bottom. Plastic soil paste is applied also where needed to cut off the influence of external atmosphere on the ceramic filter, therefore ensuring the N-HCT is reading suction from the soil matrix only, and not the RH of the external atmosphere.

The whole setup was placed on a digital balance to capture gravimetric water content changes while measuring the suction (Figure 2.13). In this part of the research however, the focus was on evaluating the suction measurements, and the gravimetric water changes are not reported (reported in Chapter 3). The gravimetric water changes were recorded at this stage to monitor the evaporation process. The sample was then sealed for 24 hours allowing paste-ceramic-soil moisture equilibrium, while monitoring for any change in suction and weight measurements. The drying was eventually produced at open laboratory atmosphere conditions.

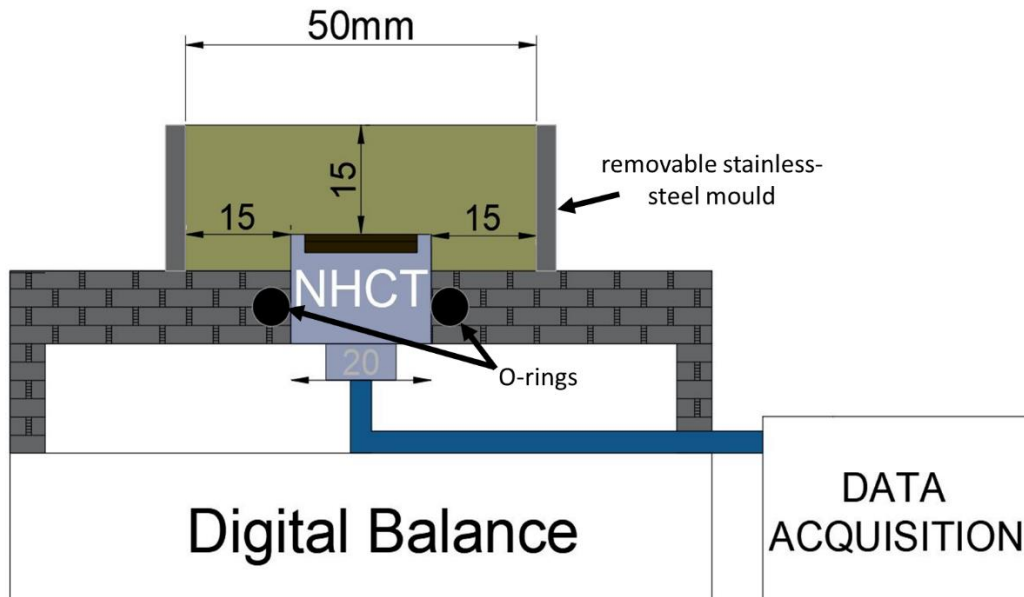


Figure 2-13. Schematic of the setup used the for continuous drying test.

The readings obtained with the N-HCTs during the continuous drying tests are presented in Figure 2.14. The pressure readings obtained with N-HCTs seem to follow the expected evolution of soil suction during continuous drying in all the tests. The initial pressure readings from the N-HCT were close to 0 kPa, before significant desaturation in the soil sample occurred as the pressure readings of the N-HCT started to progressively decrease with desaturation of the soil sample. The initial 0 kPa pressure readings varied in duration depending on the specimen initial conditions. As expected, the slurry specimen containing more initial moisture content remained saturated for a longer time before the pressure readings started to decrease (at around 3 days). After that, the pressure readings from the N-HCT were progressively decreasing in time as the soil sample desaturated, until the N-HCT cavitation. The cavitation values are indicated for each test in Figure 2.14.

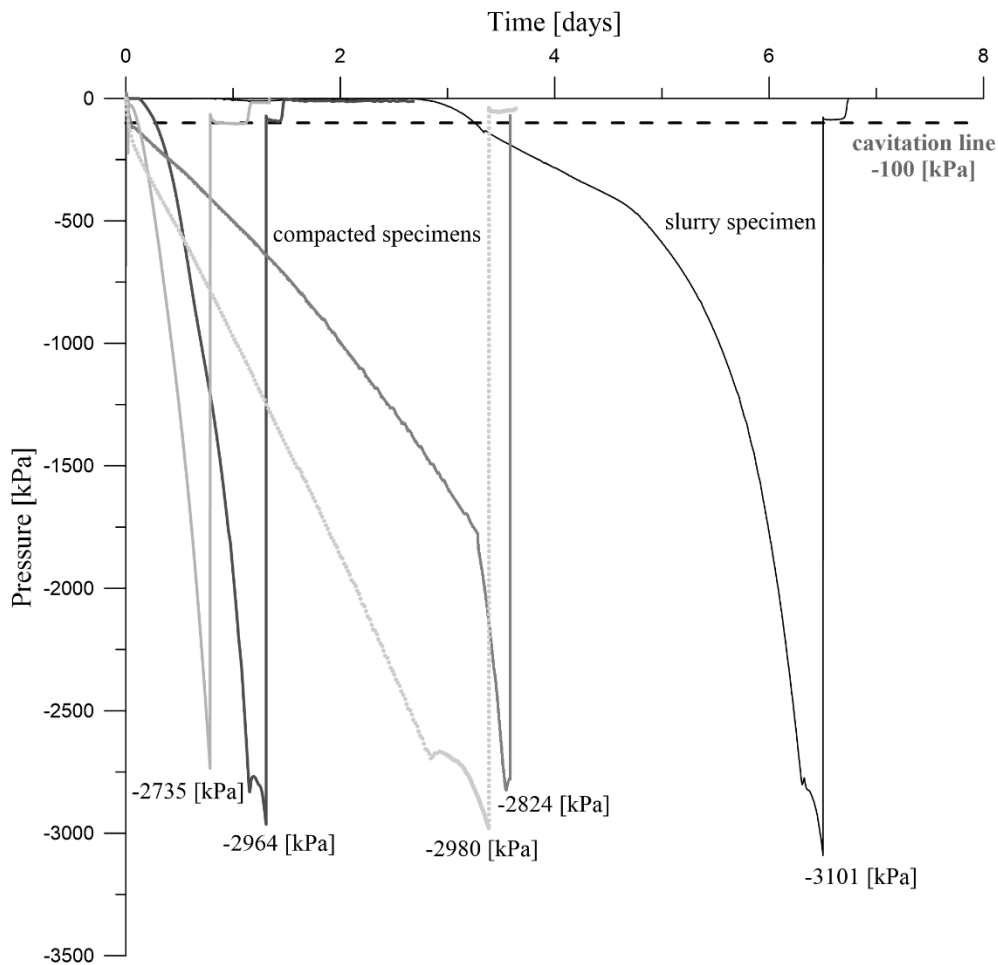


Figure 2-14. Continuous drying test with N-HCTs on the Barcelona silty clay specimen prepared from slurry with an initial water content of 34% and on four specimens from the Agrópolis clay, dynamically compacted using the Proctor hammer with an initial water content of 19% (Mendes et al., 2022).

From Figure 2.14 it is evident that, while the N-HCTs were still able to consistently record decreasing pressure values, the pattern of the suction recordings with the N-HCTs beyond 2.8 MPa appeared to be influenced by something other than the actual matric suction in the soil samples. This suggests that the reliability of the measurement with N-HCTs when recording suction values close to the pressure applied during saturation, much like the observed behaviour observed by Mendes and Buzzi (2013) in their evaporation tests, is not only influenced by the AEV of the ceramic filter, but also by the positive water pressure applied during saturation. Nevertheless, the obtained results with the N-HCTs during the continuous drying tests show that by applying a saturation pressure of 4 MPa to the N-HCTs it is possible to reliably monitor soil suction evolution in soil samples during drying to values up to 2.8 MPa. A value that is already a significant increase in the measuring range for HCTs, but also, an important step towards the development of new HCTs capable of measuring soil matric suction beyond 3 MPa.

2.10. Conclusions

High capacity tensiometers (HCTs) have been gaining more interest recently by researchers working in the experimental field of unsaturated soil mechanics. The ability to measure high suction values in drying specimens helps in understanding the unsaturated soil behaviour. Suction is directly connected to the thermo-hydro-mechanical changes in the soil, and is explicitly considered in the constitutive formulation. HCTs are increasingly used both in the laboratory and field experiment setups to monitor the suction evolution, due to their fast response and direct measurements of matric suction in the soil matrix. This is contrary to indirect methods relying on estimating the total suction from relative humidity, temperature, moisture content and electrical conductivity.

Additionally, HCTs are more appealing due to their fast reactivation times, that is the shorter and more effective saturation using pressure vessels, and due to their extended range with respect to conventional commercially available tensiometers. However, the HCTs still have the limitation of cavitation at insufficient measuring range.

A novel HCT was presented in this chapter, that has a new alumina ceramic filter with a largest pore size of 50 nm, with an AEV of 5.8 MPa, estimated using the long-Laplace equation. The N-HCT performance was evaluated in terms of its suction measuring range and reliability. A comparison is carried out between the N-HCT and common HCTs (C-HCTs) fabricated at Northumbria University using a lower AEV ceramic filter of 1.5 MPa (instead of the 5.8 MPa for N-HCT). The comparison was carried out by means of evaporation tests until the cavitation of the sensors to confirm the maximum suction measurement range. The N-HCTs range was close to 3.5 MPa, almost double that of the common HCTs in the literature, and significantly higher than the C-HCTs with a 2.8 MPa measuring range.

The design and fabrication of the datalogger, pressure vessel and corresponding connections system with the pressure and volume controller are detailed. The saturation setup used can be considered relatively complex to assemble, with respect to other commercially available tensiometers. However, once properly installed, the setup provides ease of high-quality and assured re-saturation in short times. The HCTs can be used again for suction measurements in only 10 minutes after their last cavitation.

The HCTs were also tested in sandy clay soil specimens to obtain discrete suction measurements (i.e., point measurements), and continuous drying measurements. The N-HCTs and C-HCTs were found to return relative results for high suction measurements, where the N-HCT proved its ability to perform suction measurements in higher ranges than the C-HCTs.

Plastic soil paste was applied to improve the contact between the soil and the N-HCT, and to cut off external atmospheric interference to the ceramic filter. However, it was found to influence the equilibration times needed with the soil matrix.

Continuous soil drying setups were prepared using the N-HCTs. Continuous suction measurements were carried out on multiple compacted soil specimens and a slurry specimen, made of two low plasticity clays, at the UPC-BarcelonaTech. The experimental findings highlight the capacity of the N-HCTs to continuously capture the suction changes as the samples dry progressively, up to values of 2.8 MPa. Nonetheless, the N-HCTs were capable of reading suctions beyond the 2.8 MPa value, up to 3.1 MPa in one of the cases (the slurry specimen). The pressure recordings pattern suggests that the applied positive water pressure of 4 MPa during the saturation process have limited the measuring range to that value. Despite this limit, the N-HCT still performed well in the continuous drying setups and returned reliable suction measurement results.

The N-HCT results in this chapter provide one major step towards the development of HCTs capable of measuring soil matric suction beyond 3 MPa. Such an extension in suction measurement range grants the opportunity of monitoring matric suction changes directly in the soil under study at drier regions in the field. Therefore, misestimation errors can be avoided, and estimation techniques can be enhanced. Additionally, having the extended suction measurement range helps in the calibration of numerical models in the unsaturated soil mechanics domain, and in the determination of constitutive relations. The N-HCTs are used in the following chapters to capture the soil water retention curves of soils with AEV lower than that of the N-HCT suction measurement range. This would help in capturing the transition from saturation to desaturating phases and helps in understanding the involved phenomena by providing reliable results of the porewater pressure. Likewise, the N-HCT readings in the following chapters will provide important information on the association between suction changes and the shrinkage problem, providing a valuable calibration of the involved constitutive relations.

Chapter 3

Laboratory Experimental Campaign: Evaluating Different Suction and Volumetric Measurement Techniques

Parts of this chapter have been submitted to “Engineering Geology” Journal, with the title:

“Evaluating Innovative Direct and Indirect Soil Suction and Volumetric Measurement Techniques for the Determination of Soil Water Retention Curves following Drying and Wetting Paths”.

with the co-authors:

Abdallah Najdi, David Encalada, Joao Mendes, Pere Prat, Alberto Ledesma

3.1. Introduction

One of the main characterising components of constitutive models for describing the unsaturated soil-moisture retaining capacity and flow in deformable porous material is the experimental determination of Soil Water Retention Curves (SWRCs). A SWRC is the relationship between negative porewater pressure (suction) and water content (gravimetric or volumetric) or saturation degree in the soil. The reliability and accuracy of experimentally determined SWRCs is highly dependent on the measurement methods of suction and volumetric changes in the wetting or drying paths.

SWRCs can be determined for total or matric suction where total suction consists of matric suction plus osmotic suction. In many cases where salt concentration in the soil porewater is minimal, the osmotic component can be ignored, or cautiously assumed, to draw direct comparison between total and matric suctions (Romero et al., 1999). Existing suction measurement practices are normally limited to one suction component, and to the measuring range of the technique employed (i.e., capturing either initial, intermediate, or final parts of the SWRC) as presented in Table 1.

Table 3.1. Suction measurement techniques, adapted from Bulut and Leong (2008).

Method	Suction component	Suction range [kPa]	Equilibration time for single/point measurement	Measurement Principle
Thermocouple Psychrometer	Total	300-7000	Hour	Relative Humidity
Transistor Psychrometer	Total	100-10000	Hour	
Chilled-Mirror Psychrometer	Total	100-300000	Minutes	
Filter Paper (non-contact)	Total	50-30000	5-14 days	Moisture Equilibrium
Filter Paper (in contact)	Matric	50-30000	5-14 days	
Thermal Conductivity Sensor	Matric	1-1500	Hours to Days	
Electrical Conductivity Sensor	Matric	50-1500	Hours to Days	
Dielectric Permittivity Sensor	Matric	0-100	Minutes to Hours	
Axis Translation/Pressure plate	Matric	0-1500	Days	
Tensiometer	Matric	0-100	Minutes	Direct Measurement
High Capacity Tensiometer	Matric	0-2000	Minutes	
Squeezing Technique	Osmotic	0-100000	Minutes	Electrical Conductivity

Total suction can be estimated using indirect methods by coupling suction with Relative Humidity (RH) of air inside the pores through the psychrometric law. This is carried out by means of RH thermocouples (Fredlund & Rahardjo, 1993), high-range thermocouple psychrometers (Campbell, 1979; Brown & Collins, 1980), chilled-mirror dewpoint hygrometers

(Leong et al., 2003; Agus & Schanz, 2005), and non-contact filter paper (Lu & Likos, 2004); or, by imposing specific relative humidity using salt and acidic solutions and allowing for vapour equilibrium (Delage et al., 1998). The major limitation for the total suction SWRC determination is that existing techniques can only be employed with mid- to high-suction ranges (see Table 1), lacking necessary accuracy (due to difficulties in imposing or measuring high degrees of RH) for the determination of low suction values.

The matric suction component can be estimated using indirect and direct methods. Indirect methods involve suction estimations from moisture equilibrium between the soil with a known porous media using domain reflectometry (Conciani et al., 1995), in-contact filter paper (Lu & Likos, 2004), thermal conductivity (Phene et al., 1971), electrical resistivity (Piegari & Di Maio, 2013), and dielectric permittivity sensors (Kalinski & Kelly, 1993). A specific matric suction can be imposed by altering the gas and water pressures at the soil pores using pressure plate or axis translation techniques (Guan & Fredlund, 1997; Toll, 2012). Direct matric suction measurement techniques involve direct suction determination from water tensile stress in soil pores using for instance High Capacity Tensiometers (HCTs) (Cui et al., 2007). More recently, researchers were able to determine representative parts of SWRCs by measuring matric suction directly using HCTs, while recording water content change using digital balances (Cunningham, 2000; Toker et al., 2004; Lourenço et al., 2007; Marinho & Teixeira, 2009; Liu et al., 2020). HCT results have been compared against indirect methods like filter paper, thermal conductivity sensors, and pressure plate techniques (Guan & Fredlund, 1997; Tarantino & Mongioví, 2001; Toll et al., 2015); and RH transistors and psychrometers (Boso et al., 2003; Stenke et al., 2006). In general, HCTs suction measurements have been found comparable to the other techniques, so they are considered reliable to capture initial SWRC parts. Opposite to total suction measurement techniques, direct and indirect matric suction techniques are very reliable for measuring low- to mid-suction ranges (see Table 1). These techniques, however, are not suitable or are incapable for the measurement of high suctions. Thus, matric suction techniques need to be complemented with total suction techniques to capture full SWRCs (Han et al., 2022; Hou et al., 2020).

With respect to volumetric changes, SWRCs determination needs to be carried out on specimens prepared at identical conditions to avoid discrepancies in the bulk volume quantification. Coupled with dry solid weight and gravimetric water content, bulk volume allows for the calculation of void ratio [e], volumetric water content [θ_v] and saturation degree [θ_{Sr}], all of which are parameters essential for representing the SWRC. Measuring bulk volume changes can be conducted directly on continuously drying or wetting specimens (Toll et al., 2015; Liu et al., 2020), or estimated indirectly from parallel specimens prepared at similar initial

conditions and subjected to similar drying or wetting conditions. Bulk volume change with water content under no confining conditions is defined as the Soil Shrinkage Curve (SSC) (Haines, 1923; Stirk, 1954). The SSC presents a uniform volume-water content relationship for a given set of soil. Therefore, having a representative SSC fitted model equation can readily provide indirect volume estimations of a sample for which the water content is known. This is deemed essential to estimate small-scale specimen volume (i.e., chilled-mirror dewpoint hygrometer WP4-T samples), as water content is more easily acquired. In the case of non-hysteretic volumetric behaviour for the soil in this study at least, the obtained SSC model can be used to estimate the specimen volume for the drying and wetting paths.

This chapter presents the study using separate experimental testing setups, aimed to evaluate the use of a novel High Capacity Tensiometer with a measuring range of 3.5 MPa, against other direct tensiometers and conventional indirect methods (chilled-mirror dewpoint hygrometer, relative humidity transistors and dielectric permittivity sensors). The osmotic component was proved to be insignificant of the in comparison with the matric component for the studied soil. This allowed direct combination of the obtained HCT matric suction values with the dewpoint hygrometer total suction values, providing a full-range of suction measurements. The chapter then evaluates different volumetric measurement techniques for both the drying and wetting paths conducted directly on drying specimens mounted with sensors, and indirectly on identical specimens prepared in parallel. Parallel samples are then selected as a basis of a unique SSC mathematical model for each soil batch prepared at certain initial condition. Finally, combined full-range suction readings are used to obtain a full-range SWRC by unifying volumetric measurements using the obtained SSC model.

3.2. Materials and methods

Direct and indirect measurement techniques of soil suction and volumetric changes adopted in this work for SSC and SWRC determination are presented in this section.

3.2.1. Soil characteristics

Mainly two similar and well-studied soils were used in the experimental campaign of this study: the Barcelona silty clay from UPC “North Campus” (Gens et al., 1995; Barrera, 2002; Lakshmikantha, 2009), and the low-plasticity silty clay from “Agròpolis” site next to the Llobregat river delta in Viladecans (Catalonia, Spain) (Cordero, 2019; Oorthuis, 2022). Table 3.2 below shows a summary of the main characteristics of the two soils.

Table 3.2. Soil characteristics.

	North Campus	Agròpolis
%Sand content (≤ 2 mm)	46.8	48.3
%Silt content (≤ 63 μm)	42.7	42.1
%Clay content (≤ 2 μm)	10.5	9.6
Coefficient of uniformity (C_u), and curvature (C_c)	well graded	
ρ_s (solid particles density)	2.71 [$\text{g}\cdot\text{cm}^3$]	2.70 [$\text{g}\cdot\text{cm}^3$]
w_h (hygroscopic water content)	2.2%	2.1%
LL (liquid limit)	32%	29%
PI (plasticity index)	16%	13%
Mineralogical Composition (X-ray Diffraction)	Quartz, Albite, Calcite, Feldspar and Muscovite	Quartz, Albite, Calcite, sodium microcline, dolomite, ferrous clinochlore
Scanning Electron Microscope: Average particle dimensions	18 μm \times 68 μm	37 μm \times 80 μm

The percentages of muscovite (illite) and ferrous clinochlore (chlorite) might be associated with clay minerals, which give the soil some activity and plastic behaviour.

Another main characteristic of interest in this work was to define the compaction curves under different compaction efforts: the standard Proctor (**SP**) effort ($600 \text{ kN}\cdot\text{m}^{-3}$) (ASTM D698); the modified Proctor effort ($2700 \text{ kN}\cdot\text{m}^{-3}$) (ASTM D1557); and the Scale Hammer compaction effort (specific energy $E_e=0.6 \text{ MPa}$). The Scale Hammer was carried out in a compaction mould: $\varnothing 50$ mm, h20 mm; hammer weight: 1.0 kg, and drop height 20 cm. Table 3.3 shows the optimum conditions using each of the 3 compaction efforts.

Table 3.3. Optimum compaction conditions.

	North Campus		Agròpolis	
	w_{opt} $\text{g}\cdot\text{g}^{-1}$	$\gamma_{D,max}$ $\text{g}\cdot\text{cm}^{-3}$	w_{opt} $\text{g}\cdot\text{g}^{-1}$	$\gamma_{D,max}$ $\text{g}\cdot\text{cm}^{-3}$
Standard Proctor optimum	0.130	1.89	0.160	1.802
modified Proctor optimum	0.970	2.04	0.111	2.01
Scale Hammer optimum	0.165	1.75	0.167	1.76

3.2.2. Soil batches

The soil used in the first part of this particular study, is the Agròpolis soil. The soil was prepared at three different initial gravimetric water contents ω_i initially, by mixing three 10-kg

batches of dry soil (<2 mm) with distilled water until obtaining ω_i . The batches were left for 48 hours to allow for soil-moisture equilibrium before being compacted to the corresponding required density γ_D , close to the standard Proctor optimum (A-S3), wet of optimum (A-S4), and wet of modified Proctor (MP) optimum (A-MP3), respectively. Preparation of three different batches was carried out to verify the proposed methods for complete SWRC determination at various initial conditions.

After the initial verification, more samples were prepared from both the Agròpolis (“A”) and North Campus (“NC”) soils to obtain their SSCs and SWRCs. For the Agròpolis soil, two more specimens were prepared following the standard Proctor compaction curve; two more specimens with the modified Proctor; two specimens at the Scale Hammer compaction effort; and two slurry specimens at liquid limit (LL), and 1.5 times the liquid limit (SL). Table 3.4 shows the different samples and their corresponding initial conditions: gravimetric water content (w_0), dry density (γ_D), and porosity (ϕ_0).

Table 3.4. Initial conditions of remaining specimens.

Spec.	w_0 g·g ⁻¹	γ_D g·cm ⁻³	ϕ_0 [-]	Compaction effort
A-MP1	0.089	1.96	0.278	MP – dry of optimum
A-MP2	0.120	2.00	0.262	MP – near optimum
A-MP3	0.150	1.90	0.299	MP – wet of optimum
A-S1	0.120	1.72	0.366	SP – dry of optimum
A-S2	0.150	1.80	0.336	SP – near optimum/dry
A-S3	0.172	1.79	0.339	SP – near optimum/wet
A-S4	0.210	1.68	0.380	SP – wet of optimum
A-SH1	0.120	1.42	0.470	SH – dry of optimum
A-SH2	0.150	1.65	0.401	SH – near optimum
A-LL	0.300	1.50	0.465	Liquid Limit
A-SL	0.430	1.20	0.557	SLurry (1.5×LL)

For the North Campus soil, 4 specimens were prepared from standard Proctor compaction effort and at Liquid Limit (Table 3.5).

Table 3.5. Initial conditions of remaining specimens.

Spec.	w_0 [g·g ⁻¹]	γ_D [g·cm ⁻³]	ϕ_0 [-]	Compaction effort
NC-S1	0.107	1.80	0.262	SP – dry of optimum
NC-S2	0.130	1.91	0.299	SP – optimum
NC-S3	0.165	1.87	0.366	SP – wet of optimum
NC-LL	0.32	1.51	0.336	Liquid Limit

Figure 3.1 shows the multiple compaction curves for the Agròpolis soil, with the location of the initial conditions of the tested specimens (red-filled squares).

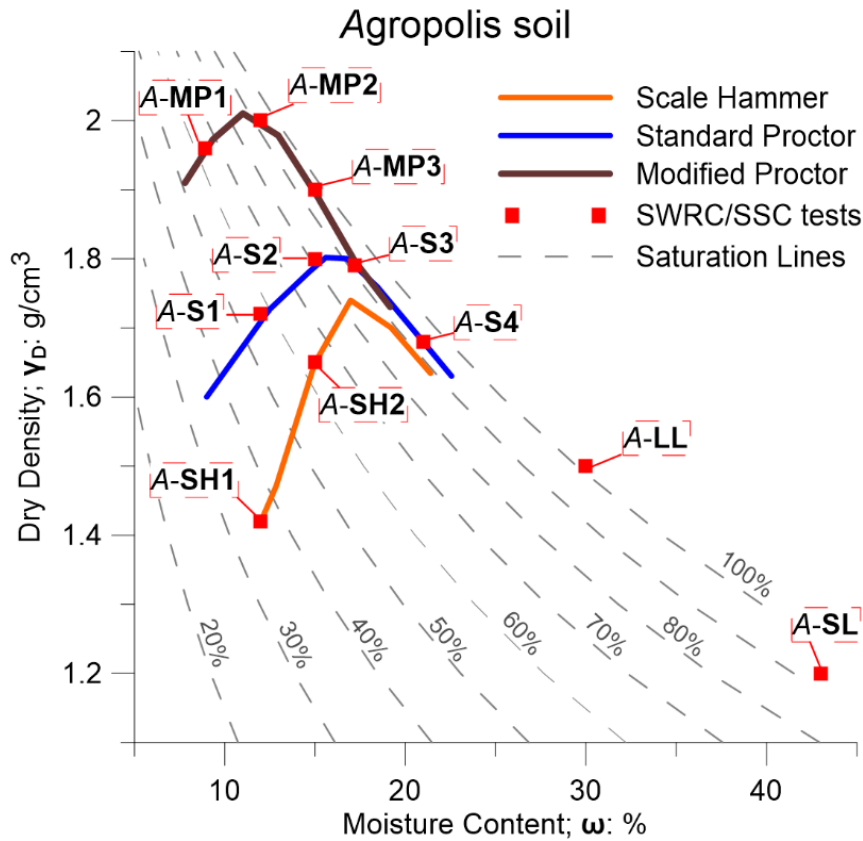


Figure 3-1. Compaction curves and initial conditions of the different specimens to be tested for SWRCs and SSCs.

3.2.3. Suction measurement techniques

Different suction measurement techniques (direct or indirect) were used either separately on parallel samples (with same initial conditions), or simultaneously on the same specimen without destabilising the soil matrix structure. In this section, a description is given of the suction measurement techniques used in this chapter.

3.2.3.1. Direct Tensiometers (UMS-T5)

Direct or commercially available traditional laboratory tensiometers directly measure soil matric suction within a 0-150 kPa range by measuring soil porewater tension. Figure 3.2 shows the UMS-T5 (UMS AG, 2018) sensor with its different components. The acrylic glass shaft length can vary between 5 cm to 15 cm. In this thesis, and particularly this chapter, the UMS-T5

sensors were placed directly in contact with different size soil specimens to measure direct matric soil suction continuously (see sections 3.3.2; 3.3.3; 5.3.4; and 6.6.1).

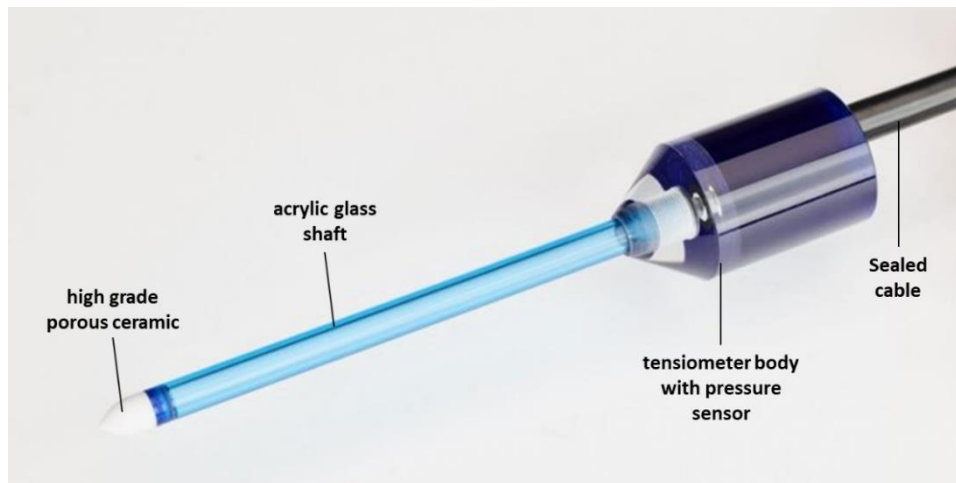


Figure 3-2. UMS T5 sensor components (UMS AG, 2018).

3.2.3.2. Northumbria High Capacity Tensiometer (N-HCT)

One of the novelties of this chapter is the use of HCTs with extended soil suction measuring range for SWRCs determination. The measuring principle is identical to direct tensiometers. However, a higher measuring range is made possible due to the use of a porous stone preventing air influx in the water reservoir (Ridley and Burland, 1993). Developed at Northumbria University (UK), the Northumbria-High Capacity Tensiometer or N-HCT is an HCT capable of measuring soil matric suction up to 3.5 MPa (Mendes et al., 2022). Similar to early designs by Ridley and Burland (1993), N-HCT is composed of a 6.8 MPa pressure transducer and a porous ceramic filter separated by a 0.5 mm³ water reservoir encased in a stainless-steel sheath. The main difference that distinguishes N-HCT from other HCTs found in literature is in the use of alumina porous ceramic filters designed with a smaller largest pore; hence, a higher Air Entry Value (AEV), resulting in a suction measuring range up to 3.5 MPa is obtained. See Chapter 2, section 2.2, for more information and details on the N-HCT fabrication and use in the laboratory.

In the N-HCT design, the >> 99.9% alumina ceramic filter (\varnothing 10mm; h=5mm) has a largest pore size diameter of 75–92 nm, determined by mercury intrusion porosimetry (Mendes et al., 2022). In a comparison with other HCTs carried out by Mendes et al. (2022), the response rates of the N-HCTs were comparable and significantly faster, even though the largest pore size within the ceramic filter of the N-HCTs was smaller than the largest pore size of the ceramic filter of the other HCTs (see section 2.9). This behaviour was attributed to the effective pore size distribution and the hydraulic conductivity of the ceramics. The pore size distribution for a 1.5 MPa ceramic filter is normally in the range 2–220 nm (Mendes et al. 2020), while that of the N-

HCT is in the range 40-92 nm. The monomodal distribution of the N-HCT ceramic results in uniform and increased flow and transmission of pressure (Mendes et al., 2022).

HCTs are required to undergo calibration, saturation and re-saturation after cavitation. Calibration happens in the positive range using a digital pressure-volume controller and a saturation vessel. A positive water pressure saturation vessel has the benefit of being quick and simple to reuse following cavitation. The calibration is then extrapolated to the negative range (Tarantino & Mongiovi, 2001). The positive pressure has been found to be highly associated with measured sustainable suction limit (Guan & Fredlund, 1997). In the case of the N-HCT, a pressure range of 4-6 MPa was applied.

N-HCTs were used in this work to determine SWRCs using the continuous approach. The continuous method is evaluated first against the discrete method to confirm non-differential evaporation or improper reading equalisation (section 3.3.1), which might eventually lead to significant misinterpretation of the SWRC. Discrete drying is based on having multiple data points at different SWRC stages by capturing single suction readings for a sample at known conditions (i.e., moisture and volume). The continuous method though, requires uninterrupted readings of all 3 variables: suction, moisture, and volume.

3.2.3.3. Dielectric water potential permittivity sensor

Dielectric water potential permittivity sensors, such as the MPS-6 sensor (Decagon Devices Inc., 2017), have a porous disc with known water retention curve using Frequency Domain Reflectometry (FDR) to indirectly obtain matric suction in the 0-2000 kPa range. Measurements are based on dielectric value estimation of the porous disc pore water at equilibrium with the soil pore water pressure (Topp et al., 1980). Figure 3.3 shows the MPS-6 sensor and its components. The MPS-6 sensors are mainly used in the field due to their tough and long-lasting capabilities, and the no need for recalibration/re-saturation.

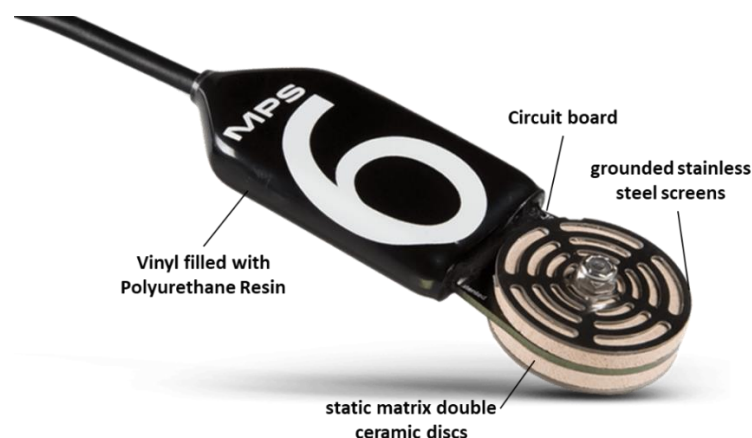


Figure 3-3. MPS-6 sensor components.

MPS-6s are typically used in the field but can also be employed in the laboratory. As with direct tensiometers and N-HCTs, MPS-6s were used in multiple setups (see sections 3.3.2, 3.3.3, and 6.6.5).

3.2.3.4. Chilled-mirror Dewpoint hygrometer (WP4-T)

A Decagon Hygrometer WP4-T PotentialMeter device (Decagon Devices Inc., 2010), based on chilled mirror dewpoint technique (Campbell et al., 2007) was used in this study. This device is adequate for measuring total suction in the 0.1-300 MPa range with a 0.1 MPa resolution. However, an operational range for suctions exceeding 1 MPa is recommended (Lu & Likos, 2004). The WP4-T soil specimen size was limited to WP4-T chamber size ($\varnothing 38$ mm; h5 mm). Specimens were prepared by dynamic compaction of a precalculated bulk soil quantity, corresponding to each soil batch, directly inside a specifically designed stainless-steel mould, to the specified height. Figure 3.4 shows the WP4-T and one of the stainless-steel specimen moulds used. Suction measurements were obtained independently using stage-approach on two specimens from each soil set for average (A-S3, A-S4 and A-MP3). At each stage, the total suction and corresponding gravimetric water content were determined before allowing the specimen to dry to the next stage, giving at least 6 hours for soil-moisture equilibration before taking any reading.

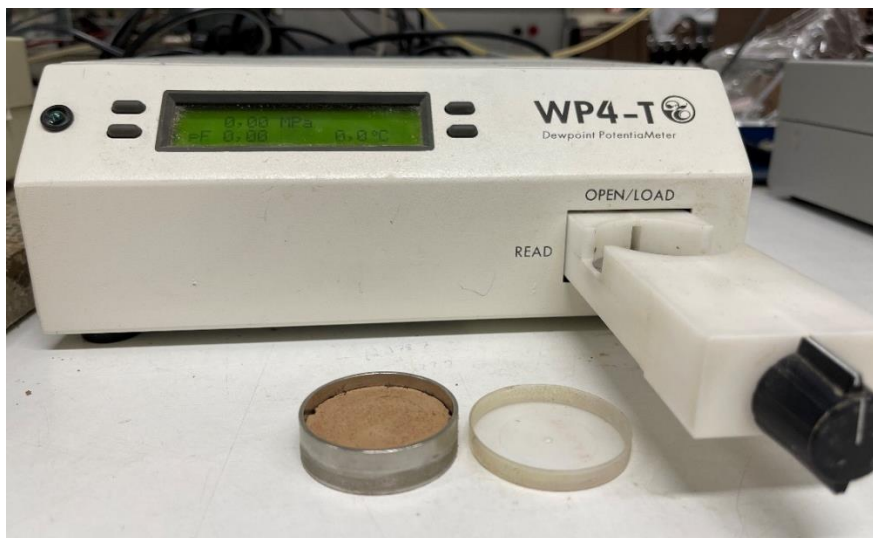


Figure 3-4. WP4-T and one of the specimens in the stainless-steel mould.

The WP4-T total suction results were indirectly compared to RH sensors, MPS-6 and N-HCTs by unifying volumetric shrinkage measurements with other setup specimens from the same set of soil as it will be explained in section 3.5.

3.2.3.5. Relative humidity sensors

Vaisala HEMP-230 soil relative humidity (RH) transistors were used to measure total suction using the psychrometric law (Fredlund & Rahardjo, 1993).

$$Total\ Suction\ [kPa] = \frac{RT\rho_w}{M_w} \ln(RH) \quad (3.1)$$

Where R is the universal gas constant ($8.314\ [J\cdot mol^{-1}\cdot K^{-1}]$), T is absolute temperature [K], M_w is the molecular mass of water ($18.016\ kg\cdot kmol^{-1}$) and ρ_w is pure water density ($1000\ kg\cdot m^{-3}$). RH transistors normally have a limited functionality for relative humidity values exceeding 99%, and their measurements can be considered reliable only in less humid conditions (i.e., in higher suction ranges).

RH sensors were used in conjunction with direct tensiometers, N-HCTs and MPS-6s (sections 3.3.3, 5.3.4, 6.6.1, and 6.6.5).

3.2.3.6. Osmotic Suction

The role of osmotic suction (OS) calculation in this work was to permit the comparison between the total and matric suction measurements. Total suction is calculated as the sum of matric and osmotic components, where the latter is due to soluble salts in pore water. These soluble salts have ions which carry out electric current, relating directly to electrical conductivity (EC). Osmotic suction can be estimated from EC (Nam et al., 2010), using equation (2) (Romero et al., 1999; Peroni & Tarantino, 2005), or equation (3) from the U. S. Salinity Laboratory Staff (1954).

$$OS\ [kPa] = 0.0240EC^{1.065} \quad (3.2)$$

$$OS\ [kPa] = 0.036EC \quad (3.3)$$

Where EC is given in $\mu S\cdot cm^{-1}$.

EC was measured using 5TE Decagon sensor, that measures volumetric water content, electrical conductivity and temperature when embedded in soil. Figure 3.5 shows the 5TE Decagon sensor with its components.

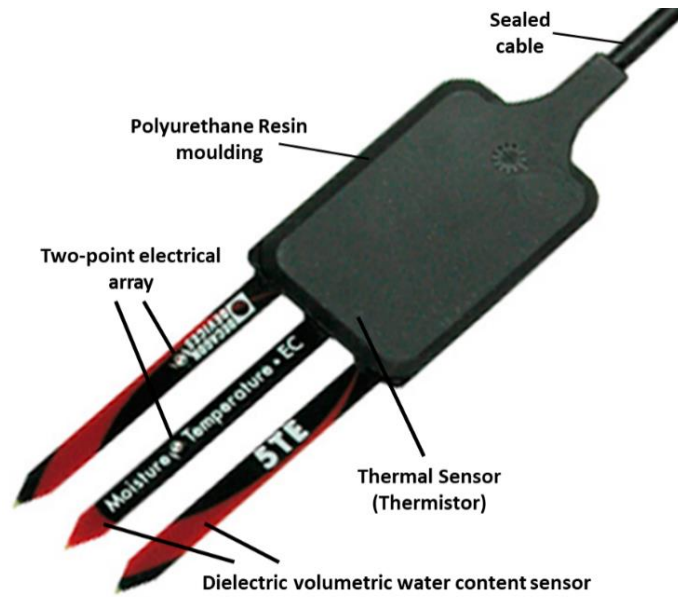


Figure 3-5. 5TE Decagon moisture, temperature, and electrical conductivity sensor.

The 5TE sensor was used in conjunction with direct tensiometers, N-HCTs, MPS-6s, and HEMP-230s in one setup in the laboratory, and also in the field in later chapter (sections 3.3.3, 3.3.4; and section 6.6.5).

3.2.3.7. Vapour Equilibrium: Salt Solutions

Vapour Equilibrium (VE) technique uses salt or acidic solutions to control the relative humidity and apply total suction on specimens hanging on rigid grids inside closed desiccators (Delage et al., 1998; Saiyouri et al., 2000). It is considered to be one of the few available methods to reach several hundred MPa in suction. However, the VE is a complex method to implement due to its associated uncertainties: (a) changes in temperature and pressure; and (b) adequately reading the relative humidity value (Delage et al., 1998).

Imposed total suction can be calculated using the established equation of thermodynamic equilibrium of solvents (Robinson & Stokes, 1959), and can be manipulated by changing the concentration of the saline or acidic solution being used. This technique might be simple to apply in the laboratory with minimum need for advanced apparatus. However, it is highly sensitive to temperature changes, proper insulation, and adequate equilibration times.

Equilibration Time

To calibrate and estimate the needed equilibration times, a series of 5 identical Hygrometer specimens ($\varnothing 38$ mm; h5 mm), prepared from the same initial conditions (A-S3), were placed into 5 different tightly closed jars (Figure 3.6).

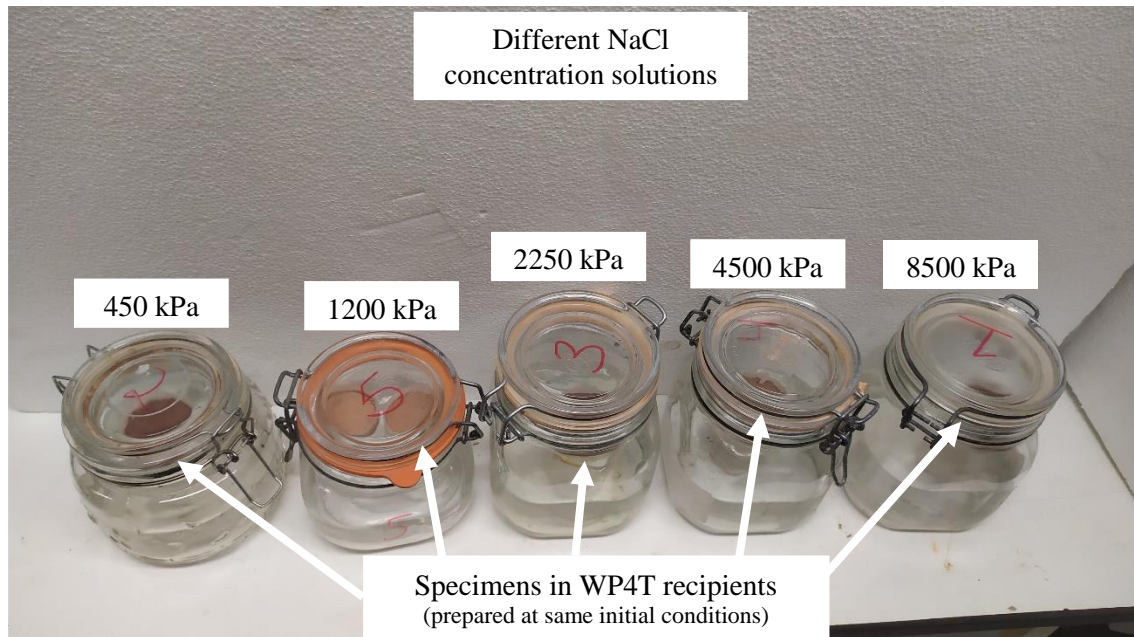


Figure 3-6. Soil specimens in Dew-point Hygrometer recipients hanging over NaCl solutions with different concentrations.

Each jar contained a different NaCl concentration solution. Table 3.6 shows water potential of NaCl at different concentrations used. The WP4-T hygrometer was used to confirm the total suction provided by each prepared solution and is provided on top of each jar in Figure 3.6.

Table 3.6. Water Potential of NaCl in Megapascals MPa at different concentrations

	Concentration [Moles.kg ⁻¹]	ψ [MPa]
1	0.10	0.454
2	0.30	1.349
3	0.50	2.242
4	1.00	4.558
5	1.90	8.660

The specimens were extracted weekly for weight and total suction measurements, until reaching residual total suction values equal to the imposed suction by the solution.

Obtaining the SWRC points

Different samples were prepared at different initial conditions (ω_i , γ_D) (Table 3.4), to coincide with the obtained SWRCs for the first 3 batches tested (i.e., A-S3, A-S4, and A-MP3). The samples were subjected to a series of gradually increasing NaCl concentration of salt solutions inside a desiccator (see Figure 3.7a and 3.7b). Total suction is applied in 6 consecutive steps every 3 weeks, with gradually increase in solution concentration, i.e., gradual increase in applied total suction (500-1000-2000-4000-8000-30000 kPa). However, saline solutions have been found to suffer limitations for suctions below 10 MPa (Delage et al., 1998). At each step

Relative humidity inside the desiccator was measured using capacitive sensors to verify the coherency with applied suction results (Villar & Gómez-Espina, 2007). Direct manual volumetric measurements were carried out using a digital calliper (0.01 mm accuracy) on the cylindrical core samples (Toker et al., 2004; Péron et al., 2007). Void ratio and gravimetric water content were computed by the end of each applied level of suction, and therefore the SWRC points was obtained.

After reaching the highest imposed suction level (i.e., 30,000 kPa), the specimens were removed from the desiccators and exposed to free atmospheric conditions in the laboratory for 2 weeks until drying completely. The specimens were then returned to the desiccators with the saline solution of 30,000 kPa to start the wetting path. After 3 weeks confinement with the same solution, the specimens were measured for weight and volume, and the saline solution was replaced with one of lower concentration (i.e., imposed total suction 8000 kPa), then 2250 kPa, and finally 500 kPa. Therefore, a total of 4 wetting points were obtained for each specimen. The whole duration of the test (drying-wetting paths) was 32 weeks.

3.2.4. Volumetric measurement techniques

Proper bulk volume quantification is critical for void ratio, volumetric water content and saturation degree calculation (essential SWRC parameters) (Wen et al., 2021).

For irregular specimen shapes, submerging specimens in fluids (e.g., kerosene, petroleum, or toluene (Sibley & Williams, 1989)) is regarded as a precise but destructive method for estimating the soil specimen volume. Using rubber balloons to protect soil specimens has been reported to be satisfactory and non-destructive (Tariq & Durnford, 1993), yet challenging to perform on sensor-carrying specimens. Other non-destructive and continuous techniques like photogrammetry can represent detailed 3D soil surface using a point cloud of irregular specimens (Li et al., 2018). Standard digital cameras can be used to develop clodometers for image rotating nonuniform clods (Stewart et al., 2012), or Digital Image Correlation (DIC) to measure deformation or strain fields (El Hajjar et al., 2020), or Digital Image Analysis (DIA) to analyse images of exposed soil surfaces (Tollenaar et al., 2017a). Moreover, 3D scanners using LiDAR technology and a turntable can also be used to continuously measure the volume of nonuniform soil samples (Wong et al., 2019).

In this work, Digital Image Analysis (DIA) and paraffin-coating (PC) were used to acquire dataset basis for analytical SSC modelling, as explained in the following sections.

3.2.4.1. Digital Image Analysis (DIA)

DIA technique is the analysis of digital images taken of different exposed surfaces simultaneously using a thresholding criterion in the ImageJ software (Rasband, 2006), following the methodology of Lakshmikantha et al. (2012). In this study, DIA was used as both a "direct" manner (DIA-D) and an "indirect" manner (DIA-ID).

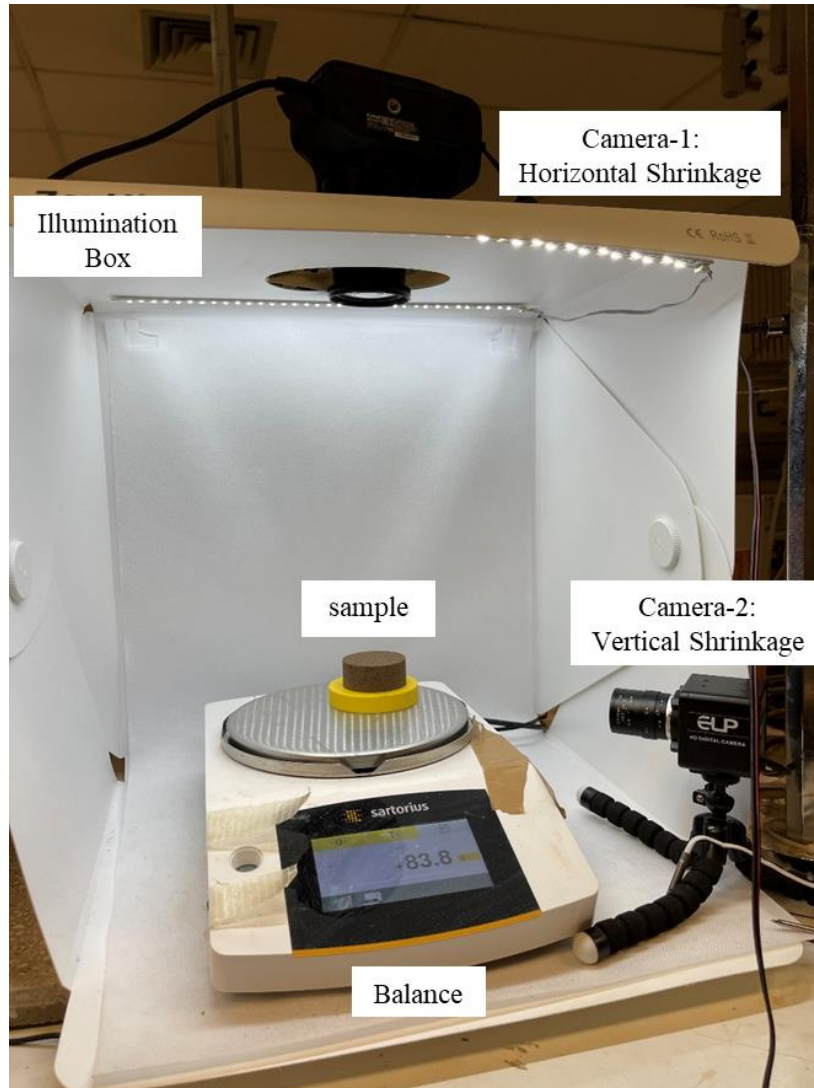


Figure 3-8. DIA procedure applied to a separate specimen.

For DIA-D, two cameras were positioned facing the top and side of the specimen, to capture the surface area and height changes simultaneously (Figures 3.8, 3.11, and 3.13). In the environmental chamber setup (Figure 3.17), the obscure walls of the specimen holder of the environmental chamber limited the use to a single camera situated above the sample to capture the horizontal shrinkage. The total volumetric deformations were then estimated based on the horizontal shrinkage measurements from top-surface images, assuming a uniform and isotropic behaviour.

For DIA-ID, the volumetric changes of parallel core samples for each of the tested soil batches were analysed. The results of both DIA-ID and DIA-D were compared over the SSC of each soil batch, to observe the effect of: (a) intrusion of rigid body sensors (Figures 3.11 and 3.13); (b) differential evaporation gradient due to exposed specimens top surfaces only (Figures 3.13 and 3.16); and (c) the isotropic deformation behaviour assumption made for the large-scale specimen (Figure 3.17).

DIA was used in different experimental setups for direct continuous and indirect continuous volumetric measurements (section 3.4.1).

3.2.4.2. Paraffin-Coating (PC)

PC has long been found to be straightforward and less expensive, producing low-error measurements (Johnston & Hill, 1945; Lauritzen, 1948). Soil specimens are covered in paraffin (of known density), before being dipped in water for volumetric estimation (based on Archimedes principle). PC was carried out to indirectly estimate the volume of smaller samples (i.e., WP4-T specimens) and confirm with both DIA results (DIA-D and DIA-ID), for the drying and wetting paths. A destructive approach like the PC was acceptable here where samples served the sole purpose of acquiring distinct volume-water content points to determine unique SSCs, in both drying and wetting paths, for each soil batch.

Identical core samples ($\varnothing 50$ mm; h20 mm) were prepared from each soil batch, by compacting to the corresponding dry density in a constant-volume mould. For each soil batch, 20 samples were subjected to gradual drying in free laboratory conditions, while another 20 samples were dried completely, before being subjected to gradual wetting. Wetting was conducted by adding 1g of water per day before tightly closing the specimen, allowing soil-moisture equilibrium. The water addition was carried out using a syringe and scattering the 1g of water to be added as evenly as possible across the specimen surface. Sample water content was monitored periodically to obtain complete SSC data points range.

3.2.4.3. SSC modelling

The aim of defining a mathematical expression for SSCs in this work was to obtain a unique void ratio-water content mathematical relationship for each soil batch. Acquired experimental SSCs for each soil set were then fitted with an established equation, considered to be distinctive for each specific soil set. In the case of the non-hysteretic volumetric behaviour observed for the soil in this study at least, the obtained SSC function can be considered as representative of both the drying wetting paths.

SSC is ordinarily classified into four stages (i) structural, (ii) normal, (iii) residual and (iv) zero shrinkage (Figure 3.9). Compaction and remoulding can be related to reducing the structural pores (Peng & Horn, 2005); subsequently, the first stage for the structureless compacted soil specimens in this study started with a uniform slope at normal shrinkage stage directly (Sposito & Giráldez, 1976; Peng et al., 2012). In this normal stage, before reaching the air entry value, the volume of evaporated water is equivalent to the shrinking soil bulk volume, signifying a saturated pores matrix (Mitchell, 1992). In the residual shrinkage stage, air enters the intra-aggregate pores, and the evaporating water volume surpasses the bulk volume reduction. In the final zero-shrinkage stage, for non-expansive clays (Lu & Dong, 2017), the soil particles do not change in configuration as water continues evaporating (Figure 3.9).

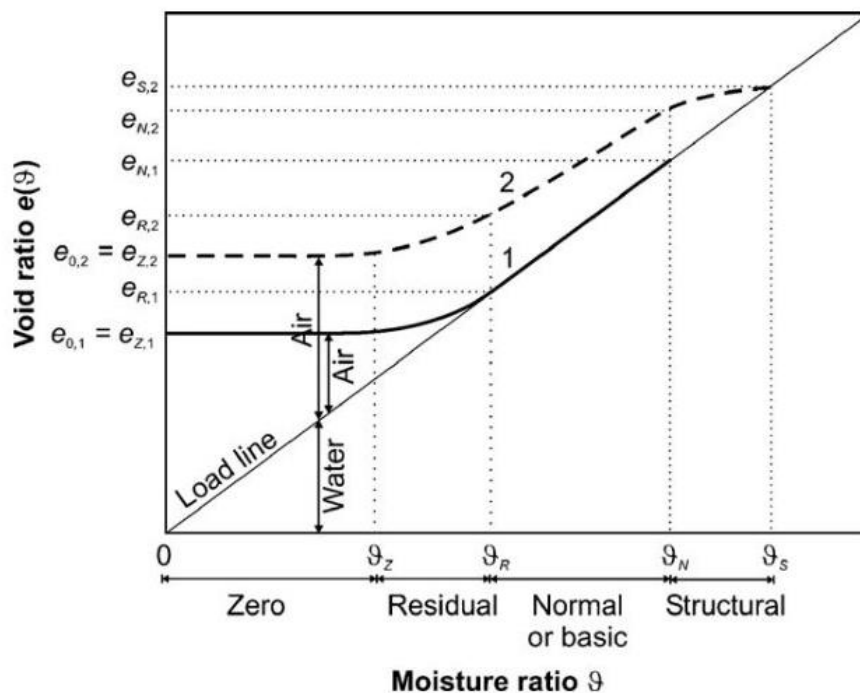


Figure 3-9. Schematic representation of a soil shrinkage characteristic curve of a non-structured soil (solid line, 1) and a well-structured soil (dashed line, 2). The subscripts S, N, R, and Z, indicate the limits of structural, normal, residual and zero-shrinkage stages (Cornelis et al., 2006).

To mathematically model these stages, multi-equations (e.g., McGarry & Malafant, 1987; Braudeau et al., 1999) or a single equation (Peng & Horn, 2005) can be used. The equations can be mathematically represented by sigmoid curves requiring 2-3 fitting parameters (Groenevelt & Grant, 2001).

In this study, one amongst many established models was selected following result suggestions by Cornelis et al. (2006) who compared nine different parametric models. They observed a best-fitting performance by a proposed modified Chertkov model (Chertkov, 2000, 2003) (ModCC,

equation 3.4), and modified Groenevelt and Grant model (equation 3.5) (Groenevelt & Grant, 2001). Both models are expressed in terms of the volumetric water content θ_V .

$$\begin{aligned}
 e &= e_0 && \text{for } 0 < \theta_V < \theta_{rl} \\
 e &= e_0 + \mu(\theta_V - \theta_{rl})^2 \frac{\rho_w^2}{\rho_s} && \text{for } \theta_{rl} < \theta_V < \theta_{AEV} \\
 e &= 2\mu_{CC}(\theta_{AEV} - \theta_{rl})\theta_V + \sigma_{CC} && \text{for } \theta_{AEV} < \theta_V < \theta_{LL} \\
 \sigma_{CC} &= e_0 - \mu_{CC}(\theta_{AEV} - \theta_{rl})(\theta_{AEV} + \theta_{rl})
 \end{aligned} \tag{3.4}$$

Where μ_{CC} is a model coefficient, ρ_w is the density of water ($1000 \text{ kg}\cdot\text{m}^{-3}$); ρ_s is the density of the solid particles ($2700 \text{ kg}\cdot\text{m}^{-3}$); θ_{LL} is the liquid limit; θ_{AEV} is the moisture ratio at air entry; θ_{rl} is the residual moisture ratio; e_0 is the void ratio at oven-dryness; and σ_{CC} is the intercept of the SSC in the proportional shrinkage zone.

The modified Groenevelt and Grant model (referred to as ModGG (Cornelis et al., 2006)) is represented by a single equation, not requiring prior definition of specific SSC properties, other than the volume at zero-shrinkage.

$$e = e_0 + \gamma_{GG} \left[\exp\left(\frac{-\xi_{GG}}{\theta_V^{\zeta_{GG}}}\right) \right] \tag{3.5}$$

Where e_0 is the oven-dry void ratio, and γ_{GG} , ξ_{GG} , and ζ_{GG} are ModGG model parameters acquired by matching the proposed equations to the experimental SSC using a nonlinear best-fitting mathematical solving method. In our case, out of the two models, results of only the ModGG were employed to represent the shrinkage behaviour for its better goodness of fit. Additionally, the less-demanding fitting process is in contrast with other SCC models requiring specific SSC properties (e.g., volumetric water content at Air Entry Value [AEV]: θ_{AEV} (Giráldez et al., 1983); normal shrinkage slope: β_{NS} (McGarry & Malafant, 1987); curvature at transition zones (Olsen & Haugen, 1998); etc.), which entails an analysis of the complete experimental SSC prior to finding its respective model. Unlike these models, the dimensionless parameters of the Groenevelt and Grant (2001) model do not pertain specifically to any known soil characteristics or have a comparable physical significance. The model equation was selected as a result of its functionality and utilised simply as a volumetric estimation tool. The nonlinear best-fit for a presented volumetric water content – void ratio dataset $[\theta - e]$, is obtained by iterating the dimensionless fit parameters presented in equation 3.5. Comparing of different models and their goodness of fit is out of the scope of the work in this chapter.

3.3. Evaluating the N-HCT performance

N-HCT is a newly developed sensor (Mendes et al., 2022) and its performance was evaluated firstly by studying the validity of using a continuous drying setup against a discrete drying technique, and secondly, by comparing against other established suction sensors as presented in Table 3.7.

Table 3.7. Experimental methods used for each set.

Soil Batch	Suction measurements		Volumetric measurements	
	Direct method	Indirect method	Direct method	Indirect method
A-S3	N-HCT continuous / discrete	WP4-T	DIA	PC; DIA; SSC model
A-S4	N-HCT; T5 tensiometer	MPS6; WP4-T		
A-MP3	N-HCT; T5 tensiometer	MPS6; RH; WP4-T		

3.3.1. Discrete versus continuous drying methods

Comparing discrete with continuous drying measurements has been previously practiced in order to validate the use of HCTs for determining the SWRC (Lourenço et al., 2011). The discrete technique (section 3.2.3.2) provides more time for soil moisture equilibrium, thus considered to present proper measurement of the matric soil suction level. However, the continuous drying technique requires less preparation and testing time (Toker et al., 2004). When the evaporation rate in the continuous method is reduced, the two methods have been noted to return comparable results (Boso et al., 2003).

3.3.1.1. Discrete Measurements

Ten cylindrical core specimens ($\varnothing 50$ mm, h20 mm) were prepared from soil batch A-S3 in a constant-volume mould with known target density, and left to dry in stages, a procedure similar to that in PC specimens preparation explained earlier (section 3.2.4.2). At each distinct stage, a specimen was measured for water content and drilled using a special round-cutting head of dimensions equal to the sensor's diameter (20 mm) at an insertion depth of 5 mm. A 2 g of plastic soil paste of the same material ($\text{Plastic Limit} \leq \omega_{paste} \cong 20\% \leq \text{Liquid Limit}$) was applied on the periphery and porous ceramic filter face to cut off external atmosphere interference and ensure direct and intimate ceramic-soil contact. This relatively wet soil paste, first in contact with the sensor ceramic, results in an initial estimation of very low suction. The sample-sensor setup was then confined tightly with an impermeable membrane and set on a balance (to detect unwanted evaporation, if any), to allow for moisture equalisation in the soil-

paste-sensor system The suction measurements increase asymptotically until reaching a constant value as moisture equilibrates between the introduced relatively-wet paste and the soil pores. Due to the relatively wet paste, the equilibration time needed by the different specimens varied in the range of 0.25-2.5 hours.

Figure 3.10 shows the preparation of the specimen: applying the plastic paste to the sensor face, drilling the specimen for sensor insertion, and sealing the sensor-specimen setup. The setup is later placed on a balance while waiting to take the discrete measurement.



Figure 3-10. Discrete specimen preparation.

3.3.1.2. Continuous Measurements

For the continuous setup, a same size core sample (\varnothing 50 mm, h 20 mm) was compacted directly over a specially fabricated frame accommodating a dummy sensor of identical dimensions (to avoid porous ceramic filter damage during dynamic compaction process). Target density was achieved by controlling the prepared bulk mass poured in the constant-volume mould. The cylindrical specimen is of the same shape of the external sensor body and its ceramic. The cylindrical shape, in addition to the central positioning of the sensor (15mm from all exposed surfaces, see Figure 3.11) ensures an all-time contact during drying shrinkage, and an equal distance from all evaporation fronts. The specimen size provided a sufficient space to accommodate the sensor embedment without affecting the soil structure integrity during the anticipated shrinkage, while avoiding larger specimens that cause a differential evaporation gradient.

Plastic paste was applied in a similar manner as the discrete setup, between the sensor ceramic and the soil. The sample was then sealed for 24 hours before starting the continuous drying,

allowing paste-ceramic-soil moisture equilibrium, while monitoring for any change in suction and weight measurements.

The setup, as shown schematically in Figure 3.11a, was placed on a digital balance to capture gravimetric water content changes. The sensor cable was secured in place to eliminate unwanted changes during the weighting process (Lourenço et al., 2011). Exposing lateral surfaces has resulted in a higher exposed surface ($A_{s,T}$) to total specimen volume (V_T) ratio ($A_{s,T}/V_T = 1.30 \text{ cm}^{-1}$). This ensures a more uniform desiccation front formation, avoiding uneven suction growth. Central positioning of the sensor (15 mm from all exposed surfaces, Figure 3.11) was to ensure an all-time contact during drying, especially during shrinkage, and an equal distance from evaporation fronts. Volumetric measurements were taken hourly using a direct DIA procedure by capturing sample height and surface area simultaneously.

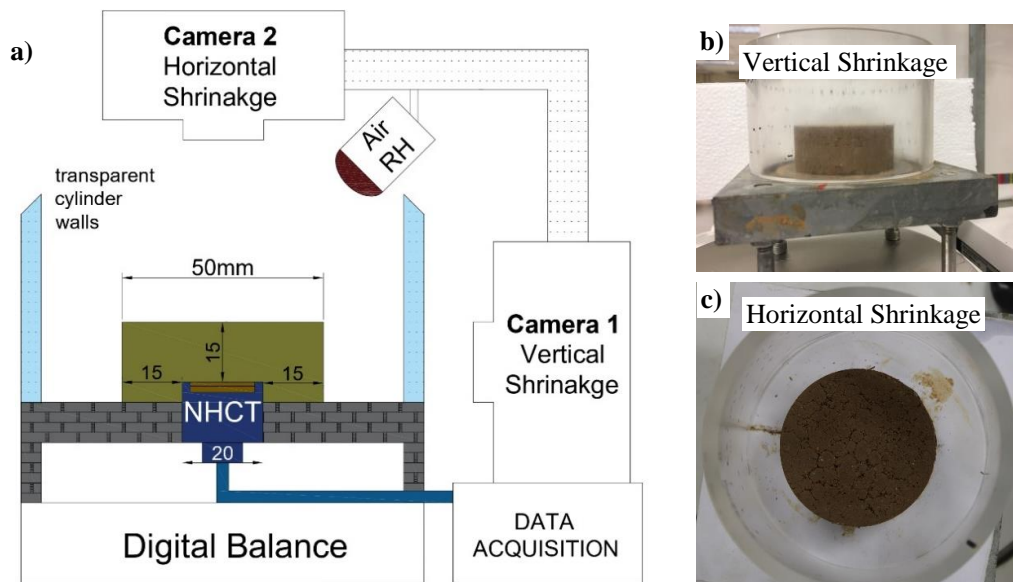


Figure 3-11. (a) Continuous drying setup sketch, with (b) Vertical, and (c) horizontal shrinkage surface images.

A clear Perspex cylinder was introduced to merely limit wind and turbulence effect on evaporation, while avoiding the obstruction of image-capturing pathway. In the absence of wind, the aerodynamic resistance magnitude increases significantly, as its calculations become based on diffusivity (Dalton's Law for latent heat flux expressions). Consequently, the inversely proportional evaporation rate reduces by 2-3 folds of magnitude (Cuadrado et al., 2022), making it theoretically sufficient to propose impeding wind and turbulence effects to significantly reduce evaporation rates. The evaporation rate was fairly constant and relatively low at around $0.03\text{-}0.05 \text{ g}\cdot\text{hour}^{-1}$, considered to be sufficient to allow for soil moisture to equalise in the soil matrix during the continuous drying test.

Figure 3.12 presents the obtained results using discrete and continuous methods. Both SWRCs demonstrated a good trend capturing agreement over the measured range. The continuous drying provided sufficient moisture equalisation between the soil pores and the ceramic. Additionally, continuous-SWRC demonstrated better development consistency compared to discrete-SWRC stage points. The continuous drying setup was safely adopted for capturing the SWRCs of the remaining batches.

Continuously measuring the wetting path seemed problematic due to the associated technical difficulties: (a) starting from a drier specimen, with suction level beyond tensiometer cavitation point; (b) expecting sample-tensiometer suction equalisation close to cavitation level; and (c) re-saturating the specimen continuously, giving enough soil moisture equilibrium time. Thus, for the wetting path, only discrete measurements were obtained. The same discrete drying specimens were oven-dried and then re-saturated gradually, each to a different saturation degree, to acquire the main-wetting curve. The gradual re-saturation process was executed manually by scattering evenly across the specimen surface multiple droplets of distilled water having a cumulative weight of 1g every 24 hours. The re-saturation process was executed carefully and at this rate to avoid a ponding-induced increase in liquid pressure at the specimen boundaries that would lead to soil structure collapse or specimen distortion due to differential saturation. The discrete measurement procedure was repeated to capture soil suction at different stages. As expected, an obvious hysteretic behaviour was observed between the drying and wetting paths (Figure 3.12).

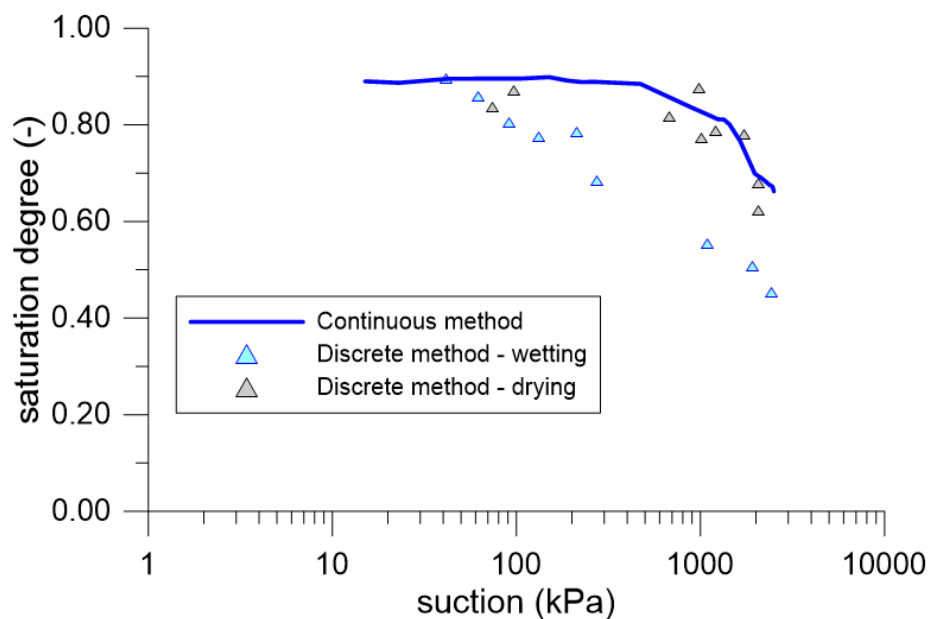


Figure 3-12. Continuous versus Discrete drying methods.

3.3.2. Comparing against matric suction measurement techniques

Comparison with other established techniques was carried out to evaluate the different direct suction measurement techniques. A similar but larger continuous drying setup was designed ($\varnothing 80$ mm, h120 mm) to evaluate N-HCT functionality against commercially available matric suction sensors (i.e., UMS-T5 and MPS-6). Soil Batch A-S4 (wet of optimum) was used, having plastic consistency, therefore easier to remould and compact in the complex geometry around different embedded sensors in a close proximity, as shown in Figure 3.13. An image of the laboratory setup is shown in Figure 3.14. An example of the horizontal and vertical shrinkage images is also given in Figures 3.15a and 3.15b, respectively.

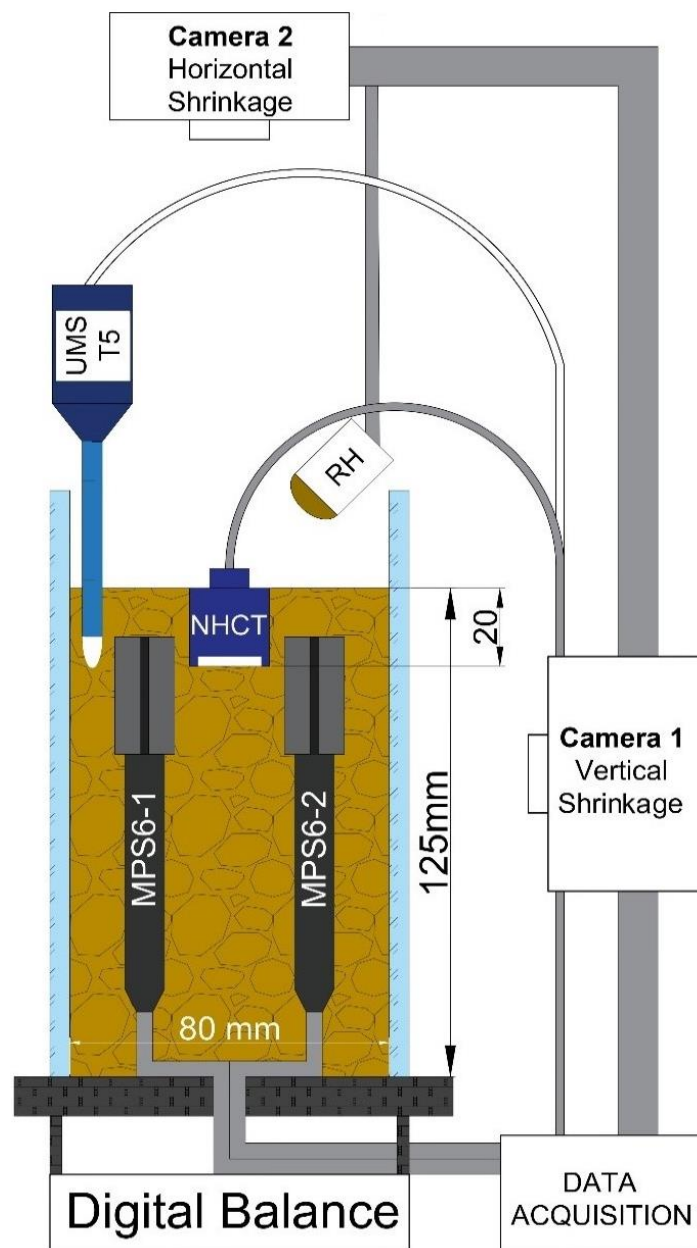


Figure 3-13. Scheme of the second continuous drying setup.

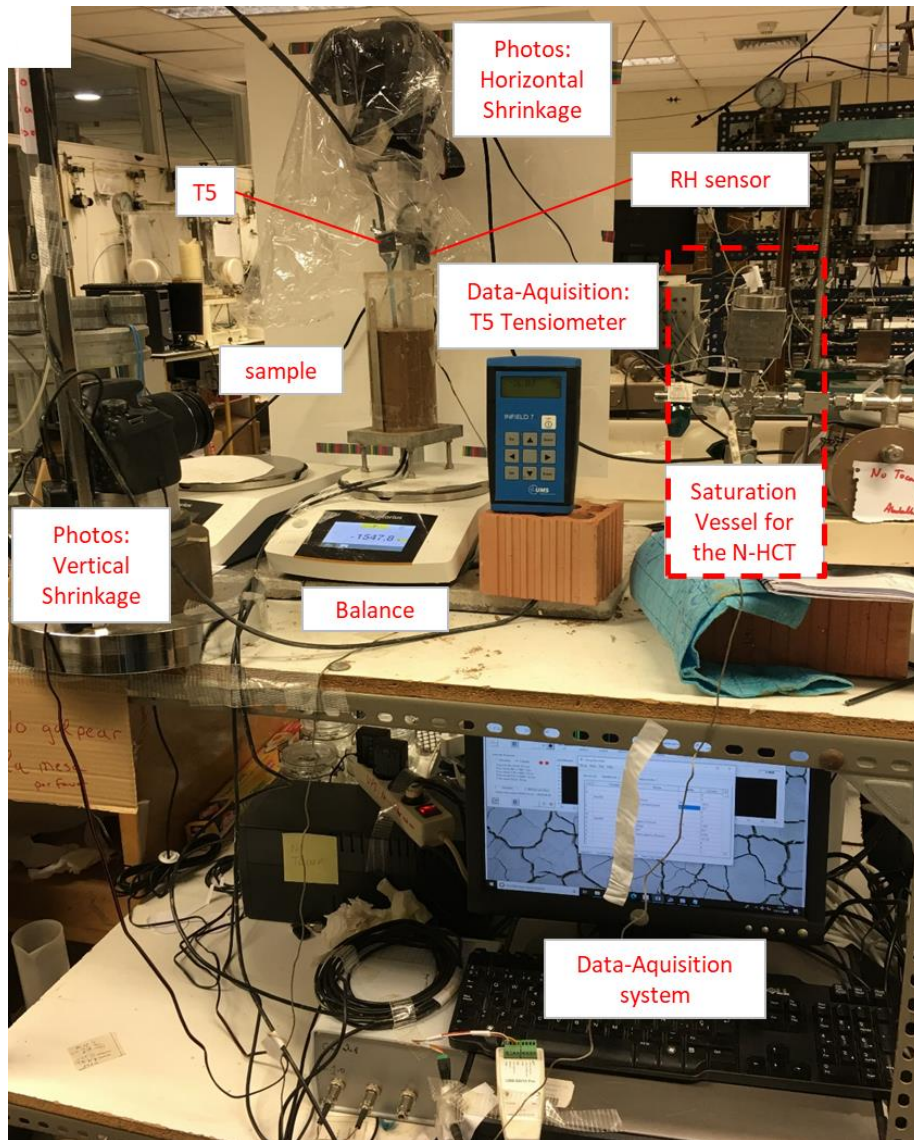


Figure 3-14. Image of the second continuous drying laboratory setup.

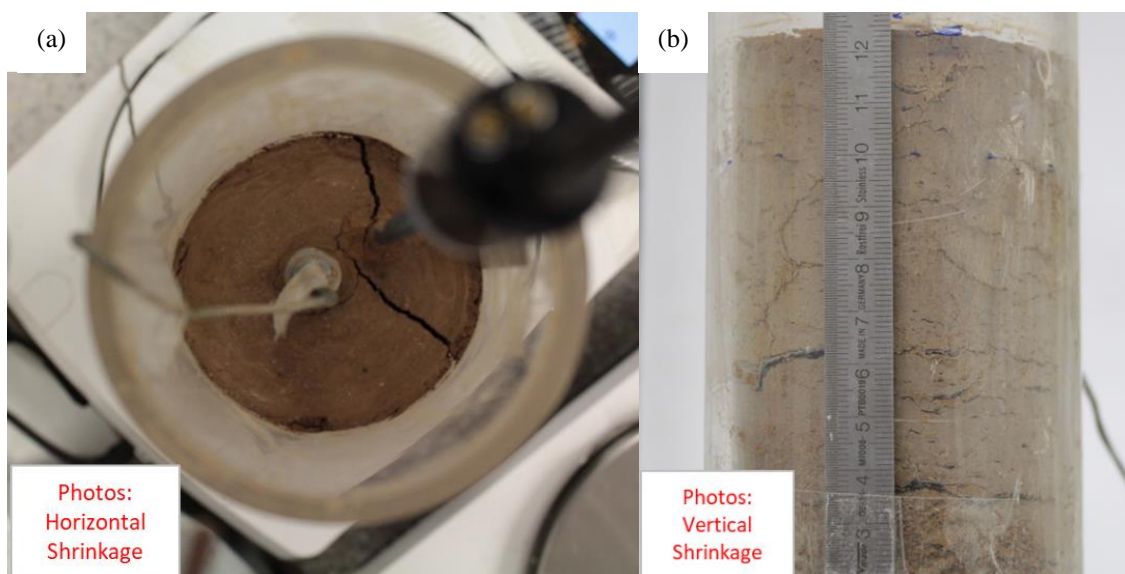


Figure 3-15. Images of (a) horizontal shrinkage; and (b) vertical shrinkage.

The results obtained with the different techniques are presented in Figure 3.16. N-HCT and UMS-T5 demonstrated a faster porewater pressure equilibration response than the MPS-6s. Only after 60-90 hours that the MPS-6s started to react, developing a similar suction development trend to that of the N-HCT and T5, yet with an almost constant delay of more than 70 hours. The reason for the delay in response of the MPS-6s is difficult to determine, however hypothesised to be partly attributed to their vertical positioning causing differential upper-part drying of their built-in porous stones, closer to the soil evaporation front. Although the specimen had a lower exposed surface to total volume ratio ($A_{s,T}/V_T = 0.08 \text{ cm}^{-1}$, compared to a ratio of 1.3 cm^{-1} in the previous setup), the evaporation rate did not exceed $0.001 \text{ g}\cdot\text{hour}^{-1}$ throughout the 400 hours that the test ran. At low evaporation rate, moisture distribution throughout the soil matrix is expected to run homogeneously.

The delayed response of the MPS-6 can originate from the working mechanism of the sensors themselves. The direct tensiometers working mechanism relies on detecting pressure changes in the pore liquid directly. The MPS-6 estimate the matric suction through the equalised moisture in its calibrated porous stone discs with that of the soil matrix. While the former mechanism (N-HCT and T5) can occur in a nearly instantaneous manner, the latter mechanism (MPS-6) is expected to encounter longer delays. Nonetheless, the N-HCT demonstrated good agreement in capturing the suction increase pattern as compared with other presented direct techniques.

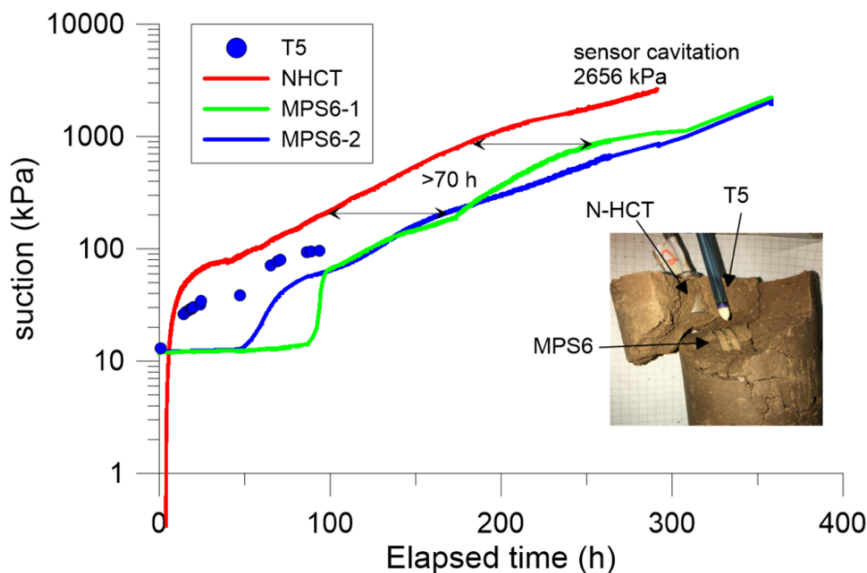


Figure 3-9. Different suction readings from the different sensors over the experiment time.

Volumetric measurements were directly obtained by simultaneously measuring surface area and vertical shrinkage (DIA-D), and assuming a uniform, but not necessarily isotropic, shrinkage behaviour. This assumption implies that the measured vertical or horizontal deformation of the surfaces using the cameras is representative of the bulk deformation.

To assess the suitability of DIA-D for specimens with anticipated non-uniform shrinkage, DIA-ID and PC were performed in parallel on cylindrical specimens ($\varnothing 50$ mm, h20 mm) prepared from the same soil batch (i.e., similar initial water content and compaction conditions). The obtained DIA-D estimation was then compared with the SSCs from the DIA-ID and PC measurements.

Some cracks and irregular deformation patterns formed on the specimen boundaries. However, the retrieved sample at the end (see image, Figure 3.16) confirmed that the sensors did not detach from the soil. The soil remained in close proximity to the sensing faces during the inward shrinkage towards the centrally-located sensors, minimizing the impact of micro-cracks and fissures.

3.3.3. Continuous uninterrupted suction measurement in large-scale soil specimens

This large-scale setup was designed with two aims: the validation of N-HCT measurements against Vaisala HEMP-230 sensors (section 3.2.3.5), and the capturing of an uninterrupted continuous and full-range suction measurement throughout different imposed drying and wetting paths. The latter is highly valuable for numerical simulations calibration for soils exposed to varying boundary conditions. An array of multiple sensors embedded to different depths were used to assess the suction development profile throughout the specimen at different depths from the exposed surface.

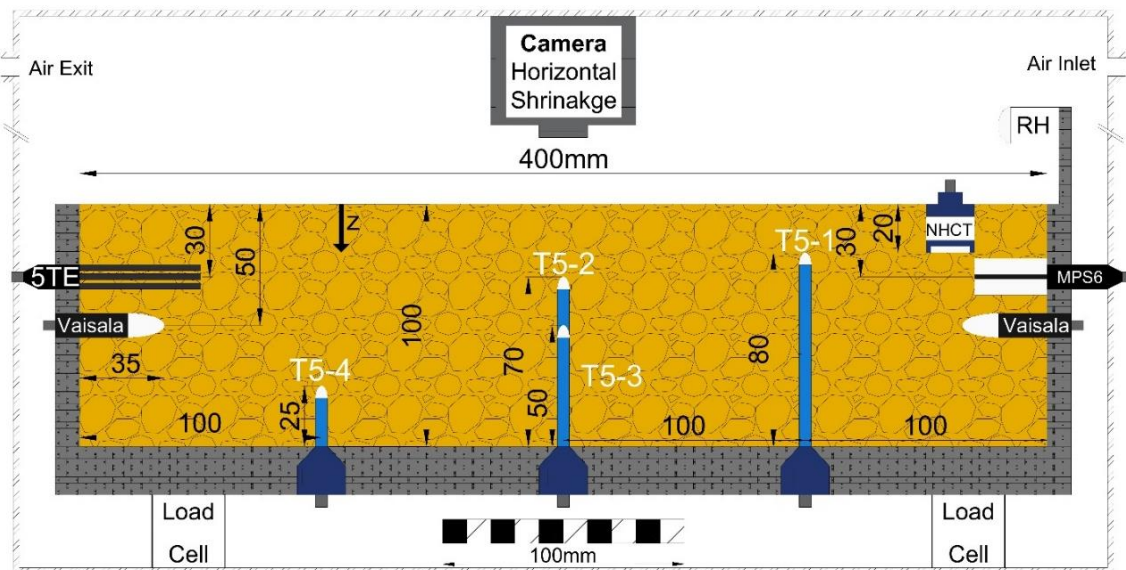


Figure 3-10. Schematic cross-section of the environmental chamber sample.

The specimen ($\varnothing 400$ mm; h100 mm) was prepared using A-MP3 (wet of modified Proctor optimum) and mounted in an environmental chamber at the Technical University of Catalonia (UPC-BarcelonaTech) laboratory (Lakshmikantha, 2009).

The compaction protocol was designed to match the energy applied in the Modified Proctor test ($2700 \text{ kN}\cdot\text{m}\cdot\text{m}^{-3}$), and to ensure the uniformity of the specimen. The specimen was dynamically compacted directly in the tray in five layers of 2 cm height, using the hammer of the modified Proctor (4.54 kg), each layer receiving 174 blows, from a 45.7 cm drop height. After compaction, the surface of the specimen was thoroughly levelled using a straight edge, and any depressions were filled to create a uniform initial surface.

Different sensors carrying out different suction measuring ranges were embedded in the specimen, namely four UMS-T5 tensiometers (0-100 kPa), one MPS-6 (10-2000 kPa), one N-HCT (0-3500 kPa), two Vaisala HEMP-230 RH sensors (>2000 kPa), and lastly one Decagon 5TE sensor for volumetric water content and electrical conductivity measurements.

Using Figure 3.17 for embedment depths reference and Figure 3.18a for spatial locations, the four UMS-T5s were positioned as follow: T5-3 at centre, mid-height; while the remaining UMS-T5s in a radial order closer to the top (T5-1 and T5-2) and bottom boundaries (T5-4). A continuous drying path was imposed using a commercial dehumidifier (DST-Seibu Giken© model DR-010B).

Weight changes were recorded using three INTERFACE© SSM series load-cells, while volumetric changes were extrapolated from surface DIA-D. Due to the obscurity of the tray sides, the DIA-D could not be implemented to measure the vertical displacements. The volume extrapolation requires assuming isotropic and uniform shrinkage behaviour, and was based on the fact that no noticeable cracks formed at the specimen surface by the of the drying stage (Figure 3.18b). Due to the relatively big specimen surface ($A_{s,T} = 1257 \text{ cm}^2$), it would have required multiple LVDTs to average the vertical displacements at the surface. For simplification, the measured surface area was considered to be representative of the total deformation in the calculations of DIA-D.

The obtained DIA-D results were used to compare against the DIA-ID and PC of the same batch A-MP3 (i.e., similar initial water content and compaction conditions), to assess the validity of applying such an assumption of uniform and isotropic deformation to estimate the volumetric deformations of a large-scale specimen.

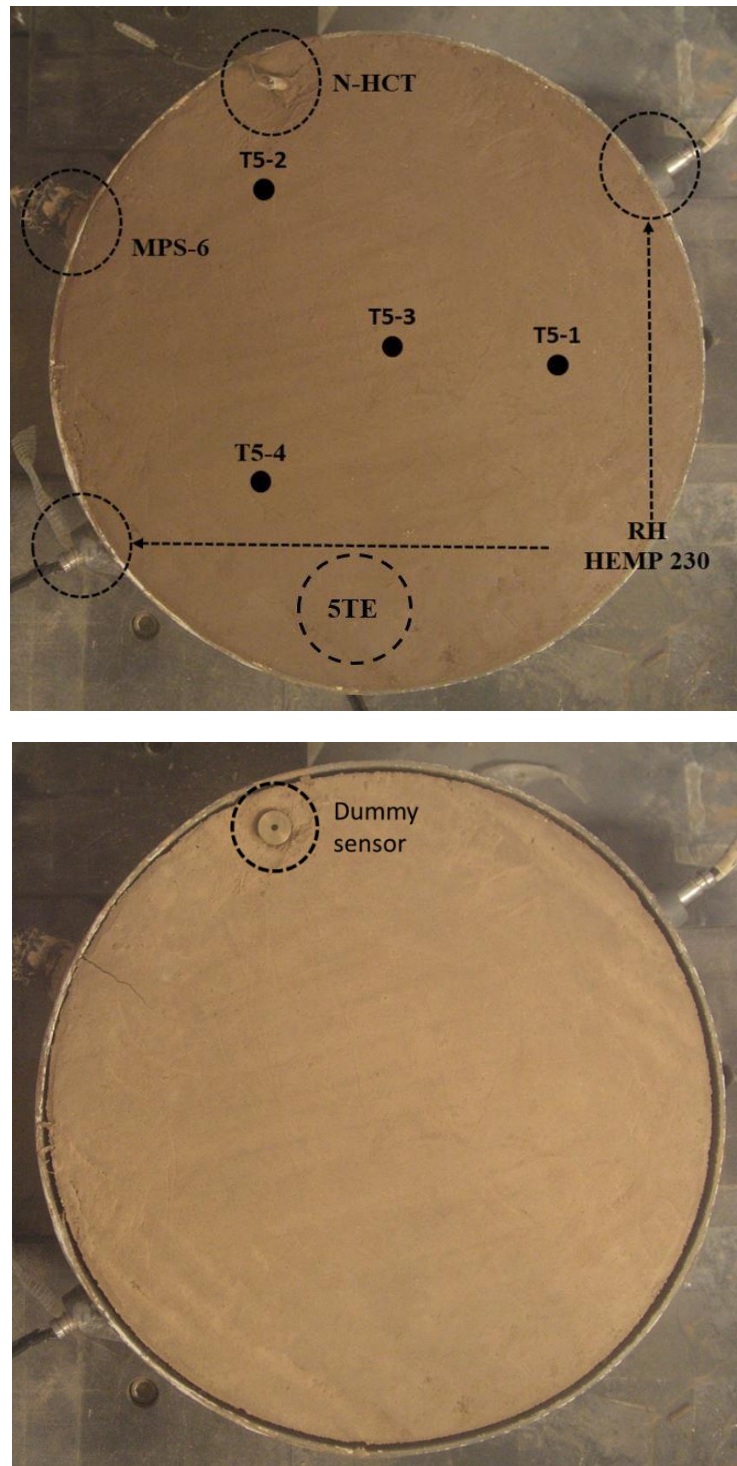


Figure 3-11. Environmental chamber sample (a) image top view (drying initiation); and (b) image top view (end of first drying stage).

The results obtained from the sensors are presented in Figure 3.19, showing that shortly after drying commenced, suction started to increase, particularly closer to the top surface (T5-1, T5-2, MPS-6 and N-HCT) and moved from the outer periphery towards the centre-bottom (T5-3 and T5-4). N-HCT and MPS-6 generally returned higher measurements than the T5s, probably due to their closer proximity to the exposed surface (Figure 3.19), both capturing a suction surge

nearly 12 hours after drying initiation. N-HCT and MPS-6 readings started diverging beyond 250 kPa. The observed divergence might be attributed to the longer equilibration times required by the MPS-6s (see Figure 3.19a). Moreover, the divergence confirms with the gradient with depth from the evaporation front (Tollenaar et al., 2017b). Beyond 1500 kPa (recorded by N-HCT), the HEMP-230 sensors were introduced in place to provide a continuous monitoring suction evolution past the N-HCT measuring range, as they behave better in slightly drier environments (see section 3.2.3.5).

With a large size specimen, having a relatively small ratio of exposed surfaces to total volume ($A_{s,T}/V_T = 0.1 \text{ cm}^{-1}$), a nonuniform desaturation and shrinkage behaviour is expected. The multiple sensors installed in this specimen were to provide a continuous measurement of suction profile development at different depths from the exposed evaporation surface, which is a valuable for validating numerical model simulations (Cuadrado et al., 2022).

Following the first 35-day-drying period, a 21-day wetting period was imposed using a nebulizing humidifier creating water-droplets without altering the atmospheric temperature (Charmax device model CX-UH06). Suction evolution was monitored using the MPS-6 and the HEMP-230s only during wetting, while the cavitated N-HCT and T5s were retrieved for re-saturation before reuse. The N-HCT was replaced with a dummy-sensor to preserve the insertion hole for the second drying stage (Figure 3.18b). Soil moisture reached equilibrium after the 21-days wetting. The HEMP-230s captured parts of the suction decrease (from >12000 kPa down to 1100 kPa), rendering unreliable readings afterwards (near saturation, high RH). This overlooked suction range (1100-0 kPa) was covered by MPS-6, demonstrating good agreement between the two sensors across the overlapping range (Figure 3.19a).

A second 60-day drying period was then applied. The N-HCT and the four T5s were reintroduced in their prior positions. A higher divergence between N-HCT and MPS-6 was observed in the second drying early stages. The reason behind this diversion is still unclear as in the first drying sensors readings were comparable. Nevertheless, it is important to mention that a delayed MPS-6s behaviour has been noticed previously only when using MPS-6s in samples following wetting paths, both in the field and laboratory (Oorthuis et al., 2018; Cordero et al., 2020). One possibility is in the fact that, while N-HCT was normally re-saturated in a pressure chamber, regaining its full functionality, the MPS-6 was re-saturated from moisture infiltration of surrounding soil-moisture into its porous ceramic discs during the exposed wetting phase, which resulted in a less than adequate saturation of the porous discs, and hence a delayed or distorted response to suction changes. When the soil suction exceeded 1500 kPa (as measured by N-HCT and MPS-6), the HEMP-230s were reintroduced to continue monitoring the suction evolution as conducted earlier.

Despite the behaviour of the different sensors, following Figure 3.19a, total and matric suction readings obtained with direct methods (T5) and indirect methods (MPS-6 and HEMP-230s) had a similar development pattern as the N-HCT readings. Moreover, the extended N-HCT measuring range overlapping the initial HEMP-230s measuring range was useful to validate the obtained HEMP-230 results. As shown in Figure 3.19a, in the 1500-3000 kPa suction overlap range, a HEMP-230 lagging was noticed stemming from longer equalisation periods typically required for RH transistors with the pores vapour. Combining multiple suction measurement techniques allowed an uninterrupted and continuous suction measurement at all ranges in drying and wetting cycles. Note that this is only possible if the osmotic suction component is relatively small enough as to be neglected.

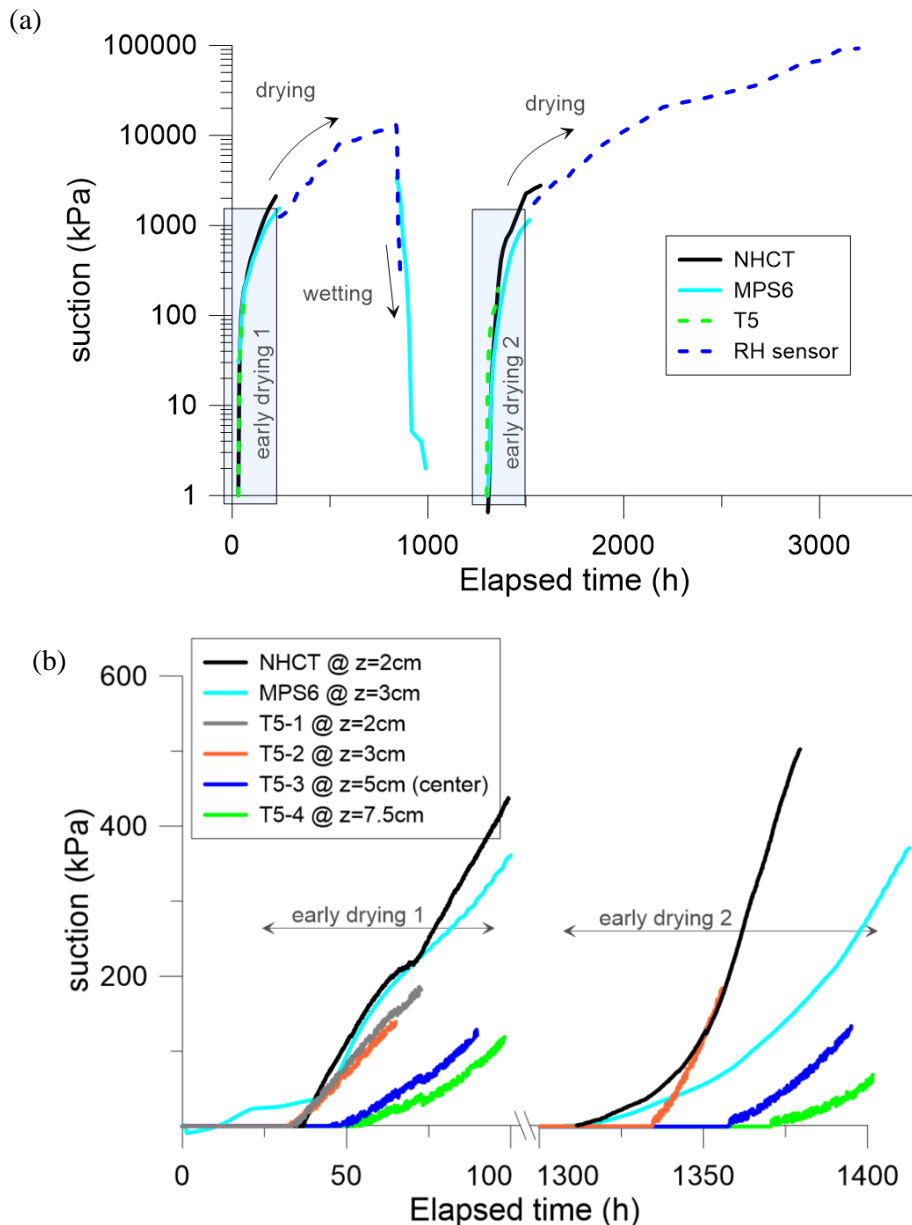


Figure 3-12. (a) Complete continuous suction evolution during drying and wetting cycles; and (b) Early-stage suction measured using different sensors at different locations during first and second drying (see Figure 3.17 for sensor position). *z: distance from top soil surface.

3.3.4. Osmotic Suction

As explained in section 3.2.3.6, the osmotic suction estimation can be carried out indirectly based on electrical conductivity (EC) measurements of the porewater. As part of the environmental chamber experimental setup shown in Figure 3.17, a 5TE Decagon sensor was embedded to measure the electrical conductivity in the soil during the drying and wetting cycles. Figure 3.20 shows the fluctuation in both the gravimetric water content and the electrical conductivity (as measured by the 5TE sensor) during the drying and wetting cycles.

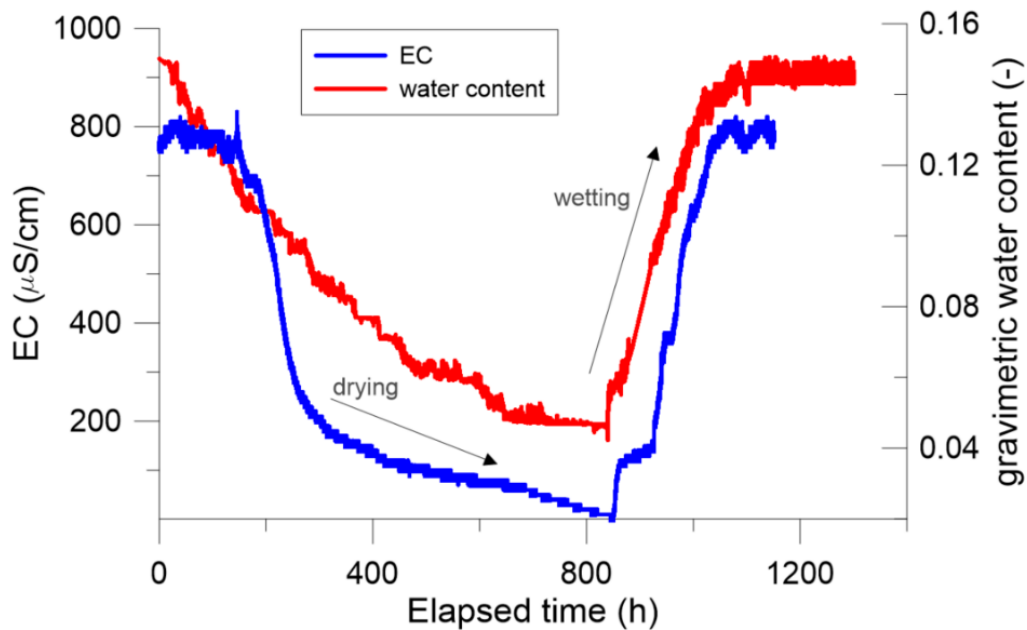


Figure 3-20. Changes in the “global” electrical conductivity and water content in the environmental chamber setup.

The figure shows a dependence in the pattern of change between the EC and the water content. EC is at its peak value near saturated conditions, maintains that value during almost the first 200 hours of drying as the water content decrease, and starts decreasing to finally reach its lowest values near dry conditions. This can be attributed to the nature of direct measurement of electrical conductivity in the soil carried out by the 5TE sensor. As the porewater evaporates, the water bridges connecting the soil particles break, and the water phase becomes noncontinuous in the soil matrix. Therefore, a greater void space forms between the soil particles and aggregates, causing a lower “global” electrical connectivity in the soil as measured by the 5TE sensor. At the same time, as the water decreases from the soil matrix, the salt concentration in the remaining porewater increases, leading to a higher electrical conductivity in the water phase, and consequently higher values of osmotic suction (Ying et al., 2022). To estimate the electrical conductivity or osmotic suction when reaching that state, the porewater at lower degree of saturation should be extracted using a squeezing technique, and the EC

measured in the extracted water would increase as the salt concentration increases, up to a limit (Mata et al., 2002).

As the sample was relatively wet and saturated initially, the obtained initial EC measurement can be considered to reflect the EC of the porewater, and therefore the osmotic suction values. The initially measured $800 \mu\text{S}\cdot\text{cm}^{-1}$ value of EC at saturated conditions for batch A-MP3 corresponds to a value of 28.5 kPa using equation 3.2, or 28.8 kPa using equation 3.3. The obtained osmotic suction results, due to their relatively small value with respect to the SWRC, and the 1 MPa value of AEV for the Agròpolis soil. This validates the combination of matric and total suction techniques for determining complete SWRCs for this particular soil with low concentration of salts.

3.3.5. VE technique: evaluation of equilibration times

The testing procedure for the Vapour Equilibrium (VE) technique is explained in section 3.2.3.7 (Figure 3.6). The experiment ran for seven consecutive weeks. The total suction measurements were obtained by the end of each week using the WP4-T apparatus. To take the readings, the specimens were removed from the tightly closed jar and sealed properly for an hour before taking the total suction measurement.

Figure 3.21 shows the time needed by different specimens to reach equilibrium. It was noticed that the lower suctions reached their respective values more rapidly but could not achieve equilibrium even after passing seven weeks. This can be attributed to the less accurate results expected for low imposed suctions using the vapour equilibrium technique (Delage et al., 1998), with less than saturated salt solutions. The higher imposed suctions (i.e., 2250, 4500 and 8500 kPa) reached equilibrium after around three weeks. Note that the equilibration time can be reduced significantly by circulating vapour using a pneumatic pump (Marcial et al., 2002).

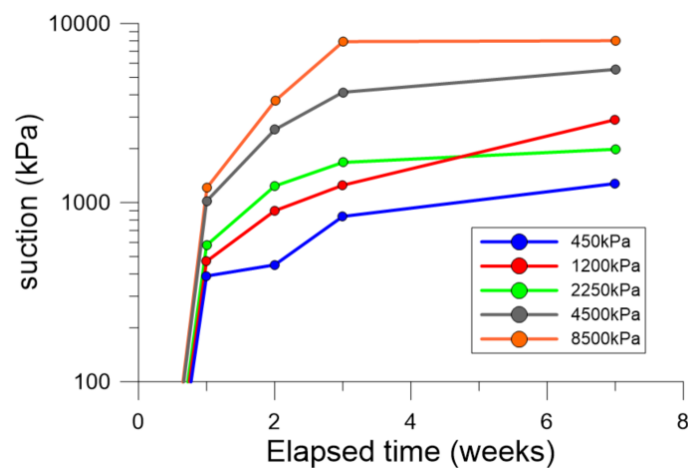


Figure 3-21. Total suction equilibration times for the VE method, measured using Hygrometer.

3.4. Volumetric measurements

As mentioned before, proper bulk volume quantification is critical for void ratio, volumetric water content and saturation degree determination, all essential SWRCs parameters. While the specimen's soil mass can be measured/monitored using scales, accurate volume estimation is more complex and problematic to obtain since the specimen size can change in shape during wetting or drying.

Different techniques, see section 3.2.4, were tested, and compared in an attempt to accurately estimate specimen volume change following drying and wetting paths. The techniques can be classified into direct (measurement is made simultaneously with suction and moisture measurements in the same sample), and indirect (on parallel samples).

3.4.1. Evaluating direct and indirect volumetric measurement techniques for determining SSC

The distinct volumetric measurement techniques were compared to evaluate their SSC capturing performance. Paraffin-coating (PC) was conducted on numerous identical samples to achieve a definitive soil shrinkage behaviour pattern, representing a generalized SSC that adequately describes shrinkage behaviour in an indirect manner for a unique set of initial conditions (i.e., for each soil batch). Digital Image Analysis (DIA) on the other hand, was used both as a direct and indirect measurement method (section 3.2.4.1).

A direct DIA (DIA-D) method was carried out differently in the three setups presented earlier: in the first two setups, two digital cameras were positioned to capture both surface area and specimen height simultaneously (Figures 3.11 and 3.13); in the third setup, the obscure mould-walls did not allow capturing specimen height changes and only the surface area was continuously captured. The formation of fissures and cracks on the specimen periphery of the second setup lead to difficulties of proper estimation of height deformation (Figure 3.15).

To evaluate the use of direct methods (DIA-D) with uniform assumption for the three setups, and isotropic assumption in the environmental chamber setup only (third setup), the results were compared against indirect DIA (DIA-ID) and PC, conducted on parallel-prepared cylindrical specimens ($\varnothing 50$ mm, h 20 mm) from each soil batch, and exposed to free-shrinkage conditions, without any sensor embedment. After the final DIA-ID residual volume measurement was taken, the specimens were paraffin-coated to compare both final DIA-ID and PC methods at the same residual timestep.

Table 3.8 shows a slightly smaller dry specimen volume detected by PC with respect to DIA-ID residual samples. The values demonstrated in Table 3.8 are averaged from two specimens tested from each soil batch.

Table 3.8. Residual void ratio for the residual specimens.

Soil Batch	A-S3	A-S4	A-MP3
$e_{residual}$ - DIA – ID	0.371	0.395	0.360
$e_{residual}$ - PC	0.368	0.390	0.355

The slightly underestimated volumetric estimations by DIA-ID, with respect to the final paraffin-coating conducted on the same residual samples, was consistent for all soil batches (Table 3.8).

As the specimen dried, the surface roughness increased due to the soil's granular texture, irregularities, and desiccation microcracks. Underestimation is most probably due to inadequacy to observe these voids, dents, and deformities, using 2D surface images and the opted digital image thresholding criterion. In the case of paraffin-coated samples, these voids can be easily filled and accounted for.

Figure 3.22 presents results from the three different techniques. Analysing the PC results, the normal shrinkage followed a similar path in the 3 soil batches, with similar normal shrinkage slope value ($\beta_{NS} = 2.75 \pm 0.2$). This value is similar to the measured soil specific gravity $G_s = 2.70$, due to the condition:

$$e = \theta_\omega \frac{\gamma_s}{\gamma_w \theta_{Sr}} \quad (3.6)$$

Where θ_ω is the gravimetric water content, γ_s is the soil particles unit weight, γ_w is the water unit weight, and θ_{Sr} the liquid degree of saturation ratio. When soil is saturated, the relationship void ratio – gravimetric water content is directly G_s .

As observed in Figure 3.22, DIA-D followed the general PC pattern behaviour, with volume change underestimation during the normal shrinkage stage for all batches. For the first two setups, the volumetric deformation was underestimated by the DIA-D method (Figure 3.22a and 3.22b). This behaviour can be attributed to the existence of relatively large rigid body sensors (with respect to the specimen size), restricting the deformation behaviour and free movement of soil.

In the third setup, the volume change using DIA-D and the isotropic shrinkage assumption was overestimated, especially as the shrinkage reached residual conditions (Figure 3.22c).

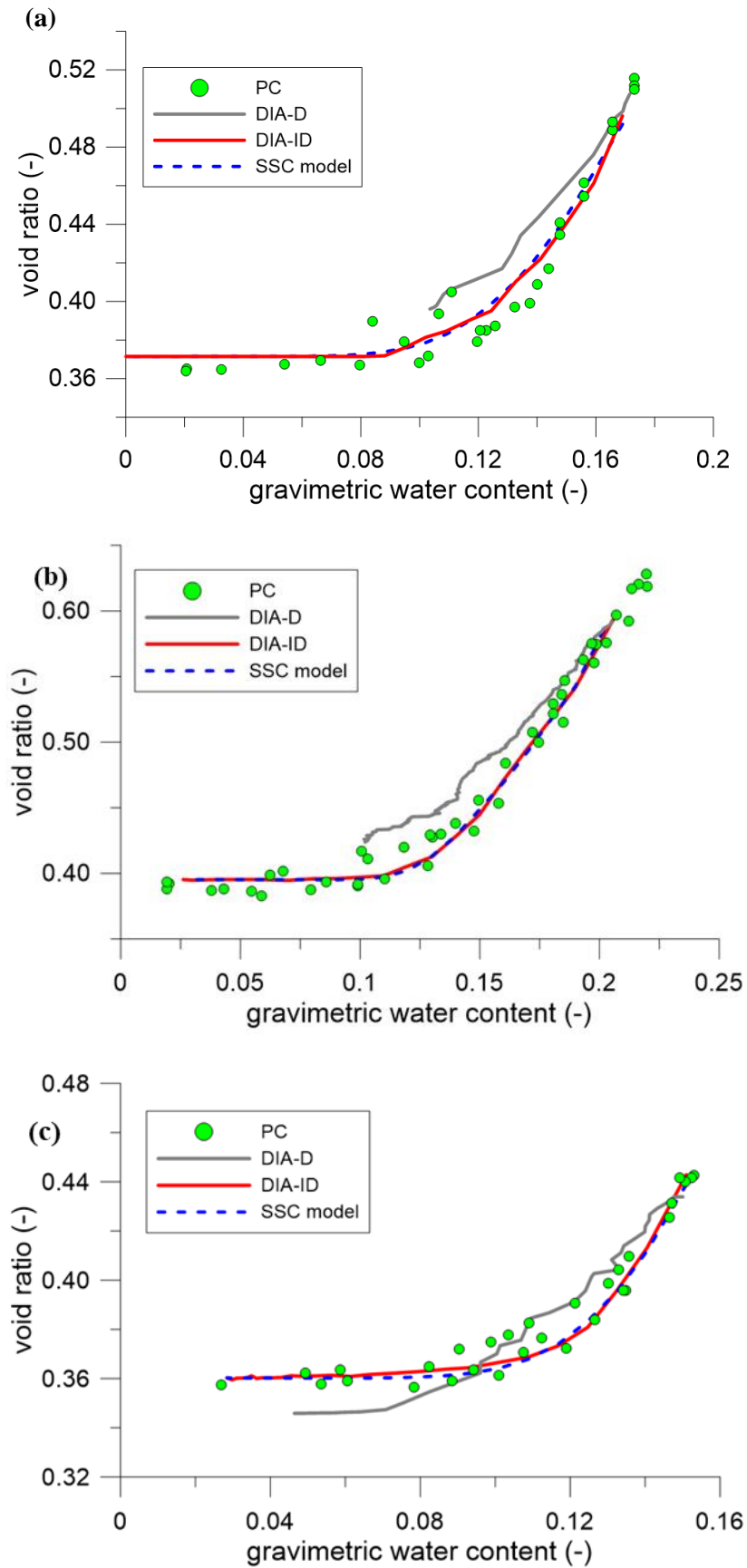


Figure 3-22. Experimental SSCs for soil batches (a) A-S3; (b) A-S4; and (c) A-MP3. (see Table 3.4 for information on the soil batches).

DIA-D shortcomings were resolved in the parallel free-shrinking samples with no sensor embedment (i.e., DIA-ID). DIA-ID results agreed well with the distinct PC points trend. In the three setups, sensor soil embedment was essential to enhance suction measurements, ensuring direct ceramic face-soil pores contact, and to seal off external environmental effects, influencing the measured soil matrix suction level.

The presence of rigid sensor bodies in the setups, relatively large with respect to specimen volume, restricted the soil uniform volumetric shrinkage process, leading to larger shear deformations. Therefore, an assumption of fully isotropic and uniform shrinkage behaviour is not entirely valid to obtain accurate volumetric estimations of specimens with embedded sensors or large-scale specimens with anticipated differential desaturation and deformation patterns. However, a direct method can still serve as an indication of the general shrinkage pattern.

Comparing SSCs obtained by the two indirect methods (i.e., DIA-ID and PC), the DIA-ID method had the advantage of being conducted on one sample at a time, and therefore delivering a uniform behaviour in the form of a uniform line (Figure 3.22), while the PC method was conducted on multiple samples. Although PC samples were prepared from the same soil batch, acquiring identical initial placement conditions was technically unfeasible for a large number of specimens. Additionally, the DIA-ID method had the advantage of obtaining simultaneous images of both height and surface area, allowing the calculation of the geometry factor, τ_{gf} :

$$1 - \frac{\Delta V}{V_i} = \left(1 - \frac{\Delta h}{h}\right)^{\tau_{gf}} \quad (3.7)$$

Where ΔV is the specimen volume change of the original volume V_i , and Δh is the specimen length increment with respect to the original length h (Towner, 1986; Bronswijk, 1990). In contrast, PC computes total specimen bulk volume only. Analysing the DIA-ID results, τ_{gf} was found to be in the 3.1-3.3 range, signifying nearly isotropic shrinkage behaviour according to the range suggested by Towner (1986) and Bronswijk (1990).

The use of similar specimens in parallel to capture different behaviour characteristics is a common practice (Lourenço et al., 2011). It was evident in this work that having separate SSCs (obtained using indirect methods) was useful to evaluate the selected primary direct method (DIA-D) and addressed the associated shortcomings.

The PC wetting-path SSCs were obtained from additional samples for each soil batch (section 3.2.4.2). The wetting process entailed adding 1g of water droplets per day to the specimen surface and leaving the specimen tightly sealed for 24 hours to ensure moisture equalisation in

the pores before taking the volumetric measurement. No major volumetric change hysteresis was noticed, and wetting-SSCs demonstrated comparably similar behaviour to the drying-SSCs.

3.4.2. SSC modelling

The aim of defining mathematical SSC models was to obtain a unique equation with defined parameters to describe the $[\theta - e]$ relationship for each soil batch. Being more uniform and in good agreement with the paraffin-coating trend, the experimental DIA-ID results were used as a $[\theta - e]$ data-input basis to find the best-fit dimensionless parameters in equation 3.5. The SSC model follows with good agreement both PC and DIA-ID experimental results (see dashed line, Figure 3.22).

Having such a defined mathematic SSC equation with specific values of fitting parameters for each unique set of soil batch can readily provide the void ratio, given the gravimetric water content at each stage, by replacing the relation of the volumetric water content $\theta_V = \theta_\omega G_s / (1 + e)$ into equation 3.5, to become:

$$e = e_0 + \gamma_{GG} \left[\exp \left(\frac{-\xi_{GG}}{[\theta_\omega G_s / (1+e)]^{\zeta_{GG}}} \right) \right] \quad (3.8)$$

Equation 3.8 is solved by iterations to find the values of void ratio for each laboratory-measured value of gravimetric water content, given the obtained specific set of values of the dimensionless fitting parameters for each of the soil batches. Since SSCs behaviour was identical in both drying and wetting paths (as explained in previous section), at least for the soil in this study, the SSC model equations can be used to describe both shrinkage and swelling in this case.

As explained in section 3.2.4.3, the selected model in this work (Groenevelt & Grant, 2001; 2002) has the advantage of requiring only the predefinition of volume at the zero-shrinkage stage and finds a nonlinear best-fit set for the obtained experimental $[\theta - e]$ data by iterating the three dimensionless parameters until finding the best fit.

A set of best-fit parameters can be still predicted for fewer given experimental $[\theta - e]$ data. This prediction method can be appealing in practice as it would significantly cut down the time-consuming analysis process of digital images, paraffin-coating, or any other selected volumetric measurement technique. Ideally, with few water content and volume measurements in the lab, the best-fit parameters and the SSC model can be obtained.

3.5. Obtaining the SWRCs

Having a defined complete-range SWRC represented on the saturation degree S_r -scale is essential for numerical constitutive models and mathematical representation of unsaturated soil behaviour. Combining different techniques to cover full suction range is a common practice. However, in order to qualify for merging on the same SWRC, these techniques have to be conducted successively on the same soil specimen, or on different samples given a unified SSC is provided for similar soil initial conditions (section 3.4.1).

N-HCT and WP4-T combined ranges provide the complete span with a relatively sufficient overlap in the 1000-3500 kPa potential scope. The overlap serves the purpose of further confirming the validity of use of the combination technique. The matric and total suction techniques combination was made possible only after neglecting the osmotic component (see section 3.3.4).

Obtained suction measurements from the previous experimental setups were also represented on the SWRCs corresponding to each batch (e.g., T5s and MPS-6s for batch A-S4 [section 3.3.2]; T5, MPS-6 and HEMP-230 for batch A-MP3 [section 3.3.3]). For the wetting path, only discrete N-HCT data was obtained due to the technical difficulties normally associated with continuous wetting HCT measurements (section 3.1, batch A-S4).

Additional wetting-path data were obtained from the MPS-6 and HEMP-230 using the environmental chamber experimental setup as explained in section 3.3. These data are demonstrated for soil batches A-S3 and A-MP3 only. For all the batches, the WP4-T specimens were subjected to gradual wetting, taking discrete suction measurements, and associated gravimetric water content readings at each stage.

Due to its small-scale, volumetric measurements on the WP4-T samples were technically unfeasible. The void ratio was obtained indirectly based on recorded gravimetric water content (see section 3.2.2). Consequently, the saturation degree can be obtained using the relation $\theta_{Sr} = \theta_{\omega} \cdot G_s / e$. The dimensionless parameters set in equation 3.4 (i.e., γ_{GG} , ξ_{GG} , and ζ_{GG}) is obtained for each batch, from the fitted SSC models based on the parallel DIA-ID results. Therefore, given only the measured gravimetric water content values of a specimen, the void ratio can be estimated using the proposed SSC modelling technique, by simply solving equation 3.8 (having obtained the defined set of fitting-parameters based on DIA-ID data).

The same procedure was followed for all the remaining techniques (i.e., continuous N-HCT, discrete N-HCT, MPS-6, T5 and HEMP-230), to unify the volumetric component, and present

all the suction measurements over a normalised scale. Therefore, the three experimental setups provided the relationship between the gravimetric water content and the suction, while the DIA-ID for each batch provided the relationship between the gravimetric water content and void ratio (through the SSC model). As discussed earlier, no significant volumetric hysteresis was observed, and the SSC model equations can be used equally for the drying and wetting volumetric change paths for the particular soil in this study.

Figure 3.23 presents the Agròpolis soil SWRCs for batches A-S3, A-S4 and A-MP3, obtained from combinations of suction measurement techniques. For the 3 presented batches, the WP4-T total suction results properly complemented the N-HCT matric results and compared well in the overlapping region (1000-3000 kPa). Final obtained measurements covered the full saturation range between the initial saturation until the residual conditions, spanning over a wide suction measurement range (1 kPa - 150 MPa).

The previously noted lag in the MPS-6 and the RH readings during the main drying path (see section 3.3.3) was reflected on the SWRCs (figure 3.23a and 3.23c). The UMS-T5s captured the initial parts of the SWRC, with readings provided up to 120 kPa. The provided UMS-T5 range was insufficient to cover the initial saturation zone measurements gap, until the total suction measurements can take over (figure 3.23b and 3.23c).

Figure 3.23c demonstrates the HEMP-230 and WP4-T drying path readings agreement in their overlapping range. The RH sensor can potentially replace WP4-T, providing a fully continuous drying SWRC by combining with N-HCT in a single drying specimen. This however requires a lower evaporation rate than what was imposed in the environmental chamber (i.e., the third experimental setup, section 3.3.3), to allow proper soil-moisture equalisation, avoiding lag in readings.

The wetting path is demonstrated for soil batch A-S3, as obtained using a combination of WP4-T, discrete N-HCT and MPS-6; and for batch A-MP3, as a combination of MPS-6 and HEMP-230. Data from RH and MPS-6 sensors generally showed lagging in wetting suction readings and demonstrated a greater hysteresis. Although the volumetric changes showed no hysteresis, the hysteresis was evident in the retention curve, and therefore in the water retention mechanism rather than the shrinkage and swelling mechanism.

The observed hysteresis in the water retention mechanism can be attributed to the cross-sectional irregularities of the void passages, the contact angle difference between advancing and receding meniscus (Azizi et al., 2017), occluded air, and drying-wetting soil history. The water retention hysteresis phenomenon topic will be further addressed in the following Chapter 4.

The unifying/combining of the SSCs/SWRCs method is applicable for different soil types of air entry value below 3000 kPa (i.e., the measuring range of the N-HCT), to get full-range SWRCs represented as suction with saturation degree or volumetric, and not gravimetric water content, better fitting with established constitutive formulations (van Genuchten, 1980; Fredlund & Xing, 1994).

The same testing methodology was applied for the remaining specimens of different soil batches. A combination between the N-HCT and WP4-T suction readings, unified over the same DIA-ID volumetric measurements was used to obtain the SWRCs for the specimens at different initial conditions that were shown in Figure 3.1 and Table 3.5. Figure 3.24 shows the different obtained SWRCs. Results from other measurements were added where applicable (e.g., VE technique or UMS-T5 tensiometer results). In all cases, the N-HCT seemed to complement well the range overlooked by the WP4-T, and the two methods were in full agreement in the overlapping range (0.6-3 MPa), therefore providing complete suction measurements between 0 and 150 MPa (i.e., the maximum recorded by the WP4-T).

The wetting path was also obtained, mainly using the VE technique and the WP4-T. Obtaining the N-HCT wetting path was considered a tedious task requiring longer time for the discrete measurement points.

The hysteresis is evident between the drying and wetting paths in all the specimens. It was less severe for specimens with dryer initial conditions (e.g., specimens A-MP1, A-S1 and A-SH1). These initially dryer specimens have a starting degree of saturation below 65%. The initially unsaturated specimens are not on the main drying path, but instead following one of the scanning curves that is bounded by both main drying and wetting paths, and therefore closer to the wetting path.

More hysteresis was detected using the vapour equilibrium technique. This can be attributed to the fact that in the wetting process, the Vapour Equilibrium technique requires much longer equilibration times, and the 3 weeks given were not enough for the soil matrix to equilibrate with the imposed atmospheric conditions. The equilibration time study in section 3.2.3.7 was aimed at the drying path only, and for smaller sample sizes (those of the WP4-T). More elaborate laboratory work is required in this domain, and future research work in the context of this thesis could include this aspect.

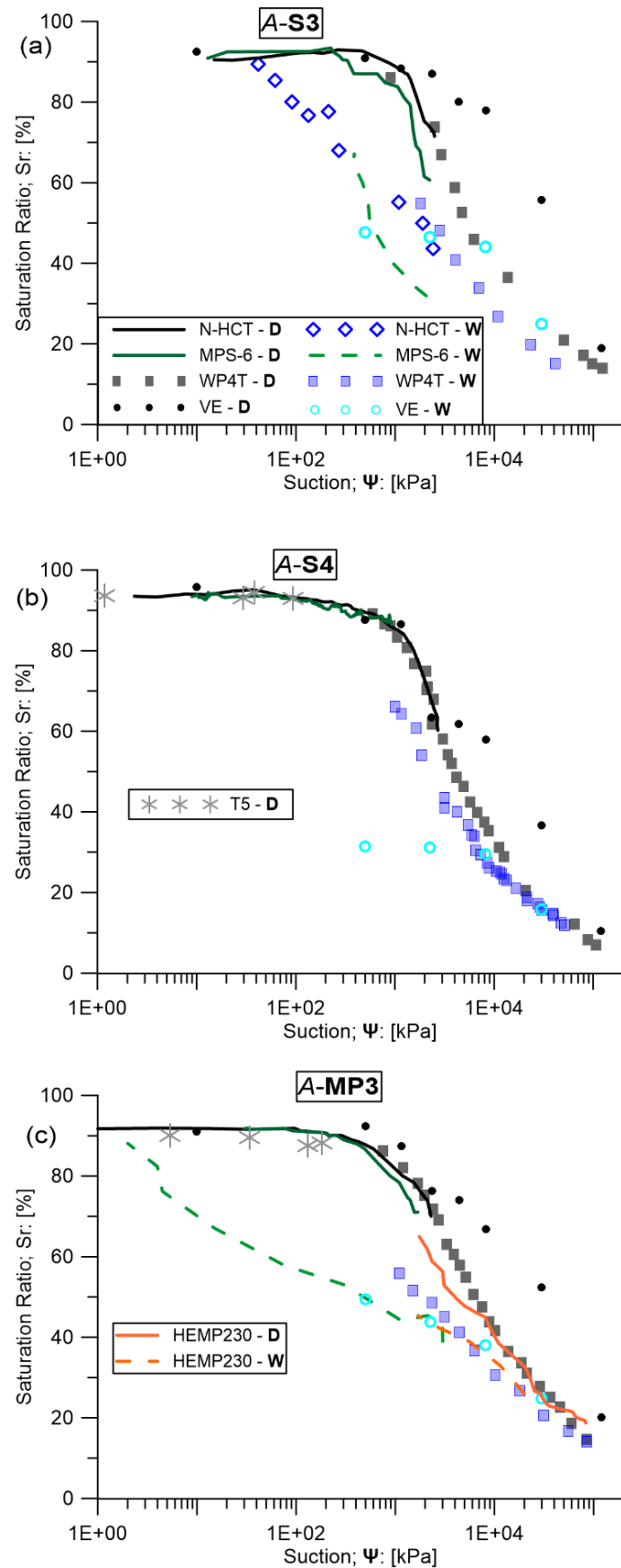


Figure 3-23. Full range SWRCs for soil batches (a) A-S3; (b) A-S4; and (c) A-MP3.

3. Laboratory Experimental Campaign: Evaluating Different Suction and Volumetric Measurement Techniques

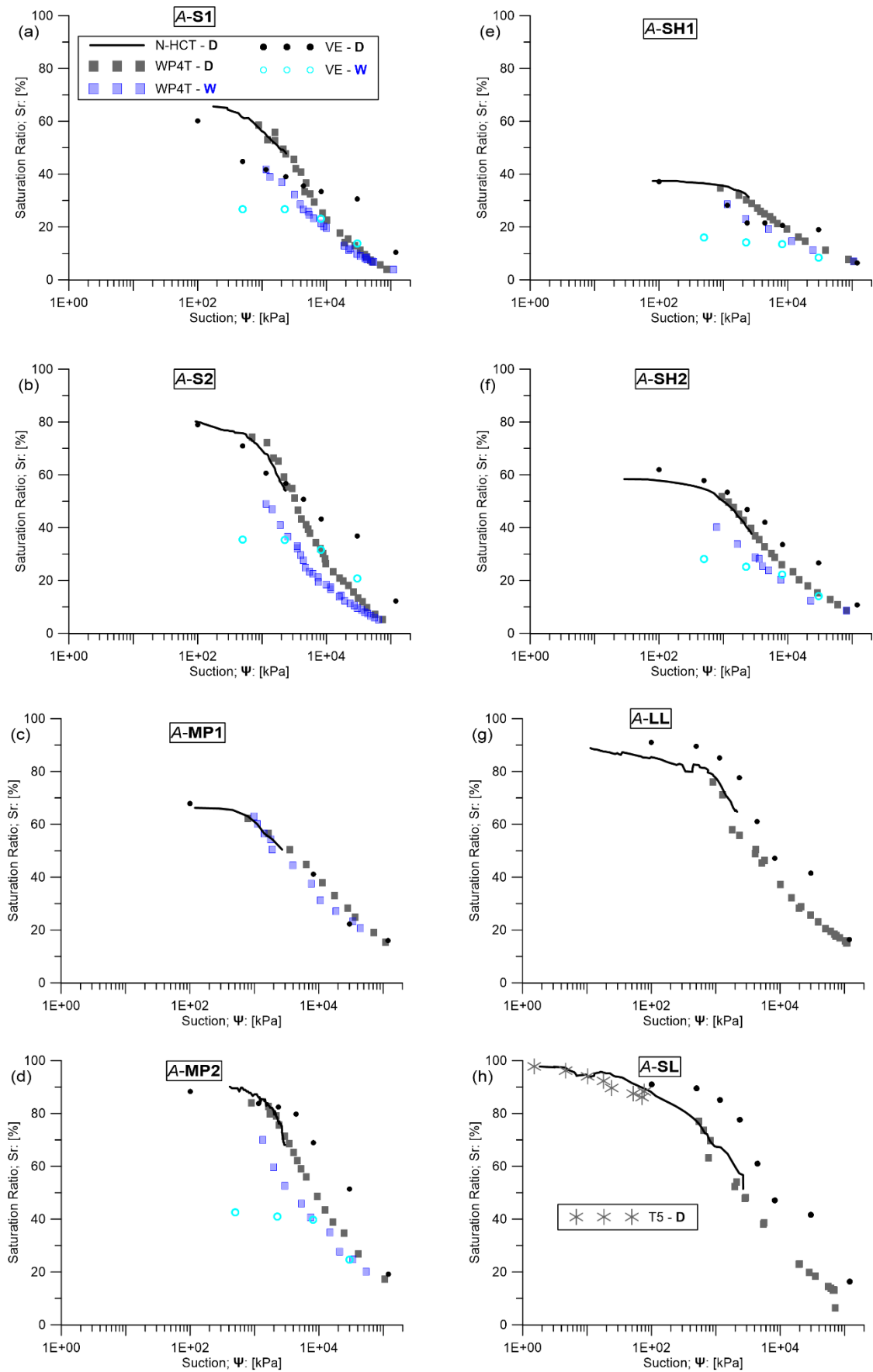


Figure 3-24. Additional SWRCs for specimens (a) A-S1; (b) A-S2; (c) A-MP1; (d) A-MP2; (e) A-SH1; (f) A-SH2; (g) A-LL; and (h) A-SL.

3.6. Conclusions

In this chapter, several procedures have been used to obtain the Soil Water Characteristic Curve and the Soil Shrinkage Curve in drying and wetting paths, including direct and indirect measurement methods. The several experimental procedures used included different suction measurement devices and techniques that measure the matric porewater pressure in the soil matrix directly. On the other hand, different methods were also used to estimate the total or osmotic suctions indirectly, whether from the relative humidity or electrical conductivity of the soil, respectively.

A continuous drying setup is proposed in this chapter which improves on existing similar continuous drying setups found in the literature. The proposed setup allows the simultaneous measurements of the three principal variables characterising the behaviour of unsaturated soils: suction, water content and void ratio. The suction measurements were carried out using the novel Northumbria-HCT (N-HCT) with an extended suction measurement range [0-3500 kPa] (see Chapter 2). The setup was placed on a balance to deduce the water content measurements from the specimen weight directly. Finally, the change in void ratio was estimated through volumetric measurements carried out using Digital Image Analysis of both the specimen surface and height. Continuous drying techniques in the literature usually face these limitations: (i) low suction measurement range provided by existing tensiometers; (ii) differential or nonhomogeneous suction growth within the soil matrix of the specimen; (iii) rapid tensiometer cavitation and improper equalisation between the tensiometer and the soil matrix due to high evaporation rates; and (iv) ceramic detachment from the soil specimen due to the soil drying shrinkage, causing ill-representation of soil matrix suction. The overall direct and continuous drying technique addresses the different limitations normally associated with similar setups, by: (i) using the novel N-HCT with an extended range that goes beyond the AEV of the soil being studied, relatively short equalisation times, and rapid re-saturation after cavitation occurs; (ii) exposing the top and lateral surfaces of the specimen, and inserting the tensiometer to a central position inside the specimen core, at relatively equal distances from all evaporating surfaces (iii) limiting the effect of wind and turbulence, therefore limiting the advective fluxes, and forcing the soil water evaporation to occur following to the much slower convection process; (iv) adequate placement of the tensiometer beneath the specimen and to its core, towards which the shrinkage occurs upon drying.

Employing different suction measurement techniques simultaneously in the same soil specimen helped in the process of evaluating each of the techniques and gave insights on their functionality. Having a direct measurement technique with an extended range provides an

overlapping with the measurement range of other techniques that was not feasible before. The overlapping in the suction measurement range (e.g., 1000-3500 kPa for N-HCT and WP4T) allows for the direct comparison in the measuring properties.

The UMS-T5 tensiometer provided fast equalisation times, close to those of the N-HCT. However, the measuring range proved insufficient to capture the desaturating process. However, the T5s provided an overlapping range (0-150 kPa) that allowed the validation of the N-HCT measurements at relatively low suctions.

As opposed to the N-HCT or UMS-T5 direct tensiometers, the MPS-6s do not have a cavitation point and can therefore provide the advantage of continuous measurement in the continuous drying-wetting cycles, without the need to be extracted and re-saturated. The re-saturation process normally entails the removal of the embedded tensiometer from the soil for re-saturation, which might affect the soil structural integrity, disturb the soil matrix, and compromise the established intimate contact between the embedded sensor and the soil matrix. Nonetheless, the MPS-6 typically functions at a less reliable range and sensitivity compared to the direct tensiometers. It continuously demonstrated lagging in the equalisation with the porewater. The low performance equalisation was more prominent in the wetting path. Additionally, the large and irregular shape of the MPS-6 shaft, and the uneven faces of its ceramics require a larger specimen size and might result in lower sample homogeneity in the vicinity of the embedded sensor. The latter is more prominent for compacted specimens at a relatively dryer conditions.

The HEMP-230 Vaisala RH sensors used in this study can indirectly compute total suction from pore moisture using the psychrometric law at higher suction ranges, that is, less saturated specimens. The RH sensor methods allows to capture the dryer range of suction measurements, therefore complementing the limited-range results by other methods (e.g., N-HCTs, MPS-6, etc.). The obtained complemented range offers continuous physical readings of suction, from highly saturated to dry soil specimens. This aspect is of utmost importance for calibrating the parameters of constitutive models for unsaturated soils, aimed at numerically simulating the drying soil behaviour and water retention mechanism. The numerical models often lack such an experimental validation of the actual physical suction level in the soil. The overlap in the measuring range between the N-HCT and the RH sensors provides an insight on the RH sensor functionality and performance. When compared to the direct method readings, the RH sensor readings demonstrated a consistent lagging pattern in the equalisation with the soil moisture. This is due to the generally slower equalisation times the transistors require to obtain a reliable physical reading of the RH values within the soil pores.

The Vapour Equilibrium (VE) technique and WP4-T were used as indirect methods, in the sense that both techniques were applied to soil specimens prepared in parallel from the same soil batches. For higher suction values, the VE technique requires higher equalisation times (multiple weeks). The equalisation times are larger for the wetting path in comparison with those of the drying path. Extra carefulness should be given to the temperature variations, salt solutions, and equalisation times when implementing the VE technique. The VE technique can be advantageous when obtaining the SWRCs for multiple specimens simultaneously, by placing these multiple specimens in the same closed desiccator containing a specific solution. The other advantage of the VE technique is that it does not need any advanced laboratory setups and sensors. All that is needed: (1) tightly closed medium where the specimens can hang over the solution, (2) salt or acidic solutions, mixed to specific concentrations, (3) balance, and (4) any adequate volumetric measurement technique. These 4 components can be relatively easily obtained in any laboratory, as opposed to the HCTs and dewpoint hygrometers.

Different volumetric measurements techniques were also evaluated in this chapter. Continuous volumetric measurements for relatively small size specimens can result in misestimations of the bulk volume. An isotropic and uniform shrinkage behaviour assumption cannot be considered entirely valid to obtain accurate volumetric estimations of specimens with embedded sensors or large-scale specimens with anticipated differential and non-homogenous desaturation and deformation patterns. The improper capture of the actual soil volume is a result of the shear and differential deformations occurring due to the presence of the embedded sensors within the relatively small specimen sizes, as opposed to specimens undergoing unsaturated free shrinkage (without mechanical restrictions). For this purpose, the Digital Image Analysis (DIA) method was also carried out indirectly (DIA-ID) on specimens drying freely (with no embedded sensors), prepared in parallel from the same soil batches. The DIA-ID results compared well with other freely drying specimens, like those of the Paraffin-Coating (PC) method. Some minor discrepancies between the DIA-ID and PC methods were only noticed at the drier stages and was mainly attributed to the specimen surface roughness.

Obtaining a coherent set of physical volumetric measurements allows the fitting of a reliable SSC model equation. A reliable fitted SSC model provides a consistent soil water-void ratio relationship. Such a consistent relationship allows the indirect estimation of void ratio values from a given experimentally measured water content value. Doing such an estimation can prove valuable for small soil samples or samples in general where the typical volumetric measurement techniques are difficult to apply. In this case, having multiple suction measurement techniques applied on multiple specimens of the same soil batch can be combined, knowing the evolution

of water content of each of these multiple samples (from which the void ratio is estimated using the fitted SSC model equation).

Therefore, a full-range SWRC can be obtained, by adequately combining suction measurement techniques that cover the whole range, and by obtaining a uniquely fitted SSC model equation pertaining to the soil batch being studied.

Chapter 4

The role of Inflexion-Point of the SWRC in the Shrinkage and Swelling Mechanism of Partially Saturated Soils

Parts of this chapter are under review for publication with the title:

“The role of inflexion-point in the shrinkage mechanism of partially saturated soils”.

with the co-authors:

Abdallah Najdi, David Encalada, Joao Mendes, Mohamed Rouainia, Pere Prat, Alberto Ledesma

4.1. Introduction

Topsoils are exposed to atmospheric conditions resulting in a certain continuous interaction transpiring between the two media. The interaction entails exchanges between the two media on the level of vapour fluxes, temperature, energy, and radiation fluxes, until an equilibrium is reached. Eventually, this will lead to evaporation of the existing water in the porous soil medium, or instead, water condensation causing saturation (i.e., wetting). Additionally, heat energy fluxes are generated due to the temperature difference between the soil and overlying atmosphere. For the unconfined topsoils under study, these thermo-hydraulic changes produce a change in the porewater pressure and in the deformable solid matrix structure of the porous soil, which contains the water in both its liquid and vapour phases. Studying the phenomenon and characterising the changes in the desaturating/saturating deformable soils involves the study of three principle variables: (i) soil-water content θ (represented by gravimetric water content θ_w [$\text{g} \cdot \text{g}^{-1}$], volumetric water content θ_v [$\text{cm}^3 \cdot \text{cm}^{-3}$], saturation-degree θ_{s_r} [%], water ratio θ_e [%] (Romero et al., 2011), etc.); (ii) volumetric changes (represented by void ratio e , volumetric strains ε_v [%], etc.); and finally (iii) soil-water matric potential (i.e. matric suction ψ [Pa]).

The study of the association between these three principal variables is situated in the heart of the unsaturated soil mechanics research domain, and have been characterised by different established relations in this domain: (a) Soil Water Retention Curves (SWRCs) describe the direct nonlinear relationship between the matric suction and the water content; (b) Soil Shrinkage Curves (SSCs) describe the relationship between the shrinkage or swelling (i.e. void ratio decrease or increase, respectively), and the fluctuating water content (i.e. decreasing or increasing, respectively); and (c) Suction-Voids Curves (SVCs) describe the relationship between the suction and void ratio.

Determining the SWRCs, SSCs, and SVCs for a soil and the corresponding involved parameters is fundamental in characterising the unsaturated deformable soils. In practice, it is widely common to obtain and represent the three curves independently, and in many cases, only one of the three curves (Perera et al., 2005; Al-Dakheeli & Bulut, 2019; amongst many). Nonetheless, to fully understand the aspects of the ensuing coupled hydromechanical behaviour requires the study of the interdependency between the three principal variables at the same time (Ridley, 1993).

Obtaining and representing one of the curves (i.e., SWRC, SSC or SVC) can provide valuable information on the relation between two of the involved variables. Establishing such dependency between two of the three variables can prove to be useful for the determination of

the other relationships. For example, for a specific soil set, a predetermined SSC can indicate indirectly the value of void ratio for a given water content (Najdi et al., 2023a), and has been generally often used to better represent the water content scale of the SWRC (Peng & Horn, 2005; Lin & Cerato, 2013; Fredlund & Fredlund, 2020). On the other hand, a predetermined SWRC can indicate the matric suction for a given water content, while a predetermined SVC can indicate the suction value at a given void ratio. Combining the information from either two of the three predetermined curves (i.e., SSC, SWRC or SVC) for a specific soil set can provide enough information for extrapolating the third curve.

The drying or wetting process of soils can be featured into multiple distinctive stages with different hydromechanical aspects. In the same way, the SWRCs, SSCs and SVCs can be each divided into multiple stages or phases according to desaturation/saturation rates and mechanisms (e.g. Vanapalli et al., 1996; Sheng et al., 2008; Lu & Dong, 2017). To define the transition between two consecutive stages or phases, multiple yielding (or transitional) points on each of the curves have been established, namely: (a) the saturation-suction (Sheng et al., 2008), (b) the AEV, (c) the SWRC inflexion-point (Dexter, 2004), (d) the shrinkage limit and (e) the residual-suction. The prevailing strong coupling between the three variables, and the mentioned association between the corresponding curves, suggest a likewise coupling also exists amongst the different stages and transition-points, that is yet to be properly established.

Both drying and wetting paths are analysed in this chapter, giving insights into the hydromechanical hysteresis phenomenon. Soils typically have distinct curves depending on the followed path, whether be it drying or wetting path. For instance, the water content for the drying SWRC path is constantly greater than the wetting SWRC path, for any given suction value. Hysteresis is expected in porous media with interconnected pores of differing sizes with entrapped air, irregularities in the cross-section of the void passages or the “ink-bottle” effect (Bear, 1969), and varying contact angle (Azizi et al., 2017). The latter (between the solid surfaces and the wetting fluid), is higher for an advancing meniscus rather than in a receding one.

The aim of this chapter is to demonstrate the coupled hydromechanical aspects of unsaturated soils undergoing desaturation or saturation, to distinguish the different drying and wetting stages, and finally to identify the corresponding transition or yielding points (i.e., the transitional points between two consecutive stages). A strong correlation is suggested between the ‘inflexion-point’ of the SWRC in the drying path (*Dry-IP*) and the well-known ‘shrinkage-limit’ transition-point. Similarly, a strong correlation is suggested between the ‘inflexion-point’ of the SWRC in the wetting path (*Wet-IP*) and the ‘swelling-limit’ transition-point. This novel correlation approach offers insights on the soil matrix and the features of the behaviour at the

microstructure level, which can be useful in defining some constitutive relations (Musso et al., 2019). Additionally, it provides a valuable calibration point, and sets an upper limit for the mechanical constitutive models dealing with the effect of suction on volumetric changes.

The analysis was based on laboratory experiments on four in-house soils and validated by additional 32 ‘SWRC-SSC’ datasets from the literature, encompassing a wide range of soil types, fabrics, and textures. Suction at inflexion-point is computed based on different water content scales and SWRC fitting functions and compared against the graphically derived ‘shrinkage-limit’.

4.2. Experimental campaign

Obtaining a consistent experimental SWRC is contingent on accurate measurements of the three variables involved at each step: water content, suction, and void changes (θ, ψ, e ; respectively). Four different soils were tested in the laboratory initially to obtain the respective (θ, ψ, e) datasets.

4.2.1. Properties of the used soils

The soils used in the preliminary experimental procedures are the Agròpolis silty clay (Cordero et al., 2020), North Campus silty clay (Cuadrado et al., 2022), B2-Bentonite, and C2-Kaolin. Table 4.1 provides a summary of the basic characteristics for the B2-Bentonite and C2-Kaolin, while those of the Agròpolis and North Campus silty clay can be consulted in Chapter 3 (see section 3.2.1). For the Agròpolis soil, five different specimens at five different initial compaction conditions were tested (see Chapter 3, section 3.2.2): (1) dry of standard-Proctor optimum (i.e., A-S1); (2) standard-Proctor optimum (i.e., A-S3); (3) wet of standard-Proctor optimum (i.e., A-S4); (4) modified-Proctor optimum (i.e., A-MP2); and (5) liquid limit (i.e., A-LL). For the Barcelona silt, two specimens were tested at plastic limit compacted to standard proctor conditions (i.e., NC-S3), and at liquid limit as a slurry (i.e., NC-LL). As for the B2-Bentonite and C2-Kaolin, both soils were tested at their respective liquid limit.

Table 4.1. Basic properties of the B2-Bentonite and C2-Kaolin used in the preliminary experimental investigation.

	Specific Gravity G_s	% fines ($\leq 2\mu\text{m}$)	Unified Soil Classification System, USCS
B2-Bentonite	2.70	100	CH
C2-Kaolinite	2.70	100	ML

4.2.2. “Porewater – Voids – Suction” datasets and dependence

Physical “Porewater Content – Void Ratio – Suction” ($\theta - e - \psi$) datasets were obtained experimentally at the geotechnical laboratories of UPC-BarcelonaTech. The adopted experimental methodology relies on measuring the three variables simultaneously for the same soil sample. Similar datasets are then obtained for the same soil but at different sets of initial conditions, for both the drying and the wetting paths. The methodology, experimental techniques, and setups used, are detailed previously in Chapter 3. For the drying path, a simplified continuous-drying setup is used (see Chapter 3, section 3.3.1.2), employing the novel N-HCT (Mendes et al., 2022) (see Chapter 3, section 3.2.3.2). The N-HCT suction measurements are complemented with suction measurements from the Dewpoint Hygrometer (WP4-T) for the drier part of the SWRC, i.e., for suctions beyond 3 MPa (see Chapter 3, section 3.2.3.4). The wetting path data were obtained using the discrete wetting method for multiple specimens made from a soil batch with the same initial conditions (see Chapter 3, section 3.5). The specimens were wetted gradually in stages. Water content, void ratio, and suction levels were measured simultaneously at each stage. The suction measurements were carried out using the WP4-T for the drier regions, and a combination of MPS-6 and discrete N-HCT readings for the wetter region.

The readings combination on the same SWRC for a defined set of initial conditions is made possible by unifying the volumetric measurements for the same soil batch of the same initial conditions. This unifying volumetric measurements process is carried out via a fitted SSC model equation (Groenevelt & Grant, 2001) (see Chapter 3, section 3.4). Physical volumetric measurements obtained from Indirect Digital Image Analysis were used as a data basis for the SSC model equation (Najdi et al., 2023a).

For each soil dataset, the simultaneously obtained ($\theta - e - \psi$) values in one direction (i.e., either drying or wetting path, separately) portrays a unique trajectory line in the 3D space. That is to say, the soil state at any point during the main drying shrinkage or main wetting swelling belongs on these particular 3D-lines. Projecting the 3D-line on the: (i) Saturation-Suction 2D-plane represents the common SWRC; (ii) on the Saturation-Void ratio plane represents the SSC; and (iii) on the Suction-Void ratio plane represents the Suction-Voids Curve (SVC). The latter is essential for calibrating mechanical models describing the effect of suction on shrinkage and swelling.

Figure 4.1 shows the 3D schematic projections for the third specimen of the Agròpolis soil (A-S3) (see Chapter 3, section 3.2.2), in the drying path only (for graphical clarity).

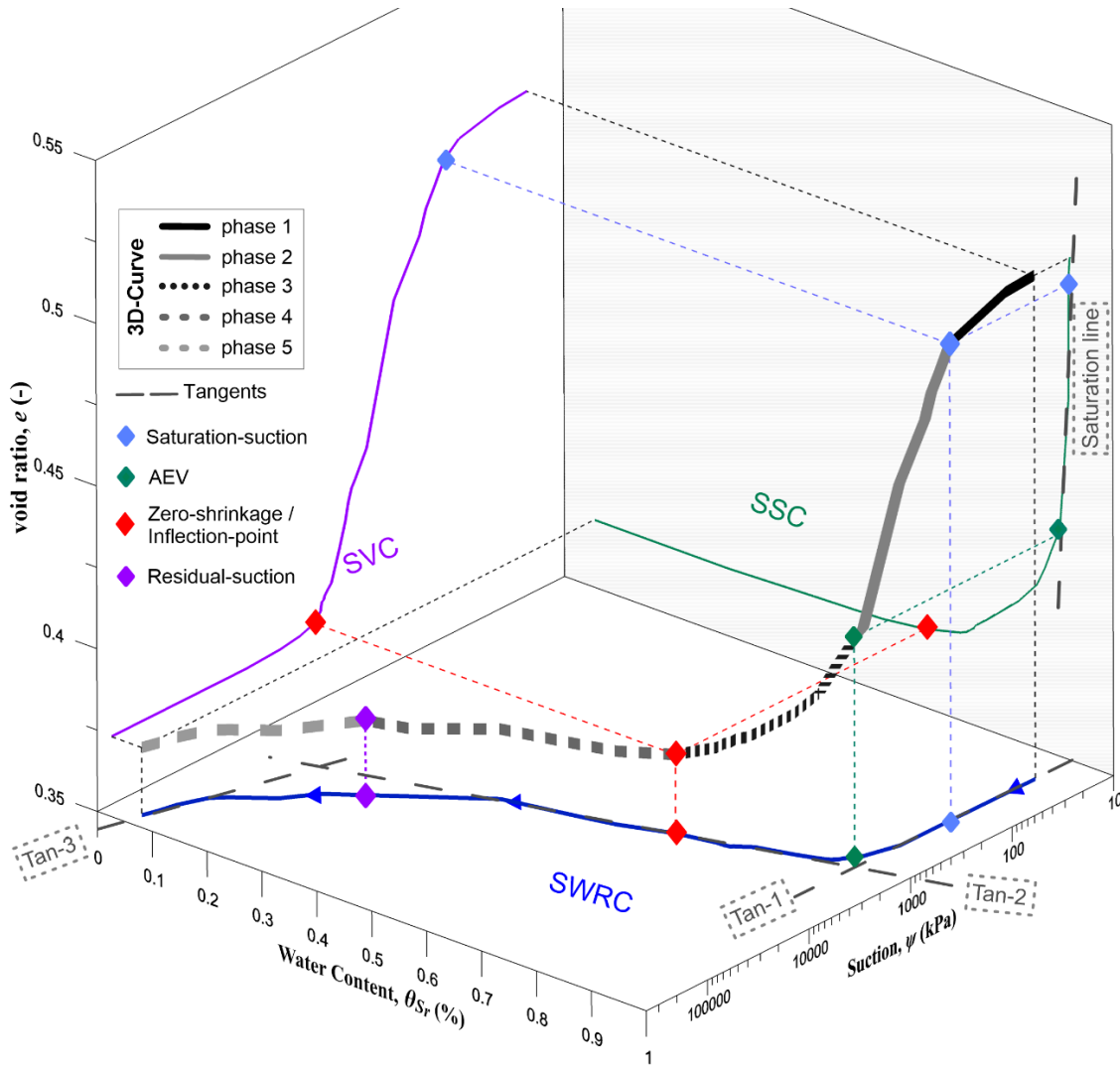


Figure 4-1. 3D schematic example of $(\theta_{Sr} - e - \psi)$ dataset for Agròpolis soil in the drying path, with projections on the SWRC, SSC and SVC 2D domains.

The 3D curve is projected vertically downwards onto the SWRC (here portrayed in terms of $\theta_{Sr} - \psi$ domain); horizontally to the right onto the SSC (i.e., $\theta_{Sr} - e$ domain), and horizontally to the left onto the SVC (i.e., $e - \psi$ domain).

Figure 4.2 shows the same sample 3D schematic including the wetting path curves. The drying path curves are given less opacity for graphical clarity, as in to mainly focus on the wetting path. Note that the figure is represented on the volumetric water content scale instead of saturation degree, to highlight the difference between two graphical selecting approaches of the AEV point taken by different researchers (to be further discussed below in section 4.4). Figure 4.2b shows the same 3D figure tilted to another viewing angle to shed more attention on the hysteretic space between the two 3D curves.

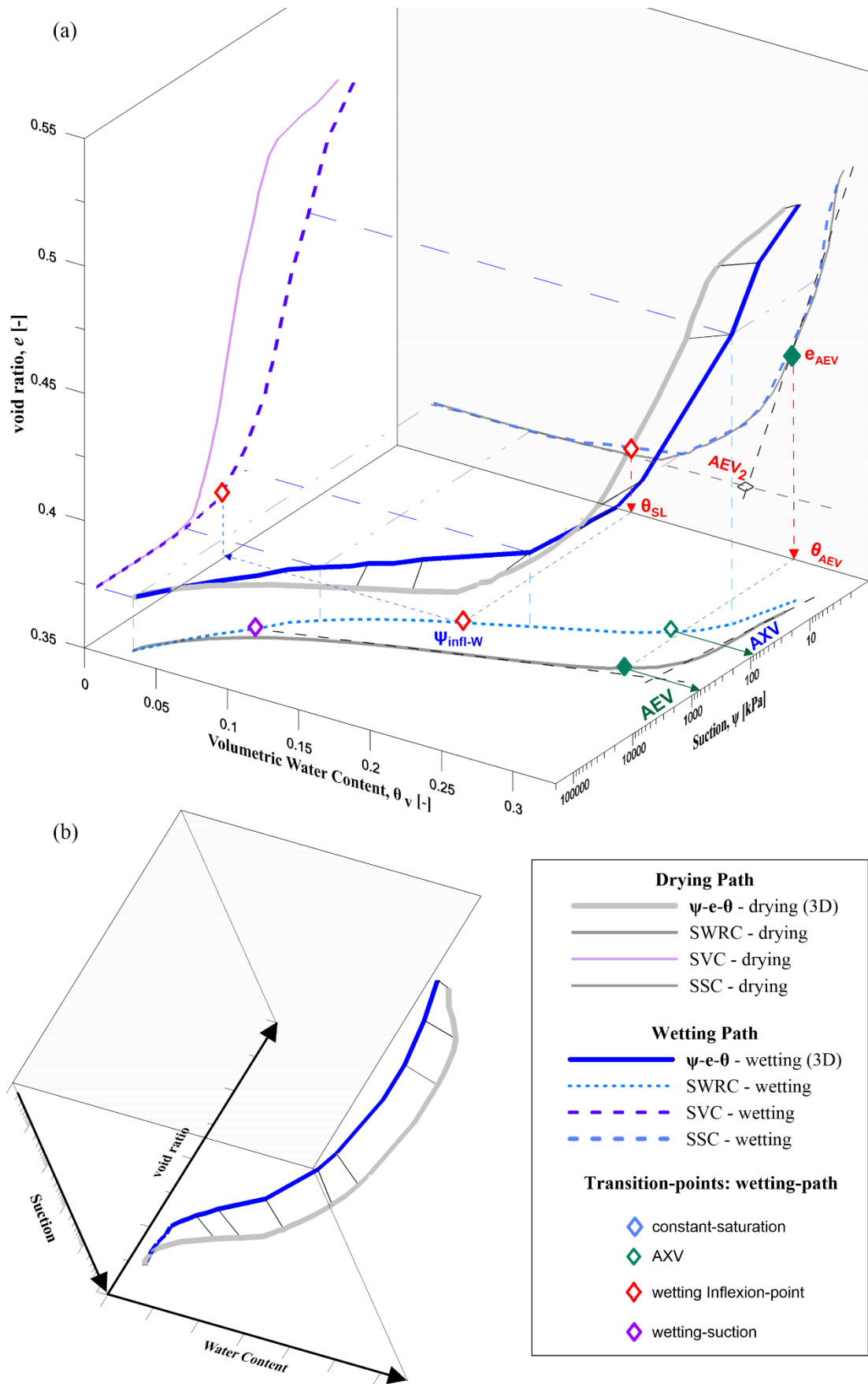


Figure 4-2. 3D schematic of the (a) ($\theta_v - e - \psi$) dataset showing the wetting path and (b) a different angle of the 3D scheme showing the hysteresis in the 3D domain.

4.3. Mathematical data fitting

The relationship between the three ($\theta - e - \psi$) variables can be mathematically represented by a single SWRC function that accounts for the effect of void ratio change (Gallipoli et al., 2003), or by a more common set of equations in 2D planes, describing the relationship between two dependent variables at a time (i.e. separate equations for SWRC, SSC and SVC).

For SSCs, mathematical models typically use multi-equations (e.g. McGarry & Malafant, 1987; Braudeau et al., 1999) or a single equation (Peng & Horn, 2005), represented by sigmoid curves requiring multiple fitting parameters (Groenevelt & Grant, 2001; Cornelis et al., 2006).

For SVCs, a single coefficient is often adopted to define the relationship between volume change and suction, which can be directly derived from the suction-void ratio relationship such as the Barcelona elastoplastic model (Alonso et al., 1990).

The SWRC inherently takes an S-shape curve form. Many empirical equations exist in the literature to mathematically represent it, using: (a) single-segment models (Brooks & Corey, 1964; van Genuchten, 1980; Fredlund & Xing, 1994); (b) two-segment models (Rossi & Nimmo, 1994; Fayer & Simmons, 1995); and (c) three-segment models (Groenevelt & Grant, 2004; Zhang, 2011).

A closer look at the implementation of these models shows that the fitting performance worsens with the increased number of segments, while improves for an increased number of fitting parameters (Du, 2020). Amongst many, the Fredlund & Xing (1994) model-*FX*, equation 4.1, and the van Genuchten (1980) model-*vG*, equation 4.2, are the most commonly used in numerical models for unsaturated soils.

$$\theta = \theta_{ls} \left\{ \ln \left[e + \left(\frac{\psi}{\alpha_{FX}} \right)^{n_{FX}} \right] \right\}^{-m_{FX}} \quad (4.1)$$

$$\theta = \theta_{rl} + (\theta_{ls} - \theta_{rl}) [1 + (\alpha_{vG} \psi)^{n_{vG}}]^{-m_{vG}} \quad (4.2)$$

Where θ stands for water content (gravimetric, volumetric or saturation-degree scale); θ_{ls} is the saturated water content; θ_{rl} is the residual water content; and α_i , n_i , and m_i are fitting parameters with the subscripts '*i: FX*' and '*i: vG*' standing for 'Fredlund and Xing (1994)' and 'van Genuchten (1980)' models, respectively. The α_i parameter is controlled by the largest pore size of the soil, surface tension and solid-liquid-air contact angle (i.e., related to the AEV); while n_i and m_i can be related to the pore-size distribution (Oh et al., 2012; Lu et al., 2013).

To better understand the evolution of retention properties, the desaturation-rate (i.e., first-order derivative) and its slope (i.e., second-order derivative) are derived for model-*FX* (equations 4.3-4.4) (Zhai & Rahardjo, 2012), and model-*vG* (equations 4.5-4.6), with respect to the typical semilogarithmic suction scale used to represent SWRCs:

Model-*FX*:

$$\frac{d\theta}{d(\log(\psi))} = \frac{d\theta}{d(\psi)} \cdot \psi \cdot \ln 10 = \frac{-m_{FX} \cdot n_{FX} \cdot \theta_{ls} \cdot \ln 10 \cdot (\psi/\alpha_{FX})^{n_{FX}} \cdot \{\ln[e + (\psi/\alpha_{FX})^{n_{FX}}]\}^{-m_{FX}-1}}{[e + (\psi/\alpha_{FX})^{n_{FX}}]} \quad (4.3)$$

$$\frac{d^2\theta}{d(\log(\psi))^2} = \frac{mn^2\theta_{ls}\ln^2 10 \left(\frac{\psi}{a}\right)^{n-1}}{a \cdot [e + \left(\frac{\psi}{a}\right)^n] \cdot \ln^{m+1} \left[e + \left(\frac{\psi}{a}\right)^n\right]} \cdot \left[1 - \frac{\left(\frac{\psi}{a}\right)^n}{e + \left(\frac{\psi}{a}\right)^n} - \frac{(m+1) \cdot \left(\frac{\psi}{a}\right)^n}{[e + \left(\frac{\psi}{a}\right)^n] \cdot \ln[e + \left(\frac{\psi}{a}\right)^n]} \right] \quad (4.4)$$

Model-*vG*:

$$\frac{d\theta}{d(\log(\psi))} = -m_{vG}n_{vG}(\theta_{ls} - \theta_{rl})(\alpha_{vG}\psi)^{n_{vG}}[1 + (\alpha_{vG}\psi)^{n_{vG}}]^{-m_{vG}-1} \quad (4.5)$$

$$\frac{d^2\theta}{d(\log(\psi))^2} = \frac{m_{vG}n_{vG}(S_{ls} - S_{rl})[1 + (\alpha_{vG}\psi)^{n_{vG}}]^{-m_{vG}-2}[(m_{vG}n_{vG} - 1)(\alpha_{vG}\psi)^{n_{vG}} - n_{vG} - 1]}{\psi} \quad (4.6)$$

4.4. Desaturation stages and the corresponding transition-points

The behaviour of desaturating deformable soil media can be divided into separate zones or ‘desaturation stages’, with each stage portraying distinctive features of the process. SSCs are ordinarily classified into four stages: (i) structural, (ii) normal, (iii) residual and (iv) zero shrinkage. Semilogarithmic SWRCs on the other hand are ordinarily classified into three stages: (i) boundary effect zone, (ii) desaturation transition zone, and (iii) residual zone (White et al., 1970; Vanapalli et al., 1996). Lastly, SVCs are ordinarily classified into two stages: (i) elastic, and (ii) plastic deformations.

The transition between two successive stages occurs at different ‘transition’ or ‘yielding’-points, which can be identified graphically or mathematically. Transition-points are considered essential soil parameters, and in many cases have a direct relation with some intrinsic soil characteristics (the air entry value, plastic-yielding, shrinkage-limit).

As the mechanical behaviour is projected onto the SWRC, it becomes apparent that the various stages from the SSCs and SVCs can most likely be distinguished from the SWRC alone (see Figure 4.1).

Five consecutive coupled desaturation stages are proposed here instead. The additional stages can be recognised by the coincidence of the: (i) saturation-suction transition point (of the SWRC), with the plastic yielding point (of the SVC), and the limit of structural shrinkage stage (of the SSC); and of the (ii) AEV (of the SWRC), with the limit of the proportional shrinkage stage (of the SSC). However, the limit of the residual shrinkage stage, or what is widely known as the shrinkage limit, is not typically distinguished through the SWRC. The term ‘shrinkage limit’ refers to the point on the SSC or SVC beyond which the rate of volumetric changes becomes insignificant upon further drying or increase in suction.

A new transition-point on the SWRC, namely the ‘inflexion-point’ (SWRC-IP), is introduced and associated to the established ‘shrinkage limit’ (SL). The term ‘shrinkage limit’ has been normally assigned to the intersection between the tangents going through normal- and zero-shrinkage stages of the SSC (e.g. Lu & Dong, 2017). In this work, the term ‘shrinkage limit’ refers to the point on the SSC, beyond which, the rate of changes in the void ratio decreases significantly, that is, the limit of the residual shrinkage stage of the SSC.

Figure 4.3 shows the desaturation-rate and the desaturation-rate-slope curves evolution corresponding to the presented SWRC (computed from first and second order derivatives of the

SWRC fitting equation, respectively). For graphical clarity, only the rate and the rate-slope obtained from model- vG (equations 4.5-4.6) results are demonstrated.

The five drying stages and corresponding transition-points are rendered more distinguishable, following the use of the $(\theta - e - \psi)$ 3D projections that link the SWRCs, SSCs and SVCs (Figure 4.1 and Figure 4.2), and the use of SWRC desaturation-rate and SWRC desaturation-rate slope (Figure 4.3).

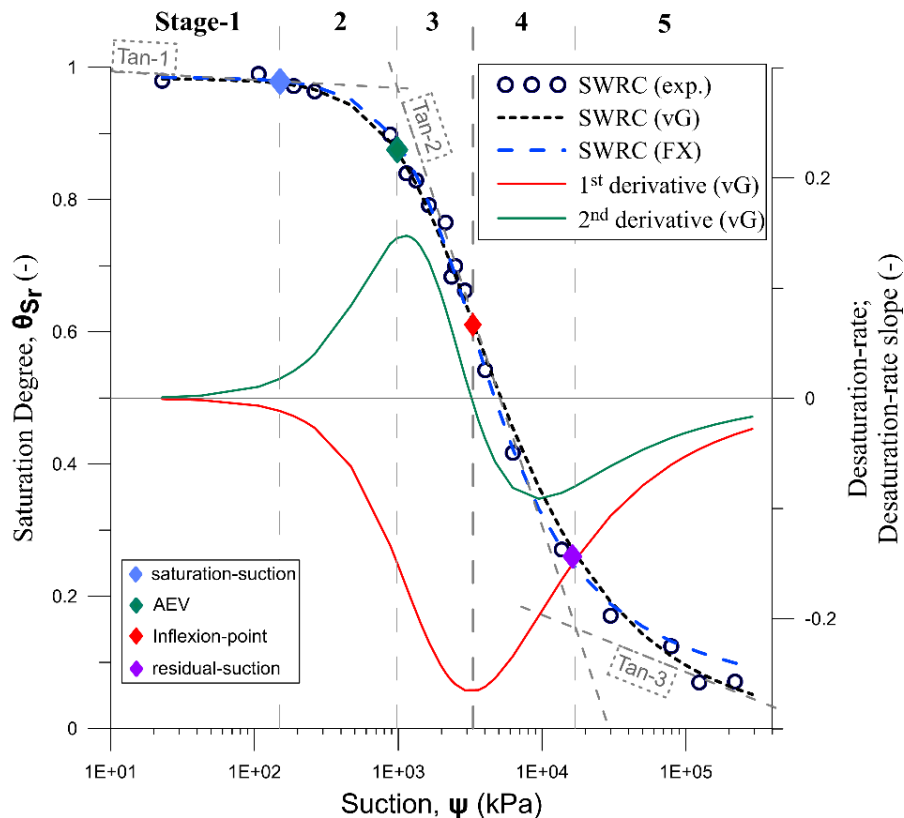


Figure 4-3. Experimental SWRC for Agropolis soil, compacted near standard Proctor optimum (A1). Model- vG and -FX SWRC fittings are shown along with the desaturation rate (1st derivative), desaturation rate slope (2nd derivative), and the four transition points from Figure 4.1.

Assuming that this relationship is valid for other silty clays, all the existing hydromechanical transition points (saturation-suction, AEV, shrinkage limit) can be obtained from the SWRC alone. The fourth SWRC transition point (residual suction) corresponds to the hydraulic behaviour and adsorption regime at very dry conditions, with negligible implications on the global mechanical response. The last point represents the oven-dry completely dry conditions. As a result, the SWRC can distinguish a total of five stages with distinctive characteristics, whether hydraulic, mechanical, or hydromechanical.

Figure 4.4 presents a conceptual model of the progressively evolving hydromechanical behaviour at the microstructural level throughout the different stages.

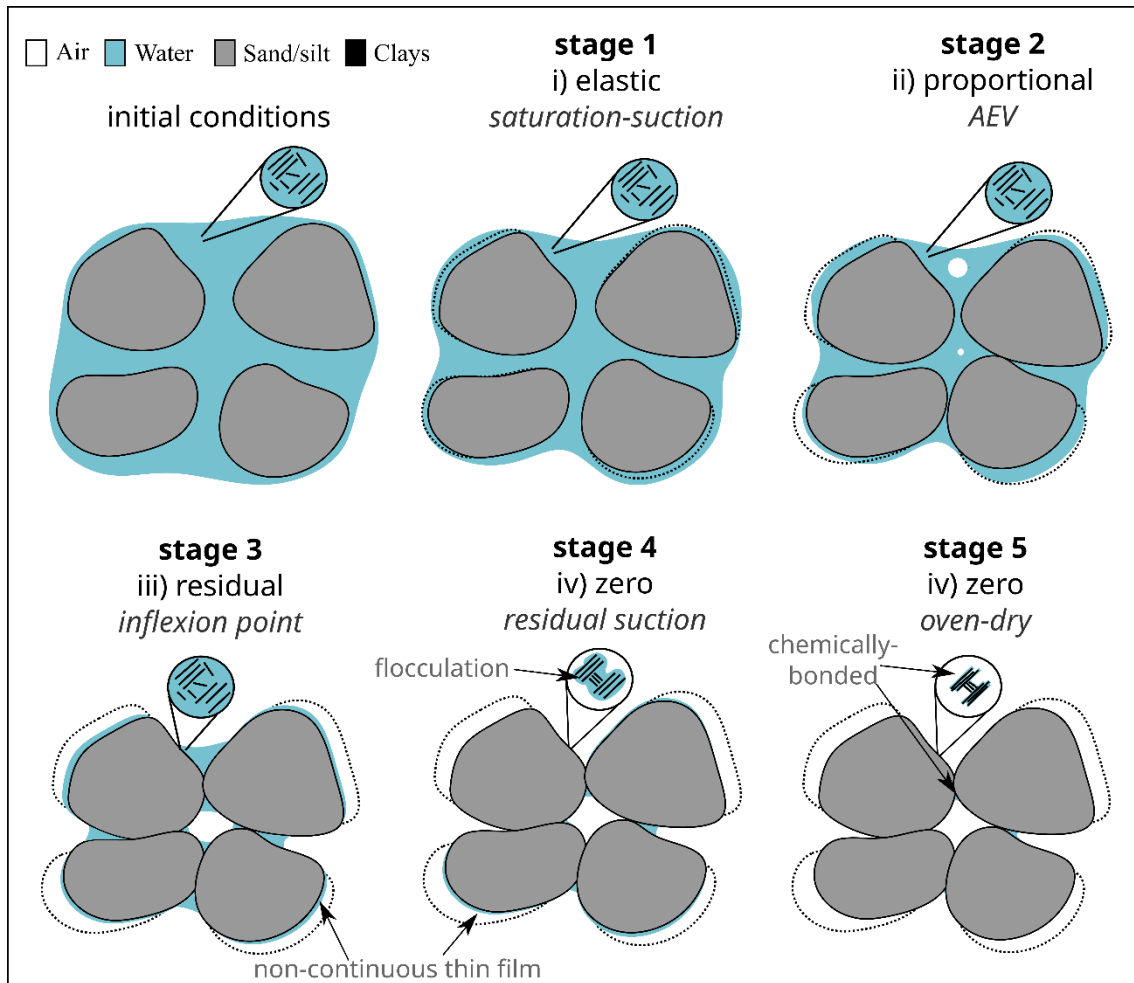


Figure 4-4. Generalised conceptual model of desaturation shrinkage stages, indicating the mechanical shrinkage regime (preceded by the order number), and the corresponding transition point (in *italic*). The dotted-line shapes depict the original location of particles.

The five stages can be then identified as the following:

4.4.1. Stage-1-d (Initial to saturation-suction)

Stage-1 drying corresponds to the proposed first subzone of the common boundary effect zone, where the latter is identified from initial saturation conditions until reaching the AEV (Vanapalli et al., 1999). In this work, the common boundary effect zone is divided into two subzones. The first subzone is identified to range from initial fully saturated conditions, until the saturation-suction transition-point. The saturated soil matrix in this first subzone is in a capillary state (Lu & Dong, 2017), and suction increases are not sufficient to drain the medium's pores (Blight, 1967).

The term ‘saturation-suction’ has been used to identify the limit of the elastic deformations caused by suction development (Sheng et al., 2008). The saturation-suction is identified from the SVC as the plastic yielding-point (Figure 4.1). Lower-scale mechanical deformations governed by elasticity are experienced until reaching this suction value. The saturation-suction is consistently lower than the AEV (Chiu & Ng, 2012). For heavily compacted, remoulded and normally consolidated soils, this point can simply coincide with the initial saturation condition.

On the SSC, the saturation-suction transition-point lies towards the initial stages of normal shrinkage, after which no more structural shrinkage is expected to occur. The void ratio lost until this stage, likely (but not exclusively) corresponds to structural pores (e.g., microcracks or loose water at the soil surface). On the SWRC, the saturation-suction is located on the first tangent drawn from initial conditions, signifying no substantial change in initial saturation. The desaturation-rate until this point is particularly low (Figure 4.3).

4.4.2. Stage-2-d (saturation-suction to AEV)

Stage-2 drying corresponds to the second subzone of the common boundary effect zone. It extends between the previously identified saturation-suction and the AEV. The latter is equivalent to the height of passive capillary rise and indicates at which suction the air permeates into the largest soil pores (Fredlund & Xing, 1994). In other words, the AEV is the matric suction that breaks the meniscus formed by water surface tension in the largest pores.

All the soil voids are still saturated during this stage (i.e., before reaching the AEV), the soil particles are in a pendular state (Lu & Dong, 2017), and the water menisci form a continuous film in contact with the soil particles (see stage 2, Figure 4.4). Any entrapped air within the soil matrix would enlarge due to the increasing negative porewater pressure magnitude as suction approaches AEV.

On the SSC, the reduction of void ratio is termed ‘basic’ (Mitchell, 1992); ‘normal’; or ‘proportional shrinkage’ (McGarry & Malafant, 1987). The latter nomenclature is due to the proportional decrease in soil volume with respect to the loss in water volume. The shrinkage follows the saturation line at a constant slope (Figure 4.1), equal to the specific gravity (Najdi et al., 2023a). High proportion of the total void ratio reduction until residual conditions generally occurs during this particular stage.

On the SWRC, the AEV can be obtained using a consistent graphical approach of tangents intersection (tan-1: saturation zone identified in Stage-1; tan-2: desorption part of the SWRC; see Figures 4.1 and 4.2). Note that, while approaching the AEV, the desaturation-rate slope approximates its maximum attained value (Figure 4.3).

The resulting intersection-point between the tangents (i.e., the AEV) is projected onto the SSC domain (throughout the volumetric water content scale in the 3D diagram of Figure 4.2). When projected, the AEV intersects with the SSC at the point where the SSC diverges from the proportional shrinkage phase (e_{AEV} on Figure 4.2), rather the point of intersection of the SSC tangents (i.e., AEV_2 on Figure 4.2). The location of the AEV_2 value is normally obtained through the intersection of SSC-tan-1 through proportional shrinkage, and SSC-tan-2 through residual shrinkage stage. The former definition of the AEV_1 reflects a rather unique point in both SWRC and SSC domains, demonstrating the existing strong coupling.

4.4.3. Stage-3-d (AEV to ‘dry-IP’/‘SL’)

Stage-3 drying corresponds to the residual-shrinkage stage of the SSC, and the first subzone of the SWRC conventional primary transition zone (Vanapalli et al., 1996). It extends between the AEV and the previously mentioned shrinkage limit. The latter can be identified, graphically and experimentally, as the transition-point beyond which the rate of change in void ratio lowers significantly (Boivin, 2007). During this drying stage, air invades the inter-aggregate pores and the amount of water on the soil particle surface or aggregate contacts reduces (stage 3, Figure 4.4).

In heterogeneous soils (e.g., silty clays), compacted dry of optimum, the soil structure is characterised by a skeleton where the finer materials (e.g., clay platelets) form a bridge connecting the larger grain aggregates (Delage et al., 1996). Whereas originally wet soils, such as slurries or compacted wet of optimum, the finer materials, once forming a matrix with the larger ones dispersed in it (i.e., silts or sands), start to coat the larger grains during this stage (Delage et al., 1996).

The advective fluxes yet control the water transport. By the end of this stage, the water menisci film is no longer continuous throughout the soil matrix. Besides its liquid state, the porewater now exists in its vapour phase, carried out by the pore-air space. Even though a high percentage of porewater quantity is lost by the end of this stage, the saturation degree remains relatively high due to the closer particle formation (lower void ratio).

On the SSC, the volume of evaporating water surpasses the reduction in soil bulk volume. The shrinkage slope becomes curvilinear and continuously decreasing until it eventually diminishes upon reaching the shrinkage limit.

On the SWRC, the shrinkage limit projection coincides with the desorption line at the point of curvature change from upwardly concave (positive 2nd order derivative) to opposite concavity

(negative 2nd order derivative). Graphically, this point is called an ‘inflexion-point’, that refers to maximum desaturation-rate magnitude and zero desaturation-rate slope (see Figure 4.3).

The value of suction at the ‘inflexion-point’ (SWRC dry-IP) can be considered as the ‘break-through’ matrix potential at which air penetrates through the soil (White et al., 1970; Dullien, 1992). Particles are rearranged in a more compact distribution pattern, that is to say, close to the residual void ratio level. Water menisci are no longer continuous and higher suction values are required to extract the remaining water, which is reflected in the decreasing desaturation-rate beyond this point (Figure 4.3). The higher value of suction required is due to the porewater thinning in the macro-pore and intra-aggregate space and its arrangement as non-continuous thin film surrounding the soil particles. The inter-aggregate space within the soil matrix has achieved a rigid skeleton that is no longer connected through water menisci. The water menisci that used to exert forces joining the particles does not connect the particles anymore, and therefore, further loss of water does not affect the shrinkage process. The remaining water at this stage exists in the interparticle dimension and is more difficult to extract.

The significance of the inflexion point of the drying path SWRC was discussed by Dexter and Bird (2001), who identified the water content at SWRC dry-IP as an optimum value for tillage. The slope at SWRC dry-IP, namely the S-index, corresponds to microstructural porosity and can be used as an indicative of the extent to which the soil porosity is concentrated into a narrow range of pore sizes (Dexter, 2004). Larger S-index values are consistent with the presence of a better defined microstructure, and mainly the textural or macro-pores are desaturating until reaching the ‘inflexion-point’ (Richard et al., 2001).

Further investigations regarding the SWRC dry-IP were developed by other few researchers. Guimarães et al. (2011) presented different expressions for obtaining the SWRC dry-IP for both an arithmetic and a logarithmic basis for suction. However, a proper link between the SWRC-IP and the SL is yet to be constituted and the physical phenomenon to be physically explained.

4.4.4. Stage-4-d (dry-IP to residual-suction)

Stage-4 corresponds to the second part of the conventional SWRC desaturation transition zone and lies within the zero-shrinkage zone of the SSC and SVC. It extends between the ‘SWRC dry-IP’ and the ‘residual-suction’.

During this stage, water exists as a thin film surrounding the tightly adsorbed soil particles (stage 4, Figure 4.4), while diffusive fluxes control the water movement in the soil matrix. Air continues to invade the pores, replacing the evaporated water, causing an increase in the interparticle stresses, and forcing conglomeration of the finer materials. The change in soil

particles configuration occurs at the micro-level in the intraparticle domain. However, this process of finer material shrinkage within the soil matrix, or reduction in the micropore space is not perceived through the conventional bulk-volumetric measurement techniques used in these types of studies (e.g., paraffin-coating, digital image analysis, balloon method, etc.). The shrinkage of the intraparticle domain can be considered insignificant with respect to changes in the interparticle void. This explains the lower, but non-zero, shrinkage rates obtained normally beyond the shrinkage limit for soils rich in finer materials, thus consisting of higher percentage of micropore space susceptible for this type of change (e.g., expansive clays and bentonites). However, in non-expansive soils with low hydrated exchangeable cations (Lu & Khorshidi, 2015), the shrinkage rates in this stage are practically zero.

The residual suction value is obtained from the intersection between the second and third tangents following a similar consistent graphical approach (Figures 4.1 and 4.3). The desaturation-rate and its slope are significantly decreasing in magnitude at this stage (Figure 4.3), meaning even greater suction values are now required to extract the remaining moisture existing mainly in the intra-aggregate space.

4.4.5. Stage-5-d (residual-suction to dry conditions)

The last drying stage ranges between the residual-suction value and completely dry conditions. It corresponds to the same previous tightly adsorbed regime controlled by the hydrated water via exchangeable cations (Lu & Khorshidi, 2015). Beyond the residual-suction, water can be chemically bonded to the soil (stage 5, Figure 4.4), entrapped in intra-particle space, or in vapour phase form hanging in the pore-air medium. The water movement is in the form of film flow controlled by diffusive fluxes, and often requires oven-drying to be extracted (Rossi & Nimmo, 1994).

4.5. Saturating (wetting) stages and the corresponding transition points

For a soil following the main wetting path, i.e., being wetted from the residual dry conditions, its behaviour, alike the main desaturating (drying) path, can be divided into separate ‘saturation stages’ with distinctive features. No distinguishable hysteresis was noticed for the SSCs of the in-house studied soils (e.g., Agròpolis and the North Campus soils). Similar behaviour has been previously reported in the literature (Lu & Dong, 2017).

The non-hysteretic volumetric behaviour signifies that the change of void ratio with respect to changes in water content is irrespective of the path the soil is following, whether be it drying or wetting. Therefore, the wetting SSC stages can follow a similar pattern to those of the drying SSC Stages:

- i. *zero swelling*: the absorbed water does not cause any increase in the void ratio.
- ii. *residual swelling*: the void ratio increases as the specimen continues to absorb more water; however, the volume of absorbed water is greater than the increase in soil bulk volume.
- iii. *proportional swelling*: the volume of absorbed water is equal to the increase in soil bulk volume.

In the same manner, the wetting SVCs are classified into two separate phases: (i) elastic and (ii) plastic deformations.

The wetting path SWRCs, similarly to the drying path SWRCs, can be classified into different zones:

- i. *residual wetting zone*: from the dry conditions, with significant decrease in suction for small increases in water content.
- ii. *saturation zone*: where the decrease in suction is almost linear with respect to the increase in water content.
- iii. *constant saturation zone*: where the soil becomes saturated, and suction diminishes.

To improve the distinction process between the different wetting stages, the saturating rate and its slope are obtained, using a similar procedure as that of the drying path.

Figure 4.5 shows the saturation-rate and the saturation-rate-slope curves evolution corresponding to the same previously presented SWRC (Figure 4.3). For graphical clarity, only model- vG (equations 4.5-4.6) results are demonstrated. The drying path is also demonstrated but to a lower opacity in order to highlight mainly on the wetting path (see Figure 4.3 for the drying path).

Four main saturation phases are proposed, and the 'SWRC wetting-IP' is associated with the swelling limit (SW). In the case of non-hysteretic SSCs, the swelling limit can be considered equal to the 'shrinkage limit' (SL). However, to avoid confusion in the nomenclature and to distinguish between the paths, the swelling limit will be referred to differently than the established drying path shrinkage limit.

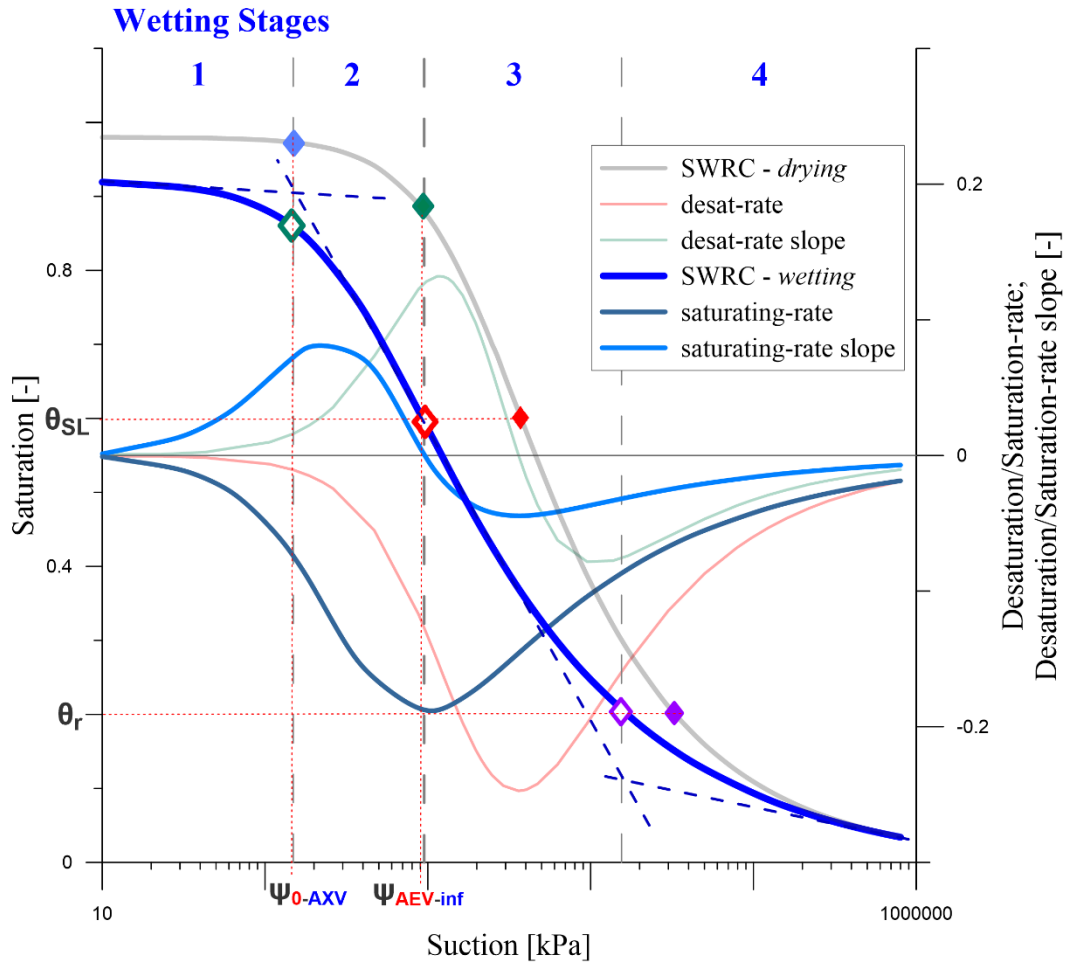


Figure 4-5. Wetting SWRC with corresponding saturation-rate, saturation-rate slope, the five wetting phases and the four transition-points from Figure 4.2.

The four wetting stages and corresponding transitional points are identified below:

4.5.1. Stage-1-w (dry conditions to WEV)

Stage-1 wetting is the initial wetting stage from dry conditions. Existing water is chemically bonded to the soil, entrapped in the intra-particle space, or exists in its vapour phase form. Any slight amount of water that gets introduced into the soil matrix will cause a rapid and exponential decrease in suction.

The first wetting stage extends until reaching the Water Entry Value (WEV). WEV is the capillary pressure value at which the water (i.e., the wetting fluid) starts to displace the air (i.e., nonwetting fluid), and to initially saturate the porous soil medium (Wang et al., 2000). WEV can be obtained using a consistent graphical approach as the intersection point between the two tangents drawn to the residual-wetting zone and the saturating zone.

4.5.2. Stage-2-w (WEV to wetting-IP)

Stage-2 wetting corresponds to the water infiltration stage where suction decreases below the WEV. Beyond this value, the saturation degree starts to increase from residual value while the void ratio remains at the residual value. On the soil swelling curve, i.e., the SSC in wetting path, this stage extends between the residual void ratio and the swelling limit.

Any increment of water during Stage-2 is being absorbed by the intra-aggregate space domain and distributes in the form of a thin film surrounding the tightly adsorbed particles. Water starts to condensate inside the pores and thus replacing the air in the inter-aggregate space. The water film surrounding the soil particles expands and water bridges are formed connecting the soil particles. The system of connected water bridges causes the advective fluxes to dominate the unsaturated flow mechanism in the porous medium, and the liquid phase relative permeability to increase.

By the end of Stage-2-w, the water menisci film is almost continuous throughout the soil matrix. This leads to an increase in the degree of liquid saturation, and a decrease in the interparticle stresses holding the finer particles together.

Stage-2 extends until the inflexion point of the SWRC in the wetting path (wetting-IP). The wetting-IP indicates the maximum saturation-rate magnitude and zero saturation-rate slope (see Figure 4.5). It can be estimated mathematically from the curve of the saturation-rate (Figure 4.5) as the point of change in curvature from upwardly concave (positive 2nd order derivative) to opposite concavity (negative 2nd order derivative).

The saturation-rate increases significantly until reaching its maximum attainable magnitude towards the end of Stage-2. The higher saturation-rate reflects the effect of the recently formed continuous water film in the soil matrix, which leads to an increase in advective fluxes (as discussed earlier).

4.5.3. Stage-3-w (wetting-IP to air expulsion value)

In the third stage, as suction continues decreasing below the wet-IP ($\psi_{inf,W}$), the water starts invading the inter-aggregate pores and further strengthens the water bridges between the soil particles. The water creates forces in the microstructure that pushes the soil particles and aggregates apart, leading to an increase in the void ratio. However, the increase in void ratio is not yet proportional to the added volume of water. This is because the soil matrix at this stage is not yet fully saturated. Therefore, the water has not yet replaced all the air in the voids.

On the SSC, this stage is identified as the curvilinear part. On the SVC, the wetting-IP can be considered as the plastic yielding point. Any further decrease in suction below the $\psi_{inf,W}$ value is associated with a higher degree of change in the void ratio.

This stage extends until reaching the Air Expulsion Value (AXV). The AXV, can be identified on the SSC as the transition point for proportional swelling part, similarly to the AEV in the drying path. On the SWRC, this point can be obtained graphically as the intersection between the two tangents passing through the saturating and constant saturation zones (Figure 4.5).

The AXV indicates the suction value below which the degree of saturation is relatively constant. Water menisci at the AXV are engulfing the soil particles and only some residual suction remains.

4.5.4. Stage-4-w (AXV to constant saturation)

The fourth and last wetting stage extends below the AXV, reaching constant degree of saturation rates. As more water is absorbed into the soil matrix, the void ratio continues to increase, at the same rate. However, at this final wetting stage, any increase in the volume of water content is equal to the increase in the bulk volume of the soil (proportional swelling). At this stage, the soil matrix reaches the maximum degree of saturation irrespective of any further added water. The soil particles are in a pendular state.

Suction continues to decrease due to the presence of occluded air bubbles (Khosravi et al., 2018), and the osmotic component. The latter, belonging to the effect of salts in the soil, is activated and becomes more mobile as the soil matrix becomes more hydraulically conductive. Air pockets decrease in volume as the porewater pressure increases (i.e., suction decreases), and accessible entrapped air is expelled. Further wetting beyond the constant saturation can eventually lead to collapse in the soil structure.

4.5. Inflexion-points of the SWRC

The association of SWRCs and SSCs or SVCs has been previously studied, yet focusing mainly on the correlation of AEV, the saturation-suction, and other curve fitting parameters (Fredlund & Houston, 2013; Wijaya et al., 2015). Nonetheless, to our full knowledge up until the day of publishing the results in this thesis, the correlation between the shrinkage and swelling limits, and the Inflexion Points of the SWRC has not been established, widely observed, or validated yet. This correlation offers insights on the soil matrix and microstructure behaviour, and provides a valuable calibration point as a limit for the effect of suction on volumetric changes.

The shrinkage or swelling limit transitional point can be estimated from experimental SSCs using a consistent graphical approach to determine the point beyond which the soil does not exhibit any significant loss in void ratio for the drying path, or the point beyond which the soil enters in the residual swelling part for the wetting path. The suction value at which it occurs (ψ_{0SL-SW}) can be obtained from the SVC, by simple graphical projection for the drying and wetting paths (Figure 4.1 and Figure 4.2, respectively), or using simple data extrapolation.

4.5.1. Locating the ‘inflexion-point’ analytically

Graphically locating the inflexion point requires a well-defined SWRC with enough data ranging between the AEV and the residual-suction points (for the drying path), or between the AXV and the WEV (for the wetting path). The well-defined set of data in this range is necessary to pinpoint the curve position where the concavity changes. Finding the curve position where the concavity changes, involves finding the maximum magnitude of SWRC desaturation-rate (Figure 4.3) for the drying path, and similarly the maximum magnitude of SWRC saturation-rate (Figure 4.5) for the wetting path.

Mathematically, the value of suction at this inflexion point (ψ_{IP}) is the root solution of the second-order derivative of the model equation used to fit the experimental SWRC data. Each of the drying and wetting path SWRCs can be fitted separately. Using the model-*FX*, rearranging equation 4.4 leads to the root solution (Zhai & Rahardjo, 2012):

$$1 - \frac{(\psi_{IP}/\alpha_{FX})^{n_{FX}}}{e + (\psi_{IP}/\alpha_{FX})^{n_{FX}}} - \frac{(m_{FX} + 1) \cdot (\psi_{IP}/\alpha_{FX})^{n_{FX}}}{\ln[e + (\psi_{IP}/\alpha_{FX})^{n_{FX}}] \cdot [e + (\psi_{IP}/\alpha_{FX})^{n_{FX}}]} = 0 \quad (4.7)$$

While using the model-*vG*, the equation transforms to:

$$\psi_{IP,vG} = \frac{\left(\frac{1}{m_{vG}}\right)^{\frac{1}{n_{vG}}}}{\alpha_{vG}} \quad (4.8)$$

The model-*vG* root solution can be determined as a function of the used fitting parameters directly, while the model-*FX* is solved using an iterative approach to find the equation roots. To calculate the water content at the inflexion point, the SWRC function (equation 4.1 or 4.2) is simply solved for the obtained suction value at the inflexion point ψ_{IP} from either Equation 4.7 or 4.8 (for model-*FX* and model-*vG*, respectively).

4.5.2. Validation

The validity of considering the inflexion point as an indicator of the shrinkage limit was first tested for the Agròpolis soil. Figure 4.6 presents the SWRCs with the SVCs of the Agropolis silty clay for four different initial placement conditions. The aim of presenting the different initial conditions was to investigate the effect of initial sample preparation and consistency on the obtained ψ_{SL} and ψ_{IP} . The SWRC fitting is shown, using model-vG, with Equation 4.8 to calculate ψ_{IP} . The water content at the inflexion point can be calculated using either of the fitting models (equations 4.7 and 4.8) for the obtained ψ_{IP} value.

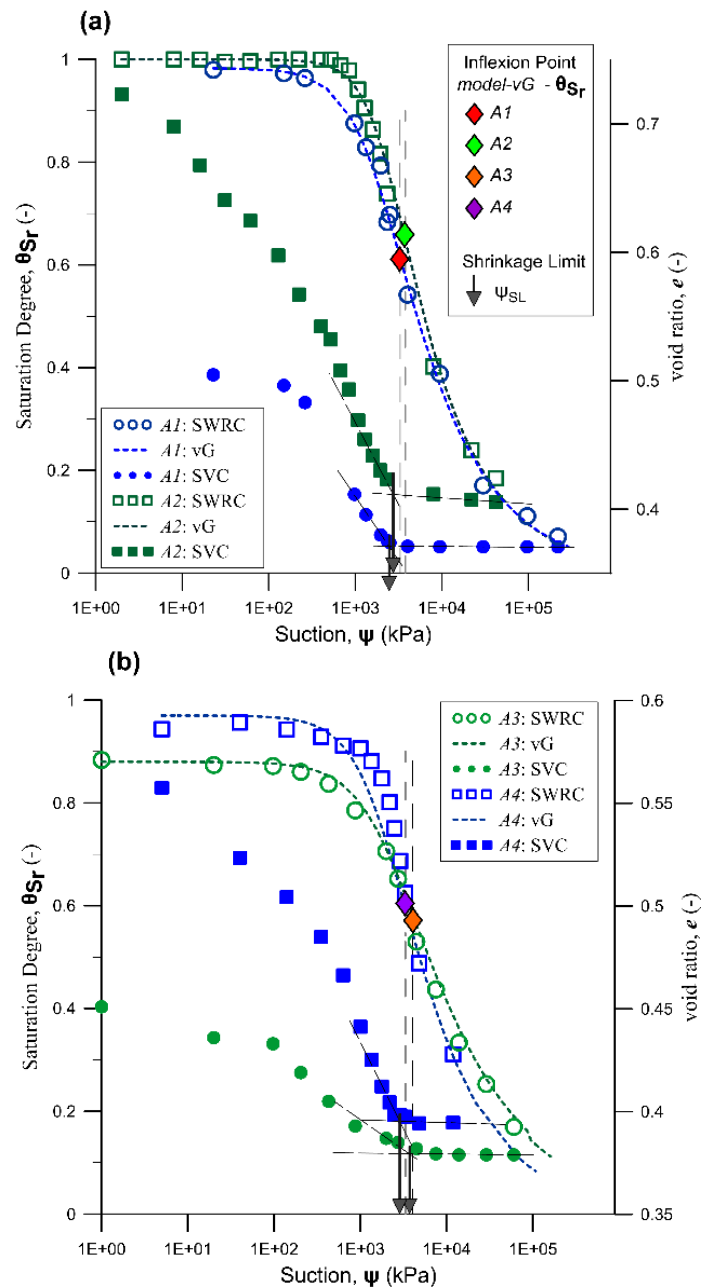


Figure 4-6. SVCs and SWRCs to the saturation degree scale for the Agròpolis soil [CL], for (a) A1 and A2; and (b) A3 and A4 initial conditions.

The shrinkage limit (ψ_{SL}) is identified as the point beyond which the soil does not exhibit any significant loss in void ratio upon any further increase in suction. ψ_{SL} can be obtained using a consistent graphical approach from the extrapolated SVCs which were based on experimental SSCs (dark downward arrows on Figure 4.6).

The initial preparation conditions did not seem to affect the inflexion point significantly. All the Agròpolis soil SWRCs seem to largely merge beyond the AEV, with ψ_{IP} in the range 3300-4100 kPa. This confirms the fact that the inflexion point is related to the size of the micro pores, which are not greatly affected by the applied compaction level (Romero et al., 2011). This observation suggests considering the inflexion point as an intrinsic soil parameter value, not majorly affected by the initial compaction level or placement conditions.

In order to validate the general correlation $\psi_{IP} = \psi_{SL}$ in the drying path, a dataset of 32 different soils (adding to the four in-house tested soils, presented in table 4.1) encompassing a wide range of soil types, fabrics, and textures, were acquired from the literature ranging from sandy, silty, clayey to highly plastic soils such as bentonites.

As for the wetting path, 10 supplementary datasets were presented for validation, in addition to 2 of the in-house soils (i.e., Agròpolis and North Campus). Generally, less data was available in the literature for the wetting path. The wetting path is mostly less studied by researchers in the domain, due to the multiple technical difficulties associated with lack of available established experimental techniques.

Different consistencies and initial compaction conditions were also presented, ranging from slurry to remoulded and compacted soil specimens. The assembled data was processed to finally provide complete (θ - e - ψ) sets of information for each presented soil. In many cases, extrapolations had to be made where the (θ - e) and (θ - ψ) data were given separately, in terms of separate SSCs and an SWRCs, respectively.

Figure 4.7a shows the Unified Soil Classification System classifications of the assembled 36 soils used for the validation, with the corresponding reference for each of the 32 literature-based datasets.

Five soils out of the 32 literature-based datasets contained information on both the drying and wetting paths (Fleureau et al., 2002; Lu & Dong, 2017). The experimental SWRCs were fitted with both models (model- vG and model- FX), for each of the three different water content scales (θ : $\theta_w, \theta_V, \theta_{Sr}$). In other words, for each soil dataset, six different fittings were made.

4. The role of Inflexion-Point of the SWRC in the Shrinkage and Swelling Mechanism of Partially Saturated Soils

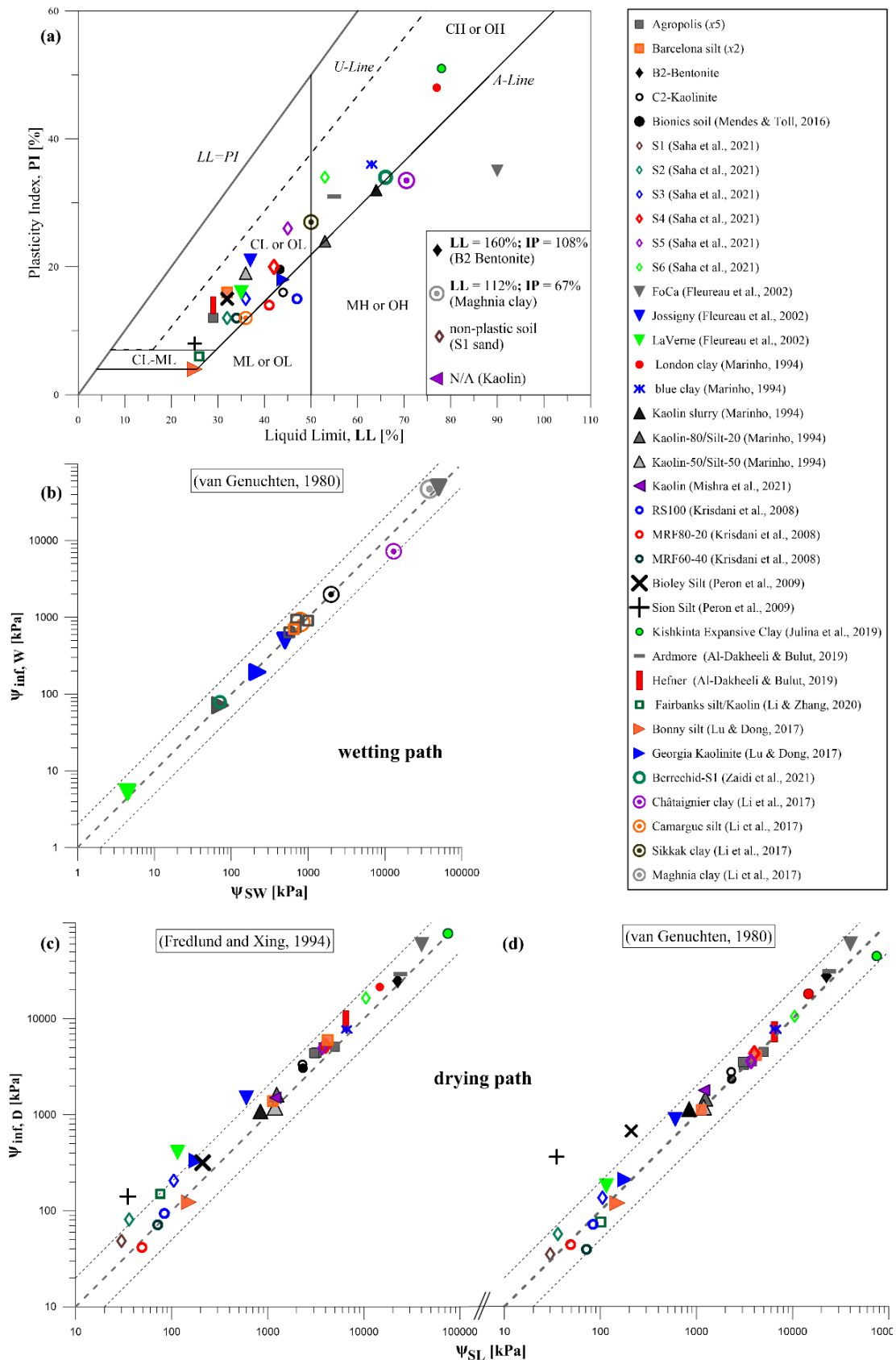


Figure 4-7. (a) The USCS classification of the different soils used for the model validation. (b) Validation of the inflexion point of the wetting path based on the θ_{S_r} -SWRC fitting parameters using model-vG; and of the drying paths using (c) model-FX and (d) model-vG. S1 (Saha et al., 2021); B2-Bentonite; and Kaolin (Mishra et al., 2021) are not included in the USCS chart: non-plastic soil; PI=108% and LL=160% therefore out of representable scale; and information not provided, respectively.

The ψ_{IP} was then calculated using equations 4.7 and 4.8, based on the fitting parameters obtained for θ_w -SWRC, θ_v -SWRC and θ_{s_r} -SWRC.

The drying path results based on the θ_{s_r} -SWRC fitting parameters against the shrinkage limit are shown separately for model-FX (Figure 4.7c) and model- νG (Figure 4.7d). The wetting path results, comparing ψ_{inf} to the suction value at swelling limit (ψ_{SW}), were shown for the model- νG fitting only, due to space constraint, since both models returned comparable fitting results.

A logarithmic instead of linear scale is used to accommodate the wide range of suction values involved (35-61000 kPa), and for a better visualisation of the $\psi_{IP}:\psi_{SL}$ or $\psi_{IP}:\psi_{SW}$ relation. A 1:1 line indicates $\psi_{IP,D} = \psi_{SL}$ for drying and $\psi_{IP,W} = \psi_{SW}$ for wetting, while points lying above the 1:1 line indicate $\psi_{IP,D} > \psi_{SL}$ for drying, or $\psi_{IP,W} > \psi_{SW}$ for wetting.

Figure 4.7 shows that for most soils, the $\psi_{IP,D}:\psi_{SL}$ or $\psi_{IP,W}:\psi_{SW}$ predominantly lies within the 2:1 ratio, indicating a consistently close ψ_{SL} and ψ_{SW} estimate using the θ_{s_r} -SWRC fitting functions methods. For soils rich in finer materials, such as expansive clays and bentonites, the shrinkage-limit occurs at higher suction values as mentioned earlier, agreeing with the higher ψ_{inf} values obtained for such soils.

The computation is highly dependent on the method followed to obtain the fitting parameters for model- νG and model-FX. Any misfit that does not reflect the physical retention properties would lead to wrong estimations of the actual inflexion point value.

The computed inflexion points still project within the residual shrinkage (drying Stage-3), even for the cases where the exact suction at shrinkage limit is not precisely captured. This finding demonstrates the validity of considering the inflexion point of the SWRC as a transitional point for hydromechanical behaviour and indicates a strong coupling that permits the interpretation of the mechanical behaviour component from the SWRC.

4.5.3. Fitting divergence

The fitting divergence is studied over the drying path only for the abundance in data found in the literature. As expected, fitting parameters based on the θ_{s_r} -SWRC returned a better $\psi_{IP}:\psi_{SL}$ prediction, favouring the expression of SWRCs on saturation-degree scale in general. The fit divergence in results between the computed ψ_{IP} and the graphically obtained ψ_{0SL} can be simply evaluated as $Divergence = \psi_{IP}/\psi_{SL}$; where a value of 1 signifies a perfect agreement between both values. The divergence can be attributed to various factors, originating from the

experimental measurements of suction or void ratio, and the SWRC fitting method. A non-representative SWRC fit (on either of the θ scales) can lead to mis-localisation of the inflexion point. Additionally, locating the shrinkage-limit can prove complex in cases where insufficient experimental measurements are provided in the proximity of that value.

The effect of the moisture-content scales used is addressed on the semilogarithmic SWRC fits, as one way to explain the divergence that can be encountered due to non-representative SWRC fits. Figure 4.8 shows the computed fit-divergence based on the different moisture-content scales (for both model- vG and model- FX), plotted against the total shrinkage proportion. The total shrinkage proportion experienced in each soil is calculated as:

$$\text{Total shrinkage} = \frac{e_i - e_0}{e_0} (\%) \quad (4.9)$$

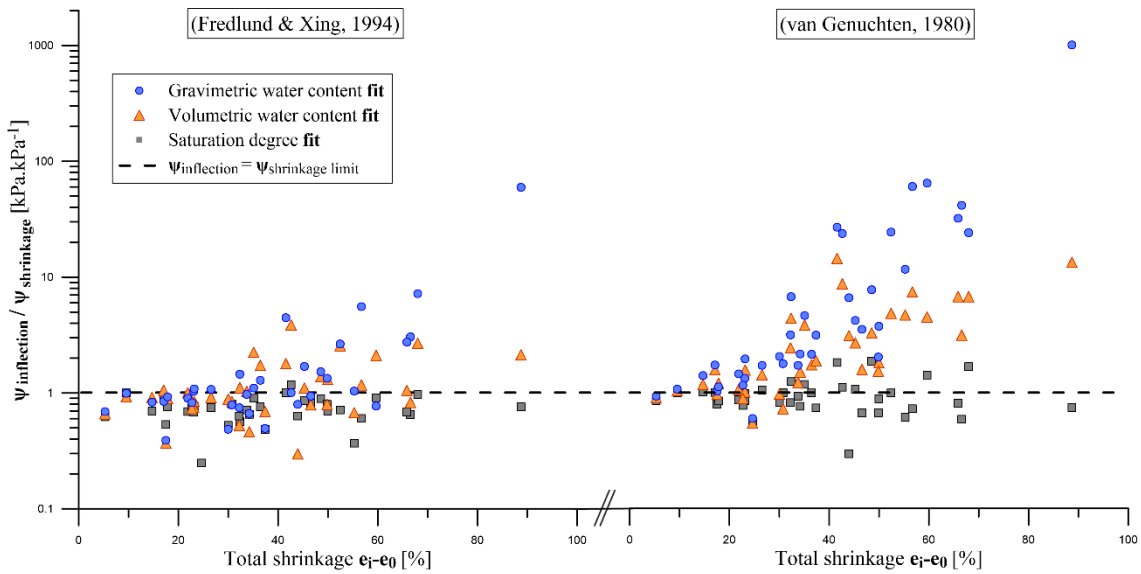


Figure 4-8. Fit-divergence for the different moisture-content scales for (a) model- FX ; and (b) model- vG .

The divergence increases exponentially for soils exhibiting higher shrinkage, especially for the θ_w -SWRC followed by the θ_v -SWRC for model- vG . The divergence result agrees with the findings of other researchers stating the significance of considering changes in void ratio (by incorporating the SSC for obtaining the SWRC), especially for soils that exhibit high shrinkage (Fredlund & Houston, 2013). The results also demonstrate the variations in obtaining the inflexion point based on the fitting water content scale or fitting function used.

4.6. Constitutive relations

Many researchers in the unsaturated soil mechanics field have dedicated to study the volumetric behaviour part. Jennings and Burland (1962) have demonstrated that the problem cannot be addressed using a single effective stress, but must combine the net stress ($p_{net} = p - P_g$) and suction ($\psi = P_g - P_l$), where p is the total stress, P_g is the gas pressure and P_l is the liquid pressure. One of the first and most commonly used constitutive model developed in the framework of independent stress state variables (suction and net stress) is that of Alonso et al. (1990). The proposed approach was adopted by many researchers in the field and was further developed and modified (e.g., Wheeler & Sivakumar, 1995; Sivakumar & Wheeler, 2000; Vaunat et al., 2000; Gallipoli et al., 2003; Wheeler et al., 2003; Sheng et al., 2008; Musso et al., 2019; amongst many).

A main common constituent of the developed models is the consideration of two independent stress state variables (i.e., net stress, and matric suction). A combined effective stress-suction uses both the average skeleton stress (Jommi, 2000) and suction for modelling the volumetric behaviour. The average skeleton stress (i.e., effective stress) can be presented as suggested by Bishop (Bishop, 1959), by modifying the Terzaghi's classical effective stress theory:

$$p' = p_{net} + \chi \cdot \psi \quad (4.9)$$

Where the Bishop parameter χ is considered dependent on the liquid degree of saturation.

In the proposed critical state framework, the volumetric changes in the elastic domain (Δv^e) are governed by two elastic swelling indices: (a) κ , for the effect of change in mean net stress; and (b) κ_s , for the effect of change in suction on the volumetric change (Alonso et al., 1990).

$$\Delta v^e = -\kappa_s \ln \left(\frac{\psi + P_{atm}}{P_{atm}} \right) - \kappa \ln \left(\frac{p_{net}}{p_{ref}} \right) \quad (4.10)$$

Where v is the specific volume ($v = 1 + e$), p_{ref} is a reference pressure, and P_{atm} (=101.3 kPa) is the atmospheric pressure. The reference and atmospheric pressures are included as a reference to make the expression dimensionally consistent and to ensure the specific volume at the given suction $v(\psi)$ or net stress $v(p_{net})$ is referring to a value of effective stress within the experimental data range (Wheeler & Sivakumar, 1995).

Beyond yielding from elastic to plastic behaviour, the isotropic virgin compression line, representing soil states when isotropically loaded to virgin conditions, describes a locus of states defined by the following form:

$$v = v(0) - \lambda \ln p' \quad (4.11)$$

Where $v(0)$ is the specific volume at $\ln p'=0$, and λ is the slope of the $v - \ln p'$ line. Therefore, the plastic volumetric changes (Δv^p) can be calculated following a similar approach by replacing the elastic swelling indices with the slope of the virgin compression line.

For the unconfined soils being studied in this thesis, the emphasis was on the suction effects on the volumetric changes rather than the effect of external applied stresses. The typical elasto-plastic framework can be given in the following form:

$$\begin{aligned} \frac{\Delta e^e}{1+e} &= -\kappa_s \ln \left(\frac{\psi + P_{atm}}{P_{atm}} \right) && \text{for } \psi < \psi_0 \\ \frac{\Delta e^p}{1+e} &= -\lambda_s \ln \left(\frac{\psi + P_{atm}}{P_{atm}} \right) && \text{for } \psi > \psi_0 \end{aligned} \quad (4.12)$$

The presented elasto-plastic framework in equation 4.12 has been mainly based on suction-controlled triaxial or odometer tests, where suction was imposed using pressure difference techniques. The imposed suction values using these techniques does not normally lead the soil to the residual dry conditions. The model, in its presented form (equation 4.12), suggests an unremitting decrease in void ratio as the suction continues developing. However, the experimental findings suggest that soils in general have a shrinkage limit, beyond which the skeleton is considered to become rigid and less affected by further increases in suction and decreases in moisture content.

Figure 4.9 shows a general relation between suction and void ratio for a compacted silty clay following a drying path (Agròpolis soil, sample A-S1). The estimation of κ_s is carried out from the slope of the elastic region, that is until reaching the saturation-suction ψ_0 . The estimation of λ_s is normally carried out from the slope of the plastic region. Commonly assumed in the literature, the plastic region extends from the yielding point (saturation-suction) until the dry conditions. This assumption leads to a misrepresentation of the soil shrinkage behaviour by overlooking the shrinkage limit and the rigid skeleton region, and finally to the underestimation of the plastic region slope. Instead, λ_s must be calculated from the slope of the limited plastic region extending between the saturation-suction and the shrinkage limit (i.e., the inflexion point; see Figure 4.9).

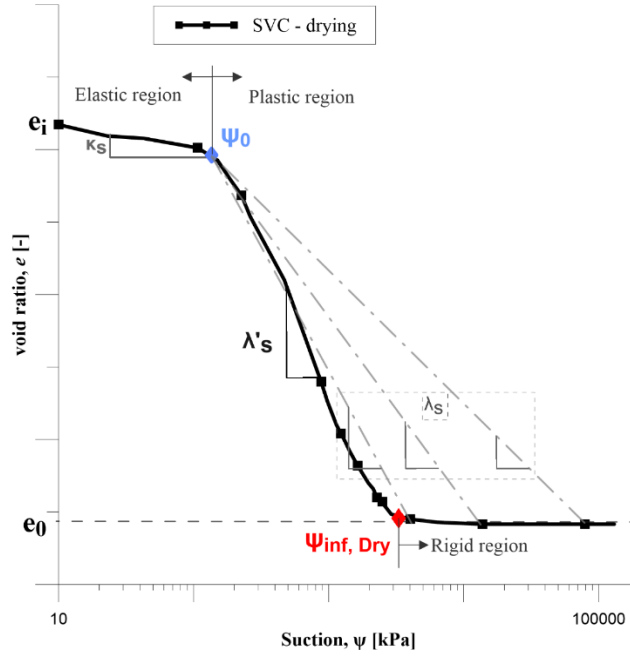


Figure 4-9. The drying SVC with the projection of the inflexion point.

The plastic region is then amended, and the following modification is proposed (equation 4.13), using the value of λ'_s as a substitute for λ_s .

$$\begin{aligned} \frac{\Delta e^e}{1+e} &= -\kappa_s \ln\left(\frac{\psi + P_{atm}}{P_{atm}}\right) && \text{for } \psi < \psi_0 \\ \frac{\Delta e^p}{1+e} &= -\lambda'_s \ln\left(\frac{\psi + P_{atm}}{P_{atm}}\right) && \text{for } \psi_0 < \psi < \psi_{inf,D} \\ \Delta e &\cong 0 && \text{for } \psi > \psi_{inf,D} \end{aligned} \quad (4.13)$$

The proposed modification suggests that no more shrinkage occurs beyond the suction value of the inflexion point of the drying path SWRC. While this might apply to a wide variety of sandy and silty soils, it needs to be further amended for clayey soils with relatively high content of finer materials. The finer materials tend to continue shrinking beyond the suction value of the inflexion point of the SWRC. Beyond the inflexion point, the conglomeration of the finer materials occurs at the micro-level in the intraparticle domain. The amount of bulk change in soil particles configuration at intraparticle domain is relatively low with respect to that at the interaggregate space domain. Soils rich in finer materials consist of a higher percentage of micropore space. Therefore, the shrinkage at this stage is more perceivable for mainly clayey soils and bentonites rich in finer materials (see section 4.4.4). The calculation of the rate of change in void ratio at this stage can vary between one soil or another, depending on the

percentage of finer materials. However, further investigation into this topic was outside the scope of the work in this chapter, and the topic is to be placed under further study in the future.

In general, the numerical simulators used to model the THM behaviour of soils include elements of coupling. In this sense, the simulators solve for the related thermal, hydraulic, and mechanical constitutive equations. The constitutive equations for unsaturated soils typically include a water retention curve to describe the relationship between the liquid degree of saturation and the liquid pressure.

A model for the SWRC is implemented into the numerical simulator. Therefore, the inflexion point of the implemented SWRC can be obtained by finding the roots of the second order derivative (see section 4.5.1). The solution for the roots of the second order derivative can be expressed in terms of the fitting parameters of the implemented SWRC. The root is obtained depending on the SWRC model used (model- νG and model- FX ; equations 4.7 and 4.8, respectively). However, the root of the model- νG can be obtained directly in terms of the fitting parameters used, while the root of the model- FX requires solving by iterations. The root of the model- νG can be directly calculated and implemented in the mechanical model through the numerical simulator.

The mechanical model can be then forced to converge to the most recent value of computed void ratio and restrain all displacements in the numerical mesh elements where the suction value has surpassed the calculated inflexion point value. The proposed numerical model is a work in progress and currently under development to be implemented in a finite-element numerical simulator.

4.7. Phenomenon of hysteresis

The change in void ratio is mainly controlled by the changes in the intraparticle domain at the macrostructure level, that is the space between the aggregates of soil particles or larger soil particles. The SSC is governed mainly by the changes in the interparticle domain. The non-hysteretic SSC performance suggests that the hysteresis in general originates from the behaviour of the finer materials. Nevertheless, the complex nature of the liquid-phase configuration in an unsaturated porous medium lead to the nonunique relationship between suction and water content.

The SWRC curve is hysteretic, which means the water content at a given soil suction for the wetting path is less than that of drying path. Interpretations and reasons for the apparent

hysteresis behaviour of unsaturated soils can be mainly attributed to the microstructure behaviour at the intraparticle domain (Klausner, 1991; Fredlund, 2011):

- irregularities in the cross-sections of the void passages or the “ink bottle” effect (Hillel, 1980).
- Pore-Size Distribution (PSD) is not identical for wetting and drying paths.
- contact angle of meniscus is different for the wetting and drying process, i.e., it is greater in an advancing meniscus than in a receding meniscus.
- entrapped air bubbles or vacuum condition during wetting causes a reduction in water content at the maximum saturation.
- thixotropic regain or aging due to wetting and drying history of the soil (Hillel & Mottes, 1996).

The drying and wetting paths of the SWRC have shown a similarity in the trend and pattern (e.g., Figure 4.5). Additionally, different transitional points between the drying and wetting paths can overlap at the same suction or saturation values. The overlapping suggests a strong correlation in terms of physical behaviour of the soil particles and the porewater. On the other hand, the difference in other values between the paths can further explain the physical phenomenon of hysteresis. Some transitional points might occur at the same suction value but different water contents: the saturation-suction in the drying path occurs at the same suction value as the AXV in the wetting path. In a similar manner, some transitional points occur at the same water content but different suction values: residual suction in the drying path, and the WEV in the wetting path.

In this section, a conceptual explanation is given of the physical phenomenon of the overlapping transitional points at opposite paths (i.e., drying, or wetting paths). An established correlation is missing from the literature and has the potential of providing a model capable of deriving the SWRC wetting path using the drying path only.

4.7.1. Saturation-suction and AXV

A strong correlation is noticed between the “drying path”-saturation-suction and the “wetting path”-AXV, where both seem to overlap at the same suction value. This correlation was noticed for the main drying-wetting cycles performed on the in-house soils (i.e., for Agròpolis and North Campus), and on main drying-wetting path sets from the literature (Fleureau et al., 2002; Lu & Dong, 2017). Both the “wetting path”-AXV and “drying path”-saturation-suction represent the maximum suction value below which the degree of saturation becomes constant. In a sense, the state of the soil is similar, regardless of the SWRC path taken (drying or wetting).

In a conceptual manner, the water menisci at both transitional points (saturation-suction and AXV) are covering the soil particles and only some residual suction remains pertaining mainly to the osmotic component. Although both transition-points coincide at the same suction value, the hysteresis in the SWRC indicates a different water content for each.

The difference in the water at saturation-suction and AXV can be largely attributed to the inaccessible entrapped air or occluded air bubbles (Khosravi et al., 2018), that could not be replaced by the water, due to a pore blockage effect (Topp, 1971). The air entrapment usually occurs after following the main drying path starting from maximum saturation values, and the main wetting path starting from residual dry conditions. This volume of entrapped air is typically expected to be eliminated for further cycles of drying and wetting paths (Pham, 2001).

4.7.2. The inflexion points

The Inflexion point of the SWRC in the main drying path coincides at the same water content as that of the inflexion point of the SWRC in the wetting path. This is contingent with the non-hysteretic behaviour in the SSC regardless of the path taken, where both the shrinkage limit and the swelling limit occur at the same moisture content. The drying and wetting cycles typically do not affect the particle size distribution of the soil, regardless of the hysteretic behaviour. Therefore, in such cases where the particle size distribution is not altered by the drying and wetting cycles, the desaturation and saturation rates at the inflexion points can be assumed to be equal. However, this assumption is limited in practice and can only be applied to soils whose structure or fabrics do not alter upon being exposed to various cycles.

4.7.3. The AEV and the wetting path inflexion point

The suction value at the AEV is equivalent to the height of passive capillary rise and the breakthrough value of the air into the continuous meniscus film formed by water surface tension in the largest pores. From a pore-size perspective, this value indicates at which suction the air permeates into the largest water-filled soil pores (Fredlund & Xing, 1994).

In the wetting path, the added water is absorbed by the intra-aggregate space domain and distributes in the form of a thin film surrounding the tightly adsorbed particles. As more water condensates inside the pores, it replaces the air in the inter-aggregate space and creates a water film surrounding the particles. With further increase in the porewater content, more water bridges are formed connecting the soils particles. The connected water bridges reduce the interparticle stresses holding the aggregates together in a tight form. Upon reaching the inflexion point of the wetting path SWRC, the swelling begins taking place (swelling limit).

Beyond that, any increase in water content will result in an unproportional (i.e., lower) increase in the bulk volume. Therefore, the value of suction at the swelling limit indicates at which suction the air starts leaving from the largest pore. The diameter of that pore where air starts leaving the system is equal to that of the largest pore diameter where the air permeates. Therefore, the AEV and the wetting-IP are expected to occur at close suction value.

4.7.4. The residual suction and the WEV

At the residual suction, the remaining moisture exists mainly in the intra-aggregate space, chemically bonded to the soil, entrapped in intra-particle space, or in vapour phase form hanging in the pore-air medium. The WEV on the other hand represents the capillary pressure at which the water starts replacing the pore-air and initially saturate the soil matrix (Wang et al., 2000). Therefore, both values correspond to the level of moisture content in the soil matrix beyond which a rapid decrease in suction occurs and the advective fluxes govern the porewater flow.

4.7.5. The AEV and the AXV

The water content at AEV (θ_{AEV}) indicates the transitional point between the proportional and residual shrinkage stages. On the other hand, the water content at AXV (θ_{AXV}) indicates the limit between the consecutive residual and proportional swelling stages. The non-hysteretic behaviour of the SSC suggests that the AEV and the AXV occur at the same porewater content ($\theta_{AEV} = \theta_{AXV}$). However, AEV and AXV occur at different suction values due to the hysteresis in the water retention mechanism.

4.8. Implications on geotechnical design

Correlating the shrinkage limit of a soil to the inflexion point of its SWRC proved its validity, at the conceptual and analytical level, for various soil types, fabrics, and textures. Such an established correlation could lead to direct and indirect implications in the geotechnical field, which can be summarised in the following points.

4.8.1. Applicability to different initial conditions

Macropores are more susceptible to collapse under external stresses, while micropores, which affect the estimation of ψ_{IP} (and consequently ψ_{SL}), are more stable and less likely to be affected by compaction. Therefore, by analysing the SWRC of a soil at certain initial conditions, distinctive features of the mechanical behaviour in response to changes in moisture content, that

is the shrinkage limit, can be predicted for the same soil at different initial placement conditions. Nonetheless, this observation cannot be generalised to all conditions where the soil is reconstituted, and its fabric is completely altered, and requires further validation.

4.8.2. Estimate of the shrinkage potential

Soils with higher shrinkage limit poses a higher shrinkage potential, volumetric strain potential, and therefore a higher potential for settlement and cracking. By knowing ψ_{SL} through ψ_{IP} (via an established SWRC), engineers can determine whether the soil being considered for their design would reach the estimated shrinkage limit. The estimation process entails predicting the suction levels in the concerned area of study, through anticipated weather conditions or groundwater levels for the considered design periods.

4.8.3. Estimate of ψ_{IP} through ψ_{SL}

The shrinkage limit can be obtained separately and indirectly through the analysis of some independent laboratory testing, such as Mercury Intrusion Porosimetry, oedometers, or unconfined shrinkage tests; or through field testing, such as the California Bearing Ratio (CBR) test and the Plate Load Test (PLT). These tests could provide information on the maximum dry density, optimum moisture content, and elasticity modulus of a soil, which can be used to estimate the shrinkage limit. The inflexion point of the SWRC, a significant point that can be used in the SWRC fitting models, can be obtained once the independently determined moisture content and suction at the shrinkage limit have been established. In addition, the slope at the inflexion point can be estimated independently using the particle-size distribution (Brooks & Corey, 1964), water retention capacity (Kosugi, 1994), or the plasticity index (Fredlund & Xing, 1994), providing a potential to capture the full SWRC behaviour in the desaturation stages.

4.9. Conclusion

An SWRC containing the three variables ($\theta - e - \psi$) can be represented in a 3D schematic to better understand the strong coupling in the hydromechanical behaviour during desaturating shrinkage. The distinctive 3D line in space can be projected on either of the planes: ($\theta - e$), ($\theta - \psi$), or ($e - \psi$) to obtain the SSC, SWRC and SVC, respectively. The SWRC desaturation-rate is computed from the first-degree derivative of the used SWRC fitting function. The desaturation-shrinkage process can then be divided into five distinctive stages, limited by four intermediate transition-points. These transition-points can be identifiable on either of the SSC, SVC, SWRC and the desaturation-rate curve, demonstrating the existing strong coupling behaviour. A conceptual model of the desaturating deformable soil particles is discussed for the

five stages based on the soil behaviour characteristics classified by the analysis of the coupling of the four mentioned curves.

The identification of the different transition-points is relatively well-established for the cases of saturation-suction, AEV, and residual-suction. Nonetheless, this study proposes a correlation between the well-known shrinkage limit and the inflexion point of the SWRC, which provided an insight on the principal mechanisms governing the unsaturated shrinkage process. An analytical and conceptual analysis explained the moisture and shrinkage states at the macro- and micro-porosity level in the intra- and inter-particle domain, as the soil matrix suction approaches the inflexion-point value. The correlation validity was tested for a selection of 36 different soils (4 in-house, 32 literature-based), covering a wide range of soil types, fabrics, and textures.

Knowing the suction and water content at the drying path SWRC inflexion point can be of great interest for understanding the soil matrix behaviour at the microstructure level, and for mechanical constitutive models dealing with unsaturated soils. Identifying the inflexion point provides a valuable calibration point for mechanical models by determining the shrinkage limit properties from the corresponding SWRC of the material being studied.

On the other hand, four consecutive wetting stages are identified with distinctive features of soil behaviour for each. The corresponding transition-points limiting between two consecutive wetting stages are identified: Water Entry Value (WEV), wetting path inflexion point (wetting-IP), and the Air Expulsion Value (AXV).

The hysteretic phenomenon is studied and a conceptual explanation of the physical behaviour of the unsaturated soil matrix during both main paths is given. Different correlations are extracted between the different transition points in the drying and wetting paths, on the suction and water content scales. The correlations are based on physical behaviour of the soil matrix and the drying and wetting mechanisms. Establishing such strong correlations can eventually lead to full estimation of the wetting path SWRC from the drying path SWRC only.

Chapter 5

Numerical Simulation of Soil Desiccation Behaviour

Parts of this chapter have been published in the “Computers and Geotechnics” Journal, with the title:

“THM Analysis of a Soil Drying Test in an Environmental Chamber: The Role of Boundary Conditions”.

on January 2022, with the co-authors:

Agustin Cuadrado, Abdallah Najdi, Alberto Ledesma, Sebastian Olivella, Pere Prat.

5.1. Introduction

The soil-atmosphere interaction leads to soil water evaporation and conditions the drying shrinkage process. Therefore, the atmospheric conditions must be adequately replicated numerically by means of hydraulic fluxes at the boundaries. This practice is still considered difficult in geotechnical analysis due to the level of complexity associated (Blight, 1997; Smits et al., 2012).

Atmospheric condition parameters affecting the soil-atmosphere interaction are associated with the relative humidity, temperature, wind, solar radiation, and precipitation. Fluctuations in any of these parameters affect the heat energy fluxes applied on the soil surface, and the lower atmosphere behaviour in contact with the soil surface. These coupled interactions are affected by the soil conditions as well. The soil porous medium subjected to desiccation conditions undergoes simultaneous Thermo-Hydro-Mechanical (THM) changes. These changes are mutually interconnected. Thermal variations in the medium generate alterations in stress conditions, mass storage, hydraulic conductivity, degree of saturation, water pressure and vapour diffusion and transfer. Conversely, hydraulic variations induce changes in thermal conductivity, and water and gas pressures, which in turn modify the patterns of gas and water flow and eventually the stress conditions in the system. The resultant volumetric strains instigate porosity changes that consecutively affect water and gas pressure distributions due to the coupled storage terms and hydraulic conductivity (Azizi et al., 2019). Additionally, the imposed boundary flux causes vapour exchange at the surface, altering the hydraulic and thermal conditions, and causing mechanical stress changes.

The complex behaviour of the deformable porous medium to the simultaneous THM changes requires an analysis that covers and integrates all the main aspects involved.

In this chapter, the THM coupled formulation of the implemented numerical approach, the boundary and vapour fluxes, and the constitutive model equations used to simulate the soil drying process and the associated THM changes, are all explained in detail. The formulation is then used to present a numerical analysis of an experimental test carried out on a slurry soil specimen undergoing drying in the laboratory environmental chamber with controlled temperature and relative humidity. The environmental chamber has been presented before in the earlier chapters (Chapter 3).

The evaporation caused by the imposed boundary conditions leads to volumetric shrinkage of the soil, and consequently its separation from the containing mould. The shrinkage causes changes in porosity, and implicit changes in the hydraulic and thermal constitutive equations.

Therefore, it is necessary to include the mechanical part in the calculations. The separation of the soil from the mould creates a new soil-atmosphere interaction surface which might affect the evaporation rate (Song et al., 2013), which in turn affect the water distribution along the soil layer (Tollenaar et al., 2017b). The continuous drying of the soil causes the formation of a dry layer near the surface which limits the vapour fluxes and the capacity of the soil to supply water from the centre of the specimen to the evaporation surface (Lehmann et al., 2008; Shahraeeni et al., 2012). This requires the use of diffusion resistance factors to adapt the calculated flows to the measurements (Camillo & Gurney, 1986; Kondo et al., 1990; van de Griend & Owe, 1994).

The aim of the work in this chapter was to identify the constitutive equations that best describe the soil behaviour, numerically identify the imposed boundary conditions with their respective transfer coefficients, and to assess the influence of the newly formed perimeter crack on the ongoing soil desiccation, which happens at a different rate from the surface. Researchers working on numerical analysis of soil desiccation cracking have frequently disregarded the boundary conditions as the main factor (Levatti et al., 2019a; Tran et al., 2019), which has proved to be of great influence experimentally, and difficult to implement in the analysis (Zeng et al., 2020; Cuadrado et al., 2022).

The final numerical model in this work is constructed to simulate the behaviour of a desiccating soil in the laboratory environmental chamber where the relative humidity and temperature are prescribed. After explaining the model and discussing the balance, constitutive and boundary conditions equations, the model is applied to simulate a specific experimental test carried out by Lakshmikantha (2009). The last part, concerning the application on Lakshmikantha's test, has been published in the *Computers and Geotechnics Journal* (Cuadrado et al., 2022). The results are presented briefly in this chapter in three different blocks having different parameter inputs and fits with the experimental results recorded in the laboratory chamber (water content, suction, soil relative humidity).

The final model was then used as a basis for a constitutive parametrical study to calibrate the best-fit parameters for different constitutive equations. The results are also used as a basis for the numerical simulations that follow in the upcoming chapter (Chapter 6), by developing the model and demonstrating the significance of accounting for the mechanical problem, the evaporation from the exposed cracks surfaces, and the environmental conditions as wind, solar radiation, and precipitation.

5.2. Numerical model

Simulations are performed using the finite element software CODE_BRIGHT (Olivella et al., 1994, 1996; Gens & Olivella, 2001). The relative formulations are explained in this section.

5.2.1. CODE_BRIGHT

For the simulations in this work, a numerical finite element model CODE_BRIGHT (COupled DEformation, BRine, Gas, and Heat Transport) was employed. The code formulation was originally constructed to model non-isothermal multiphase flow of brine and gas through porous deformable saline media. The code has clearly shown in previous cases its wide abilities to successfully capture the non-isothermal moisture transport in unsaturated porous media. Its formulation is based on numerous equations developed by several authors in the field of flow in porous medium and unsaturated soil mechanics.

After presenting the bases for further investigations on non-isothermal moisture transport in non-saturated porous media (Philip & De Vries, 1957), the application of equations for moisture and heat transport was expanded to hysteretic and inhomogeneous porous media (Milly, 1982). This was carried out assuming gas pressure is constant in space and time (Bear et al., 1991), implicating no obligation for balance equations to characterise the gas phase. This assumption is adequate when dealing with partially saturated soils and has been extended to overcome this practical simplification (Pollock, 1986; Pruess, 1987). The results have been found to have satisfactory outcomes when solving problems related to partially saturated soils (Bear et al., 1991). As for energy balance, one equation is needed since thermal equilibrium is assumed in the existing phases (Milly, 1982).

The equations of multiphase flow of water, air and nonaqueous compound have been based on multiple liquid phases and a single gaseous phase, where each phase is carrying out multiple species (Abriola & Pinder, 1985; Pinder & Abriola, 1986). The mass fraction for example, of a species i as a component of phase α is denoted as: ω_{α}^i . The superscript i is a species index and can be water (w) or air (a), while the subscript α denotes the phase that can be gaseous (g), liquid (l) or solid (s). The calculations of the hydrothermal systems controlled by liquid and vapour were formed assuming aqueous species are the only species existent in the pores, and by neglecting the effects of capillary pressure (Faust & Mercer, 1979). Therefore, for the species being regarded, the unknown would be a particular value of fluid pressure in the mass balance equation. The multiphase systems were further developed by several authors using the averaging theory (Hassanizadeh & Gray, 1979). The development led to the basic formulations of mass transport in the porous media, originating the macroscopic balance laws, and

generalized Darcy's and Fick's laws (Hassanizadeh, 1986a; b). The mass balance equations are finally determined following the compositional approach (Panday & Corapcioglu, 1989), comprising of balancing the species rather than the phases. The total phase formulation is attained by determining and adding the equation for each of the species included in that phase. Water mass balance equation was introduced instead of liquid balance equation because the phase change terms do not appear explicitly.

The most important processes of energy transfer in a porous medium are conduction, advection (due to mass flux) and phase change. The non-advective air flux is acquired as the reverse motion of the non-advective vapour flux. It is considered for each of the species inside the liquid phase where water is the main component of that species (Pinder & Abriola, 1986). The general theory of miscible displacement applies in this case, which indicates that non-advective fluxes of species inside the phase would cancel (Bear, 1979). The non-advective fluxes of species inside the fluid phases are computed through Fick's law which expresses them in terms of gradients of mass fraction of species through a hydrodynamic dispersion tensor (Bird et al., 1960; Pinder et al., 1986; Pollock, 1986; Pruess, 1987). The dispersion tensor represents the mechanical dispersion plus the molecular diffusion and is expressed as D_{α}^i . The dispersion tensor includes non-advective flux caused by molecular diffusion and by hydromechanical dispersion. While defining this tensor, the degree of saturation and the porosity of the medium perform as a dependent variable. The advective fluxes show as well in the characterization of the tensor that will be discussed later in this chapter. Advective fluxes of fluid phases will be computed using generalized Darcy's law and will be discussed further into details in its respective section later in this chapter as well. Gas pressure was assumed constant in space and time, and its phase is considered a mixture of two species: water (vapour) and air (dry). For most problems, molecular diffusion is dominant, hence the concept of binary diffusion is usually admitted (Bear, 1979).

The mechanical problem is formulated through the equation of stress equilibrium for macroscopic total stresses. In such cases as studied in this problem, both the velocities and accelerations are of insignificant value. The inertial terms are then neglected, leading to a reduction of the balance of momentum for the medium as a whole to the stress equilibrium equation (Bear & Bachmat, 1986). Whereas the balance of momentum for dissolved species and for fluid phases are reduced to constitutive equations (Fick's and Darcy's laws). The formulation of CODE_BRIGHT manages to solve the balance equations by including mass balance of the three species (air, water and solid), the equilibrium of stresses and the total internal energy balance (Olivella et al., 1994).

The basis for a comprehensive mechanical constitutive model is given in details in the papers describing the formulation of CODE_BRIGHT (Olivella et al., 1994, 1996). The problem is coupled because the evaporation of water from the soil matrix produces matrix suction, and this matrix suction produces shrinkage and cracking. At the same time, shrinkage and cracking can contribute to the desiccation process because shrinkage forces water out of the soil matrix and cracks creates new boundaries where water can evaporate. Since the variation of porosity is expressed by the solid mass balance equation, this assumption leads also to some advantages for the iterative scheme.

The numerical approach is distributed into spatial and temporal discretization where the spatial is handled using the finite element method and the temporal is handled using a system of finite difference equations. Time discretization is executed linearly using an implicit scheme of two intermediate points between the initial and final times. However, solving the problem in this case is a non-linear matter. Based on this, an iterative scheme was operated, implementing the Newton-Raphson method to solve the non-linear system of algebraic equations of the space and time discretization. The linear equations resulting from the application of the Newton-Raphson method will be solved using LU decomposition and back-substitution.

5.2.2. Balance equations

Mass balance equations are established per species rather than phases following the compositional approach (Panday & Corapcioglu, 1989). The energy balance equation however is carried out for the medium at once assuming thermal equilibrium in the existing phases (Milly, 1982). The total mass flux of a species in a phase is a result of the diffusive and dispersive non-advective flux, the advective flux caused by fluid motion and the advective flux caused by solid motion. Figure 5.1 shows an illustration of the thermo-hydraulic processes involved in the unsaturated porous medium, including the advective and conductive fluxes in the 3 phases: gas, liquid and solid.

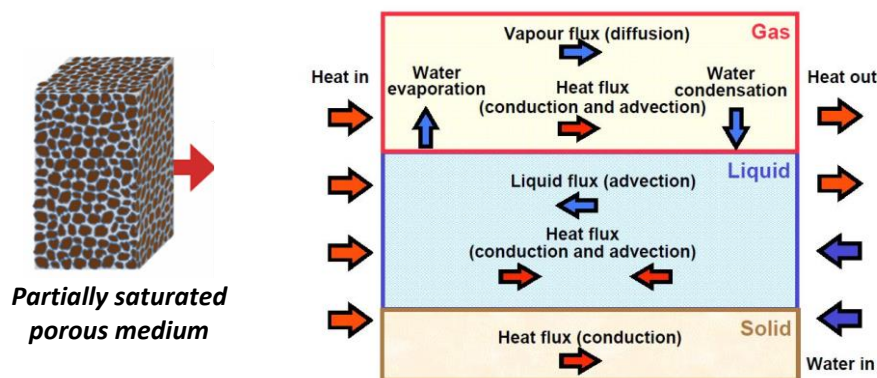


Figure 5-1. Thermo-Hydraulic processes in an unsaturated porous medium.

Air exists as dry air in the gaseous phase and dissolved air in the liquid phase. Water can exist in the liquid phase and in the gaseous phase as vapour. Consequently, advective and non-advective (diffusive or dispersive) fluxes for each of the species (dry air, water, solid) are defined separately in a constitutive outline. The total mass flux of a species in a corresponding phase (gaseous, liquid, and solid) is the sum of all fluxes triggered by fluid and solid kinesis.

Table 5.1 shows a summary of the laws and corresponding state variables for each of the involved mass balance, equilibrium, and constitutive equations.

Table 5.1. Equilibrium, constraint and constitutive equations with associated state variables.

	Law	State variable		Equation
Balance equations	Mass balance of solid	Porosity	ϕ	(5.1-5.3)
	Mass balance of water	Liquid pressure	P_l	(5.4-5.7)
	Momentum balance	Displacements	\mathbf{u}	(5.8)
	Energy balance	Temperature	T	(5.9)
Equilibrium	Psychrometric Law	Vapour concentration in gas	ρ_g^w	(5.31-5.33)
Constitutive	Darcy's Law	Liquid advective flux	\mathbf{q}_l	(5.13)
	Retention Curve	Degree of saturation	θ_{sl}	(5.12)
	Fick's Law	Non-advective vapour flux	\mathbf{i}_g^w	(5.20)
	Fourier's Law	Conductive heat flux	\mathbf{i}_c	(5.26)

5.2.2.1. Solid mass balance

The equation of mass balance in the medium can be represented in the following general form

$$\frac{\partial}{\partial t} [\rho_s(1 - \phi)] + \nabla \cdot (\mathbf{j}_s) = 0 \quad (5.1)$$

Where t is time in seconds; and ∇ is the divergence operator. The material derivative of the porosity leads to

$$\frac{D_s \phi}{Dt} = \frac{1}{\rho_s} (1 - \phi) \frac{D\rho_s}{Dt} + (1 - \phi) \nabla \cdot \frac{d\mathbf{u}}{dt} = 0 \quad (5.2)$$

Where $\frac{d\mathbf{u}}{dt}$ is the vector of solid velocities. The variation of the porosity caused by the volumetric deformation and changes in the density of the solid is obtained from the material derivative of a generic property Θ with respect to the solid

$$\frac{D_s(\Theta)}{Dt} = \frac{\partial}{\partial t}(\Theta) + \frac{d\mathbf{u}}{dt} \cdot \nabla(\Theta) \quad (5.3)$$

The equation of solid mass balance is replaced in the remaining balance equations. Consequently, the calculation of porosity changes at a transitional point is deemed redundant since it is assumed to happen at very low rates. Due to this assumption, the material derivative with respect to the solid can be approximated as a Eulerian derivative. The porosity is then integrated explicitly considering the volumetric strains, which in turn are proportional to $\nabla \cdot \frac{d\mathbf{u}}{dt}$ or volumetric strain rate. At this instant, the porosity is defined as an element-wise variable (Voss, 1984), which is a space-constant over every element centred in the node but has distinct values on every element. The vector of solid velocities is transformed from a continuous vectorial function to a nodal-discrete vectorial function.

5.2.2.2. Water mass balance

Since water is present in the liquid and gas phase, its total mass balance has associated the liquid pressure and is expressed as

$$\frac{\partial}{\partial t}(\theta_l^w S_l \phi + \theta_g^w S_g \phi) + \nabla \cdot (\mathbf{j}_l^w + \mathbf{j}_g^w) = f^w \quad (5.4)$$

Where f^w [$\text{kg} \cdot \text{m}^{-3} \cdot \text{s}^{-1}$] is an external water source term. The water fluxes in the liquid and gas phase are then expressed separately

$$\mathbf{j}_l^w = \mathbf{i}_l^w + \theta_l^w \mathbf{q}_l^w + \theta_l^w S_l \phi \frac{d\mathbf{u}}{dt} = \mathbf{j}'_l^w + \theta_l^w S_l \phi \dot{\mathbf{u}} \quad (5.5)$$

$$\mathbf{j}_g^w = \mathbf{i}_g^w + \theta_g^w \mathbf{q}_g^w + \theta_g^w S_g \phi \frac{d\mathbf{u}}{dt} = \mathbf{j}'_g^w + \theta_g^w S_g \phi \dot{\mathbf{u}} \quad (5.6)$$

Where $\mathbf{j}'_{g,l}$ is the advective part of the flow in the gaseous and liquid phases, minus the advection due to movement of the solid phase. This part of the flow is rendered negligible in case of null movements in the solid phase and becomes: $\mathbf{j}'_{g,l} = \mathbf{j}_{g,l}^w$. If the material derivative (equation 5.3) is applied to the water mass balance equation, the following relationship is obtained

$$\phi \frac{D_s(\theta_l^w S_l + \theta_g^w S_g)}{Dt} + (\theta_l^w S_l + \theta_g^w S_g) \frac{D_s \phi}{Dt} + ((\theta_l^w S_l + \theta_g^w S_g) \phi) \nabla \cdot \frac{d\mathbf{u}}{dt} + \nabla \cdot (\mathbf{j}_l^w + \mathbf{j}_g^w) = f \quad (5.7)$$

If the strains are assumed small enough, the material derivatives can be approximated as Eulerian. The porosity and volumetric strains however are not neglected, and instead appear in the equation in a term involving its variation caused by other processes. Porosity does not function only as a coefficient and is disclosed in other variables that are porosity dependent. To account for the effect of porosity changes in the water mass balance equation, the derivative term is expressed as a function of the state variable, through the balance equation for solids.

5.2.2.3. Air mass balance

Air is considered a single species. It is the main component of the gas phase and might be present as dissolved air in the liquid phase. For most part of this thesis, and unless otherwise stated, the gas pressure has been assumed constant and equal to the atmospheric pressure ($P_g = 0.1$ MPa). While the vapour was allowed in the gas phase, dissolved air was not permitted in water. Therefore, the mass balance equation of air is discarded for most part of the thesis.

5.2.2.4. Momentum balance for the medium

The inertial terms are neglected, so the momentum balance reduces to the equilibrium of stresses, where the associated unknowns are the displacements

$$\nabla \cdot \boldsymbol{\sigma} + \mathbf{b} = 0 \quad (5.8)$$

In conjunction with a constitutive mechanical model to be specified in following sections, the stresses are related to the strains, which in turn are expressed in terms of displacements. However, the balance of momentum for dissolved species or fluids is reduced to constitutive equations that are to be presented later. Following Green's theorem, the weighted residual method is applied to the equation for the treatment of the mechanical equilibrium equation.

5.2.2.5. Internal energy balance

The balance of internal energy equation is based on the previous assumptions of thermal equilibrium between the phases and established considering the internal energy of each phase. Since the expressions of both the water and the internal energies exist in the equations of all the prevailing phases, the use of the material derivative permits obtaining an equation similar to the water mass balance (equation 5.7). The material derivative can be consulted in (Gens &

Olivella, 2001). According to this, one equation is sufficient to exhibit the internal energy balance

$$\frac{\partial}{\partial t} (E_s(1 - \phi) + E_s \rho_l S_l \phi + E_g \rho_g S_g \phi) + \nabla \cdot (\mathbf{i}_c + \mathbf{j}_{Es} + \mathbf{j}_{El} + \mathbf{j}_{Eg}) = f^Q \quad (5.9)$$

Where the fluxes in the divergence term include conductive (\mathbf{i}_c) and advective terms of heat (\mathbf{j}_E caused by mass motions) generated by each species in the porous medium. f^Q is the energy supply (e.g., energy dissipation due to medium deformation). An advective heat flow occurs due to non-advective mass flux. This is triggered by the travel of a species inside a phase which ensue energy conveyance. The specific internal energies of the species are: $E_l^w = 4180(T - T_0)$ [$\text{J}\cdot\text{kg}^{-1}$]; and $E_g^w = 2.5 \times 10^6 + 1900(T - T_0)$ [$\text{J}\cdot\text{kg}^{-1}$]; where T is the temperature at a time t , and T_0 is a reference temperature that will be specified later. The internal energy of the vapour contains the latent heat of vaporization ($2.5 \times 10^6 \text{ J}\cdot\text{kg}^{-1}$).

5.2.3. Constitutive equations and equilibrium constraints

After defining the mass balance equations, the final objective is to relate the unknowns in the governing equations to the dependent variables. The degree of saturation will be expressed in terms of temperature, liquid and gas pressures and changes in porosity. The influence of porosity on the balance equations is not limited to its role as a coefficient in the equations, but also to its implicit function in other dependent variables (e.g., intrinsic permeability, thermal conductivity).

Coupling of the hydraulic and mechanical problems is made through the constitutive law and a non-symmetric global system of equations is obtained from the finite element method. The following equations in this section determine the link between the variables (both the dependent and independent ones) and the unknowns. These obtained links are substituted in the balance equations, leading to the expression of the governing balance equations in terms of the unknowns.

5.2.3.1. Mechanical equation

In order to simplify the hydro-mechanical analysis, a mechanical constitutive model with a non-linear elastic relation based on the stress state surface (Matyas & Radhakrishna, 1968; Lloret & Alonso, 1985) is chosen. This model is applicable in this case of dominant volumetric deformations where shear deformation is not very relevant. With this choice, the necessity of a complex stress point algorithm (plasticity model) can be avoided, and an explicit integration scheme can be used. The volumetric strain is then calculated in a reversible manner

$$\frac{\Delta e}{1+e} = a_1 \Delta \ln(-p') + a_2 \Delta \ln\left(\frac{\Psi + P_g}{P_g}\right) + a_3 \Delta \left[\ln(-p') \ln\left(\frac{\Psi + P_g}{P_g}\right) \right] \quad (5.10)$$

Where e is the void ratio; p' is the mean effective stress; Ψ is the suction: $\Psi = P_g - P_l$; and a_1 is the coefficient accompanying the changes in mean effective stress p' , determined from the slope of the unload/reload curve, κ , of the $(e - \ln p')$ diagram as: $a_1 = \frac{-\kappa}{(1+e)}$. Similarly, a_2 is the coefficient accompanying the volumetric strain changes due to suction, determined from the slope of the unload/reload curve, κ_s , of the $(e - \ln(P_l))$ diagram as: $a_2 = \frac{-\kappa_s}{(1+e)}$. On the other hand, a_3 is the transition coefficient between the effective stress and suction. The shear strain however is linearly elastic with the Poisson's ratio ν . The value of Poisson's ratio can be extrapolated from Barrera's extensive work on similar soil (Barcelona Silty Clay), who suggested a value of $\nu = 0.4$ (Barrera, 2002). A term for tension is introduced to avoid any tractions ($p' - \sigma_c \leq 0$). The tension value σ_c is deduced from Lakshmikantha's vast investigatory tests on Barcelona silty clay soil to directly compute the soil's tensile strength values (Lakshmikantha, 2009). The value can be deduced from the carried out tests on similar dry density and water content to this problem. Additionally, it is necessary to introduce the value of minimum bulk modulus k_{min} which is a lower bound of the stiffness modulus K [MPa]. Since the clayey soils are susceptible to smaller volumetric changes due to variations in suction than in effective stresses (Barrera, 2002), a lower magnitude of coefficient a_2 than coefficient a_1 is assigned. If a_2 and a_3 are null, suction changes do not contribute to the mechanical problem, and the bulk modulus K is calculated with this scheme:

$$d\varepsilon = a_1 d\ln(p') \rightarrow d\varepsilon = a_1 \frac{dp'}{p'} \rightarrow K = \frac{dp'}{d\varepsilon} = \frac{p'}{a_1} \quad (5.11)$$

Where ε is the volumetric deformation.

5.2.3.2. Soil Water Retention Curve (SWRC)

This curve defines the relationship between the liquid saturation ratio and suction. The chosen model (van Genuchten, 1980) was found to be a good representative of the resultant data in previous research. Multiple authors proposed correction factors to the van Genuchten model. For instant, Romero and Vaunat (2000) and Fredlund and Xing (1994) provided a correction factor for the model that intends to correlate the relation better taking into account intra- and inter-aggregate pores and their interaction and contribution in relation to capillary and specific surface area as a function of moisture. However, the final expression chosen for this work is shown in equation 5.12

$$S_e = \frac{S_l - S_{rl}}{S_{ls} - S_{rl}} = \left[1 + \left(\frac{P_g - P_l}{P} \right)^{\frac{1}{1-n(\phi)}} \right]^{-n(\phi)} \quad (5.12)$$

$$P = P_0(\phi) \frac{\sigma_w}{\sigma_{w_0}}; \quad P_0(\phi) = P_0 \exp [a_p(\phi_0 - \phi)]; \quad n(\phi) = n_0 \exp [a_n(\phi_0 - \phi)]$$

Where $(P_g - P_l)$ is the suction [MPa]; $n(\phi)$ is a material parameter and serves as a shape factor to adjust the curve, and its value is dependent on porosity changes; P_0 is related to the air entry value [MPa], also dependent on porosity change; a_p and a_n are constants controlling the magnitude of the effect of porosity change on the air entry value and shape parameters, respectively; σ_w is the surface tension measured at a certain temperature and σ_{w_0} is the surface tension measured at the reference temperature.

5.2.3.3. Intrinsic permeability

The intrinsic permeability for a continuum medium is provided similar to Kozeny's models (Kozeny, 1927). The equation holds for flow through packed beds with particle Reynolds numbers (Reynolds, 1883) up to approximately 1.0, which applies in this problem (Carman, 1937, 1956), where no considerable kinetic energy losses occur due to shifting of flow channels. The equation can be expressed as Darcy's Law for single phase flow in isotropic porous media, where flow is assumed proportional to the pressure drop while being inversely proportional to the fluid viscosity:

$$\mathbf{q}_\alpha = -\mathbf{K}_r(S_r) \cdot (\nabla P_\alpha - \rho_\alpha \mathbf{g}) \quad (5.13)$$

Where \mathbf{q} is Darcy's velocity vector; P is the pressure; ρ is the density; \mathbf{g} is the gravity vector; and \mathbf{K}_r is the permeability tensor as a function of the saturation degree S_r , and can be expressed in terms of the intrinsic permeability as

$$\mathbf{K}(S_r) = \frac{\mathbf{k}_i k_{r\alpha}}{\mu_\alpha} \quad (5.14)$$

Where μ_α is a temperature-dependent dynamic viscosity of the species; the viscosity and density are defined in other laws concerning phase properties of the medium in the following sections; $k_{r\alpha}$ is the relative permeability is defined later; \mathbf{k}_i is the intrinsic permeability tensor, a soil property that is dependent on the porosity, viscosity and temperature of the fluid, and can be expressed as:

$$\mathbf{k}_i = \frac{\mu_\alpha}{\gamma_\alpha} K_{HC} \mathbf{I} \quad (5.15)$$

Where γ_α is the specific weight; K_{HC} is the hydraulic conductivity of the soil, and \mathbf{I} is the identity tensor. The intrinsic permeability is defined for three principal directions. In the case of isotropic soil, the permeability is scalar. Combining the equations gives the final Kozeny equation for absolute (single phase) permeability, and the final form of Darcy's Law becomes:

$$\mathbf{q}_\alpha = -\frac{\mathbf{k}_i k_{r\alpha}}{\mu_\alpha} (\nabla P_\alpha - \rho_\alpha \mathbf{g}) \quad (5.16)$$

For a continuum medium, the exponential law for continuum medium (based on Kozeny's model) expresses the intrinsic permeability in terms of porosity

$$\mathbf{k}_i = \mathbf{k}_{i0} \frac{\phi^3}{(1-\phi)^2} \frac{(1-\phi_0)^2}{\phi_0^3} \quad (5.17)$$

Where \mathbf{k}_{i0} is the intrinsic permeability for the matrix at reference porosity: $\phi = \phi_0$. The parameters input into the system of equations require first defining the hydraulic conductivity of the soil specimen. This parameter depends on the initial conditions of each test prepared at different compaction levels. Values for hydraulic conductivity were interpolated from the tests carried out on samples with different initial void ratio (Cordero, 2019). The intrinsic permeability has been adopted from experimental measurements as well (Barrera, 2002; Mora Ortiz, 2016).

5.2.3.4. Liquid phase relative permeability

The parameter $k_{r\alpha}$ that appears in equation 5.16 represents the phase relative permeability for liquids and gases. The values of the phase relative permeability range between 0 and 1 depending on the saturation degree S_r . The van Genuchten model has been elected to represent the relationship between the saturation ratio and suction in the soil matrix in this chapter. Equation 5.18 expresses the relative permeability of the liquid phase consistent with the van Genuchten model:

$$k_{rl} = \sqrt{S_e} \left(1 - \left(1 - S_e^{1/n} \right)^n \right)^2 ; S_e = \frac{S_l - S_{rl}}{S_{ls} - S_{rl}} \quad (5.18)$$

Where the value of the parameter n is coherent with the shape factor parameter of the retention curve.

5.2.3.5. Gas phase relative permeability

The gas phase relative permeability is defined by default in equation 5.19

$$k_{rg} = 1 - k_{rl} \quad (5.19)$$

The selected parameter values defining the power law are provided along the other defining parameters for each corresponding model.

5.2.3.6. Fick's law

Fick's Law is used generally to describe the diffusive fluxes of vapour or air in the gas phase. Factors determining the gas phase diffusivity of porous material have been suggested to include the total porosity, air-filled porosity, moisture content and the tortuosity of drained matrix pores (Millington & Quirk, 1961; Troeh et al., 1982; Moldrup et al., 2000). The expression of non-advective fluxes can be written as

$$\mathbf{i}_g^w = -\mathbf{D}_g^w \nabla \omega_g^w = -(\phi \rho_g S_g \tau_r D_m^w \mathbf{I}) \nabla \omega_g^w \quad (5.20)$$

Where \mathbf{D}_g^w is the dispersion tensor, τ_r is the tortuosity, \mathbf{I} is the identity matrix; and D_m^w is the dispersion coefficient corresponding to the molecular diffusion of vapour in the air, and is expressed as

$$D_m^w = 5.8 \times 10^{-12} \frac{(273.15 + T)^{2.3}}{P_g} \quad (5.21)$$

Where T [°C] is the temperature. In a porous medium, the solid particles force the diffusion pathways to diverge from their original conventional lines. The diffusion factor has to be scaled with tortuosity to denote the effect of porosity on diffusion (Shen & Chen, 2007). While the tortuosity values can be assumed constant ($\tau_r = \tau_{r0}$), other laws suggest it is defined as a function of the degree of gas saturation. The latter has been proved to have more comparable results in similar problems (Cuadrado, 2019). The value of tortuosity can be expressed as

$$\tau_r = A_\tau (S_g)^{m_\tau} \quad (5.22)$$

Where A_τ and m_τ are parameters to be characterized later for each respective model.

From the first studies on thermo-hydraulic coupling (Gurr et al., 1952; Taylor & Cavazza, 1954), an increase was found to happen in the flow of vapour inside the soil compared to the Fick's Law prediction (Campbell & Norman, 1998). The increase in diffusion has been attributed to the convective vapour cells due to the volumetric changes occurring in the soil during daily cycles (Parlange et al., 1998), which requires the use of improvement factors for diffusion. These improvement factors have been used in multiple cases for more representative

results (Schelde et al., 1998; Saito et al., 2006; Bittelli et al., 2008; Sakai et al., 2009; Smits et al., 2011; Han et al., 2013).

In general, transport by advection dominates in zones of high permeability (or hydraulic conductivity) of a porous medium, such as fractures, while diffusion dominates in zones of low permeability, such as clay layers (Shen & Chen, 2007). Evidence denotes the principal role of diffusion in transport in fine-grained soils (Desaulniers et al., 1981). The use of Fick's first law to model diffusion fluxes is arguably the most common and important method in groundwater hydrology. However, most of the present models for these fluxes do not correctly represent changes in the time scale of diffusion as a function of porosity in a system of porous media (Aziz & Settari, 1979; Helmig, 1997; Chen et al., 2020). To represent the role of porosity on diffusion, the diffusion coefficient must be scaled with tortuosity (Van Cappellen & Gaillard, 1996). There are some general boundary requirements found in the literature for the values of tortuosity and its direct relationship with the porosity (Boudreau, 1996). As the porosity increases, there will be no hindrance to diffusion in the absence of any impermeable solid. However, the hindrance is complete if all pore-space disappears. The level of compaction has been suggested to affect the tortuosity values, causing an increase as the porosity decreases below 40% (Kristensen et al., 2010). Some authors related the tortuosity directly to the porosity values using empirical equations based on soil type, e.g.: Ullman et al. (1982) for sands and muds; Boudreau (1996) for fine-grained unlithified sediments. Tortuosity has been reported in previous investigations handling similar problems with values higher than 1 and acts as a factor to improve diffusion (e.g., Philip & De Vries, 1957; Saito et al., 2006; Bittelli et al., 2008). Tortuosity is highly affected by the fissures, texture and moisture content of the soil and the existence of cracks and their connectivity (Davis et al., 2005; Bozkurt et al., 2009). The tortuosity (both planar and spatial) has been found to increase as the connectedness of the crack system decrease from 1 to 0 (Chertkov & Ravina, 1999).

5.2.3.7. Dispersive fluxes

To solve for the dispersivities of vapour, dissolved air and heat, Fick's law is used likewise to compute the mechanical dispersion mass flux for heat and vapour (Campbell & Norman, 1977)

$$\mathbf{i}_\alpha^i = -(\rho_\alpha \mathbf{D}'_\alpha) \nabla \omega_\alpha^i \quad (5.23)$$

Where \mathbf{D}'_α is the mechanical dispersion tensor defined by the longitudinal and transversal dispersivities (d_l and d_t respectively), and defined as follows

$$\mathbf{D}'_\alpha = d_t |\mathbf{q}_\alpha| \mathbf{I} + (d_l - d_t) \frac{\mathbf{q}_\alpha \mathbf{q}_\alpha^t}{|\mathbf{q}_\alpha|} \quad (5.24)$$

These terms, computed through Fick's law, are proportional to gradients of mass fractions which do not belong to the set of unknowns. Fourier's law is used for the conductive heat flux, and it expresses proportionality to temperature gradients

$$\mathbf{i}_h = -(c_\alpha \rho_\alpha \mathbf{D}'_\alpha) \nabla T \quad (5.25)$$

Where c_α is the specific heat of the α phase, defined in the phase properties in following sections (see section 5.2.3.9). The mechanical dispersion heat flux tensor is defined as in equation 5.23, while accounting only for the involvement of the liquid phase dispersion.

5.2.3.8. Fourier's law

Fourier's law is implemented in the calculations of conductive heat flux, by accounting for the effect of porosity, temperature, and water content, in its form

$$\mathbf{i}_c = -\lambda_h \nabla T \quad (5.26)$$

Where λ_h [$\text{J}\cdot\text{m}^{-1}\cdot\text{s}^{-1}\cdot\text{K}^{-1}$] is the thermal conductivity parameter. The parameter is a resultant of the different phases of the porous medium. Its value is computed by providing the conductivities of the soil in both its dry ($\lambda_{h_{dry}}$) and saturated ($\lambda_{h_{sat}}$) states. The dependency on porosity is expressed using the geometric weighted mean for most of the thesis, unless otherwise stated. However, the dependence on saturation ratio is expressed linearly with the square root of saturation for most part of thesis, unless otherwise stated

$$\lambda_h = \lambda_{h_{sat}} \sqrt{S_l} + \lambda_{h_{dry}} (1 - \sqrt{S_l}) \quad (5.27)$$

The values of $\lambda_{h_{dry}}$ and $\lambda_{h_{sat}}$ can be acquired directly through laboratory testing (ASTM D5334). The values are affected by the density, salt concentration and organic matter (Abu-Hamdeh & Reeder, 2000; Abu-Hamdeh, 2003). The compaction techniques likewise exhibit an influence over the thermal conductivity, so does the compaction pressure and water content (Tang et al., 2007). The values utilized in this problem were picked from the literature for similar soil samples (Farouki, 1986; Oke, 1987; Villalobos et al., 2002).

5.2.3.9. Solid phase properties

The solid phase specific heat was set to $c_s = 1000 \text{ J}\cdot\text{kg}^{-1}\cdot\text{K}^{-1}$ and the solid phase density according to the laboratory results $\rho_s = 2700 \text{ kg}\cdot\text{m}^{-3}$. The linear thermal expansion and stress compressibility coefficients were assumed null, indicating no expansion of the solids due to temperature and pressure fluctuations respectively.

5.2.3.10. Liquid phase properties

The liquid density is assumed to vary exponentially with water and pressure fluctuations

$$\rho_l = \rho_{l0} \exp[\beta_{CL}(P_l - P_{ref}) + \alpha_{VTE}T + \gamma_{sv}\omega_l^h] \quad (5.28)$$

Where ρ_{l0} is the reference density (assumed $1002.6 \text{ kg}\cdot\text{m}^{-3}$); β_{CL} is the compressibility (assumed $4.5 \times 10^{-4} \text{ MPa}^{-1}$); α_{VTE} is the volumetric thermal expansion coefficient for water (assumed $-3.5410^{-4} \text{ }^\circ\text{C}^{-1}$); γ_{sv} is the solute variation (assumed $0.6923 \text{ kg}\cdot\text{m}^{-3}$); and P_{ref} is the reference pressure (assumed equal to the atmospheric pressure 0.1 MPa).

The liquid viscosity however is dependent on the temperature only

$$\mu_l = A_L \exp\left[\frac{B_L}{273.15 + T}\right] \quad (5.29)$$

Where $T [^\circ\text{C}]$ is the temperature and $A_L = 2.1 \times 10^{-12}$ and $B_L = 1808.5$.

5.2.3.11. Gas phase properties

The gas pressure is node-wise variable defined by its nodal values and interpolated on the elements using the shape functions (Voss, 1984). Gas pressure is assumed constant and equal to the atmospheric pressure: $P_g = P_{atm} = 0.1 \text{ MPa}$ throughout the simulations. The gas density on the other hand is solved using the law of ideal gases and Henry's law for dry air, with molecular weight of air: $M_a = 0.02895 \text{ kg}\cdot\text{mol}^{-1}$ and Henry's constant: $H_{nc} = 10000 \text{ MPa}$. The gas viscosity is computed as a function of temperature T in a similar manner to liquid viscosity

$$\mu_g = A_G \exp\left[\frac{B_G}{273.15 + T}\right] \quad (5.30)$$

Where $T [^\circ\text{C}]$ is the temperature and $A_G = 1.48 \times 10^{-12} \text{ MPa}\cdot\text{s}$ and $B_G = 119.4 \text{ }^\circ\text{C}$.

5.2.3.12. Psychrometric law

The psychrometric law lies within the equilibrium restrictions set of equations. It is also called Kelvin's law and defines the concentration of vapour (ρ_g^w) in the gas phase which is in equilibrium with the liquid phase:

$$\rho_g^w = (\rho_g^w)^0 \exp\left[\frac{-(P_g - P_l)M_w}{R(273.15 + T)\rho_l}\right] \quad (5.31)$$

Where $(P_g - P_l)$ is the suction [MPa]; M_w is the water molecular weight (0.018 kg·mol⁻¹); R is the universal gas constant (8.314 J·mol⁻¹·K⁻¹); and $(\rho_g^w)^0$ is the saturated volumetric mass content of vapour in the gaseous phase in equilibrium with a flat surface of water at the same temperature, calculated as:

$$(\rho_g^w)^0 = \frac{M_w P_{v(T)}}{R(273.15 + T)} \quad (5.32)$$

Where $P_{v(T)}$ [MPa] is the saturated vapour pressure. In case of pure water, it is calculated in terms of the temperature T [°C]:

$$P_{v(T)} = 136075 \exp \left[\frac{-5239.7}{(273.15 + T)} \right] \quad (5.33)$$

5.2.4. Boundary conditions

The conditions of the laboratory test were translated into CODE_BRIGHT using the available formulation. This required defining the mechanical and flux boundary conditions in a manner that replicates the existing physical conditions during the test.

5.2.4.1. Mechanical boundary conditions

The general mechanical boundary condition in CODE_BRIGHT incorporates a Neumann and a Cauchy type boundary condition. It is the result-of applying Green's Theorem to the divergence term which represents the stresses on the boundary. Following the classical approach, external forces are imposed on the desired boundaries by imposing displacements using a Cauchy type boundary condition (spring stiffness by displacement increment). This condition is applied in each direction by means of a prescribed force in a Cartesian coordinate system, in the following form

$$f_{x,y,z} = f_{x,y,z}^\circ + \gamma_m \cos(\alpha_{1,2,3}) (\dot{u}_{x,y,z}^\circ - \dot{u}_{x,y,z}) \Delta t \quad (5.34)$$

Where γ is a multiplier, $\cos(\alpha)$ defines the direction, \dot{u} is the displacement and the superscript $^\circ$ denotes a prescribed rate per unit time. If the specimen is not allowed to move in one or more of the directions at a certain point or line, the displacement rate is set to zero ($\dot{u} = 0$) and the multiplier γ_m is assigned a relatively large value to inflict a stationary state.

In the specimens being simulated, the bottom boundary consisted of ridged surface, restricting the lateral movement of the soil at the bottom. Thus, the condition was applied at the bottom boundary in all cases unless specified (smooth surface for comparative analysis). The sides of the specimen on the other hand were made free to move both vertically and horizontally, since the walls of the holding tray did not restrict their movement. The walls however did not permit the soil to move outside the tray. This was simulated by means of successive reactive horizontal forces along the external face (see Figure 5.2).

5.2.4.2. Flux boundary conditions

The boundary conditions can be defined in terms of the main variables or their derivatives (i.e., a fixed suction value or a fixed water flux applied to the soil surface). Soil-atmosphere interaction can be simulated by applying a time-dependent exponential soil suction profile at the soil interface (Vo et al., 2019). Experiments suggest that above the soil surface most of the boundary variables exhibit high gradients which complicate the definition of a constant value as boundary condition (Lozada et al., 2019; Cordero et al., 2020). It is therefore more convenient to impose a flux boundary condition at the soil surface for water and energy transfer.

The general form of the hydraulic boundary condition in the numerical model is obtained by adding fluxes at the nodes. For drying problems, the boundary conditions reduce to vapour (\mathbf{j}_g^w) and heat (\mathbf{j}_{ES}) fluxes. Vapour flux through the boundary is composed of three distinct terms.

$$j_g^w = \underbrace{(\omega_g^w)^0 \left(j_g^0 + \Delta j_g^0 \frac{dt}{\Delta t} \right)}_1 + \underbrace{(\omega_g^w)^0 \gamma_g \left(P_g^0 + \Delta P_g^0 \frac{dt}{\Delta t} \right) - P_g}_2 + \underbrace{\beta_g \left[(\rho_g \omega_g^w)^0 - (\rho_g \omega_g^w) \right]}_3 \quad (5.35)$$

Where dt is the current time increment and Δt is the current time step, allowing the terms to express an imposed linear variation of fluxes; the superscript “0” denotes prescribed atmospheric values; P_g is the gas pressure; j_g^0 is a prescribed gas flux; and γ_g and β_g are transfer coefficients controlling the magnitude of interactions, to be determined in the next section. The first term corresponds to a vapour flux imposed by gas injection; the second, the advective vapour flux due to pressure difference; and the third, the diffusive vapour flux due to difference in prescribed concentrations. In the particular case of drying, and considering constant gas pressure (equal to the atmospheric pressure: $P_g = P_a = 0.1$ MPa), the boundary condition is then expressed through its third term, corresponding to mass inflow or outflow taking place when the species mass fraction is prescribed at a node

$$j_g^w = \beta_g \left[(\rho_g \omega_g^w)^0 - \rho_g \omega_g^w \right] \quad (5.36)$$

Where ρ_g is the gas density approximated from the molecular weight of dry air ($M_a = 0.029 \text{ kg}\cdot\text{mol}^{-1}$); and ω_g^w is the vapour mass fraction in the air.

The physical values of relative humidity and temperature recorded in the environmental chamber are to be reproduced in the boundary flux equation. The relative humidity represents the amount of vapour currently in the air, as a percentage of the maximum or saturated value, allowing the imposed relative humidity values to be decomposed into

$$RH = \frac{\rho_v}{\rho_v^{sat}} \quad (5.37)$$

Where ρ_v^{sat} [$\text{kg}\cdot\text{m}^{-3}$] is the density of vapour in saturated air. The law of ideal gases applies in this case to get its expression

$$PV = nRT \quad (5.38)$$

Where P is the pressure, V is the volume, n is the number of moles, R is the universal gas constant and T is the absolute temperature. The density on the other hand to be expressed as:

$$\rho = \frac{nM}{V} \quad (5.39)$$

Where M is the molecular weight. Replacing equation 5.38 into equation 5.39 gives the expression of density as:

$$\rho = \frac{PM}{RT} \quad (5.40)$$

That gives the expression of vapour density in saturated air

$$\rho_v^{sat} = \frac{P_v M_w}{RT} \times 10^6 \quad (5.41)$$

Where $M_w = 0.018 \text{ kg}\cdot\text{mol}^{-1}$ is the molecular weight of water, and P_v is the saturated vapour pressure, which in case of pure water is

$$P_v = 136075 \exp \left[\frac{-5239.7}{273.15 + T} \right] \quad (5.42)$$

Therefore ρ_v^{sat} is temperature-dependent. However, the vapour density ρ_v can be expressed as a function of the imposed vapour mass fraction in air $(\omega_g^w)^0$ and the prescribed gas density $(\rho_g)^0$

$$(\omega_g^w)^0 = \rho_v \times (\rho_g)^0 \quad (5.43)$$

Where $(\rho_g)^0$ can be expressed as

$$(\rho_g)^0 = \frac{P_a M_a}{RT} \times 10^6 \quad (5.44)$$

Where the atmospheric pressure P_a is constant and equal to 0.1 MPa, $R = 8.314 \text{ J}\cdot\text{mol}^{-1}\cdot\text{K}^{-1}$, $M_a = 0.029 \text{ kg}\cdot\text{mol}^{-1}$, and T is expressed in [K]. Normally, the molecular weight of air is the sum of dry air and vapour. However, since the maximum weight of vapour that air can sustain is comparably small with that of dry air, the error is negligible, and the calculation is simplified. The imposed vapour mass fraction takes its final form:

$$(\omega_g^w)^0 = \underbrace{(RH)}_1 \times \underbrace{\frac{136075 \exp\left[\frac{-5239.7}{T}\right] \times M_w}{RT}}_3 \times 10^6 \times \underbrace{\frac{P_a M_a}{RT} \times 10^6}_4 \quad (5.45)$$

The only variables in this equation are the first term (\mathbf{RH}), which is expressed as a percentage, and the temperature T expressed in [K]. The second term in the equation above corresponds to the saturated vapour pressure (equation 5.42), which in turn is a part of the saturated vapour density in the third term (equation 5.42), while the fourth and last term corresponds to the prescribed gas density. The Relative Humidity and Temperature values are then decomposed numerically at each time step input interval into prescribed gas density and vapour mass fraction. Following this approach, the transfer coefficient β_g acquires the physical meaning of vapour diffusion coefficient at the soil-atmosphere interface.

The energy boundary condition on the other hand is expressed in terms of heat flow rate (a von Neumann-type term), prescribed temperature flux (a Cauchy-type term), and a series of other terms that represent the energy transfer caused by mass fluxes

$$j_e = j_e^0 + \gamma_e(T^0 - T) + E_g^w(j_g^w) + \dots \quad (5.46)$$

The prescribed heat flow flux j_e^0 [$\text{W}\cdot\text{m}^{-2}$] represents the solar radiation energy (R_n). In the case of solar radiation absence in the environmental chamber tests inside the closed lab, this value is

considered to be null. Following a similar scheme to the vapour flux, the boundary condition is reduced to imposed temperature changes:

$$j_e = j_e^0 + \gamma_e(T^0 - T) \quad (5.47)$$

Where γ_e is the heat transfer coefficient. In this case, γ_e acts as a thermal diffusion coefficient at the soil-atmosphere interface.

5.2.4.3. Transfer coefficients

The boundary condition must reproduce the atmospheric behaviour inside the environmental chamber. Processes of mass and heat exchange between the soil and the atmosphere through the ground surface can be quantified in terms of energy fluxes [$\text{W}\cdot\text{m}^{-2}$]. To this end, the well-known surface energy balance equation is used (Blight, 1997):

$$R_n = H + LE + G \quad (5.48)$$

This equation represents the soil-atmosphere interactions at the interface through four energy flows: absorption or emission of electromagnetic radiation through the surface (net radiation, R_n); the thermal conduction between soil surface and atmosphere (sensible heat, H); energy required for soil water evaporation or vapour condensation on the surface (latent heat, LE) and heat conduction responsible for altering the soil body temperature (heat flow, G). The fluxes are of a positive value if they are directed away from the surface, while R_n is positive when approaching the surface (Oke, 1987).

In this particular study, the test was carried out in closed laboratory conditions with negligible radiation interference. The atmospheric gradients of sensible and latent heat flows condition the evaporative demand. These flows follow Dalton's Law (Wilson et al., 1994), and are given by:

$$H = \frac{C_a(T_s - T_a)}{r_h} \quad (5.49)$$

$$LE = \frac{h_e(\rho_s - \rho_a)}{r_a + r_s} \quad (5.50)$$

Where T_s and T_a [K] are temperatures of the soil surface and air, respectively; C_a is the volumetric heat capacity of air calculated as: $C_a = \rho_a \cdot C_p$, where ρ_a is the dry air density at room temperature ($1.168 \text{ kg}\cdot\text{m}^{-3}$) and $C_p=1005 \text{ J}\cdot\text{kg}^{-1}\cdot\text{K}^{-1}$ is the specific heat capacity, typically

around $1200 \text{ [J}\cdot\text{m}^{-3}\cdot\text{K}^{-1}]$ (Stull, 1988; Wallace & Hobbs, 2006); ρ_s is the air density at the soil surface $[\text{kg}\cdot\text{m}^{-3}]$; h_e is the latent heat of evaporation $[\text{J}\cdot\text{kg}^{-1}]$; r_s is the soil surface resistance to evaporation; and r_h and r_a are aerodynamic resistance factors governing water vapour and temperature dispersion into the atmosphere.

While simulating desiccation experiments in CODE_BRIGHT, the gas pressure influence is considered to be minimal on the soil-water evaporation process. Based on this, it is assumed constant and equal to the atmospheric pressure, so the effect of air flow on water species in both phases has not been taken into account. As the flow of air is not calculated, the diffusion of vapour from the change in saturation is calculated. This option however is a possible explanation for the use of diffusion improvement factors (Philip & De Vries, 1957). The simplifications made in both the porous medium and atmospheric models are compatible. This allows the use of aerodynamic and surface resistances as transfer coefficients while simulating the soil-atmosphere interactions. The transfer coefficient β_g , necessary to impose the vapour flux boundary condition (equation 5.36), is derived by comparing against the latent heat LE (equation 5.50).

$$\beta_g [(\rho_g \omega_g^w)^0 - \rho_g \omega_g^w] = \frac{(\rho_s - \rho_a)}{r_a + r_s} \rightarrow |\beta_g| = \frac{1}{r_a + r_s} \quad (5.51)$$

Where $(\rho_g \omega_g^w)^0$ is the equivalent to atmospheric vapour density ρ_a , and $\rho_g \omega_g^w$ is the equivalent to air density at the soil surface ρ_s . On the other hand, the heat transfer coefficient γ_e , necessary to impose the reduced energy flux at the interface (equation 5.47), is derived by comparing against the sensible heat H (equation 5.49).

$$\gamma_e(T^0 - T) = \frac{C_a(T_s - T_a)}{r_h} \rightarrow |\gamma_e| = \frac{C_a}{r_a + r_s} \quad (5.52)$$

Where T^0 is the equivalent to atmospheric temperature T_a , and T is the equivalent to soil surface temperature T_s .

Aerodynamic resistance

Assuming a simplified atmospheric model, the average horizontal wind, temperature, and relative humidity only change in the vertical direction and at a slow rate. The average vertical component of the wind is assumed null on the ground and in the air as well. These assumptions signify that the latent and sensible heat fluxes are vertically transported by turbulent movement. Another condition is the homogeneity of the evaporative soil surface. This means that along this evaporative surface, the water content, temperature, vapour flow and roughness are

homogeneous. The mentioned conditions are applicable for the specimens being simulated and are compatible with the models of porous media presented in (Fetzer et al., 2017). The referred models describe the flows of water and heat in the soil and were classified in a comparative study (Fetzer et al., 2017).

These aerodynamic resistance factors have been expressed by many authors with satisfactory results (Camillo et al., 1983; Yamanaka et al., 1997; Saito et al., 2006; Cui et al., 2012). Generally, it has been observed that the two factors are used interchangeably and considered equal (Garratt, 1977; Joffre, 1982). A dimensional analysis is carried out to obtain the corresponding units for sensible and latent heat flows [$\text{J}\cdot\text{m}^{-2}\cdot\text{s}^{-1}$], leading to the resistance factors [$\text{s}\cdot\text{m}^{-1}$]:

$$r_h = r_a = \frac{1}{k^2 \bar{U}} \left[\ln \frac{z}{z_0} + \psi_H(\zeta) \right] \left[\ln \frac{z}{z_0} + \psi_M(\zeta) \right] \quad (5.53)$$

The von Kármán's constant (k) has been used to represent turbulence of fluids on non-slip surfaces. It describes how the diameter of turbulent eddies grows with height. It has been found in the literature for similar cases to have a typical value of 0.41 (Tagesson, 2012). The average profile of wind speed \bar{U} comes from the application of the theory of similarity (Stull, 1988). z is the measuring altitude of the atmospheric variables (where \bar{U} is recorded). Near the ground surface, the friction tends to reduce the wind speed until it vanishes. The height at which this occurs is identified as the roughness length z_0 . For smooth surface conditions existing in the laboratory specimen, z_0 is assumed to be equal to 0.01 cm according to classifications (Davenport et al., 2000; Šimůnek et al., 2013). $\psi_{H,M}(\zeta)$ are atmospheric stability factors for heat flux (H) and for momentum flux (M). The term ζ is a dimensionless atmospheric stability parameter that depends on the Monin-Obukhov length: a relation between shear stress created by wind and buoyancy of air by convection to produce turbulent kinetic energy (Monin & Obukhov, 1954; Obukhov, 1971). In other words, it is a measure of convective behaviour of the atmosphere represented by the so-called stability condition, or a measure of the atmospheric resistance to air displacement by convection as explained below.

The resistance of a volume of air to move vertically depends on the difference in density between such volume and that of the surrounding air. If the surrounding air is less dense, the volume tends to rise leading to convection currents that transport heat and humidity. The mixing capacity of heat and humidity depends on the turbulence that is generated in this latter movement. In this sense, turbulence can be understood as a chaotic movement of air that enhances the heat and moisture exchange, either between layers of air, or between the soil surface and the atmosphere. Therefore, the stability condition is a measure of how that

atmosphere tends to favour or suppress the turbulence that conditions the heat and humidity flow from the ground.

In general, atmospheric stability can be categorized into three distinct types: unstable, neutral, and stable. The unstable condition appears when the soil surface is warmer than the overlying layer of air in contact with that surface. The air then heats up, producing thermal updrafts that cause an increase in turbulence and result in mixing heat and moisture. In the neutral condition, the temperature of the soil surface and of the air layer are similar and thus the convection is weak. Finally, in the stable condition, the air temperature is higher than that at the ground surface and convection tends to be suppressed. Consequently, the stability factors increase the diffusion in the unstable atmosphere, reduce it in stable conditions and have no effect in the neutral condition.

In this study, the atmospheric and soil temperatures are similar. These stability factors are not incorporated in the CODE_BRIGHT formulation. However, to further investigate their effect on soil-water evaporation and cracking, Cuadrado (2019) carried out an extensive comparative study in his PhD thesis on the influence of these parameters. He employed in his analysis another Thermo-Hydraulic program (HYDRUS) which accounts for the stability factors in its iterative calculations.

The compared results for multiple cases with those of CODE_BRIGHT, verified a negligible influence on soil-water evaporation and the overall reaction of the soil matrix to the desiccation process. These terms will then be neglected in this study. This signifies a neutral atmosphere condition where the atmospheric temperature is equal to the soil surface temperature (Brutsaert, 1982). The stability factors can then be ignored, and the aerodynamic resistance becomes

$$r_h = r_a = \frac{1}{k^2 \bar{U}} \left[\ln \frac{z}{z_0} \right]^2 \quad (5.54)$$

The expression of the aerodynamic resistance comes from the field of micrometeorology. The semi-empirical log-wind-speed law has been found to fit satisfactorily experimental wind speed data, not only in the first 100 meters above ground, but also directly above bare soil surfaces (Poulsen et al., 2018). More details can be found in the literature (Stull, 1988; Wallace & Hobbs, 2006; Foken, 2008). In summary, aerodynamic resistance comes from the similarity theory to reproduce turbulent behaviour through mean values of atmospheric variables. For simulations, the best fit was achieved with chamber measurements $\bar{U} = 0.3 \text{ m}\cdot\text{s}^{-1}$ at altitude $z = 70 \text{ cm}$ above the soil surface (see Table 5.2).

In cases where the average horizontal wind speed is null, the aerodynamic resistance is then defined as

$$r_a = r_h = \frac{z_h}{D_a} \quad (5.55)$$

Where z_h is the altitude above the soil surface at which the temperature is measured, and D_a [m^2s^{-1}] is the vapour diffusivity in air at a given temperature T [K], given within the diffusion formulation later as

$$D_a = 2.12 \times 10^{-5} \left(\frac{T}{273.15} \right)^2 \quad (5.56)$$

Surface resistance

Surface resistance to evaporation r_s represents the vapour diffusion difficulty above the evaporation front. Vapour passing through the dry layer is not necessarily in equilibrium with moisture content of the pores, and the use of a surface resistance term is required (Camillo & Gurney, 1986; Kondo et al., 1990; Bittelli et al., 2008). Many authors have obtained empirical expressions in terms of the water present at the soil's upper layer. Some authors have suggested that a linear expression for the volumetric water content at the first centimetre below the surface is enough to reduce errors and evaporation corrections (Camillo & Gurney, 1986), while others propose a potential expression at the first two centimetres below surface in open-air evaporation tests (Kondo et al., 1990). Based on chamber tests with air circulation, van de Griend and Owe (1994) propose two expressions depending on the volumetric content of the first surface centimetre: exponential if it is less than 15%, and constant if greater. In all expressions, resistance increases as surface humidity reduces.

Surface resistance has been widely used, although its uniqueness is still highly debated. Each expression has been obtained from specific evaporation conditions and its application in models presents mismatches with observed measurements. Bittelli et al. (2008) implemented a coupled thermo-hydraulic model and concluded that, of the three surface resistance expressions analysed (Sun, 1982; Camillo & Gurney, 1986; van de Griend & Owe, 1994), that of van de Griend and Owe (1994) presented the best fit of their study:

$$r_s = 10 \exp [35.63(0.15 - \theta_{v0})] \quad (5.57)$$

Where θ_{v0} is the volumetric water content at the first surface centimetre. In this study, the specimen is initially slurry with volumetric water content higher than 15%. Thus, a constant value of $r_s = 10 \text{ s}\cdot\text{m}^{-1}$ has been adopted in the boundary condition calculations.

Apart from expressing it in terms of surface moisture, there are other methodologies. Teng et al. (2014) presents a method of parameterization of evaporation that considers a global resistance, obtained from the relative evaporation and using variables measured in the environmental chamber. Other authors have used the distance between the surface and the evaporation front to calculate the surface resistance (Aluwihare & Watanabe, 2003).

For more information on different equations for aerodynamic and surface resistances used in the literature, see Cuadrado (2019).

5.2.5. Model geometry

The problem is represented by a 3D model to capture the soil-water mass fluctuations, suction matrix, and other parameters development in the system. The cylindrical shape of the specimens allows it to be modelled as a cross-sectional segment, considered to be symmetric around its centric axis. The soil is considered homogeneous, with the water content and pores equally distributed throughout the specimen.

The generated mesh consisted of 1080 normally structured quadrilateral elements and 858 nodes, with the mesh refined near the boundaries. The bottom boundary restricted vertical movements only, while the rest of the boundaries were allowed to move freely in space.

While the data for suction, temperature and displacements are read directly on the nodes in the post-processor, the global gravimetric water content is computed at each and every element separately, using the calculated liquid saturation degree and void ratio for each specific element. The acquired value at an element is then projected around the symmetry axis. The procedure results in computing the volume of water in each mesh element. The global water volume in the specimen is then determined from the sum of all the 1080 elements in the mesh system. An illustration is given in Figure 5.2a for a randomly chosen element (element #506) as an example.

The sensors' location, as described in the next section, are shown on the drawing in Figure 5.2b. Since the model is considered to be axisymmetric, the 4 UMS-T5 tensiometers can be axially projected onto the modelled part, preserving their vertical scalar location. See Figure 3.17 (section 3.3.3) for a more detailed cross-section scheme of the environmental chamber specimen.

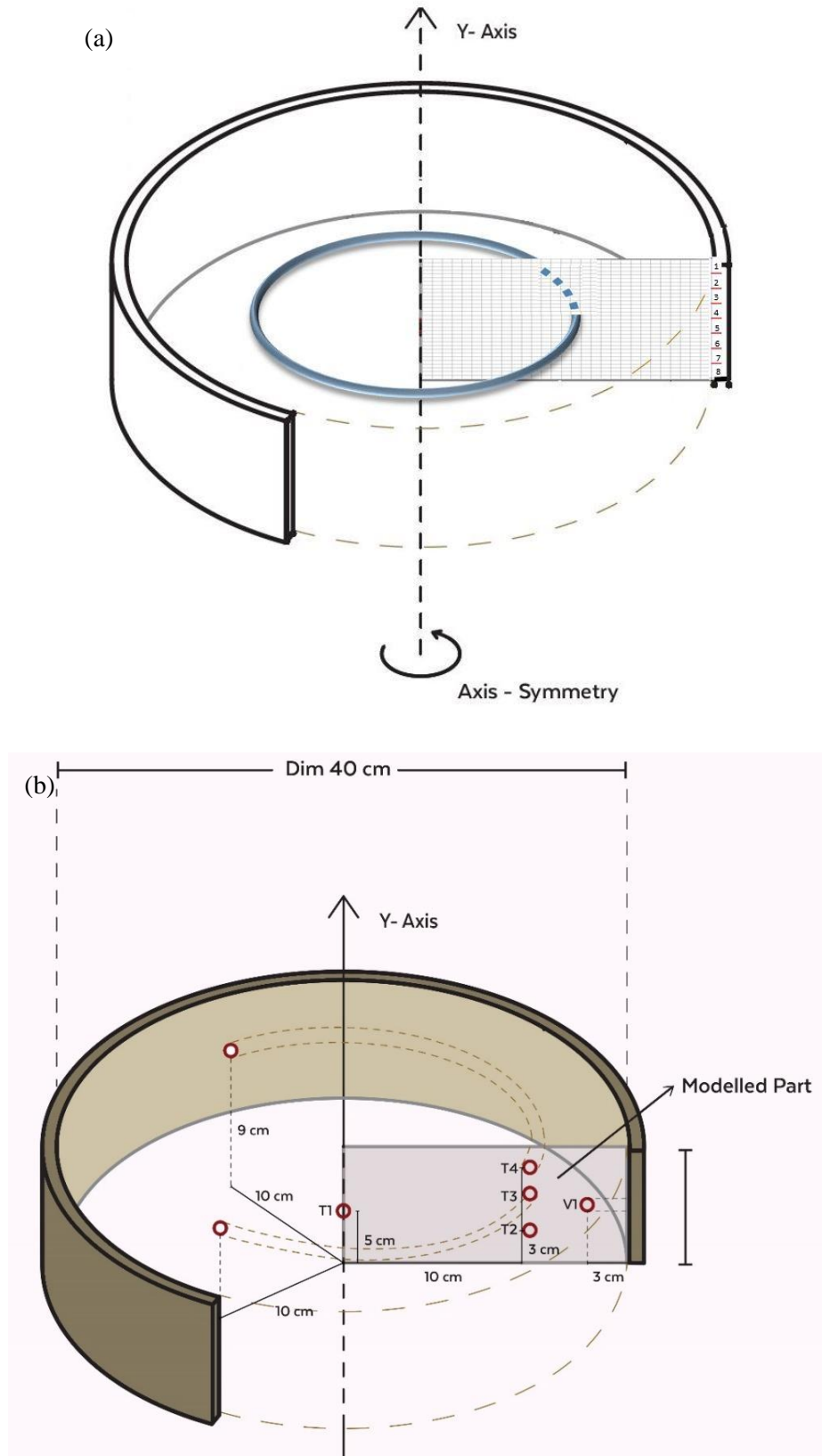


Figure 5-2. Constructed model geometry showing (a) the mesh, boundary conditions, and global gravimetric water content calculation on an element; and (b) the post-processor geometrical reflection analysis method for sensors location.

5.3. Experimental test

5.3.1. Soil characteristics

The soil used in this particular environmental chamber experiment was the Barcelona silty-clay (North-Campus). Soil characteristics and parameters are provided before in Chapter 3 (see Table 3.2).

5.3.2. Environmental chamber

The specimen was subjected to continuous drying in an existing environmental chamber at the UPC laboratory (Chapter 3, Figure 3.17). The environmental chamber is part of an ongoing research dedicated to study the mechanisms of cracking in drying soils (Lloret et al., 1998; Ávila, 2004; Rodríguez et al., 2007; Lakshmikantha, 2009), and has been mentioned in Chapter 3. Temperature was maintained using infrared lamps that were activated as temperature dropped below the designated 35 °C, and deactivated once the temperature rose above the indicated threshold, with a tolerance ± 0.1 °C.

5.3.3. The drying specimen

The soil specimen was prepared at 30% initial gravimetric water content (equal to the liquid limit of the Barcelona silty clay), and dry density $\gamma_D = 1510 \text{ kg}\cdot\text{m}^{-3}$, in the 40-10 cm cylindrical mould instrumented with different sensors (Figure 5.2b). Sensors marked T1-T4 are the UMS-T5 tensiometers (discussed in Chapter 3), inserted into the soil body at different depths to capture the suction development profile up until 100 kPa. The Vaisala® HMP-230 hygrometers (V1 and V2) (see chapter 3 also) measuring the soil relative humidity and temperature were placed at their location through the lateral boundary ten days after drying initiation, when the specimen started desaturating following cavitation of the tensiometers. The specimen ensemble was placed over three load cells (SSM) to capture weight fluctuations, attributed to soil water loss.

5.3.4. Experimental results

The total duration of the test was 110 days, but the residual moisture content was reached after 40 consecutive days of drying. The lack of internal cracks reaching the upper surface provided the advantage of eliminating associated uncertainties of quantifying evaporation from within a complex crack network, allowing the application of a homogeneous boundary condition to simulate soil-atmosphere interaction. Another advantage is the existence of the perimeter crack

between soil and mould, with a well-defined geometry that allows the application of boundary conditions on the lateral, vertical surface.

5.3.5. Imposed conditions in the environmental chamber

The value of the relative humidity was maintained close to 40% during the first 25 days, dropping below that target value between days 25 and 45. Temperature on the other hand remained constant at about 35 °C, except for days 7 to 9 where it dropped to 30 °C. However, a simplified constant value of 35 °C has been used in the numerical simulations for the whole period.

5.3.6. Internal wind circulation

The internal horizontal wind circulation created by the dehumidifier had a direct impact on the evaporation rate and needed to be quantified accordingly. Wind speed was not measured in the original test, so the atmospheric conditions were recreated inside the environmental chamber and the wind speed was measured during a similar test while the dehumidifier was activated. A high-precision sonic anemometer DS-2 (DECAGON) was mounted on an adjustable tripod to take readings at different altitudes from the specimen surface (Figure 5.3). The anemometer records an average and a maximum wind speed every minute. The recorded average (\bar{U}) and maximum (U') wind speed values are given in Table 5.2.

Table 5.2. Wind measurements in the central axis of the environmental chamber showing the vertical measurement height above the soil surface (z); the number of measurements taken (N); the average wind speed (\bar{U}) and the mean burst speed (U') recorded.

z [cm]	N	\bar{U} [m·s ⁻¹]	U' [m·s ⁻¹]
10	19	0.1	0.2
60	18	0.1	0.2
70	24	0.3	0.5
80	14	0.2	0.3

The average wind speed inside the environmental chamber does not adjust to the logarithmic profile of bare soils in open field conditions (Campbell & Norman, 1977; Hillel, 2004; Tagesson, 2012). Therefore, a use of aerodynamic resistance in the energy balance equation can be considered as an approximation, as some research has considered previously for environmental chambers, with satisfaction (van de Griend & Owe, 1994; Yamanaka et al., 1997; Cui et al., 2012). Since gust speeds reach double the average speed, wind turbulence is expected to influence vapour diffusion, favouring advective fluxes.



Figure 5-3. Anemometer mounted inside the environmental chamber for wind measurements under test conditions similar to the original.

5.4. Numerical simulations

Simulation results were presented in three blocks (A, B, C) with each model adding more complexity to its preceding, depending on previous results and analysis. Each of the blocks was divided into three distinct simulations, resulting in a total of nine simulations. However, since this work has already been published (Cuadrado et al., 2022), a summary of each block will be given only.

5.4.1. Material constitutive parameters

Table 5.3 shows the constitutive parameters fitted in all three blocks of simulations. The retention curve and intrinsic permeability, both considered an intrinsic property of the soil, are constant in all simulations. Tortuosity is set either constant or solved with the exponential law (equation 5.22): increases with the decrease of degree of saturation, thus enhancing the diffusivity and intensifying the diffusive evaporative fluxes at late stage drying, where the advective fluxes towards the surface (equation 5.5) are no longer dominant.

The mechanical problem is only introduced in block C simulations. The initial fluid-like (slurry) consistency of the specimen provides an advantage of homogeneity, while making it difficult to obtain mechanical parameters. The primary self-weight consolidation causes a thin layer of water to appear at the soil surface, and vertical shrinkage appears prior to crack initiation. A relatively high value of parameter a_1 with a low K_{min} were incorporated to reproduce the initial settling behaviour

Table 5.3. Constitutive equation parameters for blocks A, B and C.

	Parameter	block A	block B	block C		
				C1	C2	C3
Retention curve (Equation 5.12)	P_0 [MPa]	0.05				
	n	0.26				
Intrinsic permeability (Equation 5.17)	k_{i0} [m ²]	10^{-14}				
Tortuosity Fick's law (Equation 5.22)	τ_{r0}	1	-	-		
	A_τ	-	8	6	5	8
	m_τ	-	3			
Non-linear elasticity mechanical model (Equation 5.10)	a_1	-			-1	
	a_2				0	
	a_3				0	
	ν_P				0.3	
	K_{min}				0.01	

5.4.2. Boundary conditions

Table 5.4 shows the prescribed vapour concentration and gas density calculated from equations 5.45 and 5.44, respectively. These values were used as inputs in the assigned boundary conditions as indicated in each block of simulations.

Table 5.4. Conversion of measured atmospheric variables in the chamber into prescribed vapour mass fraction and gas density for the imposed boundary condition.

t (h)	$(\omega_g^w)^0$	$(\rho_g)^0$	t (h)	$(\omega_g^w)^0$	$(\rho_g)^0$	t (h)	$(\omega_g^w)^0$	$(\rho_g)^0$
0.0	0.0132	1.1213	334.4	0.0132	1.1213	769.8	0.0117	1.1224
41.8	0.0137	1.1209	376.2	0.0131	1.1214	811.6	0.0110	1.1228
81.9	0.0137	1.1210	418.0	0.0130	1.1214	853.4	0.0099	1.1235
125.4	0.0140	1.1207	459.8	0.0134	1.1212	895.2	0.0093	1.1240
167.2	0.0140	1.1208	532.9	0.0135	1.1211	937.0	0.0105	1.1232
209.0	0.0131	1.1214	576.5	0.0137	1.1209	978.8	0.0087	1.1244
252.5	0.0135	1.1211	616.5	0.0103	1.1233	1020.6	0.0088	1.1243
292.6	0.0137	1.1209	700.1	0.0119	1.1222	1062.4	0.0098	1.1236

Table 5.5 shows the assigned constant boundary conditions at the two boundaries (upper and lateral surfaces) parameters assigned for each of the three simulations in block A. Setting the transfer coefficient β_g to 0 indicates a hydraulically impermeable layer. The lower the value the lower is the diffusion gradient and evaporation rate, and vice-versa. Temperature was imposed at a constant value equal to the measured physical value in the environmental chamber.

Table 5.5. Boundary conditions for block A.

Parameter	Equation	Upper			Lateral		
		A1	A2	A3	A1	A2	A3
$(\rho_g)^0$	5.44		1.1308				1.1308
$(\omega_g^w)^0$	5.45		0.0139				0.0139
T^0 [°C]	19		35		0		35
β_g	26	10^3	0.001				0.001
γ_e	27	10^3	1				1

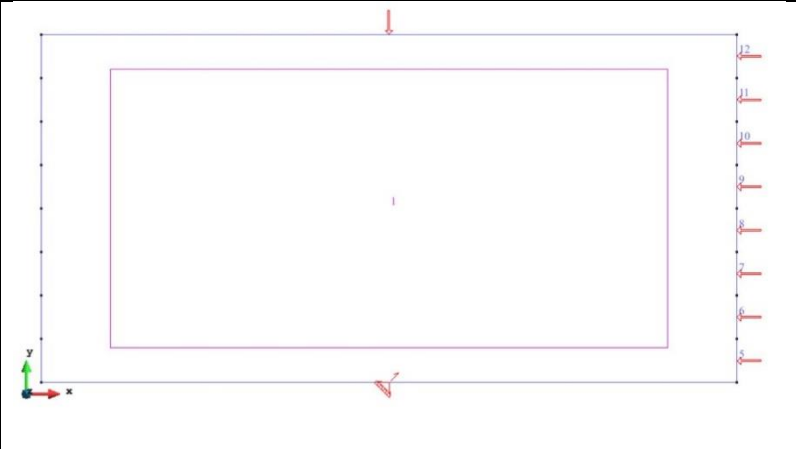
In block B, the boundary conditions are made variable, according to table 5.6. The transfer coefficients are calculated based on the aerodynamic resistance values: $\beta_g = 0.0012$ and $\gamma_g = 1.4571$ (equations 5.51 and 5.52, respectively), which in turn is based on the best-fit wind measurements at the chamber (equation 5.54).

Table 5.6. Boundary conditions for block B.

Parameter	Upper			Lateral		
	B1	B2	B3	B1	B2	B3
$(\rho_g)^0$	Table 5.4			Table 5.4	1.1308	
$(\omega_g^w)^0$	Table 5.4			Table 5.4	0.0139	
T^0 [°C]	35			35	35	
β_g	0.0012			Table 5.7	0.001	
γ_e	1.4571			10	1	

A progressive opening of the crack is assigned by activating the transfer coefficient β_g at progressive times depending on the elapsed experimental test time (table 5.7).

Table 5.7. Sequential crack segments activation time for B1 and B2.

Lateral Segments	$t_{activation}$ (h)	β_g (B1)	β_g (B2)
	81.9	0.0012	0.0004
	125.4		
	167.2		
	167.2		
	252.5		
	252.5		
	252.5		
	292.6		

For that purpose, the lateral boundary was geometrically divided into 8 equal segments (see Figure 5.2a). Each segment is activated at a different $t_{activation}$ time, depending on the crack opening propagation. At each activation time the corresponding segment is released

mechanically, replaced by the atmospheric pressure, and then the hydraulic boundary conditions are applied through the transfer coefficient β_g .

Figure 5.4 shows the sequential crack opening for the different segments.

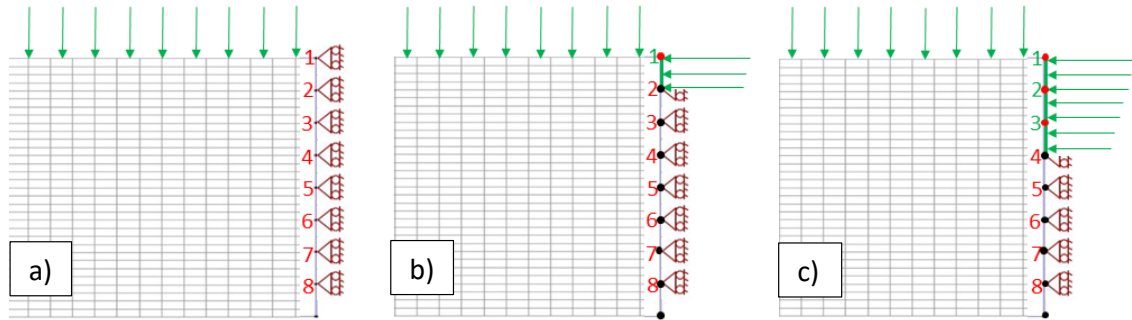


Figure 5-4. Node-release technique replicating the sequential crack-opening.

A lower β_g value assigned at the lateral boundary (crack surface) indicates a lower effective turbulent diffusion due to wind, which has been verified experimentally to impact the evaporation rate (Poulsen et al., 2020).

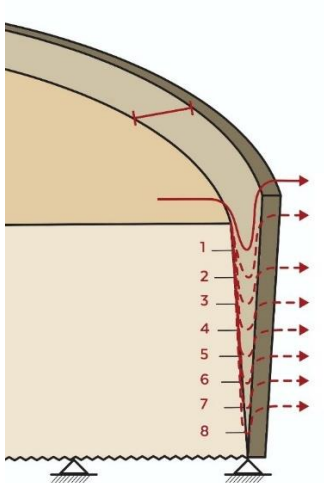
In block C (Table 5.8), a similar sequential crack activation time is assumed. However, the transfer coefficient β_g decreases with depth at the perimeter crack, implicating a reduction in wind magnitude effect at the deepest part of the crack (table 5.9).

Table 5.8. Boundary conditions for block C.

Parameter	Eq.	Upper			Lateral		
		C1	C2	C3	C1	C2	C3
$(\rho_g)^0$	16		Table 5.4		0		Table 5.4
$(\omega_g^w)^0$	18		Table 5.4		0		Table 5.4
T^0 [°C]	19		35		0		35
β_g	26		0.0012		0	0.0012	Table 5.9
γ_e	27		1.4571		0		1.4571

For the three blocks of simulation, the bottom boundary condition was impermeable to evaporation, therefore the parameters $(\rho_g)^0$, $(\omega_g^w)^0$, and β_g are equal to 0. An imposed temperature $T^0 = 35$ °C was assigned to the bottom boundary with a high transfer coefficient $\gamma_e = 10^3$ J·m⁻²·s⁻¹·°C⁻¹, indicating a high heat transfer gradient at the bottom.

Table 5.9. Sequential crack segments activation time for C3.

Lateral Segments	$t_{activation}$ [h]	β_g (C3)
	81.9	0.0012
	125.4	0.001
	167.2	0.0006
	167.2	0.0004
	252.5	0.00026
	252.5	0.00026
	252.5	0.00026
	252.5	0.00026
	292.6	0.00026

5.4.3. Discussion

The results from only the final simulation of each block are demonstrated here: simulation A3, B3, and C3. For the full range of results see Cuadrado et al., (2021).

Figure 5.5 shows the experimental results with the numerical results of the last of the three simulations from each of the blocks (i.e., simulations A3, B3, and C3). The block A simulations resulted in the conclusion that assigning a high transfer coefficient value (e.g., $\beta_g=10^3$) results in a very high diffusion gradient at the soil surface, which leads to a higher evaporation rate. On the contrary, reducing the transfer coefficient value indicates low wind speed values and evaporation occurring mainly by molecular diffusion (i.e., lower evaporation rate). Even as the crack surface allows evaporation in A3, the gravimetric water content evolution still underestimates the magnitude of evaporation (Figure 5.5a).

Suction results at the location of the sensors indicates a numerical suction surge as early as the drying starts, not capturing the constant evolution behaviour below the air entry value which was the case experimentally (Figure 5.5b). The soil relative humidity as captured by the Vaisala sensor is demonstrated against numerical results of the final simulation of each block (Figure 5.5c).

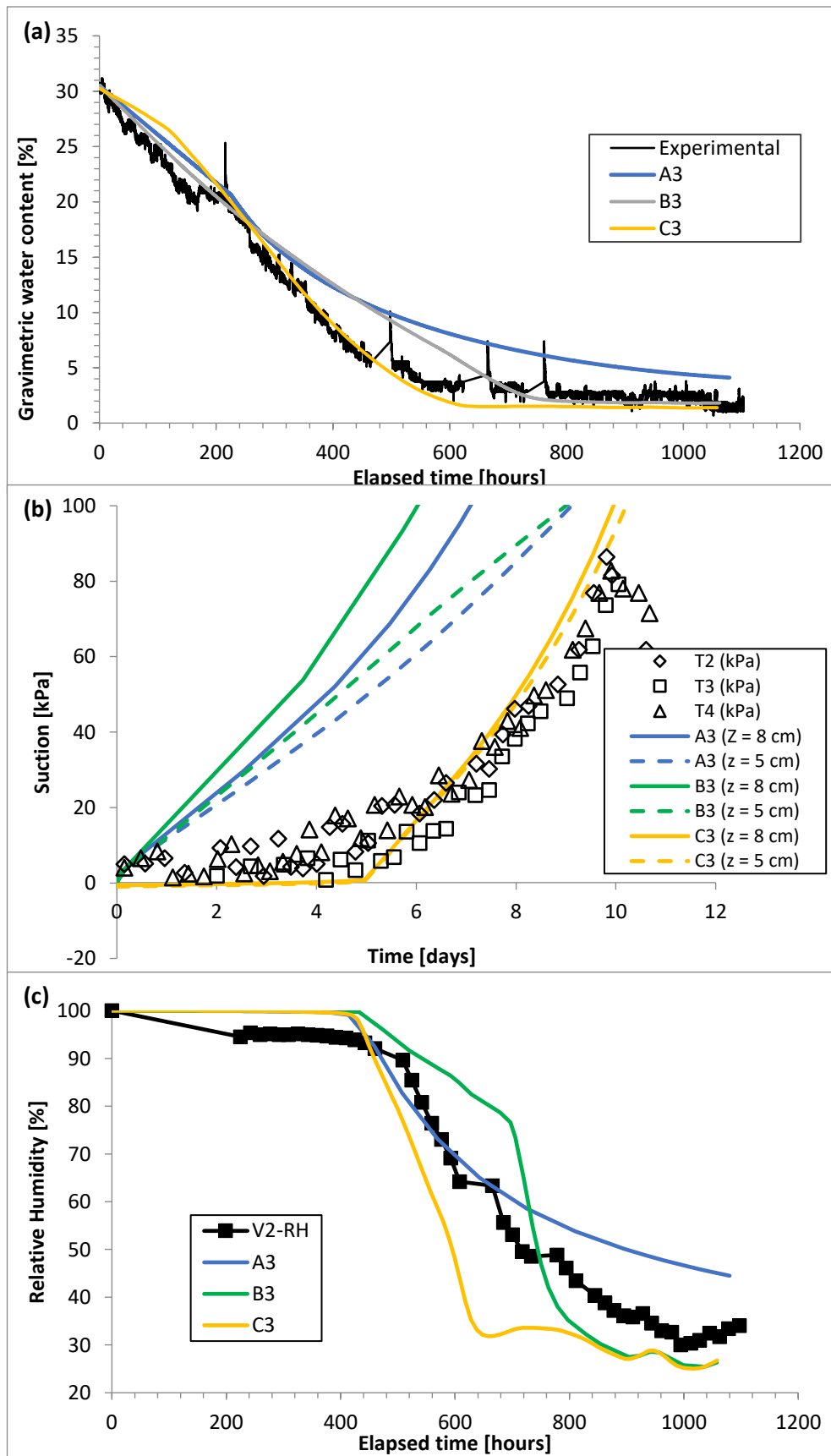


Figure 5-5. Final simulation results showing numerical versus experimental results for the (a) global gravimetric water content loss; (b) early stage suction; and (c) soil relative humidity.

The block B simulations include the added tortuosity factor (Table 5.3), as to enhance the evaporation by diffusion. The application of soil diffusion enhancement factors has been used to reproduce the measured evaporation (Parlange et al., 1998; Schelde et al., 1998; Saito et al., 2006; Bittelli et al., 2008; Smits et al., 2011; Han et al., 2013; Gran, 2015). From the first studies of thermo-hydraulic coupling (Gurr et al., 1952; Taylor & Cavazza, 1954), an increase in vapour flux inside the soil has been noted to surpass the Fick's law predictions (Campbell & Norman, 1998). From this observation stems the need to apply diffusion improvement factors (i.e., tortuosity factor). This improvement can be due to convective vapour cells as a result of soil volumetric fluctuations (shrinkage-expansion) during a day cycle (Parlange et al., 1998); due to condensation-evaporation mechanism in isolated liquid area, or due to local difference of thermal conductivities increasing the gradient (Philip & De Vries, 1957).

Block B also focuses on the magnitude of the transfer coefficient β_g assigned to the lateral surface with sequential activation times of the lateral segments implying a crack propagation from top to bottom (Table 5.7). The imposed boundary conditions are not equal to the experimental recorded values which gives a better adjustment. However, the early suction evolution behaviour was still not captured. This can be related to the fluid initial state of the soil (slurry specimen), and the initial settlement under self-weight.

In Block C, the mechanical part is added (Table 5.3), and the crack propagation is made sequential, with reducing β_g values with depth implying a reduced effect of wind within the crack opening (Table 5.9). The early-stage physical suction development behaviour is now numerically captured, and the gravimetric water content evolution is improved. It can be seen that the evaporation from the crack surface, although happening at a lower magnitude, still has an impact on the problem. This is consistent with the experimental observations of a low cracking impact on the evaporation rate at the beginning of a drying test (Tang et al., 2011; Cuadrado, 2019). At later stages, as the atmosphere within the soil cracks becomes in equilibrium with the outer atmosphere imposed on the soil top surface, its effect on evaporation increases.

5.5. Constitutive parametrical study

In the final block of simulations (i.e., block C), the mechanical model was incorporated, allowing for soil drying shrinkage. The porosity changes occurring in a soil undergoing shrinkage drying affect the hydraulic properties implicitly through the balance equations (equation 5.7), and through its direct effect in the constitutive model equations (relative permeability, intrinsic permeability, retention curve, etc.). To investigate the effect of porosity, change on the hydraulic model, the constitutive equations presented above were modified to

involve the porosity change. Additionally, another function of liquid phase relative permeability was investigated.

5.5.1. Effect of porosity change on intrinsic permeability

As the soil body dries, the pores in between soil particles shrink due to the escaping water from the macro-pores, narrowing the passages of advective water and vapour fluxes. This would lead to a decrease in the hydraulic conductivity within a continuum soil body.

However, it has been proven experimentally that soil desiccation cracks have the opposite effect on the hydraulic conductivity. In their study, Albrecht and Benson (2001) conducted desiccation tests on compacted soils with an objective to study the hydraulic conductivity as affected by desiccation. In their experimental work the specimens were compacted at 3% wet of optimum, at optimum and at 3% dry of optimum.

The specimens were subjected to four cycles of wetting and drying. The hydraulic conductivity increased for all the specimens after desiccation, but the largest increase in hydraulic conductivity and shrinkage strains occurred for specimens compacted wet of optimum water content. The hydraulic conductivity has been found to increase after desiccation by one order of magnitude (Omidi et al., 1996), or three orders of magnitude (McKay et al., 1993). However, the soils in their study have experienced fractures or internal cracks that might had created preferential hydraulic pathways.

The intrinsic permeability expression is provided based on Kozeny's model and is given by a simple exponential law with a fitting parameter b_k , instead of the expression in equation 5.17.

$$k_i = k_{i_0} \exp[b_k(\phi - \phi_0)] \quad (5.58)$$

Where the non-dimensional fitting parameter b_k controls the effect of the magnitude of change of porosity on the intrinsic permeability; and k_{i_0} [m^2] is the matrix intrinsic permeability at reference porosity $\phi = \phi_0$, a mere geometrical hydrodynamic feature impartial of the gaseous and fluid states (Stoltz et al., 2010). As the parameter b increases, the effect of porosity changes on the permeability increase (Figure 5.6), causing a higher drop in intrinsic permeability with the decrease in porosity.

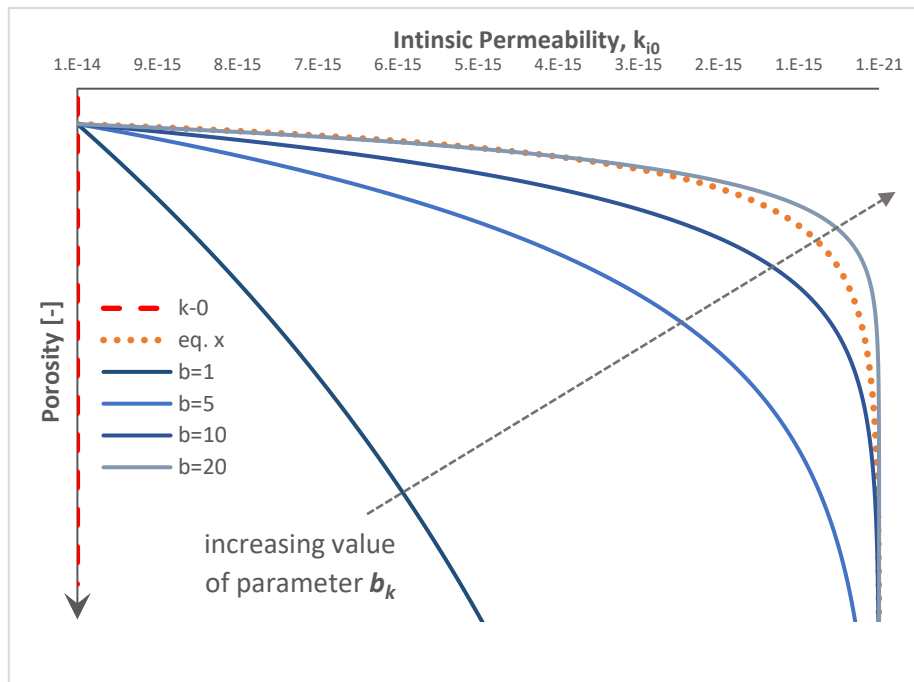


Figure 5-6. Intrinsic permeability change with decrease in porosity, following equation 5.58.

5.5.2. Effect of porosity change on SWRCs

The SWRC, the relationship between suction and water content or degree of saturation, is one of the main characterising components of constitutive models for describing the unsaturated soil-moisture retaining capacity and flow in deformable porous material (discussed in detail in chapters 3 and 4). The water retention is mainly controlled by the soil pores characteristics (Richard et al., 2001; Dexter et al., 2008; Romero & Jommi, 2008; Li & Zhang, 2009; Matthews et al., 2010). The SWRCs has been generally found to be significantly affected by the soil compaction level and void ratio (Sun et al., 2008, 2014; Ce et al., 2020; Qian et al., 2021), with existing models that incorporate the effect of void ratio on the SWRC equation (Mašín, 2010; Gallipoli, 2012). The model employed in this work is the well-established van Genuchten (1980). Many authors since then presented some modifications based on the closed-form equation of van Genuchten (1980). Some researchers introduced correction factors to the shape parameter, as to consider the effect of intra- and inter-aggregate pores, and their interaction and contribution in relation to capillary and specific surface as a function of moisture, and the effect of fabric changes (Fredlund & Xing, 1994; Romero & Vaunat, 2000; Romero et al., 2011). Others extended the model to allow for volume change in porous material (Gallipoli et al., 2003).

In this work, the effect of porosity change is incorporated in the retention curve (equation 5.12). To simplify the problem and reduce the number of fitting-parameters, it was considered that

$a_p = a_n$ (see equation 5.12, section 5.2.3.2), signifying a similar effect of porosity change on both SWRC parameters P and n . The obtained experimental retention curve for the soil being studied in this chapter at the corresponding initial conditions (slurry), was fitted using the modified form (equation 5.12). Having the two extra fitting parameters and accounting for changes in pores leads to a better fit of the experimental SWRC. See Chapter 3 for more details concerning fitting the SWRCs.

5.5.3. Liquid phase relative permeability

While liquid phase relative permeability, as seen in Darcy's law (equation 5.18), is not affected by changes in porosity, it is however affected by changes in the liquid saturation degree, and different laws exist that define the nature of the relation with the degree of saturation. Although the van Genuchten model proved to represent well the soil-water evolution in this chapter, it does not always fit with the suction and displacements development. The generalized power or Corey function (Brooks and Corey, 1964) can be fairly representative of this problem type

$$k_{r_{l,g}} = A_{r_{l,g}} S_e^{r_{r_{l,g}}} \quad (5.59)$$

Where S_e is the effective degree of saturation; and $A_{r_{l,g}}$ and $r_{r_{l,g}}$ are two Corey function adjusting parameters where the subscripts l, g refer to the liquid and gaseous phases, respectively. The values of these parameters were topic of study for many authors, acquired by end-point slope analysis for strictly hyperbolic models of three-phase flow in porous media (Juanes & Patzek, 2004), viscous coupling between two fluids flowing simultaneously in a single fracture (Burdine, 1953; Brooks et al., 1964; Fourar & Lenormand, 1998), etc. The viscous coupling model leads to simple analytical relationships between the relative permeabilities (k_{r_α}) and either saturation or fluid velocities. The estimated power law function (Burdine-Brooks-Corey) (Brooks and Corey, 1964), originally proposed for oil-water-gas flow, suggested r_{r_l} values between 2 and 4 and as a function of fluid characteristics (wetting/non-wetting phase) and pore space morphology (Burdine, 1953; Brooks et al., 1964). They found a direct relation between the value of r_{r_l} and the viscosity ratio μ . The SWRC model of Brooks and Corey (1964) is a widely used and easy to derive discontinuous empirical expression that introduces the pore size distribution index, an empirical constant. Mualem (1974, 1976) combined his series-parallel bundle of capillary tubes model with Brooks and Corey (1964) capillary pressure curve equation to find an empirical tortuosity-connectivity exponent. His approach is widely used to predict the relative hydraulic conductivity in terms of the SWRC. This approach is dependent on the r_{r_l} values. Assouline (2005) calculated the values of r_{r_l} for different silty clay soils and derived several empirical equations to relate the saturation degree

and relative permeability according to the pore size index. The Mualem approach (Mualem, 1974; 1976) can be applied to the Brooks and Corey expression to predict the relative hydraulic conductivity in terms of the SWRC. The generalized Corey power expression was often used to calculate the phase relative permeability of liquid and gas by data fitting and optimizing (Tuli et al., 2005). Some researchers proposed certain empirical methods to calculate the value of the parameter A_{r_l} , based on calculations of a tortuosity–connectivity parameter, as a function of the saturation degree (e.g., Tuli et al., 2005). Others suggested different methods for calculations of relative permeability from capillary pressure, neglecting the effect of the tortuosity and connectivity (Li & Horne, 2006).

Figure 5.7 shows the dependence of the liquid phase relative permeability k_{r_l} on the effective degree of liquid saturation S_e . The models shown all have in common the value of $r_{r_l} = 3.0$, since it was assumed an intrinsic characteristic of the soil type and not the placement or compaction conditions. However, the value of the parameter A_{r_l} was assumed dependent on initial placement conditions, therefore controlling the magnitude of effect of increasing initial water content on the relative permeability k_{r_l} . This model will be applied in Chapter 6 when dealing with soil specimens prepared at different compaction levels and initial conditions. The model provides more control over the calibration process to obtain best-fit parameters, instead of having the constant van Genuchten parameter to fit both the SWRC and the liquid phase relative permeabilities.

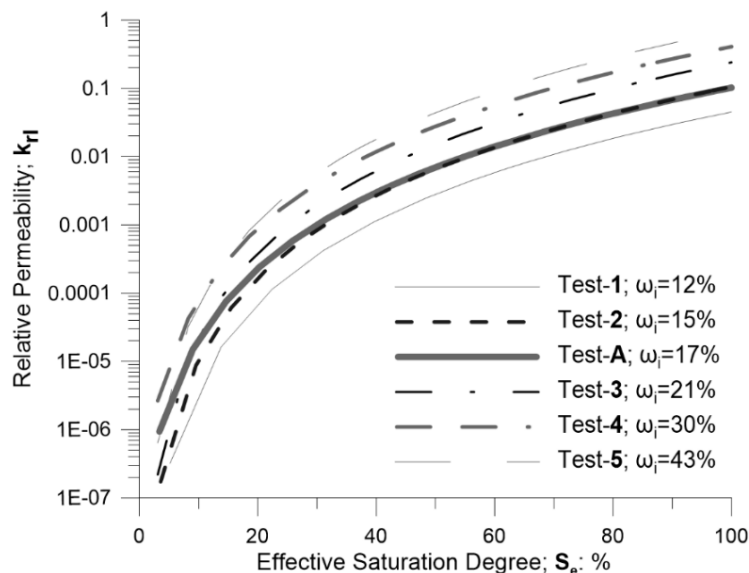


Figure 5-7. Liquid phase relative permeability dependence on liquid saturation degree, using Corey's power law.

5.5. Conclusions

The constructed numerical model is based on established concepts of unsaturated soils and vapour fluxes in deformable porous soil medium. The simulations finally reproduced to a great extent the experimental behaviour of a soil sample undergoing drying in a laboratory environmental chamber. In order to improve the quality of numerical simulation process, the numerical boundary condition must adequately reproduce the physical environmental conditions. This was carried out by translating the recorded meteorological data: relative humidity, temperature, and wind velocity into prescribed vapour mass fraction, gas density and latent heat transfer coefficient, respectively. The constitutive model set of equations was fitted to the experimental data where possible (e.g., retention curve, hydraulic conductivity, etc.). The constitutive model considers both coupled TH processes and coupled THM processes, separately, explaining the importance of considering mechanical changes in similar problems. Apart from being implicitly considered in the mass balance equations (through material derivatives), the mechanical changes (i.e., change in porosity), affect directly the constitutive equations (e.g., intrinsic permeability, SWRC, thermal conductivity). The numerical simulation results were compared against the experimental results of global gravimetric water content loss, early-stage suction (as measured by the UMS-T5 tensiometers), and soil relative humidity (as measured by the Vaisala Hemp-230 sensor). This chapter is considered as a basis for the more advanced models in the following chapters, as it shows the first attempts carried out at modelling the desiccating soil behaviour. The constitutive set of equations can be developed for different soil conditions (slurry and compacted), and to predict the mechanical changes and its effect on the THM processes. The boundary flux as well can be developed to replicate the real-time imposed environmental conditions (whether in lab or field conditions).

Chapter 6

Numerical Simulation of Laboratory Desiccation Tests and a Large-Scale Field Experiment

Parts of this chapter have been published in

1- The 4th European Conference on Unsaturated Soils (E-UNSAT 2020), with the title:

“Experimental and Numerical Analysis of Soil Desiccating Cracks in Compacted and Non-Compacted Specimens”.

On October 2020, with the co-authors:

Josbel Cordero, Abdallah Najdi, David Encalada, Pere Prat, Alberto Ledesma.

6.1. Introduction

Bare topsoils are continuously exposed to the external atmospheric conditions. These imposed atmospheric conditions interact with soil surfaces, causing exchanges and fluxes of energy, heat, and vapour. The soil-atmosphere interaction leads to mechanical changes and in many cases to surface cracking.

On site, soils are often subjected to certain compaction efforts to ensure higher stability and structural integrity. The initial moisture content governs the soil consistency and manageability. Soils with initial water content lower than the plastic limit might introduce heterogeneity and handling difficulties such as crumbling upon mixing. Meanwhile, wetter soils might be prone to higher shrinkage potential.

With the increase of use of engineered soil structures, the need arises for anticipating the drying shrinkage behaviour at different initial placement conditions and studying the involved factors. In this perspective, the previously established model (see Chapter 5) was expanded to simulate soils prepared at different compaction and initial conditions, exposed to the atmosphere. The model functionality was extended to fully reproduce the unsaturated thermo-hydrromechanical behaviour. The applied numerical hydraulic boundary condition was further developed to replicate to a high responsiveness and precision the full characteristics of the imposed atmospheric conditions. The developed model was applied to both laboratory experiments and to a large-scale experiment in the field.

The aim of this chapter is to enhance the numerical modelling of soil-atmosphere interaction problems, and present novel techniques regarding the calibration of constitutive parameters essential for the models, and the adequate interpretation of physical imposed atmospheric conditions into numerical fluxes and transfer coefficients at the soil-atmosphere interface. It presents the details needed to be included in the numerical modelling in order to achieve numerical results of utmost conformity with the physical ones.

Multiple specimens of the Agròpolis soil have been prepared at different compaction levels and water contents and exposed to varying atmospheric conditions, to better calibrate the developed numerical model, and prove its applicability to a wide range of problems. The numerical steps are firstly presented for the simulations of the seven laboratory specimens in the environmental chamber, and secondly the large-scale field experiment. All experiments were analysed following the same numerical approach. The numerical models successfully predicted the resulting soil-water evaporation, suction growth, temperature evolution, crack propagation and displacements profiles. The objective, to mathematically frame the soil characteristics and

imposed soil-atmosphere interactions, and to reduce soil behaviour prediction efforts for design project applications, was obtained.

6.2. Experiments

The soil used in all experiments is the well-studied low plasticity silty clay, extracted from Agròpolis (Chapter 3, Table 3.2). The experimental campaign consisted of three parts: (1) environmental chamber drying tests on different initial condition specimens; (2) field drying test on a large-scale specimen; (3) soil characterisation tests to estimate the essential constitutive parameters for the numerical modelling of the different experiments.

The weight of the specimens was continuously monitored throughout drying using load-cells, to measure global gravimetric water content evolution. The descriptor of superficial cracking is the Crack Intensity Factor (CIF) (Miller et al., 1998). Continuous specimen's surface photographs were processed at regular intervals using a unique image analysis technique to determine developing cracks area (Lakshmikantha et al., 2009; Cordero et al., 2020). In one of the laboratory experimental tests (S-LL), only the final CIF value is provided based on a single final-state image (Lakshmikantha, 2009).

6.2.1. Environmental chamber tests

To study the effect of initial conditions and compaction levels on the soil response to desiccation, different specimens were prepared with different initial gravimetric water content (w_0) and dry density (γ_D): four specimens following the Standard Proctor (SP) compaction curve; one specimen following the Modified Proctor (MP); and one slurry specimen at 1.5 times the liquid limit (SL). One specimen was prepared from the “North Campus” soil (see Chapter 3, section 3.2), at Liquid Limit (LL). The latter is the specimen used for modelling in the previous chapter (Chapter 5). However, in this chapter, the mechanical model complexity and boundary condition file are upgraded for a full replication of physical conditions. Table 6.1 shows the different specimens modelled in this chapter, with corresponding initial conditions and source references.

A compaction routine was defined to equalize Standard (ASTM D698) and modified Proctor (ASTM D1557) compaction effort ($600 \text{ kN}\cdot\text{m}\cdot\text{m}^{-3}$, and $2700 \text{ kN}\cdot\text{m}\cdot\text{m}^{-3}$; respectively) with that used to prepare the specimens directly inside the specimen mould in the laboratory. On the other hand, the slurry specimens were poured in the mould directly while tapping on the mould sides to eliminate entrapped air. Figure 6.1 shows the different specimens modelled in this chapter on the Proctor chart with the corresponding w_0 [$\text{g}\cdot\text{g}^{-1}$] and γ_D [$\text{g}\cdot\text{cm}^{-3}$].

Table 6.1. Initial conditions of the different experimental specimens.

Spec.	w_0 [g·g ⁻¹]	γ_D [g·cm ⁻³]	ϕ_0	Compaction effort	Source / Reference
A-MP3	0.150	1.90	0.299	MP – wet of optimum	(Najdi et al., 2023a)
A-S1	0.120	1.72	0.366	SP – dry of optimum	(Cordero, 2019)
A-S2	0.150	1.80	0.336	SP – near optimum/dry	
A-S3	0.172	1.79	0.339	SP – near optimum/wet	(Najdi et al., 2023a)
A-S4	0.210	1.68	0.380	SP – wet of optimum	(Cordero, 2019)
NC-LL	0.300	1.50	0.465	Liquid Limit	(Lakshmikantha, 2009)
A-SL	0.430	1.20	0.557	SLurry	(Cordero, 2019)
A-FE	0.435	1.19	0.561	Field Experiment - Slurry	(Cordero et al., 2020)

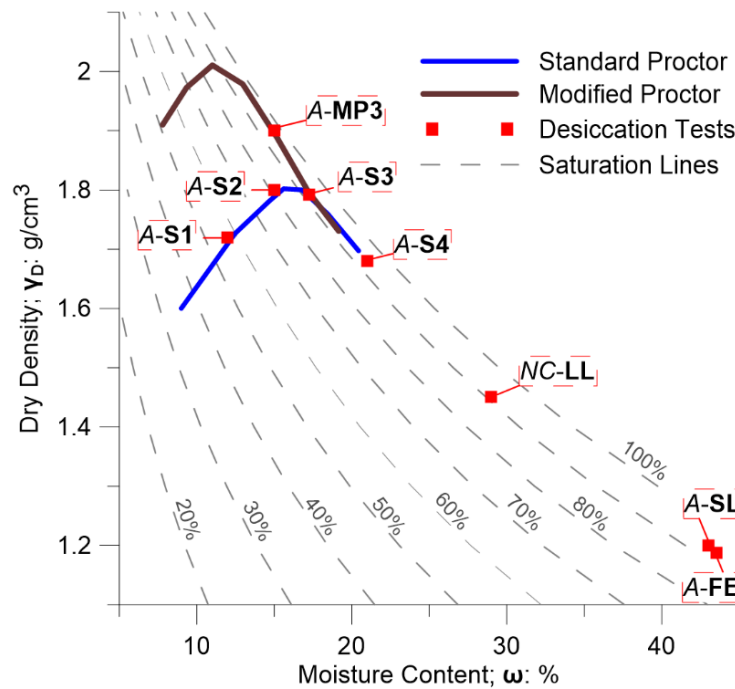


Figure 6-1. Proctor compaction curves for the Agròpolis soil, showing the specimens initial conditions.

6.2.1.1. Imposed Environmental Conditions

The specimens were subjected to desiccation inside the environmental chamber, under controlled conditions of imposed air temperature, T_a , and air relative humidity, RH_a . In each case, the target was to circulate dry air while removing wet air, maintaining $RH_a \approx 30\%$ and $T_a \approx 20^\circ\text{C}$, until achieving steady-state residual conditions. Testing times ranged between 300 to 1150 hours, depending on the initial conditions of each specimen. Recorded chamber RH_a and T_a for each experiment are shown in Figure 6.2.

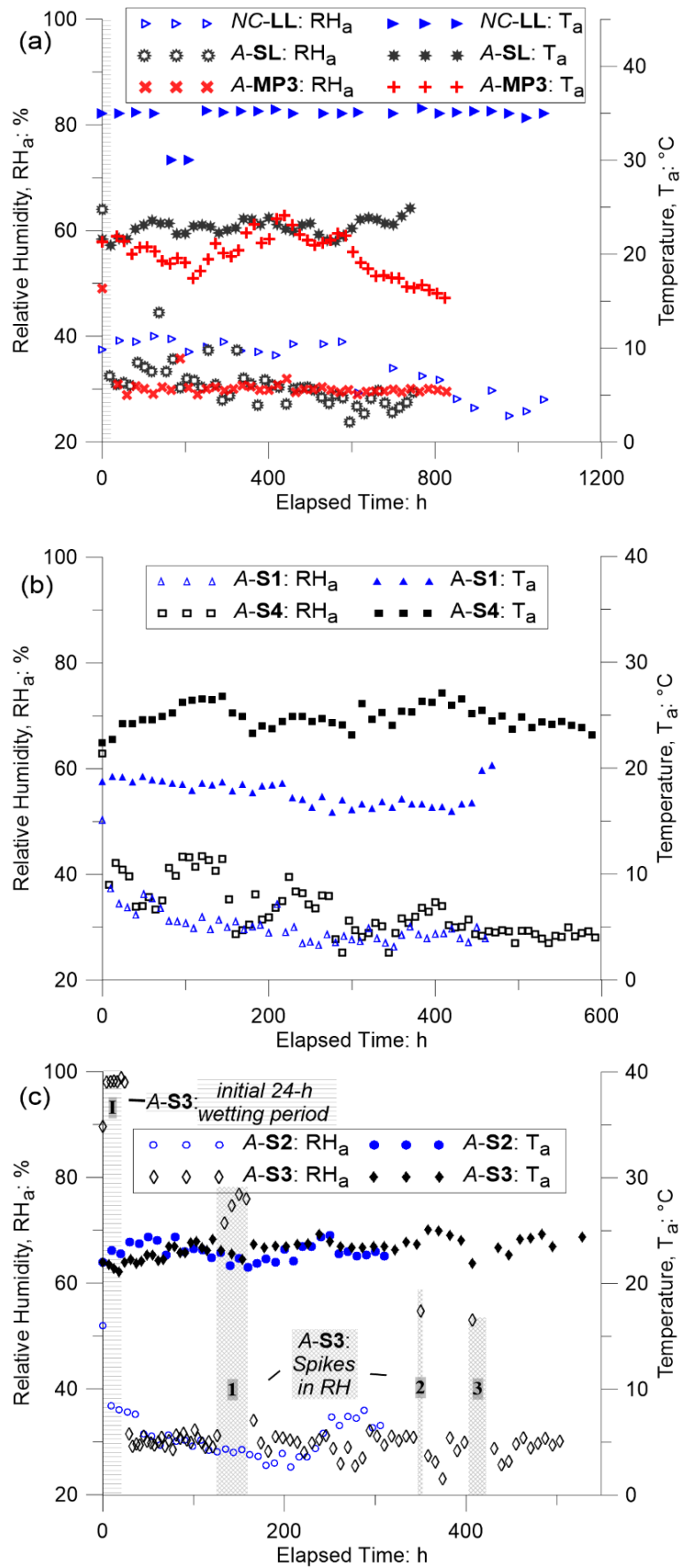


Figure 6-2. Atmospheric conditions (RH_a and T_a) imposed in the laboratory environmental chamber for (a) NC-LL, A-SL and A-MP3; (b) A-S1 and A-S4; (c) A-S2 and A-S3.

6.2.1.2. Specimens Setup

Laboratory specimens were prepared in cylindrical moulds (Chapter 5), with a grooved base restricting bottom soil movement. The mould used was 10 cm in height and 40 cm in diameter, and a larger 80 cm diameter mould was used for the slurry specimen (A-SL).

The sensors layout was similar to the one explained in Chapter 5: soil temperature T_s and relative humidity RH_s were measured using the two embedded Vaisala® HMP-230 sensors (i.e. V1 and V2), mounted on opposite sides at 3 cm from the periphery and to specimen mid-height (5cm depth); and early stage matric suction measurements were obtained through the four UMS-T5 sensors fitted at different depths throughout the soil body, with a 0-150 kPa measuring range.

Figure 6.3 shows the mould scheme (similar to Figure 3.17 in Chapter 3, section 3.3.3), adjusted spatially for the numerical model. The locations of the sensors are projected around the central axis of symmetry on a 2D cross-section for the numerical model post-processor (see section 5.2.5).

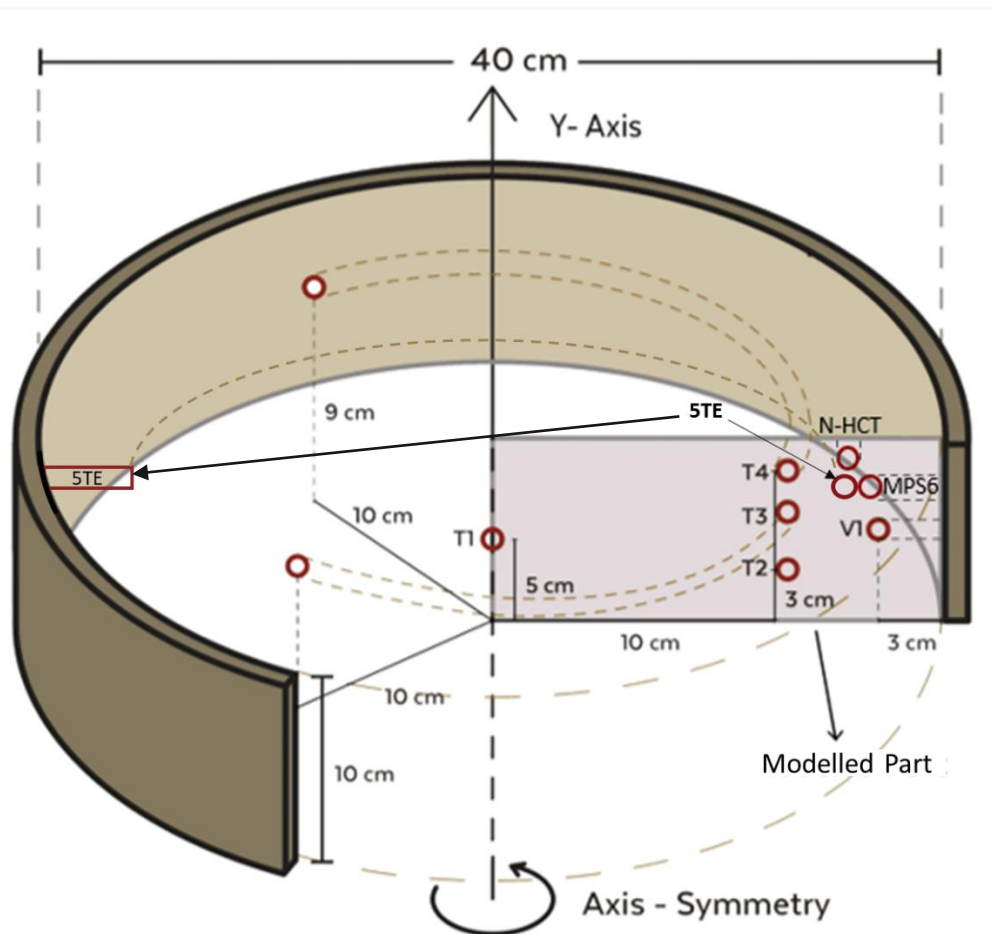


Figure 6-3. Laboratory specimen mould with projected locations of the embedded sensors around the axis of symmetry onto the modelled part.

For the work in this chapter, the environmental chamber was updated with respect to the experiment modelled in Chapter 5, with the following sensors:

- a) the Northumbria High Capacity Tensiometer (N-HCT) was embedded through the soil top surface to a 2 cm depth at 4 cm from the periphery, for wider range direct matric suction measurements [0-3500 kPa (Mendes et al., 2022)].
- b) a Dielectric water potential permittivity sensor MPS-6 (0-2000 kPa, see Chapter 3, section 3.3.4) was embedded through the mould sides to 3cm depth at 3cm from the periphery, for additional suction measurements.
- c) a 5TE Decagon sensor (Decagon Devices Inc., 2016) was embedded to a 3 cm depth through the mould sides at 3cm from the periphery, for direct θ_w measurements.

The additional sensors provided additional points of calibration with experimental data for the numerical model.

6.2.3. Large-scale field experiment

The field experiment consisted of a 3×3×0.5 m rectangular soil tray, filled with Agròpolis soil at slurry consistency: $w_{i,FE} = 43\%$ (A-FE).

Figure 6.4a shows the field experiment setup at the Agròpolis site. The rectangular tray was equipped with different sensors embedded at different locations and depths (see Figure 6.4b), to measure soil temperature, suction, volumetric water content, electrical conductivity, and heat fluxes for one year.

Atmospheric data were recorded using a Catalan Weather Services weather station, stationed at 1.5 km from the testing site location, and used to obtain the meteorological data on rainfall, wind speed and direction, and global solar radiation (Figure 6.4a). Additional external sensors were installed 10 cm above the soil surface to measure the wind speed and rainfall directly at the testing location (labels 3 and 4, respectively, in Figure 6.4a).

For further details on the sensors used, field experimental setup and results, see Cordero et al. (2021).



Figure 6-4. Field experiment: (a) setup at the Agròpolis site, (b) empty tray with different embedded sensors locations, and (c) filled tray showing thin water film forming at the surface (Cordero et al., 2021).

6.2.4. Constitutive parameters

In this section, the essential parameters necessary for the numerical constitutive model are estimated for each of the different initial conditions of the specimens. Big parts of this work, i.e., obtaining the necessary constitutive parameters, have been the focus of previous chapters. Chapters 2 and 3 explain the experimental methodology followed to obtain the SWRCs. Chapter 3 focuses also on obtaining the SSCs using the DIA and SSC modelling. The adopted experimental methodology is then expanded in Chapter 4 to obtain the Suction-Voids Curves (referred to as SVCs in Chapter 4). The latter can be then used to obtain the mechanical parameters necessary for the numerical model (e.g., suction modulus κ_s).

6.2.4.1. Mechanical parameters

In the absence of external effective stresses, except the self-weight of the specimens and the atmospheric pressure, suction-related mechanical parameters play a more significant role. These parameters are typically obtained by graphing the loading and unloading curves of the change in void ratio with respect to suction. Suction modulus κ_s , the descriptive of effect of suction on void ratio change, can be obtained from the slope of the loading curve.

An innovative technique based on environmental chamber experiments is proposed to simplify κ_s estimations. Experimental volumetric deformations, and subsequently void ratio, were projected from horizontal shrinkage results (i.e., CIF results obtained using image analysis), by assuming isotropic conditions.

On the other hand, suction measurements were obtained using a combination of the multiple embedded sensors: UMS-T5s for early-stage suction (0-150 kPa), N-HCT for medium range suction (0-3500 kPa), and the Vaisala HEMP-230 relative humidity sensors to compute the suction through the psychrometric law for the higher range suction (only applicable in drier conditions, see Chapter 3, section 3.2.3).

Figure 6.5 shows the experimental loading data, obtained from the environmental chamber results, with the corresponding linear fit and κ_s values. The latter were estimated from the linear slope for the compacted specimens.

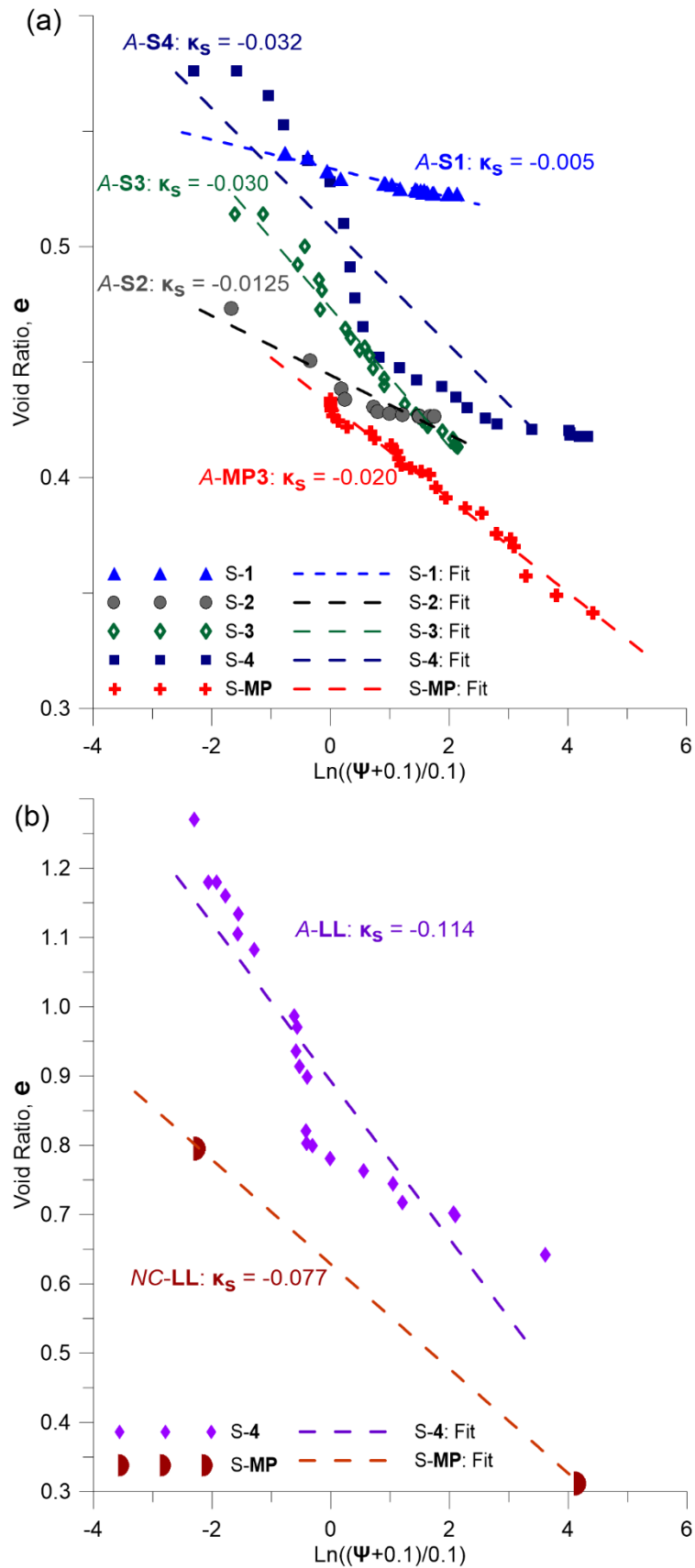


Figure 6-5. $e - \ln[(\Psi + 0.1)/0.1]$ diagram as estimated from the environmental chamber, for the (a) compacted specimens, and (b) slurry specimens.

6.2.4.2. Soil Water Retention Curves (SWRCs)

The SWRCs were experimentally obtained for different initial conditions (Najdi et al., 2023a), using a measurement combination method of N-HCT, and a dew-point hygrometer device, WP4-T PotentialMeter (Campbell et al., 2007). This meant preparing specimens with identical initial conditions to those tested in the environmental chamber. The process is explained in detail throughout Chapter 3. The different SWRCs for each set of initial conditions are provided in section 3.5 in Chapter 3 (see Figure 3.19 and Figure 3.20).

6.2.4.3. Hydraulic Conductivity

Soil hydraulic conductivity varies with initial soil compaction conditions. Figure 6.6 shows the measured values at different ϕ_0 , as provided by different experimental methods on the Agròpolis soil (Oorthuis et al., 2018; Cordero, 2019). See Chapter 5 (section 5.5.1) for the constitutive equation used for the hydraulic conductivity (equation 5.58).

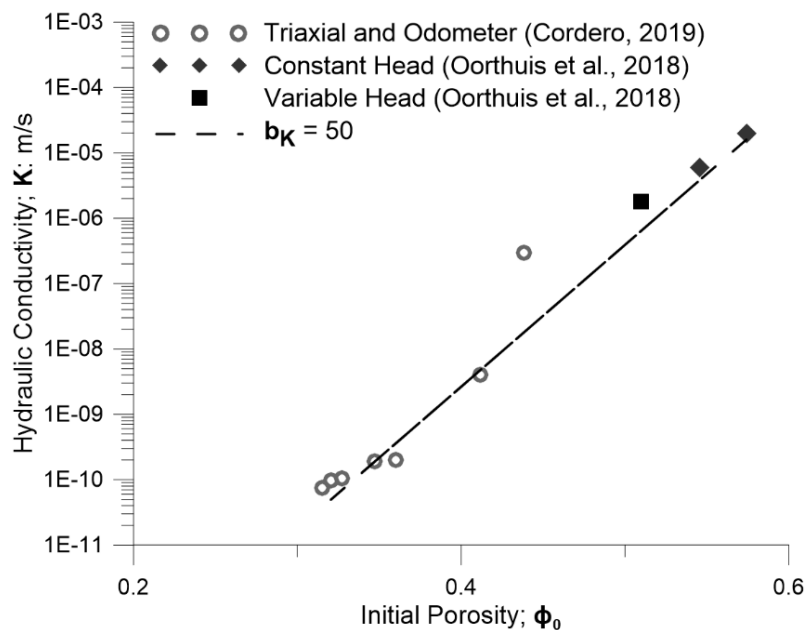


Figure 6-6. Hydraulic conductivity for the Agròpolis soil at different initial conditions, obtained using different methods (Najdi et al., *c*).

6.3. Numerical approach

Water evaporation from soil pores leads to a surge in suction, modifying the system stress field, and producing shrinkage. Shrinkage initiates volumetric and shear deformations, inducing cracks in the soil body. Consequent voids reduction affects both hydraulic and thermal conductivities, reduces advective fluxes, influences water retention behaviour, and is implicitly accounted for in the mass balance equations. Conversely, thermal changes due to flow of

energies generate variations in temperature-dependent terms like mass storage, hydraulic conductivity, water retention and pressure, and vapour diffusion and transfer. Likewise, hydraulic changes due to advective vapour fluxes and temperature gradients induce variations in thermal state, liquid, and gas pressures, and consequently stress equilibrium.

The complex coupled problem was solved using the finite element code `CODE_BRIGHT` (Olivella et al., 1996) which establishes mass balance equations following a compositional approach of balancing species rather than phases (Olivella et al., 1994; Gens & Olivella, 2001). See Chapter 5, section 5.2.1, for more details on the formulation of `CODE_BRIGHT`.

The basic numerical model features can be consulted in Chapter 5 in general and Cuadrado et al. (2022). Novel advances in this Chapter are made in the context of a highly more responsive hydraulic boundary condition (including the diffusivity and net solar radiation calculations), and a well-calibrated set of constitutive parameters.

A 2D structured mesh was created consisting of 990 nodes and 928 quadrilateral elements for the laboratory specimens. For the field experiment, a 3D structured mesh with 5408 nodes and 4375 hexahedral elements (with 8 vertices, and bounded by 6 quadrilateral faces) was created. Time steps were set at an hourly discretisation interval, with intermediate timestep control for the implicit solution based on relative error deviation prediction.

The mechanical boundary conditions were solved following a classical approach. External forces are imposed using Cauchy-type boundary conditions applied in each direction by means of prescribed forces in a Cartesian coordinate system. The bottom boundary restricted horizontal movements, reproducing the mould-base roughness. Only the specimen's self-weight and atmospheric pressure are considered, and no other external effective stresses are applied to the specimen.

The numerical approach is validated for the laboratory experiments by appropriately adjusting the constitutive parameters for initial soil conditions (i.e., hydraulic conductivity, SWRCs, and mechanical parameters). Likewise, hydraulic boundaries are adjusted according to the specific imposed chamber conditions (Figure 6.2). An additional model (*A-MP3-0*) for simulating specimen *A-MP3* was introduced, assuming non-deformable medium instead, to verify the effect of porosity change on simulating the problem.

The same numerical methodology of simulation was carried out for the field experiment on a 3D rectangular model, by adjusting the constitutive parameters for initial soil conditions, and the boundary conditions for field meteorological data. Two identical models were created to simulate the effect of considering different atmospheric data acquisition locations.

6.4. Boundary conditions

Soil-atmosphere interaction induces energy flows altering the energy equilibrium balance. Energy fluctuations take place in the form of net solar radiation (R_n), Latent Heat flow (L_E), Sensible Heat (H), and Heat Flow within the soil body (G).

The fluctuations are expressed by the well-known surface energy balance equation (Blight, 1997):

$$R_n = L_E + H + G \quad (6.1)$$

6.4.1. Flux boundary conditions

Gradients of sensible (H) and latent heat (L_E) condition the evaporative demand. The changes in imposed relative humidity on the soil surface can be represented as an imposed hydraulic flow rate (outflow) of vapour mass fraction.

Assuming constant gas pressure in space and time (Bear et al., 1991), the boundary flux equation is reduced to vapour flux j_g^w and heat flux j_{ES} , occurring due to prescribed vapour mass fraction at a node:

$$j_g^w = \beta_g \left[(\rho_g \omega_g^w)^0 - (\rho_g \omega_g^w) \right] \quad (6.2)$$

Where β_g is the gas transfer coefficient and superscript $()^0$ denotes prescribed atmospheric value. The formulation requires identifying the prescribed vapour mass fraction $(\omega_g^w)^0$ and gas density ρ_g^0 . Physical RH and T data (Figure 6.2) were converted into $(\omega_g^w)^0$ and ρ_g^0 by means of psychrometric and ideal gas laws (Cuadrado et al., 2022).

The field experiment data were acquired at two different points: (A-FE-1) using a VP3 Decagon (Decagon Devices, 2015) installed directly above soil surface; and (A-FE-2) using the Catalan Weather Services weather station stationed 1.5 km from site location.

Figure 6.7 shows the field experimental data as collected on both altitudes: air temperature T_a [°C] (Figure 6.7a); and Relative Humidity RH_a [%] (Figure 6.7b). While there is no evident standard difference between the two relative humidity measurement sources, the air temperature at closer altitude to the soil surface had a consistently higher variation between minimum and maximum values recorded.

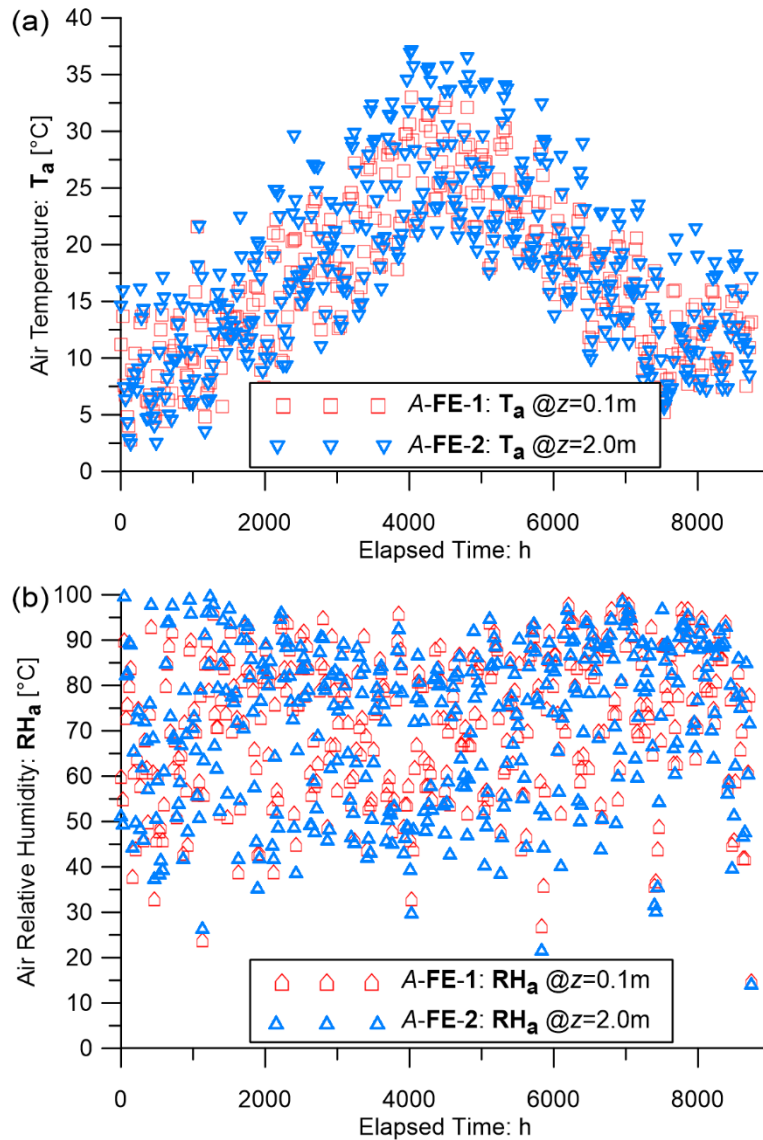


Figure 6-7. Measurements at the two altitudes ($z=0.1\text{m}$, and $z=2.0\text{m}$) of the: (a) air temperature T_a [$^{\circ}\text{C}$], and (b) relative humidity RH_a [%].

Transfer Coefficients

Gas transfer coefficient β_g is obtained by comparing against Latent Heat, expressed following Dalton's Law (Wilson et al., 1994), in terms of aerodynamic (r_a) and surface (r_s) resistances ($\text{s}\cdot\text{m}^{-1}$). Surface resistance (r_s) calculation is consistent, requiring estimations of soil surface water content.

As desiccation continues, soil becomes drier predominantly at the surface. Soil texture and dryness indicate whether it facilitates or hinders the effective diffusion. A lower diffusivity layer of few centimetres thick can reduce gas diffusion fluxes by several orders of magnitude (Bozkurt et al., 2009). Surface resistance r_s is used to quantify the difficulty of diffusion vapour on the evaporation front (Bittelli et al., 2008). Many empirical expressions relate r_s to the water

content in the upper soil layers, where its use normally reduced error and evaporation corrections (Camillo & Gurney, 1986). In all mentioned expressions, r_s increases as surface moisture decreases, creating a near-impermeable vapour barrier for advective fluxes. Some illustrations were derived based on chamber tests with air circulation, depending on the volumetric water content at surface (θ_w): exponential if it is less than 15%, and constant if greater (van de Griend & Owe, 1994)

$$r_s = \begin{cases} 10 \exp[0.15 - \theta_w] & ; \theta_w \leq 0.15 \\ 10 & ; \theta_w > 0.15 \end{cases} \quad (6.3)$$

Experimental θ_w values were obtained from the 5TE Decagon sensors installed close to the surface. r_s was automatically updated at each time-step following equation 6.3. Figure 6.8 shows the computed r_s values for the field experiment over the span of the full year. The values were computed based on the experimental θ_w values from the 5TE Decagon sensor closer to the soil surface in the field. r_s was predominately higher towards the middle of the experiment, between 4000-6000 hours elapsed time. These times coincide with the summer season, and therefore a dryer specimen especially at the surface.

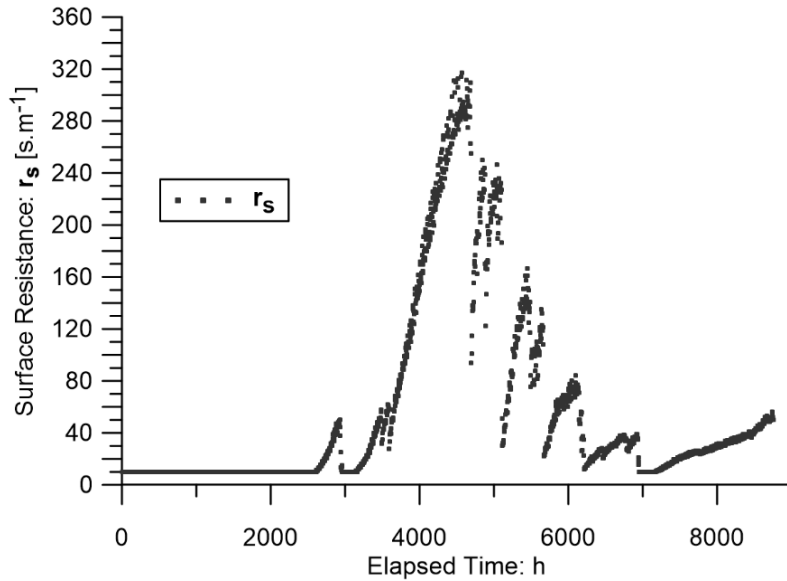


Figure 6-8. Computed r_s values for the Field Experiment A-FE.

Calculating r_a requires measuring the mean horizontal wind velocity \bar{U} above the soil surface, according to Ohm's Law (Stull, 1988; Cui et al., 2012):

$$r_a = \frac{1}{k^2 \bar{U}} \left(\ln \frac{z}{z_0} \right)^2 \quad (6.4)$$

Where $k = 0.41$ is von Kármán's constant, and $z_0 = 0.001$ m is the assumed roughness length (Cuadrado et al., 2022). See Chapter 5, section 5.2.4.3, for more information and further explanations regarding the transfer coefficients.

Environmental Chamber

The dehumidifier generates a flow of wind within the closed environmental chamber, as it injects dry air and collects wet one from different channels. A constant value $\bar{U} = 0.3$ m·s⁻¹ was measured while the dehumidifier was operational, using a Decagon DS-2 high precision sonic anemometer installed at an altitude $z = 0.7$ m (Cuadrado et al., 2022).

In the environmental chamber, the dehumidifier is programmed to “pause” once RH_a drops below designated 30% value, therefore stopping internal wind circulation. At this instance, diffusive fluxes become more pronounced, and r_a formulation is modified, becoming contingent to water vapour diffusivity in air D_a [m²·s⁻¹], at air temperature T_a [K].

$$r_a = \frac{z}{D_a}; \quad D_a = 2.12 \times 10^{-5} \left(\frac{T_a}{273.15} \right)^2 \quad (6.5)$$

An automatic criterion is set to obtain the interchangeable r_a values from equations 6.4 or 6.5, depending on whether the recorded chamber RH_a is higher or lower than 30%, respectively.

Field Experiment

\bar{U} in the field was evidently variable during the year, obtained hourly as average of two readings: (1) the maximum wind speed during the hour, and (2) the particular measurement made at this hour. The separate measurements were obtained from two locations: (A-FE-1) a Davis cup anemometer at $z = 0.1$ m above the soil surface; and (A-FE-2) at the weather station at $z = 2.0$ m.

Figure 6.9 shows the average wind speeds taken at $z = 0.1$ m and $z = 2.0$ m. The average wind speed values measured at the higher altitude from soil surface (i.e., A-FE-2, at $z = 2.0$ m), were higher throughout the year.

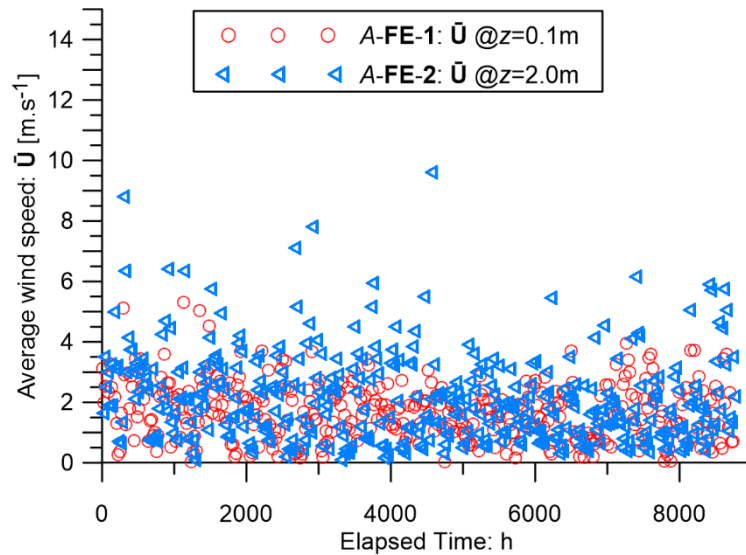


Figure 6-9. Average wind speeds as recorded at two altitudes: $z=0.1$ m, and $z=2.0$ m.

Figure 6.10 shows the computed β_g values for the field experiment, using measurements at: (A-FE-1) $z=0.1$ m; and (A-FE-2) $z=2.0$ m. Due to the lower altitude of A-FE-2, mainly affecting the calculations, β_g values were consistently higher throughout the year.

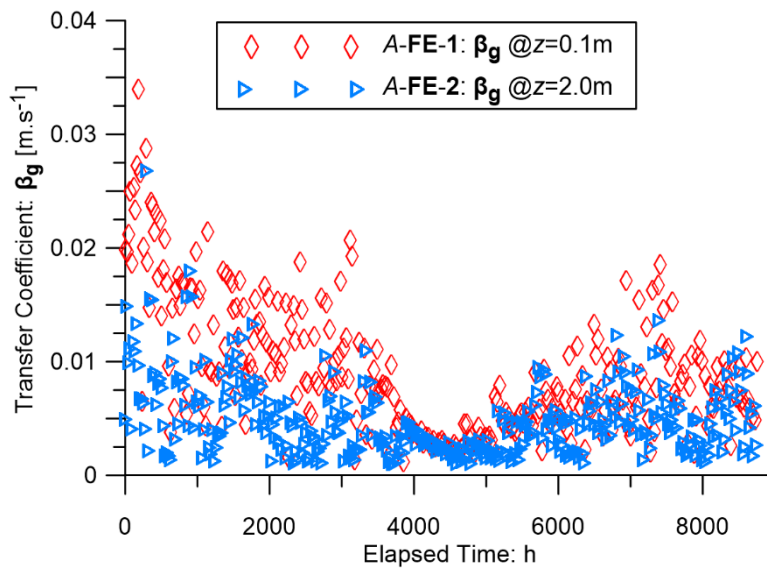


Figure 6-10. Computed β_g values from readings at different altitudes (Najdi et al., *c*).

6.4.3. Heat transfer

One equation was needed to solve the energy balance since thermal equilibrium is assumed between existing phases (Milly, 1982). Energy boundary condition \mathbf{j}_e is expressed in terms of: i) heat flow rate \mathbf{j}_e^0 (von Neumann-type term); ii) prescribed temperature flux (Cauchy-type

term); and iii) a series of terms representing the energy transfer caused by mass fluxes through the boundary.

$$\mathbf{j}_e = \underbrace{\mathbf{j}_e^0}_i + \underbrace{\gamma_e(T^0 - T)}_{ii} + \underbrace{\sum E_{phase}^{species} J_{phase}^{species}}_{iii} \quad (6.6)$$

The first term in equation 6.6 belongs to a prescribed heat flux, corresponding to net solar radiation. For closed laboratory conditions, this term is neglected. The third term is computed internally. The variable heat transfer coefficient γ_e is obtained by comparing the second term to the sensible heat H formulation, responsible for interface heat transfer:

$$\mathbf{j}_e = \gamma_e(T^0 - T) = \frac{C_a(T_s - T_a)}{r_a + r_s} \rightarrow \gamma_e = \frac{C_a}{r_a + r_s} \quad (6.7)$$

Where the imposed temperature T^0 is equivalent to the chamber air temperature T_a ; T_s is the soil surface temperature; C_a is the volumetric heat capacity of air equal to 200 [J·m⁻³·K⁻¹] at room temperature (Stull, 1988; Wallace & Hobbs, 2006). The temperature flux was applied equally at all soil surfaces, assuming that the specimen trays do not impose a heat transfer barrier.

Net Solar Radiation

For field conditions, the first term in the energy boundary condition (equation 6.6), corresponding to imposed heat flow rate \mathbf{j}_e^0 [J·s⁻¹], is prescribed to net solar radiation values.

Net solar radiation can be computed based on two methods, relying on: (1) air temperature alone (Wright & Jensen, 1972; Jensen et al., 1990), and (2) both air and soil surface temperatures (Saito et al., 2006; Cui et al., 2010). For the short time-step scale used (i.e., hourly interval), both methods have been found to return comparable variations (An et al., 2017), and can be calculated as (Jensen et al., 1990):

$$R_n = (1 - \alpha_{albedo})R_{si} - \left[m_{cld} \left(\frac{R_{si}}{R_{so}} \right) + n_{cld} \right] (m_1 + n_1 e_d^{0.5}) \sigma_{SB} (T_a^4) \quad (6.8)$$

Where $m_{cld} = 1.35$ and $n_{cld} = -0.35$ are the cloud factors; $m_{e1} = 0.35$ and $n_{e1} = -0.14$ are the emissivity factors (An et al., 2017); $\sigma_{SB} = 5.67 \times 10^{-8}$ [W·m⁻²·K⁻⁴] is the Stefan-Boltzmann constant; e_d is calculated from the dewpoint temperature T_d [°C]; R_{si} [W·m⁻²] is the global radiation measurements acquired from the weather station (Figure 6.11); and α_{albedo} is the soil surface albedo that depends on the soil surface cover, texture and water content (Van Wijk,

1963; Oke, 1987). Based on suggestions from Rosenberg et al. (1983) and Van Wijk (1963), a value of $\alpha_{albedo} = 0.23$ can be assumed for the bare silty clay of Agròpolis soil.

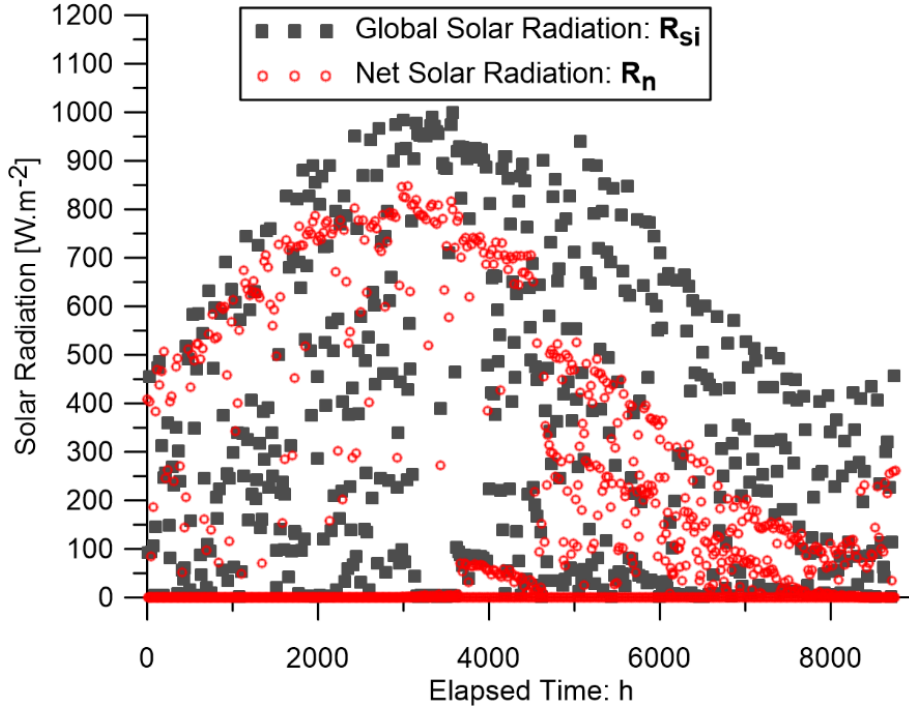


Figure 6-11. Global and net solar radiation [$\text{W}\cdot\text{m}^{-2}$].

$$e_d = 0.611 \exp\left(\frac{17.27 \cdot T_d}{T_d + 237.3}\right) \quad (6.9)$$

$$T_d = \frac{24.03 \cdot F(T, RH)}{17.625 + F(T, RH)} \text{ (}^\circ\text{C)}; \quad F(T, RH) = \ln\left(\frac{RH}{100}\right) + \frac{17.625 \cdot T_a}{243.04 + T_a} \quad (6.10)$$

R_{so} from equation 6.8 stands for the clear sky solar radiation, and can be expressed as

$$R_{so} = (0.75 + 0.00002EL_{msl})R_{sa} \quad (6.11)$$

Where $EL_{msl} = 14$ m is elevation above sea level; and R_{sa} is extra-terrestrial solar radiation (Duffie & Beckman, 1991)

$$R_{sa} = \left[\frac{24 \cdot 60}{\pi}\right] G_{sc} d_r [\cos \varphi_{lat} \cos \delta_{dc} (\sin \zeta_2 - \sin \zeta_1) + (\zeta_2 - \zeta_1) \sin \varphi_{lat} \sin \delta_{dc}] \quad (6.12)$$

Where $G_{sc} = -0.08202$ [$\text{M}\cdot\text{J}\cdot\text{m}^{-2}\cdot\text{min}^{-1}$] is the solar constant; $\varphi_{lat} = 41.3874^\circ$ is the site-specific latitude; δ_{dc} is solar declination angle calculated per day; and d_r corresponds to the relative distance between the earth and the sun during the year

$$d_r = 1 + 0.033 \cos\left(\frac{2\pi D}{365}\right) \text{ [m]} \quad (6.13)$$

Where D is the number of days counted from the beginning of the year. ζ_1 and ζ_2 are the solar time angles, at the beginning and end of the 1-hour interval, respectively:

$$\zeta_1 = \zeta_o - \frac{\pi}{24} ; \zeta_2 = \zeta_o + \frac{\pi}{24} \text{ [rad]} \quad (6.14)$$

calculated from solar time angle ζ_o at the centre of the 1-hour period:

$$\zeta_o = 15(LST - 12) \text{ [}^\circ\text{]} \quad (6.15)$$

Where LST is the time of the day in hours. Net solar radiation formulations can be further consulted in Evett et al. (2011) and An et al. (2017). The resultant R_n values (Figure 6.11) are supplied to the compiled boundary condition file as prescribed heat flow rate j_e^0 [$\text{J}\cdot\text{s}^{-1}$] over the exposed top surface area of the soil tray.

6.4.4. Rainfall

Rainfall measurements were taken at the weather station using a pluviometer. An hourly 1 mm rainfall measurement represents one litre of water per square meter per hour. Assuming a water density $\rho_{water} = 1.0$ [$\text{kg}\cdot\text{l}^{-1}$], rainfall measurements are converted to [$\text{kg}\cdot\text{s}^{-1}$], and applied as a prescribed liquid flow rate over the top specimen surface boundary [$\text{kg}\cdot\text{s}^{-1}\cdot\text{m}^{-2}$] (Figure 6.12).

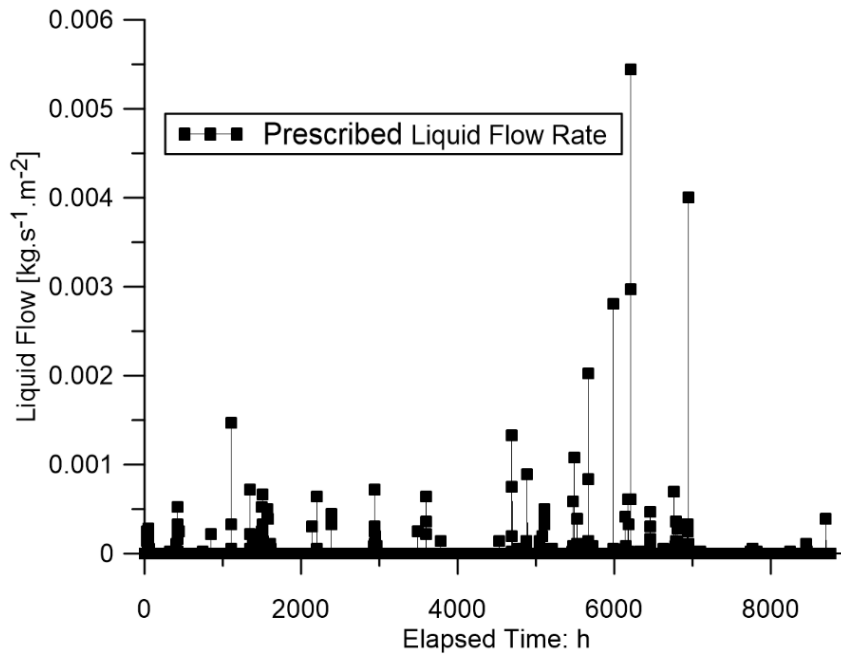


Figure 6-12. Prescribed liquid flow rate, as calculated directly from rainfall data.

6.4.5. Lateral boundary: evaporation from cracks

Crack propagation creates new soil-atmosphere interfaces (Stirling et al., 2017; Levatti et al., 2019a; Cuadrado et al., 2022), requiring an update of lateral boundary conditions. For the laboratory specimens' numerical models, the external vertical periphery was divided into 8 equally-spaced segments (1.25 cm each). Figure 6.13 below shows a schematic of the modelled part.

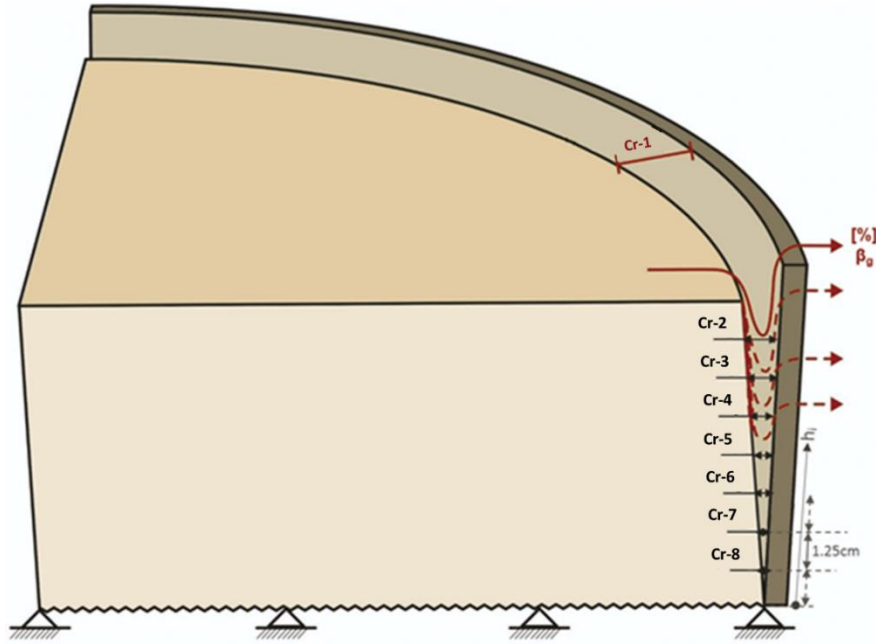


Figure 6-13. Vertical periphery segmentation replicating the perimeter crack progressive opening (Najdi et al., c).

A node-release technique is adopted (Levatti et al., 2019a), relying on setting an activation time t_n^{act} for releasing a node corresponding to segment n , when the crack width at this crack segment level (Cr_n) reaches an assumed 0.5 mm threshold. Beyond this value, the soil is assumed to detach from the mould surface. The first segment release time t_1^{act} depends directly on CIF calculations from image analysis (Cr_1). To calculate crack width at different segments, a consistent displacement profile is assumed (Figure 6.13):

$$\frac{Cr_n}{h_n} : \frac{Cr_1}{10} = \frac{Cr_2}{8.75} = \frac{Cr_3}{7.5} = \frac{Cr_4}{6.25} = \frac{Cr_5}{5} = \frac{Cr_6}{3.75} = \frac{Cr_7}{2.5} = \frac{Cr_8}{1.25} \quad (6.16)$$

Where h_n is the level height at segment n . Mechanical hinges restricting movement in peripheral nodes are removed successively at corresponding t_n^{act} , and replaced with atmospheric gas pressure ($P_g=101.3$ kPa). Once a segment is allowed free movement in planar directions (i.e., released), it becomes subjected to external environmental conditions applied at the surface, though not to the same extent.

The magnitudes of transfer coefficients are governed by \bar{U} and θ_w at internal crack surfaces, controlling r_a and r_s respectively. θ_w at surface (subsequently, r_s in equation 6.3) is considered homogeneous, and therefore the same r_s value is assumed for all exposed surfaces. However, \bar{U} within the crack opening changes with depth, affected by factors such as distance from wind source above the soil surface and crack opening width. Due to their linear relationship, β_g is reduced with the assumed decrease of wind speed. This signifies inferior transfer coefficient rates at lower parts of the cracks. Wind is assumed not to reach the specimen lower half bottom. The evaporation mechanism becomes rather diffusive than conductive (i.e., governed by equation 6.5). Table 6.2 presents the assumed profiles for each test with interpolated t_n^{act} values.

Table 6.2. Transfer coefficients per crack segments assigned for the different models.

Vertical segment, n		1	2	3	4	5	6	7	8
A-MP	%- β_g ⁽¹⁾	80	30	10	$\bar{U}=0$ ⁽²⁾	$[-]$ ⁽³⁾	$[-]$	$[-]$	$[-]$
	t_n^{act} [hrs]	24	28	32	39	48	83	162	$[-]$
A-S1	%- β_g	80	30	10	$\bar{U}=0$ ⁽²⁾	$[-]$ ⁽³⁾	$[-]$	$[-]$	$[-]$
	t_n^{act} [hrs]	45	50	65	90	$[-]$	$[-]$	$[-]$	$[-]$
A-S2	%- β_g	80	30	10	$\bar{U}=0$	$\bar{U}=0$	$\bar{U}=0$	$\bar{U}=0$	$[-]$
	t_n^{act} [hrs]	7	10	12	13	14	35	55	$[-]$
A-S3	%- β_g	80	30	10	$\bar{U}=0$	$\bar{U}=0$	$\bar{U}=0$	$\bar{U}=0$	$\bar{U}=0$
	t_n^{act} [hrs]	4	5	6	7	9	18	65	193
A-S4	%- β_g	80	30	10	$\bar{U}=0$	$\bar{U}=0$	$\bar{U}=0$	$\bar{U}=0$	$\bar{U}=0$
	t_n^{act} [hrs]	34	38	42	46	50	66	80	145
NC-LL A-SL	%- β_g	80	30	10	$\bar{U}=0$	$\bar{U}=0$	$\bar{U}=0$	$\bar{U}=0$	$\bar{U}=0$
	t_n^{act} [hrs]	40	45	50	63	65	70	75	120

⁽¹⁾ The percentage is of the applied coefficient β_g , calculated from the respective r_a and r_s .

⁽²⁾ $\bar{U}=0$: no wind circulating at this depth: aerodynamic resistance calculations based on equation 6.5, i.e., diffusivity.

⁽³⁾ $[-]$: no crack propagation beyond this depth.

In the field experiment, the crack depth was monitored manually and found to propagate at the final state up to a 20 cm depth. The model was divided vertically into five sections of 10 cm. A value of β_g equal to 80% of the surface magnitude is applied to the first 10 cm, diffusive fluxes were applied to the second 10 cm, and an impermeable layer was assumed to the bottom 30 cm.

6.5. Constitutive equations

The mechanical problem is formulated through the equations of stress equilibrium in terms of the macroscopic total stresses. Variation of porosity caused by volumetric deformations and changes in solid density is obtained from the material derivative with respect to the solid. Porosity does not function only as a coefficient but is also computed implicitly in other variables. Inertial terms are neglected and calculation of porosity changes at transitional points is deemed redundant where strain rates are insignificant. This leads to a reduction of the balance momentum for the medium as a whole to the stress equilibrium equation (Bear & Bachmat, 1986), where the associated unknowns are displacements. The hydraulic problem is formulated through the equations of unsaturated flow in porous medium, where the unknowns are the saturation degree and liquid and gas pressures. Coupling of the hydromechanical aspects is made through constitutive laws and a non-symmetric global system of equations obtained using the finite element method.

For specimens prepared at different initial conditions, adjustments in constitutive parameters are made in the context of suction modulus, hydraulic conductivity, and SWRC. The remaining parameters (e.g., thermal conductivity, diffusivity, etc.) are considered intrinsic to soil type, irrelevant of initial compaction and preparation conditions. Table 6.3 shows a summary of the different constitutive parameters for the different specimens.

Table 6.3. Constitutive parameters summary for each model.

Specimen model	initial water content ω_0 [%]	Initial void ratio e_i	Mechanical Component	Hydraulic Conductivity		SWRC		
			$a_1 = a_2$ ($= \frac{\kappa_s}{1+e_0}$)	K_{HC} [m·s ⁻¹]	A_{rl}	P_0 [MPa]	n_0	$b_n=b_p$
A-S1	12	0.54	-0.0032	$1.8e^{-10}$	0.05	2.400	0.40	1.0
A-S2	15	0.47	-0.0085	$1.0e^{-10}$	0.10	1.500	0.35	1.2
A-S3	17	0.51	-0.0199	$1.5e^{-10}$	0.15	2.500	0.35	1.5
A-S4	21	0.58	-0.0203	$2.0e^{-10}$	0.25	1.500	0.32	1.5
A-MP3	15	0.43	-0.0140	$1.0e^{-10}$	0.10	1.500	0.29	1.2
NC-LL	29	0.80	-0.0594	$1.0e^{-8}$	0.30	1.250	0.18	2.0
A-SL/S-FE	43	1.18	-0.0986	$1.0e^{-7}$	0.50	0.075	0.16	4.3

6.5.1. Mechanical component

Volumetric deformations are more dominant than shear deformations in soil desiccation shrinkage. Shear modulus G calculations were based on bulk modulus and a constant Poisson's ratio $\nu = 0.3$. A non-linear elasticity model based on stress state surfaces can be used to compute volumetric strains (Lloret & Alonso, 1985; Alonso et al., 1990).

$$\frac{\Delta e}{1+e} = a_1 \Delta \ln(-p') + a_2 \Delta \ln\left(\frac{\Psi + 0.1}{0.1}\right) + a_3 \left[\Delta \ln(-p') \ln\left(\frac{\Psi + 0.1}{0.1}\right) \right] \quad (6.17)$$

Where p' is the mean effective stress: $p' = p - P_g$; $\Psi = P_g - P_l$ is suction; a_1 and a_2 are constants calculated from the slopes κ and κ_s of the loading curves in the $e - \ln p'$ and $e - \ln[(\Psi + 0.1)/0.1]$ diagrams respectively (equation 6.18); and a_3 is an empirical coupling term which, if assumed null, makes the equation coincide with the elastic part of the Barcelona Basic Model (Alonso et al., 1990).

$$a_1 = -\frac{\kappa}{1+e}; \quad a_2 = -\frac{\kappa_s}{1+e} \quad (6.18)$$

Suction stresses are more relevant in this case, and $a_1 = a_2$ is assumed.

6.5.2. Thermo-hydraulic component

The thermohydraulic problem is relatively complex due to the highly non-linear dependence of soil properties and parameters on suction and porosity changes.

6.5.2.1. Unsaturated flow

The generalized Darcy's law represents the advective multiphase flow, proportional to the liquid pressure P_l and density ρ_l , while being inversely proportional to temperature-dependent dynamic fluid viscosity μ_l .

$$\mathbf{q}_l = -\frac{k_{rl}}{\mu_l} \mathbf{k}_i \cdot (\nabla P_l - \rho_l \mathbf{g}) \quad (6.19)$$

Where \mathbf{k}_i is the intrinsic permeability tensor (equation 6.20), a soil property dependent on porosity and defined in the three principal directions for a continuum medium; and k_{rl} is liquid phase relative permeability (equation 6.21). The intrinsic permeability expression is provided based on Kozeny's model and is given by a simple exponential law:

$$\mathbf{k}_i = \mathbf{k}_{i_0} \exp[b_K(\phi - \phi_0)] \quad (6.20)$$

Where \mathbf{k}_{i_0} [m^2] is the matrix intrinsic saturated permeability at reference porosity $\phi = \phi_0$, a geometrical hydrodynamic feature impartial of gaseous and fluid states (Stoltz et al., 2010), extrapolated from experimental hydraulic conductivity results at different porosities (section 6.2.4.3, Figure 6.6). The empirical parameter b_K controls the saturated hydraulic conductivity

dependence magnitude on porosity (Rodríguez et al., 2007). A value of $b_K = 50$ was fitted from the measured data (Figure 6.6).

Typically, k_{rl} ranges from 0 to 1 and depends on the effective degree of saturation S_e . Its formulation is defined by the generalized power law, based on Corey's functions (Brooks and Corey 1964):

$$k_{rl} = A_{rl}(S_e)^{m_{rl}}; \quad S_e = \frac{S_l - S_{rl}}{S_{ls} - S_{rl}} \quad (6.21)$$

Where m_{rl} is an empirical index defined with macroscopic models to consider the effect of soil pore-size distribution (Mualem, 1978), thus assumed constant for all specimen models ($m_{rl} = 3$); and A_{rl} is an empirical parameter defining the magnitude, dependent on initial conditions.

Specimen compaction reduces pore space and increases contact surface between aggregates, creating a greater continuity between pores filled with water in a compacted soil than in a loose one (Gupta et al., 1989). Consequently, a correlation exists between initial compaction and saturation level, and the assigned fitting parameters. The assumed empirical values are provided in Table 6.3.

6.5.2.2. Soil water retention curves (SWRCs)

A modified form of the van Genuchten (1980) model, accounting for temperature effects and porosity effects via empirical parameters b_n and b_P , is adopted to fit the experimental SWRCs presented earlier (section 2.3.2).

$$S_e = \left\{ 1 + \left[\frac{\Psi}{P_{0\phi}(\sigma_w/\sigma_{w0})} \right]^{\frac{1}{1-n_\phi}} \right\}^{-n_\phi} \quad \begin{aligned} n_\phi &= n_0 \exp[b_n(\phi_0 - \phi)] \\ P_{0\phi} &= P_0 \exp[b_P(\phi_0 - \phi)] \end{aligned} \quad (6.22)$$

Where P_0 is the reference capillary pressure related to air entry value; σ_w is surface tension at temperature T [°C]; σ_{w0} is the surface tension at the temperature where P_0 was measured; and n_0 is the shape parameter at reference porosity. b_n and b_P determine the porosity change effect on the shape parameter and capillary pressure, respectively. Both values are assumed equal in this case ($b_n = b_P$). The parameters are provided in Table 6.3.

6.5.2.3. Diffusion

Advection governs transport in higher permeability zones of the porous medium, while diffusion dominates at lower permeability zones. Non-advective fluxes of a species in a phase

are mainly comprised of two components: molecular diffusion and mechanical dispersion. Fick's law describes both vapour \mathbf{i}_g^w and air \mathbf{i}_g^a molecular diffusion in the gaseous phase in terms of the particle's coefficient of gas saturation degree S_g , temperature, and mechanical dispersion tensors in gas D_g^i (i : vapour, dissolved air, and heat). In a porous medium, the solid particles force the diffusion pathways to diverge from their original conventional lines. The diffusion factor must be scaled with tortuosity τ to denote the porosity effect (Shen & Chen, 2007).

$$\tau_r = S_g^3 \quad (6.23)$$

6.5.2.4. Heat conductivity

Conductive heat flux is expressed by Fourier's law accounting for porosity effect (geometric weighted mean), temperature and water content. $\lambda_{h_{sat}} = 0.243$ [$\text{W}\cdot\text{m}^{-1}\cdot\text{K}^{-1}$] and $\lambda_{h_{dry}} = 1.448$ [$\text{W}\cdot\text{m}^{-1}\cdot\text{K}^{-1}$] are the saturated and heat conductivity values, respectively, approximated from soils with similar properties (Villalobos et al., 2002).

6.6. Results

The numerical models are validated against experimental results based on the development of gravimetric and volumetric water content, CIF, suction, and temperature.

6.6.1. Suction results

Suction results are detailed for models A-MP and A-S3, as their corresponding experiments were better instrumented with multiple tensiometers, and therefore a wider set of experimental results is available for comparison. Figure 6.14 shows experimental and numerical suction development at different sensor locations. A closer look at an early drying stage allows for model evaluation against experimental tensiometers results (up to their cavitation). Suction increased unequally throughout the soil body soon after drying started, following the initial 24-hour wetting period, denoting both the model and sensors responsivity. Higher matric suction development occurs at points closer to the surface and lateral periphery, the forefronts of evaporation. Lowest development occurs at the central tensiometer (T5-1), though not the deepest, signifying a desaturation profile moving both vertically and laterally, coherently towards the bottom-centre. The model predicts a 30 hrs suction development delay at the MPS-6 location during early stages (Figure 6.14a). The numerical misfit, adjusted at later stages as suction increases beyond 300 kPa, can be a result of the experimental measurements.

For higher range suction (i.e., beyond 2500 kPa), suction was estimated from the psychrometric law using RH_s and T_s (HEMP-230 sensor measurements).

The dehumidifier suspension during the three separate periods in A-S3 interrupts the internal chamber wind circulation, reduces advective fluxes (τ_a calculations switch to diffusivity, i.e., equation 6.5), and causes RH_a spikes (Figure 6.2c). Consequently, both RH_a spikes and the switch to diffusivity will lead to an increase in the prescribed vapour mass fraction and pore water pressure, producing a decrease in suction during these three periods, particularly closer to the surface (Figure 6.14b).

In general, the numerical models seemed to adjust well to the changes in the environmental chamber-imposed conditions, signifying a highly responsive hydraulic boundary condition used.

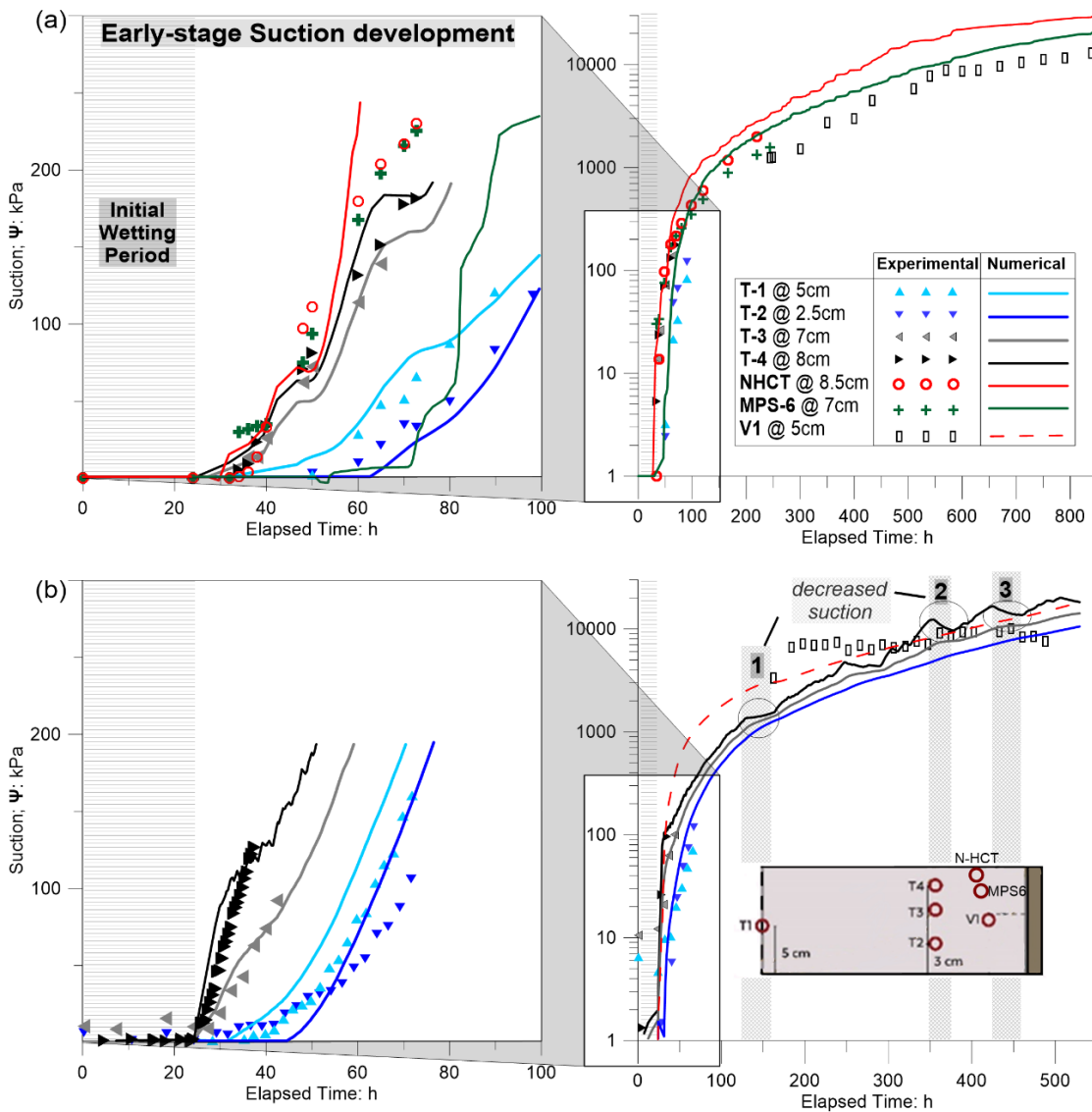


Figure 6-14. Numerical and experimental suction development at different embedded sensors locations, for specimens: (a) A-MP3; and (b) A-S3 (Najdi et al., c).

6.6.2. Gravimetric water content results

Numerical gravimetric water content was obtained from vapour and liquid saturation evolution at each mesh element. Figure 6.15 shows the experimental and numerical water content evolution. Specimens A-MP3 and A-S3 were exposed to a 24-hour initial wetting period, and their respective models replicate the negligible water loss during this period. The three dehumidifier pausing periods discussed earlier cause a decrease in water loss, more apparent during the first of the periods (Figure 10e). At the early stages of drying, the specimen was relatively saturated, and the evaporation was dominated by advective rather than diffusive fluxes. Stopping the dehumidifier induces an abrupt change from advective into diffusive fluxes, and a decrease in both suction and soil water evaporation. At later stages, the evaporation was not mainly controlled by advective fluxes, and the abrupt change did not affect the evaporation to the same extent.

The additional model A-MP-0 (assuming a non-deformable medium) achieves an overall overestimation of water loss (Figure 6.15a). The constitutive and mass balance formulation controlling vapour fluxes are porosity-dependent. As soil dries and exhibits shrinkage, its particles rearrange in a denser state causing a decrease in conductivity (equation 6.20) and suction development (equation 6.22). A rigid soil skeleton indicates a constant conductivity and vapour transfer pathways, and a uniform suction development throughout the soil matrix and a consequent continuous untampered vapour supply to the evaporation surfaces. As a result, the evaporation rate is higher, leading to a faster and more effective soil-water drainage.

6.6.3. CIF results

The models run on a rough-base assumption, restricting bottom lateral displacements. The mechanical boundary impact on the hydromechanical development was validated by resolving a set of new models with smooth base instead, allowing free bottom horizontal movements. The influence was trivial on evaporation rate, suction development, and CIF evolution and, therefore, are not shown on Figure 6.15 for graphical clarity. Although producing similar top-crack width (CIF) values, the displacement profiles are different. Figure 6.15 shows the displacement profile for the same specimen at final-state for the two simulations. More elaborate shear deformations are perceived for the rough-base model, and the uneven specimen horizontal shrinkage profile generally agrees more with the experimental observations. It remains important to properly specify the mechanical boundary conditions for better simulations.

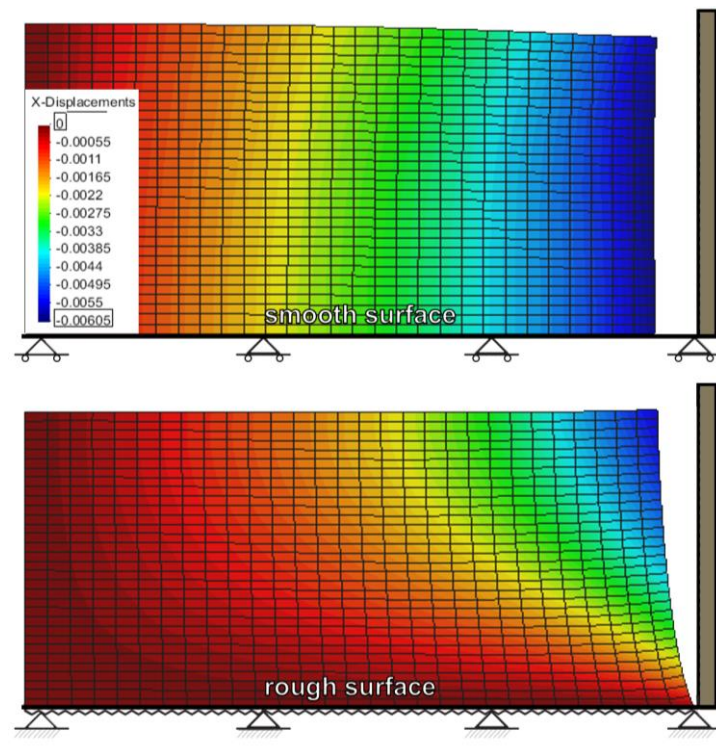


Figure 6-15. Final state shrinkage profile for two simulations on the same specimen (A-S3), considering rough versus smooth bottom mechanical boundary conditions

Numerical CIF calculations are estimated from the horizontal inward displacements along the x-axis of the top-right corner node. The node location represents the soil-body original detachment from the mould. Consequently, shrinkage is captured on the perimeter only, where the experimental results suggested a similar behaviour of the perimeter crack.

The laboratory slurry specimens (i.e., *NC-LL* and *A-SL*) exhibited internal cracks in addition to the perimeter crack. The structured mesh utilised in this study is not capable of reproducing such behaviour but was still able of capturing the global CIF magnitude, evolution tendency and residual values. Figure 6.16 shows a comparison of numerical and experimental CIF results.

The dehumidifier pausing effect for model *A-S3* was also perceivable in the CIF evolution, demonstrating the high responsivity in the mechanical aspect. Shrinkage ceased momentarily during the three periods (Figure 6.16f). The effect is more pronounced during the first spike happening at an earlier stage.

As mentioned before, at early drying stages, any change from advective to diffusive fluxes causes more pronounced effect on the soil water evaporation, and consequently the drying shrinkage process.

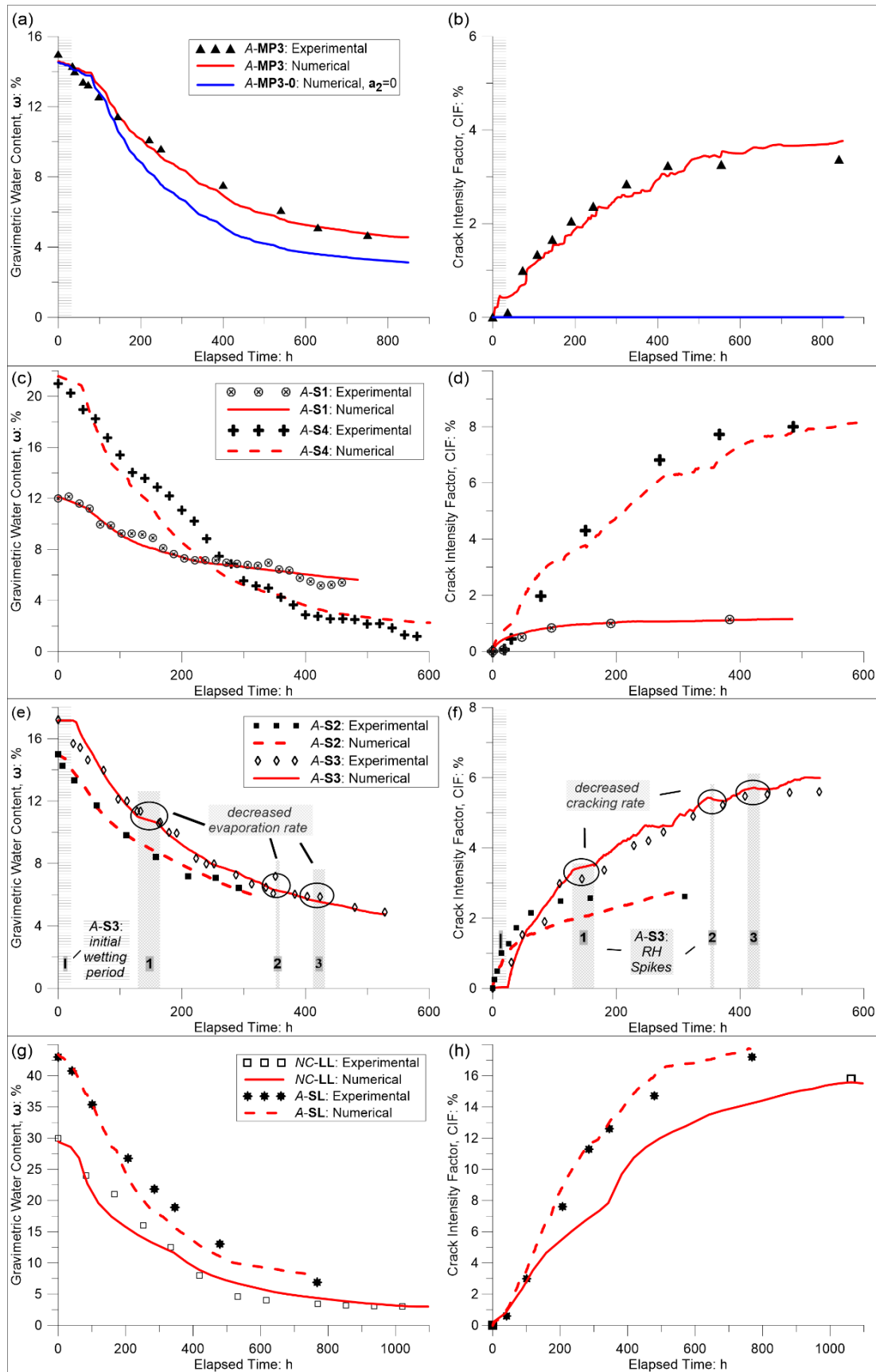


Figure 6-16. Experimental versus numerical gravimetric water content evolution for (a) A-MP3; (b) A-S1 and A-S4; (c) A-S2 and A-S3; and (d) NC-LL and A-SL; and CIF for (e) A-MP3; (f) A-S1 and A-S4; (g) A-S2 and A-S3; and (h) NC-LL and A-SL.

6.6.4. Temperature results

Figure 6.17 shows the experimental and numerical temperature results for the A-S1 and A-S2 model specimens as an example.

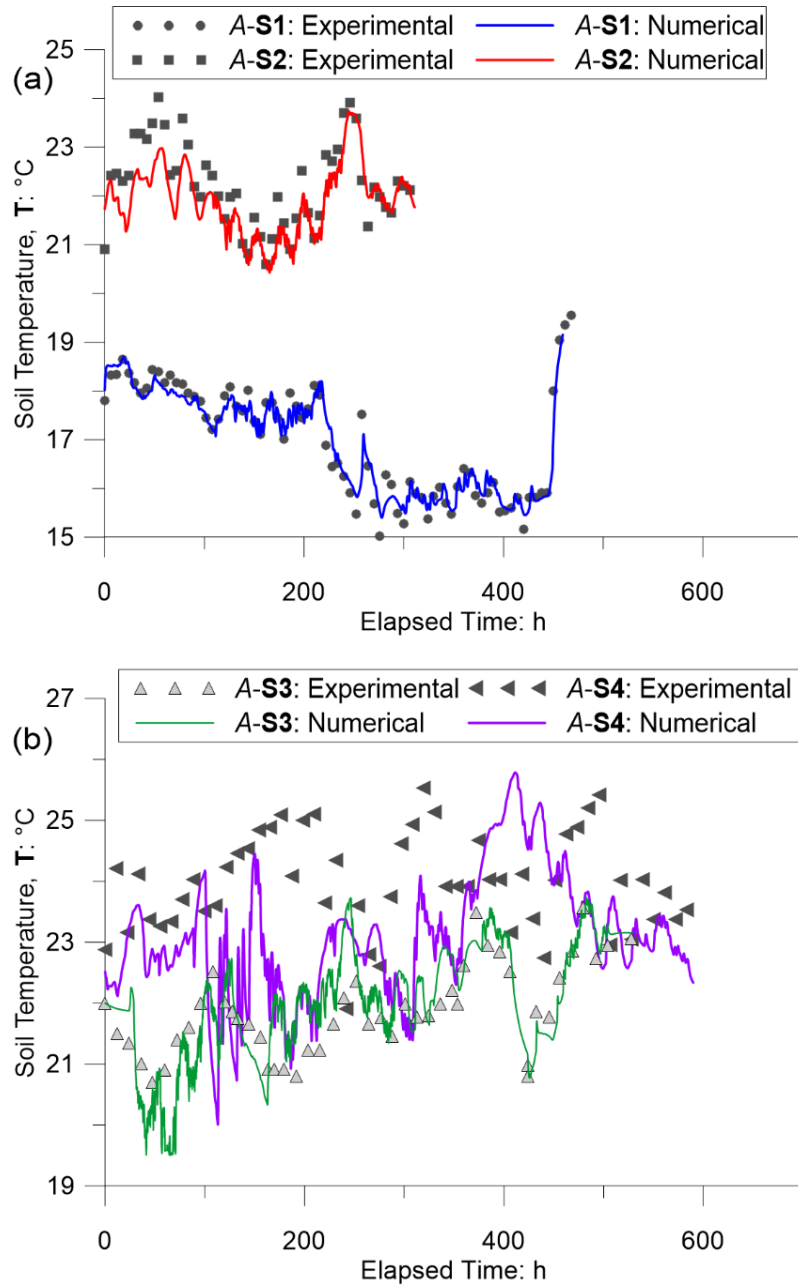


Figure 6-17. Experimental and numerical results of soil temperature evolution for specimens: (a) A-S1 and A-S2, and (b) A-S3 and A-S4.

The numerical results conform with the experimental fluctuations measured by the HEMP-230 sensors, implying an adequate implementation of thermal conductivity parameters and computation method of heat transfer coefficient.

6.6.5. Field experiment results

The model was finally validated for the large-scale field experiment (A-FE). Figure 6.18 highlights some of the experimental results obtained by Cordero et al. (2021), and the corresponding numerical simulation results, evaluated based on gravimetric water content, volumetric water content, CIF, and T_s .

6.6.5.1. Field data

Experimental MPS-6 suction readings at various depths stopped working during the summer period, as suction reached higher levels beyond the reading capacity (Figure 6.18e). Experimental θ_w and T_s readings were captured at various depths using multiple embedded 5TE sensors. Gravimetric water content w was obtained from the four load-cells, and CIF was computed from specimen surface images (Cordero et al., 2021).

6.6.5.2. Numerical results

Two identical numerical models with different boundary conditions were created. The first model considered the collected atmospheric data (i.e., \bar{U} , RH_a , and T_a) obtained directly at site location ($z=0.1$ m). The second model considered the atmospheric data collected from the weather station ($z=2.0$ m).

Gravimetric and volumetric water content

Gravimetric water content change tendency was well captured numerically throughout the year (Figure 6.18a). A-FE-1 ($z=0.1$ m) returned a generally better fit, while A-FE-2 ($z=2.0$ m) underestimated the water loss initially (first 3000 hrs), as a consequence of lower transfer coefficients values assigned (section 6.4, Figure 6.10). A similar tendency was observed for θ_w (Figure 6.18f). The different profiles at different depths were well captured numerically. However, the 5TE sensor underestimated the initial value θ_0 , which can be obtained analytically for the saturated field specimen:

$$\theta_0 = w_0 G_s (1 - \phi_0) \quad (6.25)$$

$\theta_0=0.51$ corresponds to $w_0=43\%$, and $\phi_0=0.561$ (Table 6.1). The computed value is outside the sensor measuring resolution range ($\theta_{resolution}=0.0-0.50$). However, this value of $\theta_0=0.51$ confirms better with the results of the numerical model.

Temperature

The temperature fluctuations were adequately simulated at both embedment depths (Figures 6.13c and 6.13d). The 40 cm depth temperature experienced smaller fluctuations with respect to the 15 cm, where the latter was more directly affected by daily atmospheric temperature changes. This indicates an adequate implementation of both thermal conductivity and heat transfer coefficients.

CIF

Numerical CIF results were obtained using a simplified volumetric shrinkage estimation method based on horizontal shrinkage of the four sides. The internal cracks occurring along the surface in the original experiment could not be simulated numerically. The model cannot reproduce internal cracks (e.g., through mesh de-structuration technique), and it remains outside the scope of this work.

The model replicates the tendency and magnitude of the experimental results for the major part of the experiment, up to around 5500 hrs (Figure 6.18b). Afterwards, the model predicts no further increase in volumetric shrinkage, whereas a constant increase in CIF is observed in the field. The misestimation pertains mainly to the superficial cracks. Additionally, the existing cracks are subject to continuous erosion and an increase in rain-induced wetting that leads to collapsing of their vertical walls. All of which are factors that cannot be simulated.

Comparing *A-FE-1* and *A-FE-2* shows a similar tendency prediction, with an initial CIF evolution delay (up to 3000 hrs) predicted by *A-FE-2*, which also showed less water loss during that same period.

Suction

The model replicates the different profiles in suction development tendency at different locations, confirming with experimental MPS-6 results (Figure 6.18e). However, the simulations predict a higher initial surge in suction since early drying stages (>100 hrs), compared to experimental results (>1000 hrs). This discrepancy can be attributed to multiple factors.

Slurry soil particles tend to initially settle downwards, creating a water film at the top surface which is prone to evaporate earlier than the pore water, and therefore acting as a barrier. Additionally, the initial settlements lead to vertical shrinkage and decrease in porosity, maintaining fully saturated conditions. The behaviour of a water film material of different

characteristics is not numerically replicable. Moreover, the model assumes global spatial homogeneity of soil characteristics, which is less likely to be the case for such large-scale field specimens. Finally, a simplified retention curve was adopted, based on one generic drying path SWRC fitting model, not accounting for the hysteresis effect.

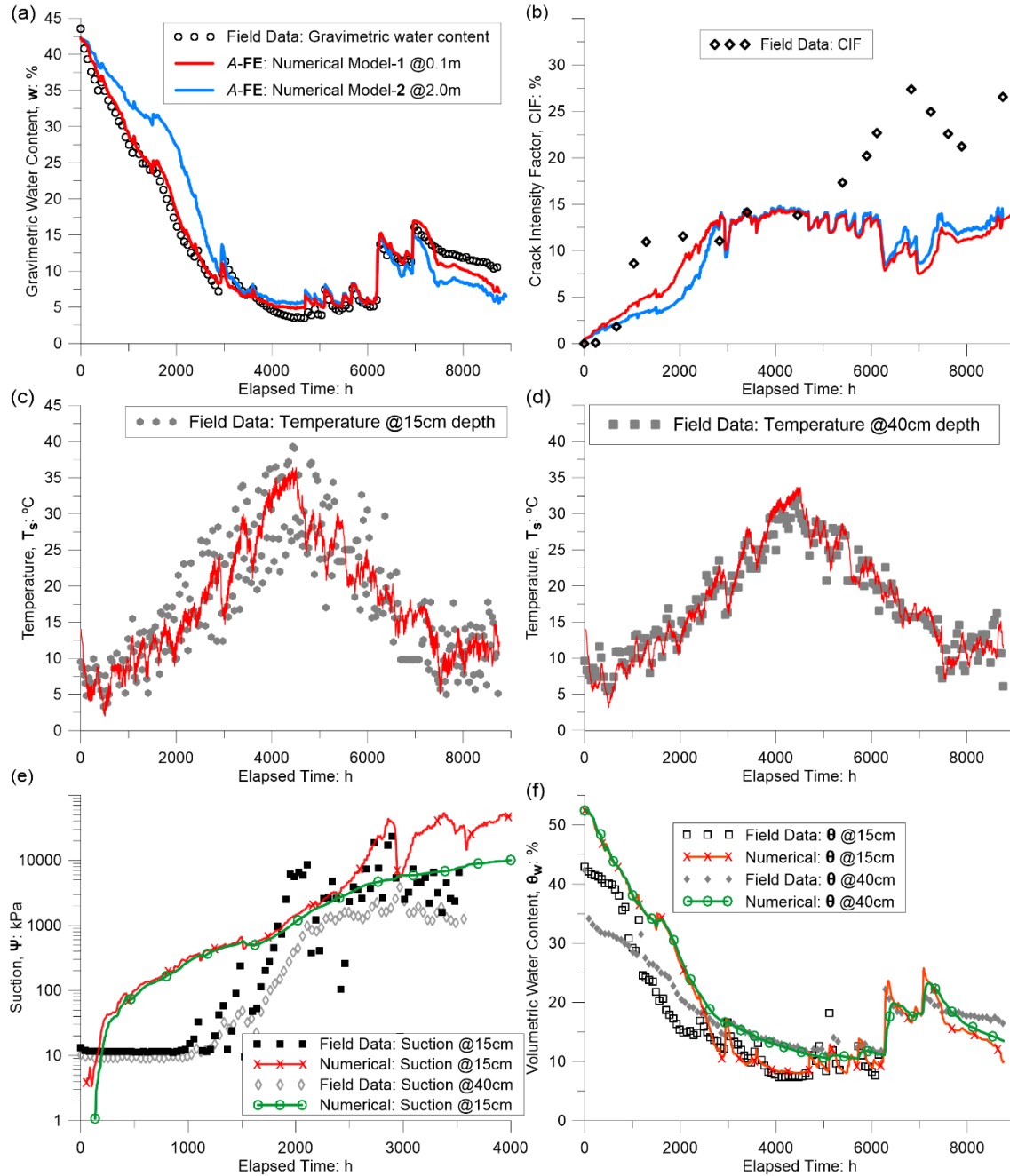


Figure 6-18. Numerical and physical results of the field experiment, showing evolution of: (a) gravimetric water content; (b) CIF; soil temperature at (c) 15 cm, and (d) 40 cm depth; (e) suction; and (f) volumetric water content.

6.7. Discussion

The analysis and comparisons made in this chapter are a part of an ongoing research carried out to define a global picture of soil-atmosphere interaction, soil-water evaporation, and desiccation cracking behaviour of soils at different initial conditions exposed to different environmental conditions.

In order to achieve better numerical prediction results that fully captures the THM behaviour of the soil, it is essential to translate mathematically the physical parameters and factors involved as effectively as possible. In this case, the involved constitutive model parameters were obtained distinctly for each set of initial conditions. Obtaining the hydraulic and mechanical constitutive parameters was a culmination of the work from previous chapters, namely Chapters 2 to 4.

The SWRC is one of the main constituents of a numerical model describing the water retention behaviour of unsaturated soil. For better results, the fitted SWRC equation (i.e., the modified van Genuchten) must reproduce the experimental physical data. For this purpose, a specific SWRC was obtained experimentally for each set of soil prepared at different initial conditions (see Chapter 3). Each of the obtained SWRCs was fitted separately and different fitting parameters were obtained for each batch of soil with different initial conditions. The hydraulic conductivity was obtained experimentally using a triaxial test for samples at different compaction levels. A direct relationship is drawn between the soil porosity and the hydraulic conductivity. This relationship indicated the constitutive parameters necessary to implement the generalised Darcy's law, where the intrinsic permeability expression is provided based on Kozeny's model. Moreover, the thermal conductivity was obtained through soils with similar composition and features from the literature.

The mechanical constitutive parameters were found separately for each batch of soil. The suction-related parameter (κ_s), that describes the relation between suction and void ratio. The κ_s parameter is normally obtained from suction-controlled odometer or triaxial tests, where different levels of suction are imposed progressively at constant confining stresses (Blatz et al. 2008). The deformations for each level of applied suction are measured and a direct relationship between the suction and void ratio is obtained, from which the κ_s value is estimated. The environmental chamber tests served as a suction-controlled experiment in a sense that both suction and void ratio were measured progressively. The level of suction was measured directly using the set of embedded sensors (i.e., UMS-T5, N-HCT, MPS-6 and HEMP-230), while the changes in void ratio were estimated indirectly from the horizontal shrinkage results obtained using DIA.

On the other hand, the assigned boundary conditions replicated the imposed atmospheric conditions. The boundary condition formulation accounted for all the involved factors in the soil-atmosphere interaction problem. The collected meteorological data were mathematically transformed into imposed fluxes of energy, heat, and liquid, and into transfer coefficients:

- (a) Recorded global solar radiation values were transformed to net solar radiation and inputted in the boundary condition as imposed heat flow rate j_e^0 [$\text{J}\cdot\text{s}^{-1}$].
- (b) Atmospheric temperature was imposed on the soil surfaces.
- (c) Rainfall data were inputted as liquid infiltration.
- (d) Atmospheric relative humidity was imposed as vapour flux j_g^w .
- (e) Wind speed was used to estimate the aerodynamic resistance r_a , which governs the magnitude of the transfer coefficients.

Accounting for all the imposed meteorological data at short-interval periods leads to refined boundary conditions that numerically replicates the full experimental conditions with higher responsiveness rate.

The CIF evolution results demonstrated the adequacy of the adopted non-linear elasticity mechanical model and the κ_s parameter. Non-linear elasticity was adopted due to its proven capability to model suction effects on shrinkage, and the relative simplicity in experimentally obtaining its parameters. However, the formation of intensive internal cracks, the collapse of cracks due to rain-induced wetting periods, and the erosion of the cracks could not be replicated numerically using the non-linear elasticity model. Therefore, the numerically predicted CIF values can be an underestimate of the experimental data, especially for larger-scale specimens exposed to uncontrolled external atmospheric conditions.

Mesh refinement was critical to the problem. However, especially in the 3D simulations of the larger-scale specimen, refining the mesh added exponentially to the computational time. For the field experiment model, cubical mesh elements of 5 cm sides were initially adopted (a total of 40931 nodes and 36000 elements). Further mesh refinement did not improve the results considerably, while a coarser mesh proved sufficient and returned comparable results. The final adopted coarser mesh consisted of 5408 nodes and 4375 hexahedral elements with dimensions $5\times 12\times 12$ cm. Proper time intervals were also fundamental, particularly in the assigned boundary conditions, to capture the daily fluctuations in the energy balances at soil surface. Time-stepping refinement added linearly to the computational time. A minimum of six steps per 24 hours was found satisfactory (i.e., four-hours timestep), with respect to both the computational time and the replication of the fluctuations in the daily energy fluxes.

The model in general can be considered reliable in predicting future soil behaviour in the field for long-term exposures, provided an adequate set of atmospheric data is available. The model can be further enhanced by incorporating the effect of repeated hydraulic loading and unloading (caused by rainfalls and drying periods) on the on the water retention, hydraulic conductivity, and soil fabric into the constitutive formulation (Azizi et al., 2019)

6.8. Conclusion

The work in this chapter presents the culmination of works carried out in the previous chapters: (a) obtaining the relevant constitutive parameters experimentally (Chapters 2 and 3), (b) fitting the experimental data for different soil batches prepared at different initial conditions, (Chapters 3 and 4) and (c) building the basis of the numerical model and the boundary conditions (Chapter 5).

Laboratory and field desiccation experiments were interpreted in the framework of unsaturated soil mechanics by a numerical FEM considering THM coupling of the processes involved. The numerical model proved its applicability to soils prepared at a wide range of initial water contents and densities, by adjusting the corresponding constitutive parameters. Different constitutive parameters were assigned to each model according to the collected experimental data for: (i) the mechanical model, (ii) SWRC, and (iii) hydraulic conductivity.

The same approach was carried out for the imposed atmospheric conditions for each corresponding model. The applied boundary conditions were further refined by adding an automatic interchanging criterion for the wind effect: (a) in the case of wind, advective fluxes dominate the computation of aerodynamic resistance (therefore the transfer coefficients); and (b) in the case of no wind, diffusivity dominate the computations. Additionally, the imposed numerical boundary conditions accounted for all the collected meteorological data to provide more relevant replication results. In all the studied cases, the numerical results showed a high responsiveness to rapid and abrupt changes in the imposed atmospheric conditions. For the field experiment, better simulations were obtained where the imposed atmospheric conditions were measured at an altitude nearest to the soil surface.

Furthermore, the model accounted for evaporation from the recently opened crack lateral surfaces. A propagation mechanism is proposed for releasing the lateral boundaries where the cracks are supposed to occur, according to the experimental CIF results. This mechanism added to the refining of the numerical predictions.

The numerical model successfully simulated the evolution of water content, suction, temperature, and shrinkage for all the experiments. The objective of this chapter was to ultimately provide a reliable and fully functioning model, critical for the design process, to predict the hydromechanical behaviour of soils in engineering works prepared at any initial conditions and exposed to varying open and long-term atmospheric conditions.

Chapter 7

Thesis Conclusions

This chapter presents the conclusions of the thesis. First, a brief summary of the contributions and conclusions from each chapter is presented separately, then a general conclusion is given, and finally some remarks about future lines of work are provided.

7.1. Brief Summary

In this section, a brief summary of each of the chapters is given, emphasizing the contributions and novelties produced from that particular chapter:

7.1.2. Chapter 2: Novel High Capacity Tensiometer

In Chapter 2, a newly developed High Capacity Tensiometer (HCT) was tested in collaboration with Northumbria University. The new tensiometer (referred to as N-HCT) has a design similar to other HCTs developed in the literature: (i) a ceramic filter with specific Air Entry Value (AEV), (ii) a pressure transducer to take the readings, (iii) a small water reservoir in between the ceramic filter and the water reservoir, and (iv) a stainless-steel sheath encapsulating these components. Reading water pressures below the absolute atmospheric pressure is made possible due to the high AEV of the ceramic filter. The AEV of the ceramic filter is controlled by the largest pore size within the ceramic. The smaller the largest pore is, the higher the expected measuring range can be. The newly developed N-HCT is equipped with an alumina ceramic filter with an estimated AEV of 5.8 MPa, as opposed to the typical values of 1.5 MPa by other ceramic filters used in the common HCTs. The N-HCT functionality and measuring range were tested against the common HCTs, built with the same design (apart from the ceramic filter type). Cavitation results show a maximum attainable suction measurement range beyond 3 MPa. Testing the N-HCT in continuous and discrete drying soils showed similar suction measurement range beyond 3 MPa, and a quick equalisation and re-saturation required time. The N-HCT is considered reliable for use in experimental setups to study the water retention behaviour of unsaturated soils, and therefore used in the following chapters.

7.1.3. Chapter 3: Laboratory Experimental Campaign: Evaluating Different Suction and Volumetric Measurement Techniques

In Chapter 3, different suction and volumetric measurement techniques were presented and evaluated. The used techniques were classified into direct and indirect, based on the measuring mechanism. The suction measurement methods used were: (i) commercially available tensiometers (UMS-T5), to directly measure matric suction; (ii) N-HCT, to directly measure matric suction; (iii) dielectric water potential permittivity sensor (Decagon MPS-6) , to indirectly measure matric suction; (iv) chilled-mirror dewpoint hygrometer (Decagon WP4-T) , to indirectly measure total suction for smaller soil specimens prepared in parallel; (v) soil relative humidity sensors (Vaisala HEMP-230), to indirectly estimate the total suction using the psychrometric law; (vi) electrical conductivity and volumetric water sensors (Decagon 5TE), to indirectly estimate the osmotic suction component; and (vii) vapour equilibrium using salt solutions, to indirectly measure total suction for parallel soil specimens. On the other hand, the volumetric measurement methods used were: (i) Digital Image Analysis (DIA), directly on specimens containing embedded sensors (DIA-D), and indirectly on specimens prepared in parallel (DIA-ID); (ii) Paraffin-Coating (PC), indirectly on parallel specimens; and (iii) Soil Shrinkage Curve (SSC) models, to indirectly estimate the void ratio of a specimen with given measured water content.

The suction measurement techniques were evaluated using different continuous drying experimental setups, and compared against total suction results from the WP4-T. The comparison between the matric and total suction measurements was made practical after proving the insignificance of the osmotic suction component using the electrical conductivity sensor method. The comparison between the different readings was made throughout the overlapping ranges.

Different SSCs were obtained, specific to each batch of soil prepared at different initial conditions. The SSCs were then fitted using an established SSC model equation. The fitted SSC equation was then considered intrinsic to the corresponding soil batch and used as a volumetric estimator for a given gravimetric water content (which is considered to be easily attainable experimentally). Having this fitted SSC equation for each soil batch allows determining uniform and complete-range Soil Water Retention Curves (SWRCs) by combining the suction measurements and water content readings obtained for each batch.

7.1.4. Chapter 4: The role of Inflexion-Point of the SWRC in the Shrinkage and Swelling Mechanism of Partially Saturated Soils

There are three principal variables describing the unsaturation shrinkage or saturation swelling behaviour of soils: (1) water content, in terms of gravimetric water content, volumetric water content, saturation degree; (2) volumetric changes, in terms of volumetric strains, porosity, void ratio; and (3) porewater pressure (i.e., matric suction). The continuous drying setup proposed in Chapter 3 (with the N-HCT) is used to obtain the evolution of these three principal variables simultaneously. The data allows the drawing of the SWRCs (porewater pressure – water content), SSCs (water content – void ratio), and SVC (Suction-Voids Curve). Coupling of the three curves, along with the desaturation rate of the SWRC (first order derivative), allows the identification of five consecutive desaturating stages in the drying path, four saturating stages in the wetting path, and the corresponding transitional points (i.e., the yielding points between two consecutive stages). An analytical, conceptual and mathematical analysis is given to each stage, explaining the physical behaviour at the macro and microstructure levels.

A special attention is paid to the inflexion point of the SWRC, where it was found to consistently coincide with the shrinkage limit of the same given soil. The inflexion point of the SWRC identifies the transition in the shrinkage process from intraparticle to interparticle domain, that is to say, the SWRC inflexion point indicates the point at which the macropores no longer shrink due to drying, whereas the shrinkage continues in the micropores.

On the other hand, a connection between the saturation-suction value (obtained from the end of the saturated stage of the SWRC), and the mechanical plastic yielding point has been established in the literature and confirmed in this study.

Multiple conclusions were driven for the wetting path as well, regarding the identification of the Water Entry Value (WEV), the Air Expulsion Value (AXV) and the inflexion point of the wetting path SWRC.

Identifying these transitional points on the SWRC directly indicates the strength of the hydromechanical coupling in the unsaturated soils behaviour, where the mechanical parameters (elastic to plastic yielding point, shrinkage-limit) can be obtained solely from the SWRC. This is of great interest for mechanical constitutive models for unsaturated soils since it can provide valuable calibration points and an upper limit to the suction effect on volumetric changes.

The proposed correlation between the inflexion points and the shrinkage and swelling limits is validated for a set of 36 different soils encompassing different soil types, fabrics and textures.

This gives the typical SWRCs an innovative role as indicators of soil mechanical behaviour and offers insights on the soil matrix and microstructure behaviour.

7.1.5. Chapter 5: Numerical Simulation of the Soil Desiccation Behaviour

Chapter 5 justifies the basis of the numerical Finite Element Modelling (FEM) process and the numerical simulator used. The chapter starts by explaining the formulation of the mass balance equations and the compositional approach adopted. The constitutive equations are introduced to relate the unknowns in the governing balance equations to the dependent variables while accounting implicitly for the influence of porosity changes. In the next part, the formulation of the boundary conditions is explained. The relevant parameters pertaining to the vapour and energy fluxes on the surface are obtained by comparing against the well-known energy balance equation and its corresponding formulation. The porewater evaporation from the perimetral cracks is accounted for by a progressive release of the lateral boundaries.

The chapter then presents the numerical analysis of an experimental soil drying test carried out on an initially slurry soil specimen with controlled temperature and relative humidity in a laboratory environmental chamber. The environmental chamber imposed drying conditions are translated into vapour and heat fluxes and transfer coefficients in the numerical boundary conditions. The soil parameters are translated into the constitutive parameters necessary to run the model. The simulations are provided in three separate blocks with gradually added complexity. Only a summary of the results and the gradual complexity approach are presented in the chapter. The simulations were assessed against experimental results on the basis of reproducing the evolution of the gravimetric water content, suction profile and soil relative humidity.

7.1.6. Chapter 6: Numerical Simulation of Laboratory Desiccation Tests at Different Initial conditions, and one Large-Scale Field Experiment Exposed to Free Atmospheric Conditions

The chapter presents a continuation of the previous one, with added complexities and refining to make the numerical model adaptable to different testing procedures, soil initial conditions, and imposed atmospheric conditions. The constitutive equations are adapted by including: (a) the

effect of suction on the volumetric changes, (b) the effect of porosity change on the SWRC, thermal conductivity and hydraulic conductivity, and (c) the power law for the liquid phase relative permeability. The hydraulic boundary conditions now account for: (a) net solar radiation in the field as heat flow rate; (b) the effect of soil surface resistance on the transfer coefficients; (c) the null wind effect on the diffusivity in the environmental chamber as the dehumidifier automatically switches off when the imposed relative humidity goes below the designated 30% value; (d) the rainfall in the field as a liquid infiltration rate; and (e) the varying atmospheric relative humidity and temperature at smaller intervals.

The chapter then presents the numerical simulation of seven laboratory experiments in the environmental chamber, each carried out at a different set of initial conditions (water content and compaction level). Finally, a similar simulation was carried out for a large-scale field experiment exposed to external atmospheric conditions over the span of one full year.

The results demonstrate the high responsiveness of the numerical boundary conditions and the full capture of the THM behaviour of the drying soil, in terms of the evolution of: (i) gravimetric water content; (ii) suction profile at different depths for the duration of the experiment; (iii) volumetric water content; (iv) temperature profile; (v) CIF, estimated numerically from the perimetral shrinkage; and (vi) displacement profiles. The results showed the significance of having direct atmospheric measurements on site for better numerical replication. Having such a full-model is contingent on proper identification of the soil constitutive parameters and the atmospheric variables.

7.2. General Conclusion

The research from this work is part of an ongoing investigation on the volumetric and hydraulic behaviour of deformable partially saturated soils. The objective of the research was first aimed at studying the soil cracking mechanism. To capture the cracking mechanism, a good comprehension of the principles of unsaturated soil mechanics is needed. One of the main principal variables characterising unsaturated soils is suction. Measuring and quantifying suction is of utmost importance, as it relates to different constitutive parameters and characteristics of the desaturating soil. To adequately quantify it in a direct manner, one must use HCTs. As such, the Northumbria N-HCTs were acquired and validated, as a first step towards expanding the understanding of the volumetric and hydraulic behaviour of the unsaturated soils.

The main aim from this work was to finally achieve a fully capable numerical model that can replicate, to a high accuracy, the THM behaviour of soils exposed to external atmospheric conditions. Having such a fully capable model would significantly reduce the uncertainties regarding the design process of any infrastructure project using soils as engineered material (e.g., embankments, liners, slopes, landfills). To obtain such a powerful model, the constitutive equations and their corresponding parameters must be well-defined. First, the SWRCs of different soils at varying initial conditions were obtained using advanced experimental techniques, employing direct and indirect suction and volumetric measurements methods (N-HCT, Digital Image Analysis). Having the SWRCs and SSCs helped in getting the relationship between suction and void ratio, and therefore obtaining the related parameters of the mechanical model. Other parameters were obtained by fitting to experimental results (hydraulic conductivity, relative permeability).

The next step was to characterise the boundary conditions. This entailed all the relevant factors: wind, temperature, relative humidity, rainfall, and solar radiation. Each of these factors was incorporated in the formulation of the imposed numerical boundary condition. The relevant formulation to translate these factors into a numerical boundary condition was obtained by comparing against established energy balance equations, and from meteorological science. The factors were translated into liquid infiltration rate from rainfall, imposed vapour concentration from atmospheric relative humidity, imposed heat flow rate from net solar radiation and atmospheric temperature, and transfer coefficients from wind speed and soil surface resistance. The resulting model successfully captures with high responsivity the THM behaviour of the laboratory specimens prepared at different compaction levels, and the larger-scale field experiment. In its current form, the developed numerical model can predict the soil-atmosphere interaction process of soil structures exposed to external atmospheric conditions. This prediction feature is valuable for advanced designs of infrastructures using soils as engineering materials.

7.3. Future works

The future works herein are planned to go on after this thesis and are also presented as suggestions for other researchers. The remarks for future lines of work can be divided into four separate fields:

7.3.1. Experimental

- Further improving or refurbishing of the HCTs and expanding its suction measurement range by: (i) developing new ceramic filters with higher AEV, and (ii) enhancing the first saturation and re-saturation by increasing the positive water pressure applied.
- Obtaining the wetting path SWRCs for all the soil batches with different initial conditions (only few wetting paths were obtained in comparison to the number of drying paths in the SWRCs).
- Developing a continuous wetting setup with the N-HCT to compare against the discrete wetting measurements, and to better represent and understand the wetting path. The need for more equalisation times was noticed in the wetting path for the few measurements taken.
- Study the hysteresis phenomenon with respect to the three principal variables. Hysteresis was noticed to occur in SWRCs and SVCs, however when it comes to the relationship between water content and void ratio (i.e., SSC), there was no evidence of major hysteresis in the volumetric behaviour.

7.3.2. Environmental chamber

- Carrying out more experiments in the environmental chamber on different compaction levels: the Scale-Hammer compaction effort, and static compaction.
- Applying wetting stages in the environmental chamber by only increasing the RH of the overlying atmosphere. This can be carried out by avoiding the condensation of water droplets on the surface that occurs due to the functioning technique of the humidifier used (nebuliser). To achieve that, the specimens must be hanging above a pure distilled water solution in a tightly closed chamber, similar to the functionality of a large-scale desiccator.
- Studying the maximum attained water content (maximum saturation) that can be achieved by only increasing the RH, while avoiding water droplet condensation on the specimen soil surface. This will allow the study of different saturation rates, and the understanding of the variation between conductive and advective fluxes in the wetting path.

7.3.3. Field experiments

- Carrying out more field experiments on the different compaction levels that have already been tested in the environmental chamber. Studying the different compaction level specimens in the field would further verify the importance of carrying out preliminary less-expensive laboratory tests in the environmental chamber. Additionally, it will further verify the applicability of the same numerical model with the same constitutive parameters for different geometries.

7.3.4. Numerical

- Implementing another mechanical model for the mechanical prediction of unsaturated soil behaviour during the drying and wetting cycles. The new mechanical model must replicate the change in void ratio and the cracking process as well. The formation of plastic strains, large volumetric strains, and collapsing must be accounted for in the mechanical model.
- Introducing a mesh defragmentation technique by setting a detachment criterion at the joints between mesh elements resembling the location of the crack initiation. The criterion can be implemented by setting a threshold on the achieved tensile stress or suction at the joints.

References

Abou Najm, M.; Mohtar, R.H.; Weiss, J.; Braudeau, E., 2009: Assessing internal stress evolution in unsaturated soils. *Water Resources Research*, **45**.

Abriola, L.M.; Pinder, G.F., 1985: A Multiphase Approach to the Modeling of Porous Media Contamination by Organic Compounds: 1. Equation Development. *Water Resources Research*, **21**, 11–18.

Abu-Hamdeh, N.H.; Reeder, R.C., 2000: Soil Thermal Conductivity Effects of Density, Moisture, Salt Concentration, and Organic Matter. *Soil Science Society of America Journal*, **64**, 1285–1290.

Abu-Hamdeh, N.H., 2003: Thermal properties of soils as affected by density and water content. *Biosystems Engineering*, **86**, 97–102.

Abu-Hejleh, A.N.; Znidarčić, D., 1995: Desiccation Theory for Soft Cohesive Soils. *Journal of Geotechnical Engineering*, **121**, 493–502.

Agus, S.S.; Schanz, T., 2005: Comparison of four methods for measuring total suction. *Vadose Zone Journal*, **4**, 1087–1095.

Al-Dakheeli, H.; Asce, S.M.; Bulut, R.; Asce, M., 2019: Interrelationship between Elastic Deformation and Soil-Water Characteristic Curve of Expansive Soils. *Journal of Geotechnical and Geoenvironmental Engineering*, **145** (4).

Albrecht, B.A.; Benson, C. H., 2001: Effect of Desiccation on Compacted Natural Clays. *Journal of Geotechnical and Geoenvironmental Engineering*, **127**, 67–75.

Alonso, E.; Olivella, S.; Arnedo, D., 2006: Mechanisms of gas transport in clay barriers. *Cuadernos de geología ibérica. Journal of iberian geology: an international publication of earth sciences*, 175–196.

Alonso, E.; Gens, A.; Josa, A., 1990: A constitutive model for partially saturated soils. *Géotechnique*, **40**, 405–430.

Aluwihare, S.; Watanabe, K., 2003: Measurement of Evaporation on Bare Soil and Estimating Surface Resistance. *Journal of Environmental Engineering*, **129**, 1157–1168.

- Amarasiri, A.L.; Costa, S.; Kodikara, J.K., 2011: Determination of cohesive properties for mode I fracture from compacted clay beams. *Canadian Geotechnical Journal*, **48**, 1163–1173.
- Amarasiri, A.L.; Kodikara, J.K., 2013: Numerical Modeling of Desiccation Cracking Using the Cohesive Crack Method. *International Journal of Geomechanics*, **13**, 213–221.
- An, N.; Hemmati, S.; Cui, Y.J., 2017: Assessment of the methods for determining net radiation at different time-scales of meteorological variables. *Journal of Rock Mechanics and Geotechnical Engineering*, **9**, 239–246.
- Asahina, D.; Houseworth, J.E.; Birkholzer, J.T.; Rutqvist, J.; Bolander, J. E., 2014: Hydro-mechanical model for wetting/drying and fracture development in geomaterials. *Computers and Geosciences*, **65**, 13–23.
- Assouline, S., 2005: On the relationships between the pore size distribution index and characteristics of the soil hydraulic functions. *Water Resources Research*, **41**, 1–8.
- ASTM D1557, 2021: Standard Test Methods for Laboratory Compaction Characteristics of Soil Using Modified Effort (56,000 ft-lbf/ft³ (2,700 kN-m/m^{3ASTM International, **04.08**, 13.}
- ASTM D698-12, 2021: Standard Test Methods for Laboratory Compaction Characteristics of Soil Using Standard Effort (12,400 ft-lbf/ft³ (600 kN-m/m^{3ASTM International, **04.08**, 13.}
- Ávila, Á.G., 2004: *Estudio de la retracción y el agrietamiento de arcillas: Aplicación a la arcilla de Bogotá*. *PhD Thesis*, Universitat Politècnica de Catalunya, Barcelona.
- Aziz, K.; Settari, A., 1979: Petroleum reservoir simulation. *Applied Science Publishers*, London.
- Azizi, A.; Jommi, C.; Musso, G., 2017: A water retention model accounting for the hysteresis induced by hydraulic and mechanical wetting-drying cycles. *Computers and Geotechnics*, **87**, 86-98.
- Azizi, A.; Musso, G.; Jommi, C., 2019: Effects of repeated hydraulic loads on microstructure and hydraulic behaviour of a compacted clayey silt. *Canadian Geotechnical Journal*, **57**, 1.
- Bagheri, M.; Rezaia, M.; Mousavi Nezhad, M., 2018: Cavitation in high-capacity tensiometers: Effect of water reservoir surface roughness. *Geotechnical Research*, **5**, 81–95.
- Barrera, M., 2002: *Estudio experimental del comportamiento hidromecánico de suelos colapsables*. *PhD Thesis*, Universitat Politècnica de Catalunya, Barcelona.

- Bear, J., 1969: Hydrodynamic Dispersion. *Roger J. M. de Wiest (ed.) Flow through porous media. Academic Press, New York.*, 109–199.
- Bear, J., 1979: Dynamics of Fluids in Porous Media. *Dover Publications, New York.*
- Bear, J.; Bachmat, Y., 1986: Macroscopic modelling of transport phenomena in porous media. 2: Applications to mass, momentum and energy transport. *Transport in Porous Media*, **1**, 241–269.
- Bear, J.; Bensabat, J.; Nir, A., 1991: Heat and mass transfer in unsaturated porous media at a hot boundary: I. One-dimensional analytical model. *Transport in Porous Media*, **6**, 281–298.
- Bird, R.B.; Stewart, W.E.; Lightfoot, E.N., 1960: *Transport Phenomena. Contraceptive delivery systems*, Vol. 1.
- Bishop, A., 1959: The Principle of Effective Stress. *Technisk Ukeblad*, **106**, 859–863.
- Bittelli, M.; Ventura, F.; Campbell, G.S.; Snyder, R.L.; Gallegati, F.; Rossi Pisa, P., 2008: Coupling of heat, water vapor, and liquid water fluxes to compute evaporation in bare soils. *Journal of Hydrology*, **362**, 191–205.
- Blight, G.E., 1967: Effective Stress Evaluation for Unsaturated Soils. *Journal of the Soil Mechanics and Foundations Division*, **93**, 125–148.
- Blight, G. E., 1997: The Rankine Lecture. *Géotechnique*, **47**, 713–767.
- Boivin, P., 2007: Anisotropy, cracking, and shrinkage of vertisol samples Experimental study and shrinkage modeling. *Geoderma*, **138**, 25–38.
- Boso, M.; Romero, E.; Tarantino, A., 2003: The use of different suction measurement techniques to determine water retention curves. In: Schanz, T. (ed.), *Unsaturated Soils: Experimental Studies*. Springer-Verlag, Berlin, pp. 171–181.
- Boudreau, B.P., 1996: The diffusive tortuosity of fine-grained unlithified sediments. *Geochimica et Cosmochimica Acta*, **60**, 3139–3142.
- Bozkurt, O.; Pennell, K.G.; Suuberg, E.M., 2009: Simulation of the Vapor Intrusion Process for Non-Homogeneous Soils Using a Three-Dimensional Numerical Model. *Ground water monitoring & remediation*, **29**, 92.

- Braudeau, E.; Costantini, J.M.; Bellier, G.; Colleuille, H., 1999: New Device and Method for Soil Shrinkage Curve Measurement and Characterization. *Soil Science Society of America Journal*, **63**, 525–535.
- Bronswijk, J.J.B., 1990: Shrinkage Geometry of a Heavy Clay Soil at Various Stresses. *Soil Science Society of America Journal*, **54**, 1500–1502.
- Brooks, R.H.; Corey, A.T., 1964: *Hydraulic properties of porous media*. Colorado State University [Hydrology and Water Resources Program], Fort Collins.
- Brown, R.W.; Collins, J.M., 1980: A Screen-Caged Thermocouple Psychrometer and Calibration Chamber for Measurements of Plant and Soil Water Potential. *Agronomy Journal*, **72**, 851–854.
- Brutsaert, W., 1982: Evaporation into the Atmosphere: Theory, History and Applications. *Environmental Fluid Mechanics*, **1**.
- Bulut, R.; Leong, E.C., 2008: Indirect Measurement of Suction. *Geotechnical and Geological Engineering*, **26**, 633–644.
- Burdine, N.T., 1953: Relative Permeability Calculations From Pore Size Distribution Data. *Journal of Petroleum Technology*, **5**, 71–78.
- Cai, G.; Zhou, A.; Sheng, D., 2014: Permeability function for unsaturated soils with different initial densities. *Canadian Geotechnical Journal*, **51**, 1456–1467.
- Camillo, P.J.; Gurney, R.J.; Schmugge, T.J., 1983: A soil and atmospheric boundary layer model for evapotranspiration and soil moisture studies. *Water Resources Research*, **19**, 371–380.
- Camillo, P.J.; Gurney, R.J., 1986: A resistance parameter for bare-soil evaporation models. *Soil Science*, **141**, 95–105.
- Campbell, G.S.; Norman, J.M., 1977: An Introduction to Environmental Biophysics. *Heidelberg Science Library*. Springer, New York.
- Campbell, G. S., 1979: Improved thermocouple psychrometers for measurement of soil water potential in a temperature gradient. *Journal of Physics E: Scientific Instruments*, **12**, 739.
- Campbell, G. S.; Norman, J.M., 1998: An Introduction to Environmental Biophysics. Springer, New York.

- Campbell, G.S.; Smith, D.M.; Teare, B.L., 2007: Application of a Dew Point Method to Obtain the Soil Water Characteristic. *Experimental Unsaturated Soil Mechanics*. Springer, Berlin Heidelberg, **112**, 71–77.
- Cao, T.D.; Thota, S.K.; Vahedifard, F.; Amirlatifi, A., 2021: General Thermal Conductivity Function for Unsaturated Soils Considering Effects of Water Content, Temperature, and Confining Pressure. *Journal of Geotechnical and Geoenvironmental Engineering*, **147**, 04021123.
- Carman, P.C., 1937: Fluid Flow through Granular Beds. *AIChE*, **15**, 150.
- Carman, P.C., 1956: Flow of gases through porous media, *Butterworths*, London.
- Caruso, M.; Tarantino, A., 2004: A shearbox for testing unsaturated soils at medium to high degrees of saturation. *Géotechnique*, **54**, 281–284.
- Ce, Z.; Xi-Jun, Z.; Guo-Qing, C.; Jian, L.; Cheng-Gang, Z., 2020: Analysis of applicability of SWRC equation to different types of soils and its prediction method considering initial dry density. *Japanese Geotechnical Society Special Publication*, **8**, 194–199.
- Chen, H.; Chen, K.; Yang, M.; Xu, P., 2020: A fractal capillary model for multiphase flow in porous media with hysteresis effect. *International Journal of Multiphase Flow*, **125**, 103208.
- Chertkov, V.Y.; Ravina, I., 1999: Tortuosity of Crack Networks in Swelling Clay Soils. *Soil Science Society of America Journal*, **63**, 1523–1530.
- Chertkov, V.Y., 2000: Modeling the pore structure and shrinkage curve of soil clay matrix. *Geoderma*, **95**, 215–246.
- Chertkov, V.Y., 2003: Modelling the shrinkage curve of soil clay pastes. *Geoderma*, **112**, 71–95.
- Chiu, C.F.; Ng, C.W.W., 2012: Coupled water retention and shrinkage properties of a compacted silt under isotropic and deviatoric stress paths. *Canadian Geotechnical Journal*, **49**, 928–938.
- Conciani, W.; Hermann, P.S.; Soares, M.M., 1995: The time domain reflectometry to study matrix suction. *Proceedings of the 1st Int. Conf. on Unsaturated Soils*, Paris, **3**, 1481–1486.
- Copernicus, 2022: C3S launches data and apps for water management | Copernicus. *European Commission - Copernicus, Europe's eyes on Earth*.

- Cordero, J.; Najdi, A.; Encalada, D.; Prat, P. C.; Ledesma, A., 2020: Experimental and numerical analysis of soil desiccating cracks in compacted and non-compacted specimens. *E3S Web of Conferences, UNSAT 2020*. EDP Sciences, **195**, 03021.
- Cordero, J.A., 2019: Experimental analysis of soil cracking due to environmental conditions. *PhD Thesis*. Universitat Politècnica de Catalunya, Barcelona.
- Cordero, J.A.; Prat, P.; Ledesma, A., 2021: Experimental analysis of desiccation cracks on a clayey silt from a large-scale test in natural conditions. *Engineering Geology*, **292**, 106256.
- Cornelis, W.M.; Corluy, J.; Medina, H.; Díaz, J.; Hartmann, R.; Van Meirvenne, M.; Ruiz, M. E., 2006: Measuring and modelling the soil shrinkage characteristic curve. *Geoderma*, **137**, 179–191.
- Corte, A.; Higashi, A., 1964: Experimental research on desiccation cracks in soil. U.S. Army Materiel Command Cold Regions Research & Engineering Laboratory.
- Costa, S.; Kodikara, J.; Shannon, B., 2013: Salient factors controlling desiccation cracking of clay in laboratory experiments. *Géotechnique*, **63**, 18–29.
- Cuadrado, A., 2019: Análisis THM de la interacción suelo-atmósfera en suelos arcillosos sometidos a desecación. *PhD Thesis*. Universitat Politècnica de Catalunya, Barcelona.
- Cuadrado, A.; Najdi, A.; Ledesma, A.; Olivella, S.; Prat, P., 2022: THM analysis of a soil drying test in an environmental chamber: The role of boundary conditions. *Computers and Geotechnics*, **141**, 104495.
- Cui, Y.J.; Tang, A.M.; Mantho, A.T.; De Laure, E., 2007: Monitoring Field Soil Suction Using a Miniature Tensiometer. *Geotechnical Testing Journal*, **31**, 95–100.
- Cui, K.; Défossez, P.; Cui, Y.J.; Richard, G., 2010: Soil compaction by wheeling: Changes in soil suction caused by compression. *European Journal of Soil Science*, **61**, 599–608.
- Cui, Y. J.; Ta, A.N.; Hemmati, S.; Tang, A.M.; Gatmiri, B., 2012: Experimental and numerical investigation of soil-atmosphere interaction. *Engineering Geology*, **165**, 20–28.
- Cunningham, M.R., 2000: The mechanical behaviour of a reconstituted, unsaturated soil. *PhD Thesis*. Imperial College London.
- Cunningham, M.R.; Ridley, A.M.; Dineen, K.; Burland, J.B., 2003: The mechanical behaviour of a reconstituted unsaturated silty clay. *Géotechnique*, **53**, 183–194.

- Davenport, A.G.; Grimmond, C.S.B.; Oke, T.R.; Wieringa, J., 2000: Estimating the roughness of cities and sheltered country. *15th conference on probability and statistics in the atmospheric sciences/12th conference on applied climatology*, Asheville, NC, American Meteorological Society, Applied climatology, 96-99.
- Davis, G.B.; Rayner, J.L.; Trefry, M.G.; Fisher, S.J.; Patterson, B.M., 2005: Measurement and Modeling of Temporal Variations in Hydrocarbon Vapor Behavior in a Layered Soil Profile. *Vadose Zone Journal*, **4**, 225–239.
- Decagon Devices, 2015: *Decagon Devices VP-3 Operating Manual*.
- Decagon Devices Inc., 2010: *WP4C Dewpoint Potential Meter Operator's Manual*. Pullman WA.
- Decagon Devices Inc., 2017: *MPS-2 & MPS-6 Dielectric Water Potential Sensors - Operator's Manual*.
- Delage, P.; Howat, M.D.; Cui, Y.J., 1998: The relationship between suction and swelling properties in a heavily compacted unsaturated clay. *Engineering Geology*, **50**, 31–48.
- Desaulniers, D.E.; Cherry, J.A.; Fritz, P., 1981: Origin, age and movement of pore water in argillaceous Quaternary deposits at four sites in southwestern Ontario. *Journal of Hydrology*, **50**, 231–257.
- Dexter, A.R.; Bird, N.R.A., 2001: Methods for predicting the optimum and the range of soil water contents for tillage based on the water retention curve. *Soil and Tillage Research*, **57**, 203–212.
- Dexter, A.R., 2004: Soil physical quality: Part I. Theory, effects of soil texture, density, and organic matter, and effects on root growth. *Geoderma*, **120**, 201–214.
- Dexter, A.R.; Czyz, E.A.; Richard, G.; Reszkowska, A., 2008: A user-friendly water retention function that takes account of the textural and structural pore spaces in soil. *Geoderma*, **143**, 243–253.
- Dong, Y.; McCartney, J.S.; Lu, N., 2015: Critical Review of Thermal Conductivity Models for Unsaturated Soils. *Geotechnical and Geological Engineering*, **33**, 207–221.
- Drumm, E.C.; Boles, D.R.; Glenn, V.W., 1977: Desiccation Cracks Result in Preferential Flow. *Environmental Geotechnics*, 22–26.

- Du, C., 2020: Comparison of the performance of 22 models describing soil water retention curves from saturation to oven dryness. *Vadose Zone Journal*, **19**.
- Duffie, J.; Beckman, W., 1991: *Solar Engineering of Thermal Processes*. 2nd edn. John Wiley & Sons Inc, New York.
- Dullien, F.A.L., 1992: *Porous Media: Fluid Transport and Fluid Structures*. 1st edn. Academic Press Limited.
- EDF, 2019: How climate change plunders the planet. *Environmental Defense Fund*, www.edf.org.
- El-Maarry, M.R.; Watters, W.; McKeown, N.K.; Carter, J.; Noe Dobrea, E.; Bishop, J.L.; Pommerol, A.; Thomas, N., 2014: Potential desiccation cracks on Mars: A synthesis from modeling, analogue-field studies, and global observations. *Icarus*, **241**, 248–268.
- El Hajjar, A.; Ouahbi, T.; Eid, J.; Hattab, M.; Taibi, S., 2020: Shrinkage cracking of unsaturated fine soils: New experimental device and measurement techniques. *Strain*, **56**.
- Encalada, D.; Najdi, A.; Mendes, J.; Prat, P.; Ledesma, A., 2023: Influence of Compaction on the Soil Shrinkage and Swelling Curves. *UNSAT 2023 8th International Conference on Unsaturated Soils*.
- Evet, S.R.; Prueger, J.H.; Tol, J.A., 2011: Water and Energy Balances in the Soil–Plant–Atmosphere Continuum. In: Huang, P. M., Y. Li & M. E. Sumner (eds.), *Handbook of Soil Sciences: Properties and Processes*. 2nd edn. CRC Press., Boca Raton, Florida, 6–44.
- Farouki, O., 1986: Thermal properties of soils. *Trans tech publications*, Clausthal-Zellerfeld, **11**.
- Faust, C R.; Mercer, J.W., 1979: Geothermal reservoir simulation: 1. Mathematical models for liquid- and vapor-dominated hydrothermal systems. *Water Resources Research*, **15**, 23–30.
- Fayer, M.J.; Simmons, C.S., 1995: Modified Soil Water Retention Functions for All Matrix Suctions. *Water Resources Research*, **31**, 1233–1238.
- Fetzer, T.; Vanderborcht, J.; Mosthaf, K.; Smits, K.M.; Helmig, R., 2017: Heat and water transport in soils and across the soil-atmosphere interface: 2. Numerical analysis. *Water Resources Research*, **53**.

- Fleureau, J.M.; Verbrugge, J.C.; Huerigo, P.J.; Gomes Correia, A.; Kheirbek-Saoud, S., 2002: Aspects of the behaviour of compacted clayey soils on drying and wetting paths. *Canadian Geotechnical Journal*, **39**, 1341–1357.
- Foken, T., 2008: *Micrometeorology*. Springer Berlin Heidelberg.
- Fourar, M.; Lenormand, R., 1998: A Viscous Coupling Model for Relative Permeabilities in Fractures. *SPE Annual Technical Conference and Exhibition*, New Orleans, Louisiana.
- Fredlund, D.G.; N.R. Morgenstern, 1977: Stress state variables for unsaturated soils. *Journal of Geotechnical and Geoenvironmental Engineering*, **103**, 447–466.
- Fredlund, D.G.; Rahardjo, H., 1993: *Soil Mechanics for Unsaturated Soils*. John Wiley & Sons, Inc., Hoboken, NJ, USA.
- Fredlund, D.G.; Xing, A., 1994: Equations for the soil-water characteristic curve. *Canadian Geotechnical Journal*, **31**, 521–532.
- Fredlund, D.G., 2000: The 1999 R.M. Hardy Lecture: The implementation of unsaturated soil mechanics into geotechnical engineering. *Canadian Geotechnical Journal*, **37**, 963–986.
- Fredlund, D.G.; Houston, S.L., 2013: Interpretation of soil-water characteristic curves when volume change occurs as soil suction is changed. *Advances in Unsaturated Soils - Proceedings of the 1st Pan-American Conference on Unsaturated Soils, PanAmUNSAT 2013*. Taylor and Francis - Balkema, 15–31.
- Fredlund, D.G.; Fredlund, M.D., 2020: Application of ‘estimation procedures’ in unsaturated soil mechanics. *Geosciences (Switzerland)*, **10**, 1–22.
- Gallipoli, D.; Wheeler, S.J.; Karstunen, M., 2003: Modelling the variation of degree of saturation in a deformable unsaturated soil. *Géotechnique*, **53**, 105–112.
- Gallipoli, D., 2012: A hysteretic soil-water retention model accounting for cyclic variations of suction and void ratio. *Géotechnique*, **62**, 605–616.
- Garratt, J.R., 1977: Review of Drag Coefficients over Oceans and Continents. *Monthly Weather Review*, **105**, 915–929.
- Gens, A.; Alonso, E.; Lloret, A., 1995: Effect of structure on the volumetric behaviour of a compacted soil. *Proceedings of the first international conference on unsaturated soils, UNSAT 95*, Paris, France. **1**, 83–88.

- Gens, A.; Olivella, S., 2001: THM phenomena in saturated and unsaturated porous media. *Revue Française de Génie Civil*, **5**, 693–717.
- Giráldez, J.V.; Sposito, G.; Delgado, C., 1983: A General Soil Volume Change Equation: I. The Two-Parameter Model. *Soil Science Society of America Journal*, **47**, 419–422.
- Gran, M., 2015: Coupled heat and water flow dynamics in dry soils: Application to a multilayer waste cover. *PhD Thesis*. Universitat Politècnica de Catalunya, Barcelona.
- Groenevelt, P.H.; Grant, C.D., 2001: Re-evaluation of the structural properties of some British swelling soils. *European Journal of Soil Science*, **52**, 469–477.
- Groenevelt, P.H.; Grant, C.D., 2002: Curvature of shrinkage lines in relation to the consistency and structure of a Norwegian clay soil. *Geoderma*, **106**, 235–245.
- Groenevelt, P.H.; Grant, C.D., 2004: A new model for the soil-water retention curve that solves the problem of residual water contents. *European Journal of Soil Science*, **55**, 479–485.
- Grotzinger, J.P.; Arvidson, R.E.; Bell, J.F.; Calvin, W.; Clark, B.C.; Fike, D.A.; Golombek, M.; Greeley, R.; Haldemann, A.; Herkenhoff, K.E.; Jolliff, B.L.; Knoll, A.H.; Malin, M.; McLennan, S.M.; Parker, T.; Soderblom, L.; Sohl-Dickstein, J.N.; Squyres, S.W.; Tosca, N.J. et al., 2005: Stratigraphy and sedimentology of a dry to wet eolian depositional system, Burns formation, Meridiani Planum, Mars. *Earth and Planetary Science Letters*, **240**, 11–72.
- Guan, Y.; Fredlund, D.G., 1997: Use of the tensile strength of water for the direct measurement of high soil suction. *Canadian Geotechnical Journal*, **34**, 604–614.
- Santos, G.G.; Medrado da Silva, E.; Leandro Marchão, R.; Marques da Silveira, P.; Bruand, A.; James, F.; Becquer, T., 2011: Analysis of physical quality of soil using the water retention curve: Validity of the S-index. *Comptes Rendus Geoscience*, **343**, 295–301.
- Gupta, S.C.; Sharma, P.P.; DeFranchi, S.A., 1989: Compaction Effects on Soil Structure. *Advances in Agronomy*, **42**, 311–338.
- Gurr, C.G.; Marshall, T.J.; Hutton, J.T., 1952: Movement of water in soil due to a temperature gradient. *Soil Science*, **74**.
- Haines, W.B., 1923: The volume-changes associated with variations of water content in soil. *The Journal of Agricultural Science*, **13**, 296–310.

- Han, J.; Zhou, Z.; Liu, J.; Zbicinski, I.; Zhang, Z., 2013: Dynamics of Soil Water Evaporation during Soil Drying: Laboratory Experiment and Numerical Analysis. *The Scientific World Journal*, **2013**.
- Han, Z.; Zhao, G.; Lin, J.; Fan, K.; Zou W., 2022: Influences of temperature and moisture histories on the hydrostructural characteristics of a clay during desiccation. *Engineering Geology*, **297**, 106533.
- Hassanizadeh, M.; Gray, W.G., 1979: General conservation equations for multi-phase systems: 1. Averaging procedure. *Advances in Water Resources*, **2**, 131–144.
- Hassanizadeh, S.M., 1986a: Derivation of basic equations of mass transport in porous media, Part 1: Macroscopic balance laws. *Advances in Water Resources*, **9**, 196–206.
- Hassanizadeh, S.M., 1986b: Derivation of basic equations of mass transport in porous media, Part 2: Generalized Darcy's and Fick's laws. *Advances in Water Resources*, **9**, 207–222.
- Helmig, R., 1997: Multiphase flow and transport processes in the subsurface : a contribution to the modeling of hydrosystems. Springer-Verlag.
- Hillel, D., 1980: *Fundamentals of Soil Physics*, **1**.
- Hillel, D.; Mottes, J., 1996: Effect of plate impedance, wetting method, and aging on soil. *Soil Science*, **102**, 135–139.
- Hillel, D., 2004: *Introduction to Environmental Soil Physics*. Elsevier Inc.
- Hou, X.; Qi, S.; Li, T.; Guo, S.; Wang Y.; Li, Y., 2020: Microstructure and soil-water retention behaviour of compacted and intact silt loess. *Engineering Geology*, **277**, 105814.
- IPCC, 2022: *Climate Change 2022: Impacts, Adaptation, and Vulnerability*. Contribution of Working Group II to the Sixth Assessment Report of the Intergovernmental Panel on Climate Change [H.-O. Pörtner, D.C. Roberts, M. Tignor, E.S. Poloczanska, K. Mintenbeck, A. Alegría, M. Craig, S. Langsdorf, S. Löschke, V. Möller, A. Okem, B. Rama (eds.)]. Cambridge University Press.
- Jennings, J.E.B.; Burland, J.B., 1962: Limitations to the Use of Effective Stresses in Partly Saturated Soils. *Géotechnique*, **12**, 125–144.
- Jensen, M.; Burman, R.; Allen, R., 1990: *Evapotranspiration and Irrigation Water Requirements*. ASCE, New York.

- Joffe, S.M., 1982: Momentum and heat transfers in the surface layer over a frozen sea. *Boundary-Layer Meteorology*, **24**, 211–229.
- Johnston, J.R.; Hill, H.O., 1945: A Study of the Shrinking and Swelling Properties of Rendzina Soils. *Soil Science Society of America Journal*, **9**, 24–29.
- Jommi, C., 2000: Remarks on the constitutive modelling of unsaturated soils. *Experimental Evidence and Theoretical Approaches in Unsaturated Soils*, 147–162.
- Juanes, R.; Patzek, T.W., 2004: Relative Permeabilities for Strictly Hyperbolic Models of Three-Phase Flow in Porous Media. *Transport in Porous Media*, **57**, 125–152.
- Kalinski, R.; Kelly, W., 1993: Estimating Water Content of Soils from Electrical Resistivity. *Geotechnical Testing Journal*, **16**, 323–329.
- Khosravi, A.; Shahbazan, P.; Pak, A., 2018: Impact of hydraulic hysteresis on the small strain shear modulus of unsaturated sand. *Soils and Foundations*, **58**, 344–354.
- Klausner, Y., 1991: Fundamentals of Continuum Mechanics of Soils. Springer-Verlag, London.
- Kleppe, J.; Olson, R., 1985: Desiccation Cracking of Soil Barriers. In: Johnson, A., R. Frobel, N. Cavalli & C. Pettersson (eds.), *Hydraulic Barriers in Soil and Rock*, ASTM International, West Conshohocken, PA, p. 275.
- Kodikara, J.K.; Barbour, S.L.; Fredlund, D.G., 2000: Desiccation cracking of soil layers. *Unsaturated soils for Asia. Proceedings of the Asian Conference on Unsaturated Soils, UNSAT-ASIA 2000*, Singapore, 693–698.
- Kondo, J.; Saigusa, N.; Sato, T.; Kondo, J., 1990: A Parameterization of Evaporation from Bare Soil Surfaces. *Journal of Applied Meteorology and Climatology*, **29** (5), 385–389.
- Konrad, J.M.; Ayad, R., 1997: Desiccation of a sensitive clay: field experimental observations. *Canadian Geotechnical Journal*, **34**, 929–942.
- Kosugi, K., 1994: Three-parameter lognormal distribution model for soil water retention. *Water Resources Research*, **30**, 891–901.
- Kozeny, J., 1927: Ueber kapillare Leitung des Wassers im Boden. *Sitzungsber Akad. Wiss., Wien*, **136**, 271–306.
- Kristensen, A.H.; Thorbjørn, A.; Jensen, M.P.; Pedersen, M.; Moldrup, P., 2010: Gas-phase diffusivity and tortuosity of structured soils. *Journal of Contaminant Hydrology*, **115**, 26–33.

- Lakshmikantha, M.R., 2009: Experimental and theoretical analysis of cracking in drying soils. *PhD Thesis*. Universitat Politècnica de Catalunya, Barcelona.
- Lakshmikantha, M.R.; Prat, P.; Ledesma, A., 2009: Image analysis for the quantification of a developing crack network on a drying soil. *Geotechnical Testing Journal*, **32**, 1–11.
- Lakshmikantha, M.R.; Prat, P.; Ledesma, A., 2012: Experimental evidence of size effect in soil cracking. *Canadian Geotechnical Journal*, **49**, 264–284.
- Lakshmikantha, M.R.; Prat, P.; Ledesma, A., 2013: Evidences of hierarchy in cracking of drying soils. *Geotechnical Special Publication*, 782–789.
- Lakshmikantha, M.R.; Prat, P.; Ledesma, A., 2018: Boundary effects in the desiccation of soil layers with controlled environmental conditions. *Geotechnical Testing Journal*, **41**, 675–697.
- Lauritzen, C.W., 1948: Apparent specific volume and shrinkage characteristics of soil materials. *Soil Science*, **65**, 155–179.
- Lehmann, P.; Assouline, S.; Or, D., 2008: Characteristic lengths affecting evaporative drying of porous media. *Physical Review E - Statistical, Nonlinear, and Soft Matter Physics*, **77**, 056309.
- Leong, E.C.; Tripathy, S.; Rahardjo, H., 2003: Total suction measurement of unsaturated soils with a device using the chilled-mirror dew-point technique. *Géotechnique*, **53**, 173–182.
- Levatti, H.; Prat, P.; Ledesma, A., 2019: Numerical and experimental study of initiation and propagation of desiccation cracks in clayey soils. *Computers and Geotechnics*, **105**, 155–167.
- Li, K.; Horne, R.N., 2006: Comparison of methods to calculate relative permeability from capillary pressure in consolidated water-wet porous media. *Water Resources Research*, **42**.
- Li, X.; Zhang, L.M., 2009: Characterization of dual-structure pore-size distribution of soil. *Canadian Geotechnical Journal*, **46**, 129–141.
- Li, L.; Zhang, X.; Li, P., 2018: Evaluating a new method for simultaneous measurement of soil water retention and shrinkage curves. *Acta Geotechnica*, **14**, 1021–1035.
- Lin, B.; Cerato, A.B., 2013: Hysteretic soil water characteristics and cyclic swell-shrink paths of compacted expansive soils. *Bulletin of Engineering Geology and the Environment*, **72**, 61–70.
- Liu, G.; Toll, D.G.; Kong, L.; Asquith, J.D., 2020: Matric suction and volume characteristics of compacted clay soil under drying and wetting cycles. *Geotechnical Testing Journal*, **43**.

- Lloret, A.; Alonso, E., 1985: State surfaces for partially saturated soils. *Proceedings of the eleventh international conference on soil mechanics and foundation engineering*, San Francisco.
- Lloret, A.; Ledesma, A.; Rodriguez, R.L.; Sánchez, M.J.; Olivella, S.; Suriol, J., 1998: Crack initiation in drying soils. *Proceedings of the Second International Conference on Unsaturated Soils*, Beijing, China, **1**.
- Lourenço, S.; Gallipoli, D.; Toll, D.; Evans, F.; Medero, G., 2007: Determination of the Soil Water Retention Curve with Tensiometers, *Experimental Unsaturated Soil Mechanics*, **112**, 95–102.
- Lourenço, S.D.N.; Gallipoli, D.; Toll, D.G.; Augarde, C.E.; Evans, F.D., 2011: A new procedure for the determination of soil-water retention curves by continuous drying using high-suction tensiometers., *Canadian Geotechnical Journal*, **48**, 327–335.
- Lozada, C.; Caicedo, B.; Thorel, L., 2019: A new climatic chamber for studying soil-atmosphere interaction in physical models. *International Journal of Physical Modelling in Geotechnics*, **19**, 286–304.
- Lu, N.; Likos, W.J., 2004: *Unsaturated Soil Mechanics*. Hoboken, Wiley.
- Lu, N.; Kaya, M.; Collins, B.D.; Godt, J.W., 2013: Hysteresis of Unsaturated Hydromechanical Properties of a Silty Soil. *Journal of Geotechnical and Geoenvironmental Engineering*, **139**, 507–510.
- Lu, N.; Asce, F.; Dong, Y.; Asce, A.M., 2015: Closed-Form Equation for Thermal Conductivity of Unsaturated Soils at Room Temperature. *Journal of Geotechnical and Geoenvironmental Engineering*, **141**, 04015016.
- Lu, N.; Khorshidi, M., 2015: Mechanisms for Soil-Water Retention and Hysteresis at High Suction Range. *Journal of Geotechnical and Geoenvironmental Engineering*, **141**, 04015032.
- Lu, N.; Dong, Y., 2017: Correlation between Soil-Shrinkage Curve and Water-Retention Characteristics. *Journal of Geotechnical and Geoenvironmental Engineering*, **143**, 04017054.
- Marcial, D.; Delage, P.; Cui, Y.J., 2002: On the high stress compression of bentonites. *Canadian Geotechnical Journal*, **39**, 812–820.
- Marinho, F.A.M.; Take, W.A.; Tarantino, A., 2008: Tensiometric and axis translation techniques for suction measurement. *Geotechnical and Geological Engineering*, **26**, 615–631.

- Marinho, F.A.M.; Teixeira, P.F., 2009: The Use of a High Capacity Tensiometer for Determining the Soil Water Retention Curve. *Soil and Rocks*, **32**, (2), 91–96.
- Mašín, D., 2010: Predicting the dependency of a degree of saturation on void ratio and suction using effective stress principle for unsaturated soils. *International Journal for Numerical and Analytical Methods in Geomechanics*, **34**, 73–90.
- Mata, C.; Romero, E.; Ledesma, A., 2002: Hydro-chemical effects on water retention in bentonite-sand mixtures. *Proc. 3rd Int. Conf. on Unsaturated Soils, UNSAT 2002*, **1**, 283-288.
- Matthews, G.P.; Laudone, G.M.; Gregory, A.S.; Bird, N.R.A.; de G. Matthews, A.G.; Whalley, W.R., 2010: Measurement and simulation of the effect of compaction on the pore structure and saturated hydraulic conductivity of grassland and arable soil. *Water Resources Research*, **46**, 5501.
- Matyas, E.L.; Radhakrishna, H.S., 1968: Volume Change Characteristics of Partially Saturated Soils. *Géotechnique*, **18**, 432–448.
- McGarry, D.; Malafant, K.W.J., 1987: The Analysis of Volume Change in Unconfined Units of Soil. *Soil Science Society of America Journal*, **51**, 290.
- McKay, L.D.; Cherry, J.A.; Gillham, R.W., 1993: Field experiments in a fractured clay till: 1. Hydraulic conductivity and fracture aperture. *Water Resources Research*, **29**, 1149–1162.
- Meilani, I.; Rahardjo, H.; Leong, E.C.; Fredlund, D.G., 2002: Mini suction probe for matric suction measurements. *Canadian Geotechnical Journal*, **39**, 1427–1432.
- Mendes, J.; Najdi, A.; Encalada, D.; Prat, P.; Ledesma, A., 2023: Towards the development on new high capacity tensiometers capable of measuring soil matric suction beyond 3 MPa. *Canadian Geotechnical Journal*, **59**, (9).
- Mendes, J.; Toll, D.G.; Augarde, C.E.; Gallipoli, D., 2008: A system for field measurement of suction using high capacity tensiometers. *Unsaturated Soils: Advances in Geo-Engineering - Proceedings of the 1st European Conference on Unsaturated Soils, E-UNSAT 2008*, 1–8.
- Mendes, J.; Buzzi, O., 2014: Performance of the University of Newcastle high capacity tensiometers, *Unsaturated Soils: Research & Applications*, **1**.
- Mendes, J.; Toll, D.G., 2016: Influence of Initial Water Content on the Mechanical Behavior of Unsaturated Sandy Clay Soil. *International Journal of Geomechanics*, **16**, D4016005.

- Mendes, J.; Gallipoli, D.; Boeck, F.; Tarantino, A., 2020: A comparative study of high capacity tensiometer designs. *Physics and Chemistry of the Earth, Parts A/B/C*, **120**, 102901.
- Mendes, J.; Najdi, A.; Encalada, D.; Prat, P. C.; Ledesma, A.; Jamali, A.; Buzzi, O.; Walter Bruno, A.; Toll, D.; Gallipoli, D., 2023: High-capacity Tensiometers: design performance and behaviours. *UNSAT 2023 8th International Conference on Unsaturated Soils*.
- Miller, C. J.; Mi, H.; Yesiller, N., 1998: Experimental analysis of desiccation crack propagation in clay liners. *Journal of the American Water Resources Association*, **34**, 677–686.
- Millington, R.J.; Quirk, J.P., 1961: Permeability of porous solids. *Transactions of the Faraday Society*, **57**, 1200–1207.
- Milly, P.C.D., 1982: Moisture and heat transport in hysteretic, inhomogeneous porous media: A matrix head-based formulation and a numerical model. *Water Resources Research*, **18**, 489–498.
- Mitchell, A.R., 1992: Shrinkage Terminology: Escape from “Normalcy”. *Soil Science Society of America Journal*, **56**, 993–994.
- Moldrup, P.; Olesen, T.; Gamst, J.; Schjønning, P.; Yamaguchi, T.; Rolston, D.E., 2000: Predicting the Gas Diffusion Coefficient in Repacked Soil Water-Induced Linear Reduction Model. *Soil Science Society of America Journal*, **64**, 1588–1594.
- Monin, A.S.; Obukhov, A.M., 1954: Basic laws of turbulent mixing in the surface layer of the atmosphere. *Originally published in Tr. Akad. Nauk SSSR Geophys. Inst.*, **24**, 163–187.
- Mora Ortiz, R.S., 2016: Efectos de la microestructura en el comportamiento hidromecánico de suelos compactados. *Doctoral Thesis*. Universitat Politècnica de Catalunya, Barcelona.
- Morris, P.H.; Graham, J.; Williams, D.J., 1992: Cracking in drying soils. *Canadian Geotechnical Journal*, **29**, 263–277.
- Mualem, Y., 1974: A conceptual model of hysteresis. *Water Resources Research*, **10**, 514–520.
- Mualem, Y., 1976: Hysteretic models for prediction of the hydraulic conductivity of unsaturated porous media. *Water Resources Research*, **12**, 1248–1254.
- Mualem, Y., 1978: Hydraulic conductivity of unsaturated porous media: Generalized macroscopic approach. *Water Resources Research*, **14**, 325–334.

- Musso, G.; Azizi, A.; Jommi, C., 2019: A microstructure-based elastoplastic model to describe the behaviour of a compacted clayey silt in isotropic and triaxial compression. *Canadian Geotechnical Journal*, **57**, 7.
- Nahlawi, H.; Kodikara, J.K., 2006: Laboratory experiments on desiccation cracking of thin soil layers. *Geotechnical and Geological Engineering*, **24**, 1641–1664.
- Najdi, A.; Encalada, D.; Mendes, J.; Prat, P.; Ledesma, A., 2023a: Evaluating innovative direct and indirect soil suction and volumetric measurement techniques for the determination of soil water retention curves following drying and wetting paths. *Engineering Geology*. submitted: *second round of review*.
- Najdi, A.; Encalada, D.; Mendes, J.; Rouainia, M.; Prat, P.; Ledesma, A., (b): The role of inflexion-point in the shrinkage mechanism of partially saturated soils. *Submitted for publication, Géotechnique*.
- Najdi, A.; Cuadrado, A.; Prat, P.; Ledesma, A., (c): Numerical analysis of soil desiccating cracks in different compaction levels and imposed atmospheric conditions. *Submitted for publication, Computers and Geotechnics*.
- Nam, S.; Gutierrez, M.; Diplas, P.; Petrie, J.; Wayllace, A.; Lu, N.; Muñoz, J. J., 2010: Comparison of testing techniques and models for establishing the SWCC of riverbank soils. *Engineering Geology*, **110**, 1–10.
- NASA, 2005: Effects | Facts – Climate Change: Vital Signs of the Planet. *Earth Will Continue to Warm and the Effects Will Be Profound*.
- Nishimura, T.; Fredlund, D.G., 2000: Relationship between shear strength and matric suction in an unsaturated silty soil. *Unsaturated Soils for Asia*. 1st edn. CRC Press, 563–568.
- Obukhov, A.M., 1971: Turbulence in an atmosphere with a non-uniform temperature. *The Institute of Theoretical Geophysics of the Academy of Sciences of the U.S.S.R.*
- Oh, S.; Lu, N.; Kim, Y. K.; Lee, S. J.; Lee, S. R., 2012: Relationship between the Soil-Water Characteristic Curve and the Suction Stress Characteristic Curve: Experimental Evidence from Residual Soils. *Journal of Geotechnical and Geoenvironmental Engineering*, **138**, 47–57.
- Oke, T.R., 1987: *Boundary Layer Climates*. 2nd edn. Methuen.
- Olivella, S.; Carrera, J.; Gens, A.; Alonso, E.E., 1994: Nonisothermal multiphase flow of brine and gas through saline media. *Transport in Porous Media*, **15**, 271–293.

- Olivella, S.; Gens, A.; Carrera, J.; Alonso, E., 1996: Numerical formulation for a simulator (CODE_BRIGHT) for the coupled analysis of saline media. *Engineering Computations*, **13**.
- Olsen, P.A.; Haugen, L.E., 1998: A new model of the shrinkage characteristic applied to some Norwegian soils. *Geoderma*, **83**, 67–81.
- Omid, G.H.; Thomas, J.C.; Brown, K.W., 1996: Effect of desiccation cracking on the hydraulic conductivity of a compacted clay liner. *Water, Air, and Soil Pollution* 1996 89:1, **89**, 91–103.
- Oorthuis, R.; Hürlimann, M.; Fraccica, A.; Lloret, A.; Moya, J.; Puig-Polo, C.; Vaunat, J., 2018: Monitoring of a full-scale embankment experiment regarding soil-vegetation-atmosphere interactions. *Water (Switzerland)*, **10**, 1–23.
- Oorthuis, R., 2022: Monitoring and analysis of soil-vegetation-atmosphere interactions at slope and catchment scale : Implications for mass-wasting in natural and man-made slopes. *Doctoral Thesis*. Universitat Politècnica de Catalunya, Barcelona.
- Panday, S.; Corapcioglu, M.Y., 1989: Reservoir transport equations by compositional approach. *Transport in Porous Media*, **4**, 369–393.
- Parlange, M.B.; Cahill, A.T.; Nielsen, D.R.; Hopmans, J.W.; Wendroth, O., 1998: Review of heat and water movement in field soils. *Soil and Tillage Research*, **47**, 5–10.
- Peng, X.; Horn, R., 2005: Modeling Soil Shrinkage Curve across a wide range of soil types. *Soil Science Society of America Journal*, **69**, 584–592.
- Peng, X.; Zhang, Z.B.; Wang, L.L.; Gan, L., 2012: Does soil compaction change soil shrinkage behaviour?. *Soil and Tillage Research*, **125**, 89-95.
- Perera, Y.Y.; Zapata, C.E.; Houston, W.N.; Houston, S.L., 2005: Prediction of the soil-water characteristic curve based on grain-size-distribution and index properties, *Advances in Pavement Engineering*, Geo-Frontiers Congress.
- Péron, H.; Hueckel, T.; Laloui, L., 2007: An Improved Volume Measurement for Determining Soil Water Retention Curves. *Geotechnical Testing Journal*, **30**, 100167.
- Peroni, N.; Tarantino, A., 2005: Measurement of osmotic suction using the squeezing technique. *Unsaturated Soils: Experimental Studies*, 159–168.
- Pham, H.Q., 2001: An Engineering Model of Hysteresis for Soil-Water Characteristic Curves. *PhD Thesis*. University of Saskatchewan, Saskatoon, SK.

- Phene, C.J.; Hoffman, G.J.; Rawlins, S.L., 1971: Measuring Soil Matric Potential in situ by Sensing Heat Dissipation within a Porous Body: I. Theory and Sensor Construction. *Soil Science Society of America Journal*, **35**, 27–33.
- Philip, J.R.; De Vries, D.A., 1957: Moisture movement in porous materials under temperature gradients. *Transactions American Geophysical Union*, **38**, 222–232.
- Piegari, E.; Di Maio, R., 2013: Estimating soil suction from electrical resistivity. *Natural Hazards and Earth System Sciences*, **13**, 2369–2379.
- Pinder, G.F.; Abriola, L.M., 1986: On the simulation of nonaqueous phase organic compounds in the subsurface. *Water Resources Research*, **22**, 109S–119S.
- Pollock, D.W., 1986: Simulation of fluid flow and energy transport processes associated with high-level radioactive waste disposal in unsaturated alluvium. *Water Resources Research*, **22**, 765–775.
- Poulsen, T.G.; Furman, A.; Liberzon, D., 2018: Effect of near-surface wind speed and gustiness on horizontal and vertical porous medium gas transport and gas exchange with the atmosphere. *European Journal of Soil Science*, **69**, 279–289.
- Poulsen, T.G.; Cai, W.; Garg, A., 2020: Water evaporation from cracked soil under moist conditions as related to crack properties and near-surface wind speed. *European Journal of Soil Science*, **71**, 627–640.
- Pruess, K., 1987: TOUGH User's Guide. *Lawrence Berkeley Lab, CA (USA); Nuclear Regulatory Commission, Washington, DC (USA). Div. of Waste Management.*
- Qian, J.; Lin, Z.; Shi, Z., 2021: Soil-water retention curve model for fine-grained soils accounting for void ratio–dependent capillarity. *Canadian Geotechnical Journal*, **59**, 498–509.
- Rasband, W.S. 2006: ImageJ. *US national Institute of Health, Bethesda, Md.*
- Ravindran, S.; Gratchev, I., 2022: Effect of Water Content on Apparent Cohesion of Soils from Landslide Sites. *Geotechnics Journal: Recent Advances in Geotechnical Engineering*, special issue, **2**, 385–394.
- Reuters, 2021: U.N. climate report likely to deliver stark warnings on global warming | www.reuters.com.

- Reynolds, O.R., 1883: XXIX. An experimental investigation of the circumstances which determine whether the motion of water shall be direct or sinuous, and of the law of resistance in parallel channels. *Philosophical Transactions of the Royal Society of London*, **174**, 935–982.
- Richard, G.; Cousin, I.; Sillon, J.F.; Bruand, A.; Guérif, J., 2001: Effect of compaction on the porosity of a silty soil: influence on unsaturated hydraulic properties. *European Journal of Soil Science*, **52**, 49–58.
- Ridley, A.M.; Burland, J.B., 1993: A new instrument for the measurement of soil moisture suction. *Géotechnique*, **43**, 321–324.
- Ridley, A.M., 1993: *The measurement of soil moisture suction. PhD Thesis*. Imperial College London (University of London).
- Robinson, R.A.; Stokes, R.H., 1959: Electrolyte Solutions: The measurement and interpretation of conductance. *Journal of The Electrochemical Society*, **107**, 250C.
- Rodríguez, R.; Sánchez, M.; Ledesma, A.; Lloret, A., 2007: Experimental and numerical analysis of desiccation of a mining waste. *Canadian Geotechnical Journal*, **44**, 644–658.
- Romero, E.; Gens, A.; Lloret, A., 1999: Water permeability, water retention and microstructure of unsaturated compacted Boom clay. *Engineering Geology*, **54** (1), 117-127.
- Romero, E.; Vaunat, J., 2000: Retention curves of deformable clays. *International Workshop on Unsaturated Soils; Experimental evidence and theoretical approaches in unsaturated soils*, International Workshop on Unsaturated Soils; Experimental evidence and theoretical approaches in unsaturated soils, 91–108.
- Romero, E.; Jommi, C., 2008: An insight into the role of hydraulic history on the volume changes of anisotropic clayey soils. *Water Resources Research*, **44**, 5.
- Romero, E.; Della Vecchia, G.; Jommi, C., 2011: An insight into the water retention properties of compacted clayey soils. *Géotechnique*, **61**, (4), 313-328.
- Rosenberg, N.J.; Blad, B.L.; Verma, S.B., 1983: *Microclimate: The Biological Environment*, Wiley and Sons, **2**.
- Rossi, C.; Nimmo, J.R., 1994: Modeling of soil water retention from saturation to oven dryness. *Water Resources Research*, **30**, 701–708.

- Saito, H.; Šimůnek, J.; Mohanty, B.P., 2006: Numerical Analysis of Coupled Water, Vapor, and Heat Transport in the Vadose Zone. *Vadose Zone Journal*, **5**, 784–800.
- Saiyouri, N.; Hicher, P.Y.; Tessier, D., 2000: Microstructural approach and transfer water modelling in highly compacted unsaturated swelling clays. *Mechanics of Cohesive-frictional Materials*, **5**, 41–60.
- Sakai, M.; Toride, N.; Šimůnek, J., 2009: Water and Vapor Movement with Condensation and Evaporation in a Sandy Column; Water and Vapor Movement with Condensation and Evaporation in a Sandy Column. *Soil Science Society of America Journal*, **73**, 707–717.
- Sánchez, M.; Manzoli, O.L.; Guimarães, L.J.N., 2014: Modeling 3-D desiccation soil crack networks using a mesh fragmentation technique. *Computers and Geotechnics*, **62**, 27–39.
- Schelde, K.; Thomsen, A.; Heidmann, T.; Schjønning, P.; Jansson, P.E., 1998: Diurnal fluctuations of water and heat flows in a bare soil. *Water Resources Research*, **34**, 2919–2929.
- Shahraeeni, E.; Lehmann, P.; Or, D., 2012: Coupling of evaporative fluxes from drying porous surfaces with air boundary layer: Characteristics of evaporation from discrete pores. *Water Resources Research*, **48**.
- Shen, L.; Chen, Z., 2007: Critical review of the impact of tortuosity on diffusion. *Chemical Engineering Science*, **62**, 3748–3755.
- Sheng, D.; Fredlund, D.G.; Gens, A., 2008: A new modelling approach for unsaturated soils using independent stress variables. *Canadian Geotechnical Journal*, **45**, 511–534.
- Sibley, J.; Williams, D., 1989: A Procedure for Determining Volumetric Shrinkage of an Unsaturated Soil. *Geotechnical Testing Journal*, **12**, 187.
- Šimůnek, J.; Šejna, M.; Saito, H.; Sakai, M.; van Genuchten, M., 2013: The HYDRUS-1D Software Package for Simulating the One-Dimensional Movement of Water, Heat, and Multiple Solutes in Variably-Saturated Media. Riverside, California.
- Sivakumar, V.; Wheeler, S.J., 2000: Influence of compaction procedure on the mechanical behaviour of an unsaturated compacted clay Part 1: Wetting and isotropic compression. *Géotechnique*, **50**, 359–368.
- Smits, K.M.; Cihan, A.; Sakaki, T.; Illangasekare, T.H., 2011: Evaporation from soils under thermal boundary conditions: Experimental and modeling investigation to compare equilibrium- and nonequilibrium-based approaches. *Water Resources Research*, **47**.

- Smits, K.M.; Ngo, V.V.; Cihan, A.; Sakaki, T.; Illangasekare, T.H., 2012: An evaluation of models of bare soil evaporation formulated with different land surface boundary conditions and assumptions. *Water Resources Research*, **48**.
- Song, W.K.; Cui, Y.J.; Tang, A.M.; Ding, W.Q., 2013: Development of a Large-Scale Environmental Chamber for Investigating Soil Water Evaporation. *Geotechnical Testing Journal*, **36**.
- Sposito, G.; Giráldez, J.V., 1976: Thermodynamic Stability and The Law of Corresponding States in Swelling Soils. *Soil Science Society of America Journal*, **40**, 352–358.
- Stannard, D.I., 1992: Tensiometers. Theory, construction, and use. *Geotechnical Testing Journal*, **15**, 48–58.
- Stein, N.; Grotzinger, J.P.; Schieber, J.; Mangold, N.; Hallet, B.; Newsom, H.; Stack, K.M.; Berger, J. A.; Thompson, L.; Siebach, K. L.; Cousin, A.; Le Mouélic, S.; Minitti, M.; Sumner, D.Y.; Fedo, C.; House, C.H.; Gupta, S.; Vasavada, A.R.; Gellert, R. et al., 2018: Desiccation cracks provide evidence of lake drying on Mars, Sutton Island member, Murray formation, Gale Crater. *Geology*, **46**, 515–518.
- Stenke, F.; Toll, D.G.; Gallipoli, D., 2006: Comparison of Water Retention Curves for Clayey Soils Using Different Measurement Techniques. *Unsaturated Soils 2006*, 1451–1461.
- Stewart, R.D.; Abou Najm, M.R.; Rupp, D.E.; Selker, J.S., 2012: An Image-Based Method for Determining Bulk Density and the Soil Shrinkage Curve. *Soil Science Society of America Journal*, **76**, 1217–1221.
- Stirk, G., 1954: Some aspects of soil shrinkage and the effect of cracking upon water entry into the soil. *Australian Journal of Agricultural Research*, **5**, 279.
- Stirling, R.A.; Hughes, P.; Davie, C.T.; Glendinning, S., 2015: Tensile behaviour of unsaturated compacted clay soils-A direct assessment method. *Applied Clay Science*, 123–133.
- Stirling, R.A.; Glendinning, S.; Davie, C.T., 2017: Modelling the deterioration of the near surface caused by drying induced cracking. *Applied Clay Science*, **146**, 176–185.
- Stoltz, G.; Gourc, J.P.; Oxarango, L., 2010: Liquid and gas permeabilities of unsaturated municipal solid waste under compression. *Journal of Contaminant Hydrology*, **118**, 27–42.
- Stull, R.B., 1988: An introduction to boundary layer meteorology. Atmospheric and Oceanographic Sciences Library, ATSL, **13**.

- Sun, D.; Sheng, D.; Xiang, L.; Sloan, S.W., 2008: Elastoplastic prediction of hydro-mechanical behaviour of unsaturated soils under undrained conditions. *Computers and Geotechnics*, **35**, 845–852.
- Sun, S.F., 1982: Moisture and heat transport in a soil layer forced by atmospheric conditions. *University of Connecticut*.
- Sun, W.; Sun, D.; Fang, L.; Liu, S., 2014: Soil-water characteristics of Gaomiaozhi bentonite by vapour equilibrium technique. *Journal of Rock Mechanics and Geotechnical Engineering*, **6**, 48–54.
- Tagesson, T., 2012: *Turbulent transport in the atmospheric surface layer*. CM Gruppen AB. Stockholm.
- Take, W.A.; Bolton, M.D., 2003: Tensiometer saturation and the reliable measurement of soil suction. *Géotechnique*, **54**, 159–172.
- Tang, A. M.; Cui, Y J.; Le, T.T., 2007: A study on the thermal conductivity of compacted bentonites. *Applied Clay Science*, **41**, 181–189.
- Tang, C.S.; Shi, B.; Liu, C.; Suo, W.Bin; Gao, L., 2011: Experimental characterization of shrinkage and desiccation cracking in thin clay layer. *Applied Clay Science*, **52**, 69–77.
- Tarantino, A.; Mongiovi, L., 2001: Experimental procedures and cavitation mechanisms in tensiometer measurements. *Geotechnical and Geological Engineering*, **19**, 189–210.
- Tariq, A.U.R.; Durnford, D.S., 1993: Soil volumetric shrinkage measurements: A simple method. *Soil Science*, **155**, 325–330.
- Taylor, S.A.; Cavazza, L., 1954: The Movement of Soil Moisture in Response to Temperature Gradients1. *Soil Science Society of America Journal*, **18**, 351.
- Teng, J.; Yasufuku, N.; Liu, Q.; Liu, S., 2014: Experimental evaluation and parameterization of evaporation from soil surface. *Natural Hazards*, **73**, 1405–1418.
- The World Bank, 2021: 10 Things the World Bank Group is doing on Climate Change. *Factsheet*.
- Toker, N.K.; Germaine, J.T.; Sjoblom, K.J.; Culligan, P.J., 2004: A new technique for rapid measurement of continuous soil moisture characteristic curves. *Géotechnique*, **54**, 179–186.

- Toll, D.; Asquith, J.D.; Fraser, A.; Hassan, A.A.; Liu, G.; Lourenço, S.D.N.; Mendes, J., 2015: Tensiometer techniques for determining soil water retention curves. *Sixth Asia-Pacific Conference on Unsaturated Soil*. Taylor & Francis, London, 15–22.
- Toll, D.G.; Lourenço, S.D.N.; Mendes, J.; Gallipoli, D.; Evans, F.D.; Augarde, C.E.; Cui, Y.J.; Tang, A.M.; Rojas, J.C.; Pagano, L.; Mancuso, C.; Zingariello, C.; Tarantino, A., 2011: Soil suction monitoring for landslides and slopes. *Quarterly Journal of Engineering Geology and Hydrogeology*, **44**, 23–33.
- Toll, D.G., 2012: Chapter 4: The behaviour of unsaturated soil. In: Huat, B. B. K., D. G. Toll & A. Prasad (eds.), *Handbook of Tropical Residual Soils Engineering*. 1st edn. CRC Press.
- Tollenaar, R.N.; van Paassen, L.A.; Jommi, C., 2017a: Observations on the desiccation and cracking of clay layers. *Engineering Geology*, **230**, 23-31.
- Tollenaar, R.N.; van Paassen, L.A.; Jommi, C., 2017b: Small-scale evaporation tests on clay: influence of drying rate on clayey soil layer. *Canadian Geotechnical Journal*, **55**, 3.
- Topp, G., 1971: Soil-Water Hysteresis: the Domain Theory Extended to Pore Interaction Conditions. *Soil Science Society of America Journal*, **35**, 219–225.
- Topp, G.C.; Davis, J.L.; Annan, A.P., 1980: Electromagnetic determination of soil water content: Measurements in coaxial transmission lines. *Water Resources Research*, **16**, 574–582.
- Towner, G.D., 1986: Anisotropic shrinkage of clay cores, and the interpretation of field observations of vertical soil movement. *Journal of Soil Science*, **37**, 363–371.
- Trabelsi, H.; Jamei, M.; Zenzri, H.; Olivella, S., 2012: Crack patterns in clayey soils: Experiments and modeling. *International Journal for Numerical and Analytical Methods in Geomechanics*, **36**, 1410–1433.
- Tran, D.K.; Ralaizafisolariovony, N.; Charlier, R.; Mercatoris, B.; Léonard, A.; Toye, D.; Degré, A., 2019: Studying the effect of desiccation cracking on the evaporation process of a Luvisol – From a small-scale experimental and numerical approach. *Soil and Tillage Research*, **193**, 142–152.
- Troeh, F.R.; Jabro, J.D.; Kirkham, D., 1982: Gaseous diffusion equations for porous materials. *Geoderma*, **27**, 239–253.

- Tuli, A.; Hopmans, J.W.; Rolston, D.E.; Moldrup, P., 2005: Comparison of Air and Water Permeability between Disturbed and Undisturbed Soils. *Soil Science Society of America Journal*, **69**, 1361–1371.
- U.S. Salinity Laboratory Staff, 1954: Diagnosis and Improvement of Saline and Alkali Soils. USDA Agriculture Handbook no. 60. *U.S. Government Printing Office, Washington, USA*.
- Ullman, W.J.; Aller, R.C., 1982: Diffusion coefficients in nearshore marine sediments. *Limnology and Oceanography*, **27**, 552–556.
- UMS AG, 2018: User Manual Pressure Transducer Tensiometer. München.
- Van Cappellen, P.; Gaillard, J.F., 1996: Biogeochemical dynamics in aquatic sediments. (G. Balint, B. Antala, C. Carty, J.M. A. Mabieme, I.B. Amar & A. Kaplanova, *Reviews in Mineralogy & Geochemistry*, **34**, 335–376.
- van de Griend, A.A.; Owe, M., 1994: Bare soil surface resistance to evaporation by vapor diffusion under semiarid conditions. *Water Resources Research*, **30**, 181–188.
- van Genuchten, M.T., 1980: A Closed-form Equation for Predicting the Hydraulic Conductivity of Unsaturated Soils. *Soil Science Society of America Journal*, **44**, 892–898.
- Van Wijk, W.R., 1963: Physics of Plant Environment. *Quarterly Journal of the Royal Meteorological Society*, **90**, 382.
- Vanapalli, S.K.; Fredlund, D. G.; Pufahl, D.E.; Clifton, A.W., 1996: Model for the prediction of shear strength with respect to soil suction. *Canadian Geotechnical Journal*, **33**, 379–392.
- Vanapalli, S.K.; Fredlund, D.G.; Pufahl, D.E., 1999: The influence of soil structure and stress history on the soil–water characteristics of a compacted till. *Géotechnique*, **49**, 143–159.
- Vaunat, J.; Romero, E.; Jommi, C, 2000: An elastoplastic hydro-mechanical model for unsaturated soils. *Experimental Evidence and Theoretical Approaches in Unsaturated Soils*, 1, 18.
- Villalobos, J.F.; Mateos, L.; Orgaz, F.; Fereres, E., 2002: *Fitotecnia : bases y tecnologías de la producción agrícola*. Mundi-Prensa, Madrid.
- Villar, M.V.; Gómez-Espina, R., 2007: Retention Curves of Two Bentonites at High Temperature. *Experimental Unsaturated Soil Mechanics*. Springer Berlin Heidelberg, 267–274.

- Vo, T.D.; Pouya, A.; Hemmati, S.; Tang, A.M., 2019: Modelling desiccation crack geometry evolution in clayey soils by analytical and numerical approaches. *Canadian Geotechnical Journal*, **56**, 720–729.
- Voss, C.I., 1984: SUTRA Users's Guide, U.S. Geological Survey, *Water Resources investigations, Report 48-4369*. Reston, Virginia.
- Wallace, J.M.; Hobbs, P.V., 2006: Atmospheric Science: An Introductory Survey. Elsevier Inc. **2**.
- Wang, Z.; Wu, L.; Wu, Q.J., 2000: Water-entry value as an alternative indicator of soil water-repellency and wettability. *Journal of Hydrology*, **231–232**, 76–83.
- Wen, T.; Wang, P.; Shao, L.; Guo, X., 2021: Experimental investigations of soil shrinkage characteristics and their effects on the soil water characteristic curve. *Engineering Geology Journal*, **284**, 106035.
- Wheeler, S.J.; Sivakumar, V., 1995: An elasto-plastic critical state framework for unsaturated soil. *Géotechnique*, **45**, 35–53.
- Wheeler, S. J.; Sharma, R.S.; Buisson, M. S. R., 2003: Coupling of hydraulic hysteresis and stress-strain behaviour in unsaturated soils. *Géotechnique*, **53**, 41–54.
- White, N.F.; Duke, H. R.; Sunada, D.K.; Corey, A.T., 1970: Physics of Desaturation in Porous Materials. *Journal of the Irrigation and Drainage Division*, **96**, 165–191.
- Wijaya, M.; Leong, E.C.; Rahardjo, H., 2015: Effect of shrinkage on air-entry value of soils. *Soils and Foundations*, **55**, 166–180.
- Wilson, G.W.; Fredlund, D.G.; Barbour, S.L., 1994: Coupled soil-atmosphere modelling for soil evaporation. *Canadian Geotechnical Journal*, **31**, 151–161.
- Wong, J.M.; Elwood, D.; Fredlund, D.G., 2019: Use of a three-dimensional scanner for shrinkage curve tests. *Canadian Geotechnical Journal*, **56**, 526–535.
- Wright, J.L.; Jensen, M.E., 1972: Peak Water Requirements of Crops in Southern Idaho. *Journal of the Irrigation and Drainage Division*, **98**, 193–201.
- Yamanaka, T.; Takeda, A.; Sugita, F., 1997: A modified surface-resistance approach for representing bare-soil evaporation: Wind tunnel experiments under various atmospheric conditions. *Water Resources Research*, **33**, 2117–2128.

Yesiller, N.; Miller, C.J.; Inci, G.; Yaldo, K., 2000: Desiccation and cracking behavior of three compacted landfill liner soils. *Engineering Geology*, **57**, 105–121.

Ying, Z.; Benahmed, N.; Cui, Y.J.; Duc, M., 2022: Determining osmotic suction through electrical conductivity for unsaturated low-plasticity soils. *Journal of Rock Mechanics and Geotechnical Engineering*, **14**, 1946-1955.

Zeng, H.; Tang, C. S.; Cheng, Q.; Zhu, C.; Yin, L.Y.; Shi, B., 2020: Drought-Induced Soil Desiccation Cracking Behavior With Consideration of Basal Friction and Layer Thickness. *Water Resources Research*, **56**, e2019WR026948.

Zhai, Q.; Rahardjo, H., 2012: Determination of soil–water characteristic curve variables. *Computers and Geotechnics*, **42**, 37–43.

Zhang, D.; Wang, J.; Chen, C., 2020: Gas and liquid permeability in the variably saturated compacted loess used as an earthen final cover material in landfills. *Waste Management*, **105**, 49–60.

Zhang, Z.F., 2011: Soil Water Retention and Relative Permeability for Conditions from Oven-Dry to Full Saturation. *Vadose Zone Journal*, **10**, 1299–1308.